7th International Conference on Magnetic Resonance Microscopy

"The Heidelberg Conference"

Organized by the Division of Spatially Resolved Magnetic Resonance of the Groupement Ampère

September 20th-25th, 2003
Snowbird Ski and Summer Resort
Snowbird, Utah, USA

BOOK OF ABSTRACTS

Table of Contents

WELCOME

Welcome to the 7th International Conference on Magnetic Resonance Microscopy (ICMRM) – also called the "Heidelberg Conference' - in the beautiful resort of Snowbird, Utah. Snowbird is nestled in the Wasatch Mountain range, immediately east of Salt Lake City.

The main conference is from Sept. 21-25 and is preceded by an Educational Program on Sept. 20-21. The first two meetings, in 1991 and 1993, were in Heidelberg and were followed by the 1995 meeting in Würzburg. Then the ICMRM crossed the Atlantic (as well as the Great Plains) and was held in Albuquerque, New Mexico in 1997. It returned to Heidelberg in 1999 and was next held in Nottingham in 2001. The current European participants for the most part will not only have crossed the Atlantic and the Great Plains, but will have crossed the Rocky Mountains as well.

The ICMRM is held under the auspices of the "Division of Spatially Resolved Microscopy" of the AMPERE Society. It traditionally has included many areas of magnetic resonance and imaging. In addition to sessions on biology, medicine, solid-state physics, chemistry, materials, porous media, diffusion/flow, instrumentation, and novel techniques, there will be a special Symposium on Non-Clinical Functional Magnetic Resonance, a Young Investigators' Session, and sessions on NMR in Gases and Hyperpolarized Nuclei.

The Educational Program consists of 3 sessions - Saturday morning, Saturday afternoon, and Sunday morning. The tutorial lectures will be presented by 7 outstanding scientists who have been chosen for their pedagogic skills as well as their scientific stature.

Approximately 200 people have booked rooms at Snowbird for the Conference. At last count 184 scientists have registered for the ICMRM. Of this number 78 have registered for both the Educational Program and the General Conference.

The General Meeting will open on Monday (Sept. 22) with a Keynote Lecture by Prof. Alex Pines. In addition, the General Program will include 24 invited talks, 4 talks by Young Investigator finalists, 42 contributed oral talks, and 97 contributed poster papers. (101 poster papers had been accepted, but 4 were eliminated due to difficulties of the presenters in obtaining visas.) All abstracts submitted for contributed oral presentation were initially read and scored by at least 2 members of the Program Committee, with the final decisions made by at least three members of the Local Organizing Committee.

Fifteen abstracts were submitted for the Young Investigators Program, of which 4 were selected for presentation in the Young Investigators Session. The finalists were chosen by a special committee on the basis of their submitted abstracts. The four finalists have their conference fees waived and will each present a 30-minute talk. The winner will be announced during the banquet on Thursday night, and will also receive a cash award.

Headquarters Hotel:
The headquarters hotel will be the Cliff Lodge at Snowbird, where all scientific sessions and some of the social sessions will be held. There will be a message board, and incoming telephone calls can be routed to you during the Conference. (The phone number for incoming calls is (801) 521-6040, ext. 5000.) In addition, computer facilities with Internet capability are available for participants. Snowbird personnel will be available to answer questions about the Snowbird facilities as well as recreational opportunities in the Snowbird area.

Registration:
Upon arrival, **all** participants (even those not staying at the Cliff Lodge) should go to the Conference registration desk at the Coat Room of the Cliff Lodge located in the foyer in front of the Ballrooms. There, you will pick up the welcome package. This package describes the many facilities and recreational opportunities at Snowbird and will include, among other things, this Book of Abstracts and a CD-Rom, as well as other items (e.g., name tags, special announcements, etc.)

The registration desk will be open as follows:

Saturday:	8:00 AM to 5:00 PM
Sunday:	8:00 AM to 6:00 PM
Monday:	8:00 AM to 6:00 PM
Tuesday:	8:00 AM to 1:00 PM
Wednesday:	8:00 AM to 6:00 PM
Thursday:	8:00 AM to 3:00 PM

Questions about registration and the Conference should be addressed to Meghan Webb or to Pat Burrus.

Venues for Scientific Sessions:
The Educational Program will be held in the Magpie Room, and the keynote, invited, and oral talks will be held in Ballrooms I and II. The poster sessions will be held in Ballroom III. In addition, the many corporate sponsors will have exhibits in the foyer in front of the Ballrooms.

There will be meeting of members of the Executive Committee and officers of the Spatially Resolved Division of the AMPERE Society on Monday, starting immediately after Session II (at about 1:00 PM). This meeting will be in the Wasatch Room (of the Cliff Lodge) and will include a complimentary lunch.

Information for Presenters:
For oral contributors: Presentations will be made using either PowerPoint or overhead transparency projector. For those using PowerPoint, your presentation should be uploaded to a single computer (which we will provide) by the morning of your presentation, preferably prior to the start of the first session or, for later speakers, during the first coffee break. Both a Macintosh G4 (running OS X) and a PC (running Windows 2000 or XP) will be available. Please bring your presentation on some form of portable media (CD-ROM, ZIP disk, or USB memory device).

For poster contributors: Poster size will be 46 inches wide by 48 inches high (117 cm by 122 cm). For those in Poster Session I on Monday evening, you may put up your posters any time prior to the session; they must be removed by Tuesday evening. For those in Poster Session II on Wednesday evening, you may put up your posters on Tuesday evening or Wednesday morning and they should stay there until the close of the conference.

Meals and other sources of food and refreshment:
The General Conference will be preceded in the evening of Sunday, Sept. 21, by a "Welcome Reception" in the Golden Cliff Room of the Cliff Lodge. This reception will start at 7:00 PM and will last until 9:00 PM (or whenever the refreshments run out).

Each morning a continental breakfast will be available for all registrants. During the Education Sessions (Saturday and Sunday) breakfasts will be served starting at 8:00 AM in the Magpie Room. During the General Conference (Monday through Friday), breakfast will be served at the back of Ballroom II, starting at 7:00 AM each day.

During the two poster sessions, light food will be served in Ballroom III.

Each half-day will be punctuated by a short "coffee break".

The Conference Banquet will be held in the Golden Cliff Room, starting at 7:30 PM on Thursday night (Sept. 25). This will be the last official event of the 7th ICMRM.

Box lunches will be provided for participants in the Conference Excursion on Tuesday afternoon.

In addition, there are a number of restaurants in the Snowbird area. These are described in the "Welcome Packet".

Bars are available in front of both the Aerie restaurant and the Mexican Cantina restaurant. These bars are normally open until 10:00 PM; however, during the ICMRM both bars will stay open as long as customers are there.

Recreational Opportunities and Excursion:
"Octoberfest" will be held Snowbird during weekends (Saturday and Sunday) in September. This occurs at the Deck in front of the Snowbird Plaza, and includes German music, food etc.

A tram ride to the top of Hidden Peak (11,000 ft altitude) is available at reduced prices to all conference participants. Hidden Peak is the mountain opposite the Snowbird resort.

In addition, there are many scenic hiking trails available both in Little Cottonwood Canyon (containing Snowbird and Alta) and in Big Cottonwood Canyon (containing Brighton and Solitude). Please see Pat Burrus or Snowbird personnel for suggestions.

The Conference excursion will involve travel in the Wasatch Mountains and includes visits to the Sundance Film Institute and to Park City, famous not only for skiing but also for holding the annual Sundance Film Festival (the major film festival for independent films). The excursion will also include driving up the canyon of the Provo River, with views of Bridal Veil Falls, Mt. Timpanogos, Deer Creek Reservoir, and Jordanelle Reservoir.

Sponsorship:
We are grateful to the following donors, who have generously provided support for this conference:

American Chemical Society
ATK Thiokol
Bruker Biospin
Cambridge Isotopes
Coherent Laser Group
Digital Signal Technology
Doty Scientific
Isotec (Division of Sigma-Aldrich)
Magnex Scientific
MR Technology
Quantum Magnetics
Perseus Books
Rapid Biomedical
Resonance Instruments, Inc.
Siemens Medical Solutions
Spectra Gases
Tecmag
Varian

Executive Steering Committee for 7th ICMRM:
David C. Ailion, University of Utah (Chair)
Robert E. Botto, Argonne National Laboratory (Co-Chair)
Eiichi Fukushima, New Mexico Resonance (President of Division)
Axel Haase, University of Wuerzburg (Secretary General of Division)
Peter J. McDonald, University of Surrey (past Chair)

Local Organizing Committee:
David C. Ailion, Department of Physics, University of Utah
Karen Anderson, ATK Thiokol Propulsion Lab
Pat Burrus, University of Utah Conference Services
Gernot Laicher, Department of Physics, University of Utah
Dennis Parker, Department of Radiology, University of Utah
Ronald Pugmire, Department of Chemistry, University of Utah
Kimberlee Potter, Department of Cellular Pathology and Genetics, Armed Forces Institute of Pathology Annex
Brian Saam, Department of Physics, University of Utah
Robert Wind, Pacific Northwest National Laboratory (PNNL)

The Program Committee for the 7th ICMRM consists of both the Local Organizing and the Executive Steering Committees.

Executive Committee of the Spatially Resolved Division of the AMPERE Society:

Chair:	E. Fukushima
Vice-Chair:	K. Kose
Treasurer:	R. Kimmich
Secretary General:	A. Haase
Vice Secretary General:	R. Botto
Former Division Chair:	P. Lauterbur
Conference Chair 2003:	D. Ailion
Former Conference Chairs:	R. Bowtell, P. McDonald
Advisors:	L. Berliner, B. Blümich

Acknowledgments:
The Chair is very grateful to the various members of the Executive Steering and Local Organizing Committees, who put in a lot of time both in planning the conference and in obtaining sponsorship funds. Particular thanks go to Gernot Laicher and Brian Saam who, together with the Chair, had weekly planning meetings during most of the winter and spring. Brian Saam, in particular, has created and maintained the Conference website.

The Chair would also like to specifically thank members of the secretarial staff (Heidi Frank, Shannon Ricks, Sandra Borgstrom, and Amber Cannon) of the University of Utah Physics Department for their help in typing the program and communicating with the various contributors.

We hope that you have an enjoyable and scientifically rewarding time at the 7th ICMRM.

Do you have enough space for MRI?

We have good news for you.

MRmicro

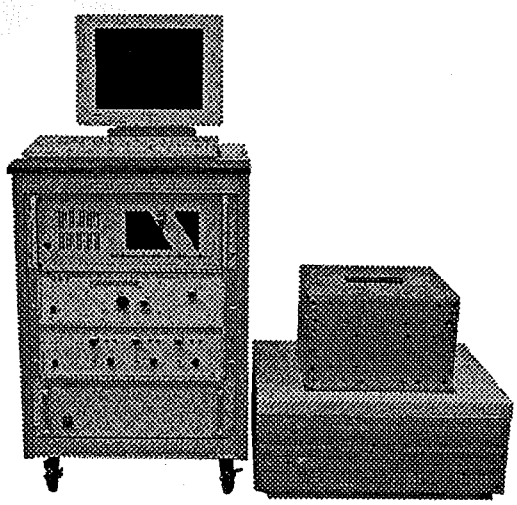

Compact system

MRmicro10 is an MR microscope that does not require a large room. The ring-type Halbach permanent magnet and the compact MRI console made MRmicro10 possible.

High performance at low cost

MRmicro10 is a high-performance yet reasonably priced MR microscope that is based on MRTechnology's "commercial-off-the-shelf" design philosophy.

Powerful software

The smart pulse compiler of MRmicro10 allows you to program pulse sequences with a simple text editor. The data acquisition and image processing software runs on Windows(R) for added convenience.

MRTechnology, Inc.
169-1 Kouya, Tsukuba, 300-2642 Japan
http://www.mrtechnology.co.jp
E-mail: info@mrtechnology.co.jp

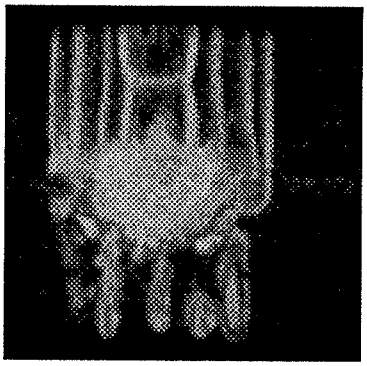

Welsh onion (60 μm)^3

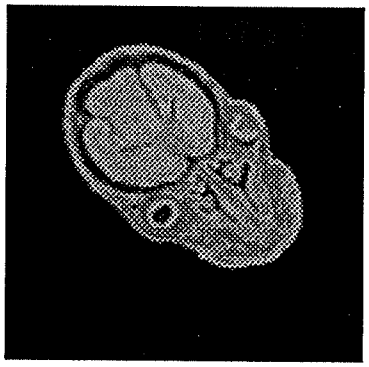

Mouse fetus, *in vitro* (100 μm)^3

Mouse fetus, *in vitro* (100 μm)^3

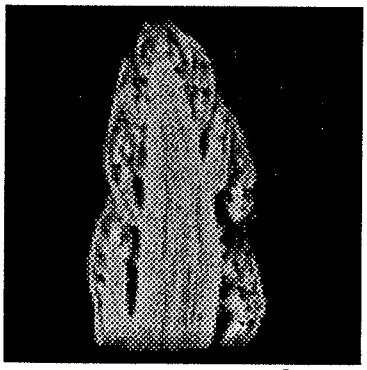

Asparagus (200 μm)^3

Mouse fetus, *in vitro* (150 μm)^3

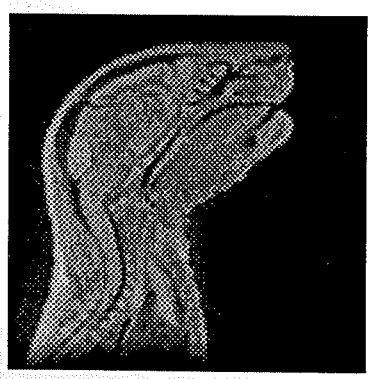

Mouse fetus, *in vitro* (150 μm)^3

Corporate Sponsorship of the 7th ICMRM

We gratefully acknowledges the financial support of our sponsors:

GOLD LEVEL: MRTechnology SIEMENS

SILVER LEVEL: Doty Scientific RESONANCE RAPID Biomedical Biomedizinische Geräte GmbH

BRONZE LEVEL:

The American Chemical Society
ATK Thiokol
Bruker Biospin
Cambridge Isotope Laboratories
Coherent Laser Group
Digital Signal Technology
Isotec
Magnex Scientific
Perseus Books Group
Quantum Magnetics
Spectra Gases
Tecmag
Varian

ICMRM PROGRAM

MONDAY, SEPT. 22 - MORNING

8:00 - 9:00 AM WELCOME AND KEYNOTE

8:00-8:15 **WELCOME**

8:15-9:00 **KEYNOTE LECTURE (Chair: *David C. Ailion*)**
Alexander Pines, *MR Spectroscopy and Microscopy at Various Distances and Angles.*

9:00 - 10:51 AM SESSION I: SOLID STATE NMR/NQR
Chair: *David C. Ailion*

INVITED LECTURES

9:00-9:30 **Robert Blinc**, *Disorder in $BaTiO_3$ and $SrTiO_3$.*

9:30-10:00 **Sean E. Barrett**, *Optically Pumped NMR of Quantum Wells Using a Bottoms Up Approach to Study Electron Spin Physics on Sub-Micron Length Scales.*

CONTRIBUTED LECTURES

10:00-10:17 **A. J. Fagan, G. R. Davies, J. M. S. Hutchinson, D. J. Lurie,** *Continuous Wave NMR Imaging of Short T_2 Materials.*

10:17-10:34 **Stephanie Vierkötter, Catherine Ward, David Gregory,** *Quadrupole Resonance: A Different "Spin" on Nondestructive Inspection of Polymeric Fiber-Reinforced Composite Structures.*

10:34-10:51 **Peter J. McDonald**, *Water Distribution and Skin Formation in Semi-Crystaline Polymer Layers Cast From Solution: A Magnetic Resonance Imaging Study.*

10:51 - 11:15 AM COFFEE BREAK

11:15 - 12:55 PM SESSION II: NOVEL NMR TECHNIQUES I
Chair: *Paul T. Callaghan*

INVITED LECTURES

11:15-11:45 **Michael V. Romalis**, *High Resolution Atomic Magnetometers.*

11:45-12:15 **Gil Navon**, *^2H DQF Spectroscopic MRI as a Tool for the Study of the Microstructure and Biomechanics of Articular Cartilage.*

CONTRIBUTED LECTURES

12:15-12:35 **Bruce J. Balcom, Meghan Halse, Bryce MacMillan,** *Centric Scan SPRITE MRI.*

12:35-12:55 **Janez Stepišnik**, *MR Microscopy of Flow Dynamics in Porous Structures.*

MONDAY, SEPT. 22 - AFTERNOON

12:55 - 2:20 PM **LUNCH**

2:20 - 3:58 PM **SESSION III: MATERIALS NMR**
Chair: ***Karen L. Anderson***

INVITED LECTURE

2:20-2:50 **Steven W. Sinton,** *Single-Sided Magnetic Resonance Relaxometry and Elastography of Elastomer Structures.*

CONTRIBUTED LECTURES

2:50-3:07 **Stephen D. Beyea, S. Jill Glass, Andrew McDowell,** *Non-Destructive Microstructural Characterization of Ceramics: Spatially Resolved Gas Adsorption using NMRI.*

3:07-3:24 **Nina C. Shapley, Marcos A. d'Avila, Jeffrey H. Walton, Ronald J. Phillips, Stephanie R. Dungan, Robert L. Powell,** *Kinetics and Mechanism of Mixing in Concentrated, Oil-In-Water Emulsions.*

3:24-3:41 **Farida Grinberg, Günter Majer,** *Long-Time Scale Molecular Dynamics of Ordered Fluids.*

3:41-3:58 **David Last, Ludovic De Rochefort, Françoise Peyrin, Geneviève Guillot,** *3D MR Microscopy of Trabecular Bone: Architecture Parameters by Reference to High Resolution Microtomography (Synchrotron Radiation) on Matched ROIs.*

3:58 - 4:20 PM **COFFEE BREAK**

4:20 - 5:58 PM **SESSION IV: NMR IN GASES**
Chair: ***Gernot Laicher***

INVITED LECTURE

4:20-4:50 **Mark S. Conradi,** *Probing Lung Microstructure With Laser-Polarized ^{3}He Gas Diffusion.*

CONTRIBUTED LECTURES

4:50-5:07 **L. Hedlund, Z. Vujaskovic, E. Ward, W. Kurylo, C. Wheeler, G. Cofer, G. A. Johnson,** *Hyperpolarized ^{3}He Detection of Radiation-Induced Lung Injury in Rats.*

5:07-5:24 **R. H. Acosta, S. Han, P. Blümler, S. Appelt, H. W. Spiess,** *Simultaneous MRI of Hyperpolarized ^{3}He and ^{129}Xe in Lungs.*

5:24-5:41 **Dean O. Kuethe, Rebecca Montano, Natalie Adolphi,** *Imaging Lung Tissue is Not So Difficult*

5:41-5:58 **Natalie Adolphi, Dean O. Kuethe,** *First T_1 Images of Inert Fluorinated Gases in Lungs.*

6:00 - 8:00 PM **POSTER SESSION I**
(Snacks will be served during the poster sessions.)

TUESDAY, SEPT. 23 - MORNING

8:30 - 10:28 AM **SESSION V: BIOMEDICAL MAGNETIC RESONANCE I**
Chair: ***G. Allan Johnson***

INVITED LECTURES

8:30-9:00 **R. Mark Henkelman**, *MR Microscopy for High Throughput Mouse Phenotyping.*

9:00-9:20 **Robert A. Wind**, *In vivo High-resolution Proton NMR Spectroscopy in a Rotating Mouse.*

CONTRIBUTED LECTURES

9:20-9:37 **S.C. Grant, J.M. Wilson, M.S. Petrik, S.J. Blackband C.A. Shaw,** *MR Microscopy of an Exogenous ALS-PDC Mouse Model: High-Resolution T_2^* - and Diffusion-Weighted Imaging at 17.6 T.*

9:37-9:54 **Y. Seo, A. Takamata, T. Ogino, H. Morita, M. Murakami,** *Water Permeability of Capillaries in the SFO of Rats Determined by T_1 Relaxation Time Measured by ^1H MRI.*

9:54-10:11 **Yoshimasa Matsuda, Shinya Ono, Tomoyuki Haishi, Katsumi Kose,** *MR Microscopy of a Large Human Embryo Collection (Kyoto Collection) Using a Four-Channel Super-Parallel MR Microscope at 2.34 T.*

10:11-10:28 **T. Weber, T. Neuberger, V. Behr, I. Wieland, U. Bogdahn, A. Haase, A. Steinbrecher, C. Faber,** *Central Nervous System* In-Vivo *MR Microscopy at 17.6 T.*

10:28 - 10:55 AM **COFFEE BREAK**

10:55 - 12:55 PM **SESSION VI: YOUNG INVESTIGATORS**
Chair: ***Robert E. Botto***

10:55-11:25 **Sascha Köhler,** *Investigation of the Microstructure of The Heart: Comparison Between T_2*, Diffusion Tensor, and SSFP Imaging.*

11:25-11:55 **Elke Kossel,** *Flow measurements below 50 μm: NMR microscopy experiments in lithographic model pore spaces.*

11:55-12:25 **Song-I Han,** *Amplification of Xenon NMR and MRI by Remote Detection.*

12:25-12:55 **Juan Perlo,** *3D Imaging With a Single-Sided NMR Sensor.*

12:55 PM **GROUP PHOTO**

TUESDAY, SEPT. 23 - AFTERNOON

1:30PM - ?? **CONFERENCE EXCURSION** (optional)

There will be an additional charge for the excursion, which will include a box lunch for each participant.

WEDNESDAY, SEPT. 24 – MORNING

8:30 - 10:21 AM **SESSION VII: NOVEL NMR TECHNIQUES II**
Chair: ***Charles H. Pennington***

INVITED LECTURES

8:30-9:00 **G. Allan Johnson,** *Image Based Phenotyping.*

9:00-9:30 **Russell E. Jacobs,** *Looking Deeper into Development Applications of High Resolution MRI in Developmental Biology.*

CONTRIBUTED LECTURES

9:30-9:47 **Henk Van As, Daniel Polders, P. Adrie de Jager, Frank J. Vergeldt,** *Diffusion and Displacement Analysis in Heterogeneous, Multicompartment (Bio-) Systems by PFG-Multi-Echo NMR/MRI.*

9:47-10:04 **A.G.Webb,** *Improving the Spatial Point Spread Function in Magnetic Resonance Microscopy Using Variable-Time Phase Encoding.*

10:04-10:21 **Pablo J. Prado, Serge Bobroff,** *Exo-MRI.*

10:21 - 10:45AM **COFFEE BREAK**

10:45AM - 12:36 PM **SESSION VIII: BIOLOGICAL NMR**
Chair: ***Kimberlee Potter***

INVITED LECTURES

10:45-11:15 **Charles H. Pennington,** *Magnetic Resonance Microscopy at the Micron Scale, and "DESIRE".*

11:15-11:45 **Edward W. Hsu,** *Diffusion Tensor Microscopy: From Molecules to Organs.*

CONTRIBUTED LECTURES

11:45-12:02 **Davide Santoro, Walter Köckenberger**, *Optimization of Indirect Detected ^{13}C Spectroscopy and Micro Imaging Experiments for In-Vivo Applications in Plants.*

12:02-12:19 **Buntoku Sugihara, Hidehito Tochio, Masahito Morita, Sewon Ki, Azusa Okada, Tetsuro Kokubo, Masahiro Shirakawa,** *In-Vivo ^{31}P MRI Monitoring of Gene Expression in Yeast Cells.*

12:19-12:36 **Ilja Kaufmann, Lars Wegner, Ulrich Zimmermann, Axel Haase,** *3D NMR Microscopy of Intact Plant Root Systems.*

WEDNESDAY, SEPT. 24 – AFTERNOON

12:36 - 2:10 PM **LUNCH**

2:10 - 3:48 PM **SESSION IX: DIFFUSION/FLOW**
Chair: ***Joseph D. Seymour***

INVITED LECTURE

2:10-2:40 **Rainer Kimmich,** *Probing into Transport of Fluids in Porous Media on Length Scales from Millimeters to Nanometers by NMR.*

CONTRIBUTED LECTURES

2:40-2:57 **K.G. Hollingsworth, J.P. Hindmarsh, A.J. Sederman, L.F. Gladden and M.L. Johns,** *Fast Magnetic Resonance Characterization of Multi-Phase Liquids.*

2:57-3:14 **Dmitriy A. Yablonskiy, G. Larry Bretthorst, and Joseph J.H. Ackerman,** *Statistical Approach in the Theory of Diffusion Attenuated MR Signals in Biological Systems.*

3:14-3:31 **Alexandre A. Khrapitchev, Siegfried Stapf, Paul T. Callaghan, Bernhard Blümich,** *From Porous Media to Fluidized Beds – the Next Step of Complex Fluid Dynamic Investigations.*

3:31-3:48 **Galina E. Pavlovskaya,** *Velocity Fields During the Contraction Flow of Viscoelastic Fluids.*

3:48 - 4:20 PM **COFFEE BREAK**

4:20 - 6:00 PM **SESSION X: NOVEL NMR TECHNIQUES III**
Chair: ***Robert A. Wind***

INVITED LECTURES

4:20-4:50 **Bernhard Blümich,** *Unilateral NMR: Concepts and Applications of the NMR-MOUSE.*

4:50-5:20 **Bryan H. Suits,** *Advances in Spin-1 NQR for Explosives Detection in the Field: Implications for NQR imaging.*

CONTRIBUTED LECTURES

5:20-5:40 **Yang Xia, Paul T Callaghan,** *Imaging the Tubeless Siphon by NMR Microscopy*

5:20-6:00 **Markus Küppers, Siegfried Stapf, Bernhard Blümich,** *NMR Velocity Studies on a Falling Liquid Film.*

6:00 - 8:00 PM **POSTER SESSION II**

(Snacks will be served during the poster sessions.)

THURSDAY, SEPT. 25 – MORNING

8:30 - 10:11 AM **SESSION XI: NMR HARDWARE/ INDUSTRIAL APPLICATIONS**

Chair: ***Eiichi Fukushima***

INVITED LECTURES

8:30-9:00 **Tomoyuki Haishi,** *Compact NMR/MRI Systems Using Permanent Magnetic Circuits.*

9:00-9:30 **Koji Saito,** *Industrial Application of NMR imaging to Steel Making Process.*

CONTRIBUTED LECTURES

9:30-9:37 **Stephen R. McComb,** *Industry Trends and New Product Development for Hyperpolarization of Noble Gases.*

9:37-9:54 **Katsumi Kose, Yoshimasa Matsuda, Takeaki Kurimoto, Sadanori Tomiha, Seitarou Hashimoto, Yukako Yamazaki, Tomoyuki Haishi, Shin Utsuzawa,** *Development of a Compact MRI for Bone Volume Density Measurements.*

9:54-10:11 **Volker C. Behr, M. Oechsner, D. Gareis, I. Wieland, T. Neuberger, A. Haase, C. Faber,** *First Evaluation of Very High Field Multi-Channel Probes for Double-Resonant- and Quadrature-Detection at 17.6 T.*

10:11 - 10:35AM **COFFEE BREAK**

10:35 - 11:25 AM **SESSION XII: HYPERPOLARIZED NUCLEI**

Chair: ***Gil Navon***

INVITED LECTURE

10:35-11:05 **Angelo Bifone,** *Hyperpolarized Nuclei: Beyond Helium and Xenon.*

CONTRIBUTED LECTURE

11:05-11:25 **Satyanarayana Anala, Galina E. Pavlovskaya, Prakash Pichumani, Todd J. Dieken, Michael D. Olsen, and Thomas Meersmann,** *High Density Xenon-129 Optical Pumping for In-Situ NMR Spectroscopy of Methane Combustion.*

11:25 AM - 12:33 PM SESSION XIII: CHEMICAL AND SOLID STATE APPLICATIONS

Chair: ***Robert Blinc***

CONTRIBUTED LECTURES

11:25-11:42 **Ruediger Voelkel, Rudolf Berg, Samantha Champ,** *NMR Imaging of Swollen Superabsorbent Polymers.*

11:42-11:59 **Melanie M. Britton,** *Applications of NMR to the Study of Traveling Waves and Convection in Autocatalytic Reactions.*

11:59-12:16 **K. Kumagai, K. Kakuyanagi, M. Matsuda, and M. Hasegawa,** *Magnetic Field Induced Antiferromagnetic Order in the Vortex Core of HTSC Studied by Spatially-Resolved NMR.*

12:16-12:33 **Mladen Barbic, Axel Scherer,** *Atomic Resolution Magnetic Resonance "Diffraction".*

THURSDAY, SEPT. 25 – AFTERNOON

12:33 - 1:50 PM LUNCH

1:50 - 3:31 PM SESSION XIV: BIOMEDICAL MAGNETIC RESONANCE II

Chair: ***R. Mark Henkelman***

A. Symposium on Non-Clinical Functional Magnetic Resonance

INVITED LECTURES

1:50-2:11 **Harold Swartz,** *Overview of the Use of Magnetic Resonance to Measure Function* In

2:11-2:32 **Jeff Dunn,** *Physiological MRI (pMRI): Current Capabilities and Future Possibilities.*

2:32-2:53 **Robert Weisskoff,** *Molecular Imaging with MRI: Making Contrast the "Old Fashioned" Way.*

2:53-3:14 **Periannan Kuppusamy,** *Functional EPR Imaging: Tissue Redox Status & Oxygenation.*

B. Other Biomedical Applications

CONTRIBUTED LECTURE

3:14-3:31 **Philipp Mörchel, Volker Herold, Cornelius Faber, Eberhard Rommel, Axel Haase,** *High field In-Vivo Quantitative 3D Motion Mapping of Murine Myocardium with Phase Contrast MRI.*

3:31 – 3:55 PM **COFFEE BREAK**

3:55 - 6:18 PM **SESSION XV: POROUS MEDIA**

Chair: ***Peter J. McDonald***

INVITED LECTURES

3:55-4:40 **THE MR TECHNOLOGY LECTURE**
Paul T. Callaghan, *Rheo-NMR-Microscopy: Localizing the Physics of Soft Matter.*

4:40-5:10 **Yi-Qiao Song,** *Novel Techniques for Porous Media Research.*

CONTRIBUTED LECTURES

5:10-5:27 **R. W. Mair, R. Wang, M. S. Rosen, D. Candela, and R. L. Walsworth,** *NMR Studies of Xenon Gas Flow in Porous and Granular Media.*

5:27-5:44 **Jonathan Mitchell, Sue C. Stark, and John H. Strange,** *Modified Behaviour on a Nanoscopic Level of Materials Confined in Porous Systems.*

5:44-6:01 **Quan Chen, Murray K. Gringas, and Bruce J. Balcom,** *Pore Filling Mechanism of Spontaneous Imbibition in Porous Media Determined by Internal Field Effect and Conical-SPRITE MRI.*

6:01-6:18 **I.V. Koptyug, A.A. Lysova, A.V. Kulikov, V.A. Kirillov, V.N. Parmon, R.Z. Sagdeev,** *Magnetic Resonance Imaging and Spectroscopy of Catalytic Reactions*

6:18- 6:30 PM **CLOSING SESSION**

7:30 - ? **BANQUET**

(Winner of the Young Investigator's Competition will be announced during the banquet.)

POSTER SESSION I
MONDAY SEPTEMBER 22, 2003 6:00 – 8:00 PM
(Snacks will be served during the poster sessions.)

P-01 **Kai Kremer, Nicolae Goga, Bernhard Blümich,** *On-Line Monitoring with the NMR-MOUSE® during Tire Production*

P-02 **Federico Casanova, Juan Perlo, and Bernhard Blümich,** *Flow Characterization Using a Single-Sided NMR Probe*

P-03 **Xiaohong Ren, Siegfried Stapf, Bernhard Blümich,** *NMR Study of Changing Morphology of Porous Al_2O_3 during Deactivation and Regeneration*

P-04 **Xiaohong Ren, Siegfried Stapf, Bernhard Blümich,** *Dynamic microscopy of flow in model fixed-bed reactors*

P-05 **L.Grunin, M.Bruder, B.Blümich, D.Karasev, I.Ivanov, I.Nikolaev,** *Imaging of Materials with Multiple NMR-MOUSE Sensors and Caterpillar*

P-06 **C. Blümich, S. Anferova, V. Anferov, A.L. Segre, C. Federici, and B. Blümich,** *Investigation of artificial paper aging by the NMR-MOUSE*

P-07 **Mark W. Hunter' Paul T.Callaghan, Robin Dykstra, and Craig D. Eccles,** *Design and Construction of a Portable One-Sided Access NMR Probe*

P-08 **Robin Dykstra, Paul T. Callaghan, Craig D. Eccles, & Mark W. Hunter,** *A Portable NMR System for Remote Measurements*

P-09 **Antoine Lutti and Paul T. Callaghan,** *Study of the Behaviour of an L_3-Phase under Shear using Rheo-NMR*

P-10 **Justin P. Gage, Sarah L. Codd, Robin Gerlach, and Joseph D. Seymour,** *NMR Imaging of Microbial Transport in Porous Media*

P-11 **Jennifer R. Brown, Joseph D. Seymour and Sarah L. Codd,** *Microfluidics of Colloidal Particles by NMR PGSE Measurements*

P-12 **James C. Mabry, Sarah L. Codd, Scott C. Busse, and Joseph D. Seymour,** *MR microscopy of water distribution and dynamics in Polymer Electrolyte Membranes (PEMs)*

P-13 **Erica L. Gjersing, Sarah L. Codd, Phil S. Stewart, and Joseph D. Seymour,** *NMR Microscopy of Biofilm Structure and Bioreactor Fluid Dynamics*

P-14 **James E. Maneval, Braunen E. Smith, Eiichi Fukushima,** *NMR Study of the Flowing Layer in a Granular Media in a Rotating Drum*

P-15 **Silke Sheppard, Andy J. Sederman, Dimitris A. Verganelakis, Mike L. Johns, Mick D. Mantle, Lynn F. Gladden,** *Probing Pore-Scale Velocity Fields During Fluid Flow in Porous Media: Displacement Propagators of Non-Newtonian Fluids in Sedimentary Rocks*

P-16 **Bertram Manz, Frank Volke, Daniel Goll, Harald Horn,** *MRI Measurements of Local Flow Velocities and Structure in Biofilm Systems*

P-17 **Joshua J. Young, Bruce J. Balcom, Theodore W. Bremner, Pavol Szomolanyi,** *Crack Detection in Porous Materials*

P-18 **Gregory Stoch, Fred Goora, Bruce C. Colpitts, Bruce J. Balcom,** *Electron Paramagnetic Resonance Imaging using a pure phase encoding technique*

P-19 **Andrew McDowell, S. Jill Glass, and Steven D. Beyea,** *Imaging Gases in Ceramics: Application of Techniques for Microstructural Characterization*

P-20 **Dean O. Kuethe, Robert E. Botto, Jeana Quintana, Natalie Adolphi, Steven Beyea,** *Coal is Impermeable*

P-21 **Makoto Yamaguchi, Takahiro Ohkubo, Kazuo Kobori, Kazunori Suzuki, Yasuhisa Ikeda, Koji Saito, and Stephen Altobelli,** *Detection of Fractures and Pores in Granite by Magnetic Resonance Microimaging and T_2 Measurement*

P-22 **Maxim Terekhov, Dieter Höpfel,** *MRI investigation of porous media using thermally polarized fluorinated gases.*

P-23 **G. Maddinelli, and N. Mancini,** *NMR flow measurements as an aid to the simulation of fluid dynamics in oil production technology*

P-24 **Marcos A. d'Avila, Nina C. Shapley, Jeffrey H. Walton, Stephanie R. Dungan, Ronald J. Phillip, and Robert L. Powell,** *Mapping a Flow Pattern Transition via Velocity Imaging*

P-25 **L. Backhouse, M. Dias, J.P. Gorce, J. Hadgraft, P.J. McDonald, J.W. Wiechers,** *GARField Magnetic Resonance Profiling of Skin Hydration*

P-26 **Saša Baumgartner, Gojmir Lahajnar, Ana Sepe, Igor Serša, Julijana Kristl,** *Investigation of the State and Dynamics of Water in Hydrogels of Cellulose Ethers by MR Microscopy*

P-27 **Wenlin Huang, Lynn C. Francesconi, Tatyana Polenova,** *^{51}V Magic Angle Spinning Solid State NMR Spectroscopy of Vanadium Substituted Polyoxometalates: A Sensitive Probe for Geometric and Electronic Environment*

P-28 **Neela Pooransingh, Ekaterina Pomerantseva, Martin Ebel, Sven Jantzen, Dieter Rehder, Tatyana Polenova,** *^{51}V Solid-State Magic Angle Spinning Spectroscopy and DFT Studies of Oxovanadium (V) Complexes Mimicking the Active Site of Vanadium Haloperoxidases*

P-29 **C. B. Nelson, T. Su, W. A. Harrison, and P. C. Taylor,** *Structural And Photostructural Properties Of Chalcogenide Glasses*

P-30 **T. N. Rudakov, V. T. Mikhaltsevitch,** *Transient effects in nitrogen-14 quadrupolar spin-systems*

P-31 **Kaz Nagashima, Hironobu Saitoh,Takahiro Sugano,** *Magnetic Resonance Imaging of Water-Sealing Clays used for Waste Disposal Sites*

P-32 **Kuniyasu Ogawa, Shinichiro Naruse** *Local heat flux measurements using MRI : Non-uniformity of heat transfer in an ice thermal storage capsule pack*

P-33 **Igor L. Moudrakovski, G.E. McLaurin, John A. Ripmeester,** *High Pressure NMR Microimaging Studies of Gas Hydrate Formation*

P-34 **Takahiro Ohkubo, Ryou Tanaka, Koji Saito, Yasuhisa Ikeda,** *Nuclear Magnetic Resonance of Hyperpolarized ^{129}Xe in aqueous Na-montmorillonite emulsions*

P-35 **Kimberly Pierce, Song-I Han, Alex Pines,** *Visualization of complex gas dynamics by laser-polarized Xe-129 NMR*

P-36 **Vasiliki Demas, Jeffrey Reimer, Carlos Meriles, Dimitris Sakellariou, Songi Han, Alex Pines,** *An Approach to MR Spectroscopy and Imaging in Permanently Inhomogeneous Magnetic Fields*

P-37 **K. Münnemann, S. Han, F.W. Häsing, B. Blümich, S. Appelt,** *Xenon NMR at very high concentrations*

P-38 **Mineyuki Hattori, Norio Ohtake, Ryo Tanaka, Morio Murayama, Kazuhiro Homma, Moyoko Saito, Toshiharu Nakai, and Takashi Hiraga,** *Automated Hyperpolarized ^{129}Xe Gas Generator for Biomedical MRI/S Applications*

P-39 **Kevin R. Minard, Don S. Daly, Gary R. Holtom, Loel E. Kathmann, Paul D. Majors, Brian D. Thrall and Robert A. Wind,** *A Combined Confocal/^{1}H-NMR Microscopy Study of Water Dynamics and Compartmentalization in Apoptotic CHO Cells*

P-40 **Kevin R. Minard, Rick A. Corley, Chuck Timchalk, Harold E. Trease, Charles G. Plopper, and Jack R. Harkema,** *^{1}H-NMR Microscopy of Respiratory Airway Architecture in Laboratory Animals Structure Change of Articular Cartilage with Weight-bearing in terms of 1H-NMR Relaxation Behavior*

P-41 S.C. Grant, N.E. Simpson, S.J. Blackband, and I. Constantinidis, *MR Microscopy and Spectroscopy of in vitro Alginate Constructs: The Engineering of a Bioartificial Pancreas*

P-42 S.C. Grant, L. Zhang, A. Siram, P.R. Hof, P.K. Thanos, N.D. Volkow, D. Grandy,S.J. Blackband, and H. Benveniste, *Mapping the Mouse Brain: MR Microscopy, Structural Verifications & Volumetrics on Excised Normal & Mutant C57BL6/J Brains at 17.6 T*

P-43 T. Weber, T. Neuberger, N. Weidner, M. Vroemen, A. Müller, G. Giegerich, U. Bogdahn, A. Haase, A. Steinbrecher, and C. Faber, *Imaging of Spinal Cord Disease Models in the Rat Post Mortem at 17.6 T*

P-44 Bianca Hogers, Madelon L. Fekkes, Cees Erkelens, Robert E Poelmann, *Imaging of Embryonic Development*

P-45 Kazuya Ikoma, Yoshiteru Seo, Yasuo Mikami, Yoshiaki Kusaka, Daisaku Tokunaga, Yoshinori Marunaka, Toshikazu Kubo, *Evaluation of the Internal*

POSTER SESSION II
WEDNESDAY SEPTEMBER 24, 2003 6:00 – 8:00 PM

(Snacks will be served during the poster sessions.)

P-46 T.A.J. Hopper, R. Meder and J.M. Pope, *Comparison of High-resolution MRI, Optical Microscopy and SEM in Quantitation of Trabecular Architecture in the Rat Femur*

P-47 Catherine Jones and Jim Pope, *Mapping the refractive index distribution through the crystalline lens using magnetic resonance micro-imaging (μMRI)*

P-48 Catherine Jones and Jim Pope, *Measuring the optical properties of the eye lens using magnetic resonance micro-imaging (μMRI)*

P-49 M. Rosario López-González, William M. Holmes and Paul T. Callaghan, *Evidence of shear banding and velocity fluctuations in wormlike micelles using NMR*

P-50 Davide Santoro, Walter Köckenberger, *Quantification of the attenuation in the polarisation transfer efficiency induced by diffusion through magnetic field gradients: Simulations and experiments*

P-51 Ben Newling, Bruce J. Balcom, Christopher Poirier, Dale Roach, Yang Zhi, *Single-Point MRI of Fast, Turbulent Gas Flow*

P-52 **Yuesheng Cheng, Bryce MacMillan, Rod P. MacGregor, Bruce J. Balcom,** *Direct Detection of Hydrocarbon Displacement in a Model Porous Soil with Magnetic Resonance Imaging*

P-53 **Alexei V. Ouriadov, Rodney P. MacGregor, Bruce J. Balcom,** *Thin Film MRI – High Resolution Depth Imaging with a Local Surface Coil and Spin Echo SPI*

P-54 **Kumud Deka, Bruce J. Balcom, Igor V. Mastikhin, Rod P.MacGregor,** *Density Profiling, ^1H and Heteronuclei, with a Half-K-Space SPRITE Technique*

P-55 **Igor Mastikhin, B.J. Balcom, D. Goodyear, P. Szomolanyi, N.J. Shah,** *Spiral SPRITE MRI of Compact Bone*

P-56 **Igor Mastikhin,** *Rapid Measurement of RF Flip Angles and T_1 for samples with long T_1 and short T_2**

P-57 **A.G.Webb, L.Ciobanu, A.Purea, T.Neuberger, and C.Pennington,** *Relative signal-to-noise efficiencies of phase- and frequency-encoding methods in NMR microimaging*

P-58 **Igor Serša, Slobodan Macura,** *Spectral Resolution Enhancement by Spectroscopic MR Microscopy*

P-59 **I. Martin-Vicente, M. J. D. Mallett, P. Blümler,** *NMR Imaging of pico-Tesla fields?*

P-60 **H.-B. Ko, P. Blümler, H. W. Spiess,** *Characterization of Mechanical Induced Changes in Polyoxymethylene by NMR/MRI*

P-61 **Stephen Altobelli, Tang-Tat Ng,** *Tri-Axial Testing combined with MRI*

P-62 **Sue C Stark & John H Strange,** *The study of solid – liquid interactions using T1rho spectroscopy*

P-63 **Frank J. Vergeldt, Carel W. Windt, P. Adrie de Jager, Henk Van As,** *Advanced MRI microscopy at low magnetic field strength*

P-64 **Carel Windt, Frank Vergeldt, Adrie de Jager, Henk Van As,** *Playing with propagators: investigating water transport and tissue properties in plants using flow imaging and combined flow-T_2 imaging*

P-65 **Ilja Kaufmann, Axel Haase,** *Contour averaging*

P-66 **Ilja Kaufmann, Lars Wegner, Ulrich Zimmermann, Axel Haase,** *Diffusion barriers for macromolecules in intact plant roots*

P-67 **Volker C. Behr, I. Wieland, M. Oechsner, D. Gareis, T. Weber, T. Neuberger, A. Haase, C. Faber,** *An improved Probebase and Resonator Setup for in-vivo body MR Imaging of small mammals at 17.6 T*

P-68 **Volker C. Behr, I. Wieland, M. Oechsner, D. Gareis, T. Neuberger, D. Haddad, A. Haase, C. Faber,** *Resonator Designs and Results for Microscopic in-vivo and ex-vivo MRI at Highest Field Strengths up to 17.6 T*

P-69 **J.C. Tsai, T. Weber, T. Neuburger, A. Purea, V. Behr, A. Hasse, A. Webb,** *High Field Magnetic Resonance Microscopy of Pig Cartilage*

P-70 **Sascha Köhler, Jens Maier, Karl-Heinz Hiller, Axel Haase, Peter M. Jakob,** *NMR-microscopy with TrueFISP at 11.75 T*

P-71 **Artem Goloshevsky, Jeffrey H. Walton, Mikhail V. Shutov, Scott D. Collins, Jeffrey S. de Ropp, Michael J. McCarthy,** *Development of Low Field NMR Microcoils*

P-72 **T. Shirai, Y. Matsuda, T. Haishi, S. Utsuzawa, K. Kose,** *A Mouse MRI using a Yokeless Permanent Magnet*

P-73 **Christoph H. Arns, Arthur Sakellariou, Tim Senden, Adrian P. Sheppard, Rob M. Sok, Mark A. Knackstedt,** *Numerical simulations of NMR responses on micro-tomographic images*

P-74 **Shohji Tsushima, Kazuhiro Teranishi, Shuichiro Hirai,** *NMR Microscopy for Measurement of Water Distribution in a Polymer Electrolyte Membrane under Fuel Cell Operation*

P-75 **Shuichiro Hirai, Shohji Tsushima, Kazuhiro Teranishi,** *Time-series NMR Microscopy to Measure Dehydration Process of a Polymer Electrolyte Membrane in Fuel Cell Startup*

P-76 **Toshihiro Ozeki, Katsumi Kose, Tomoyuki Haishi[3], Shunichi Nakatsubo, Yoshiyuki Matsuda,** *NMR Imaging of Drainage Channels in Sea Spray Icing*

P-77 **T. Kurimoto, T. Shirai, Y. Matsunaga, Y. Matsuda, T. Haishi, S. Utsuzawa,K. Kose, H. Yoshioka,** *Development of Compact MRI Systems for Sports Injuries*

P-78 **Jörg Felder,** *Efficient and Linear RF Power Amplifier for Unilateral NMR Apparatus*

P-79 **F. W. Hersman, M. I. Hrovat, R. W. Mair, I. Muradyan, J. Ng, S. Patz, M. S. Rosen, I. C. Ruset, L. L.Tsai and R. L. Walsworth,** *A Human Scale, Open-Access Low Field MRI System*

P-80 **Stephen J. Dodd, John Roby, Peter T. Fox,** *A simple cooled copper radio frequency coil*

P-81 **Stephen J. Dodd, Trevor J. Andrews, Jack L. Lancaster, Peter T. Fox,** *T_2 relaxometry in the mouse brain*

P-82 **Trevor J. Andrews, Jack L. Lancaster, Carmen Contreres-Sesvold, Stephen J. Dodd,** *Low SNR Performance of a 3-Pool Model for Myelinated Tissue*

P-83 **Jian Zhi Hu, Hanne C. Bertram, Donald N. Rommereim, and Robert A. Wind,** *High Sensitivity, High Resolution ^{1}H NMR Spectroscopy of Excised Muscle Tissues Using Slow MAS*

P-84 **Jian Zhi Hu, and Robert A. Wind,** *High Resolution ^{1}H NMR Spectroscopy in Intact Biological Objects Using Slow Magic Angle Spinning*

P-85 **Paul D Majors, Jian Z Hu, Fred J Brockman, James K Fredrickson, Yuri A Gorby, Eric A Hill, William P Kovacik, Jeffrey S McLean, and Robert A Wind,** *In-situ MR microscopy and spectroscopy of microbial communities*

P-86 **Cornelius Faber, Thomas Hörnschemeyer, Axel Haase,** *Non-invasive investigation of insect morphology with NMR microscopy*

P-87 **Thomas Neuberger, H. Schneider, D. Haddad, A. Purea, M. Westhoff, A. Haase, U. Zimmermann,C. Faber, A. Webb,** *NMR microscopy of the lipid distribution in air-dry branches of the resurrection plant* Myrothamnus flabellifolia

P-88 **Armin Purea, Daniel Haddad, Thomas Neuberger, Axel Haase, Andrew G. Webb,** *The effects of chemical fixation on intracellular NMR relaxation times*

P-89 **D. Haddad, A. Purea, M. Schmidt, M. Haas-Rioth, H.H.A. Oelschläger, A. Haase,** *MR-Histology: Embryonal and Fetal Brain Development in Bovines*

P-90 **Kimberlee Potter, Paul Anderson, Noritaka Isogai, William Landis,** *Magnetic Resonance Microscopy of Tissue Engineered Phalanges*

P-91 **Prem N. Gambhir, Young J. Choi, Michael J. McCarthy,** *NMR Relaxation Time of Navel Oranges – A Screening Parameter for Identifying Freeze-Damage*

P-92 **Natalia Hernández-Sánchez, Pilar Barreiro, Margarita Ruiz-Altisent, Jesús Ruiz-Cabello, Xavier Gimeno, Sebastián Idelsohn, Sandra Aguilar,** *Detection of freeze injury in oranges by Magnetic Resonance Imaging*

P-93 **J. Constantin Széles, Jana Kainerstorfer, Bence Csapo, Csilla Balássy, Raschid Hoda, Markus Klarhöfer, Peter Polterauer,** *Examples for clinical application of NMR Microscopy*

P-94 **Yang Xia, Hisham Alhadlaq,** *Early Detection of Osteoarthritis in Cartilage by μMRI and PLM*

P-95 **Jeeva Munasinghe, Garry Zhang, Sandra L. Hofmann, Alan Koretsky and, Anil B. Mukherjee,** *Evaluation of Brain Atrophy in PPT Gene-Targeted Mice by MRI*

P-96 **Dieter Höpfel, Maxim Terekhov,** *High Resolution MRI of Limbs using a Low Cost/ Low Field Resistive Magnetic System*

P-97 **Anatoly A. Khripov, V. I. Chizhik, K. Nishinari,** *Applications of surfactant micelles as a sensitive NMR probe in physics of biopolymer systems*

Introduction to Nuclear Magnetic Resonance

Yang Xia
Department of Physics, Oakland University, Rochester, MI 48309, USA

Nuclear Magnetic Resonance (NMR) relies on a number of interactions between an external magnetic field (B_0) and an atomic nucleus, with the nuclear Zeeman interaction predominates the others [1-3]. At the heart of the NMR phenomenon is the proportionality between the precessional frequency of the nuclear spins and the magnetic field in which the nuclei are immersed. If the magnetic field is perfectly uniform and we only consider the dominant Zeeman interaction, the Larmor precession frequency (□) of the nuclear spin is simply □B_0, where □ is a constant.

In conventional NMR spectroscopy [4], a sample is placed in a magnetic field that is made as uniform as possible, so that the resonant frequency of the nuclei becomes sensible of *solely* the local environment in the sample (chemical composition and structure, molecular interactions). A unique phenomenon of NMR is that many weak nuclear interactions can still be observed and quantified in the presence of Zeeman interaction, a consequence of remarkable coherence times exhibited by spin ensembles. Several NMR parameters can characterize different aspects of chemical environment in a sample. For example, the frequency shift of the resonant peak measures the electron orbital modification of the magnetic environment experienced by a nucleus in an atom or molecule; the intensity of the resonant peak can be used to perform a nuclear count; and the splitting pattern of the resonant peak provides a means to determine the spin-spin coupling in the nuclear system via the electron polarization through the molecular orbital.

In NMR imaging [5-7], by contrast, a sample is placed in a magnetic field that is deliberately made non-uniform, so that the resonant frequency of the nuclei becomes spatially encoded, enabling the non-invasive and non-destructive exhibition of a sample's internal structure. Since the publication of the first NMR image in 1973, its potential for medical diagnosis was noticed immediately and NMR whole-body scanners (known as MRI scanners) are now routinely used as an indispensable diagnosis tool, with a clinical resolution on the order of $(1\ \text{mm})^3$. With the scaling down of the receiver coil and the fine tuning of the instrument, the resolution of NMR images can be less than $(100\ \mu\text{m})^3$, where the imaging technique is termed NMR microscopy [8]. Between these two resolution extremes, small scale applications of imaging, 'NMR macroscopy', have proven to be extremely useful in various scientific and industrial applications.

To introduce the fundamentals of NMR, the following concepts will be discussed: basic quantum mechanical concepts of NMR, semi-classical treatments of NMR using Bloch Equations, Fourier transformation and FT NMR, basic instrumentational and experimental aspects, spin manipulations using simple pulse sequences, brief descriptions of nuclear interactions and relaxations, and the influence of magnetic field inhomogeneity on simple NMR spectra (a prelude to the application of the magnetic field gradient in NMR imaging) [9].

<u>References</u>

[1] E Purcell, H Torrey, R Pound, *Phys. Rev.* **69**, 37-38 (1946).
[2] F Bloch, W Hansen, M Packard, *Phys. Rev.* **69**, 127 (1946).
[3] A Abragam, *The Principles of Nuclear Magnetism*, Clarendon, Oxford (1960).
[4] R Harris, *Nuclear Magnetic Resonance Spectroscopy - A Physicochemical View*, Longman, Essex (1983).
[5] P Lauterbur, *Nature* **242**, 190-191 (1973).
[6] P Mansfield, P Grannell, *J. Phys. C: Solid State Phys.* **6**, L422 (1973).
[7] P Blümler, B Blümich, R Botto, E Fukushima, eds *Spatially Resolved Magnetic Resonance: Methods, Materials, Medicine, Biology, Rheology, Geology, Ecology, Hardware*, Wiley-VCH, Weinheim (1998).
[8] P Callaghan, *Principles of Nuclear Magnetic Resonance Microscopy*, Oxford University Press, Oxford (1991).
[9] A more extensive list of the NMR references can be found at http://www.oakland.edu/~xia.

Acknowledgement: Oakland University (Research Excellence Fund in Biotechnology, Bennett NMR Facility), NIH (R01 AR45172).

NMR Instrumentation

Steven M. Wright
Department of Electrical Engineering, Texas A&M University,
College Station, TX, 77843-3128, USA

Introduction

The cost of whole body MRI may remain high for some time, as the cost of the large superconducting magnets remains the principle factor in determining the cost of most clinical systems; however, for applications such as MR microscopy it may be possible to used much smaller magnets. In turn, the cost and complexity of many other system components fall accordingly, and an NMR spectrometer can be assembled relatively straightforwardly [1-4]. NMR systems consist of a just few basic subsystems: a transmitter, receiver, pulse programmer, gradients, RF coil and magnet. This talk will discuss some of the technology available for making laboratory NMR systems and upgrades to existing systems.

The Pulse Programmer

Until recently, the pulse programmer was usually a standalone unit that clocked out instructions downloaded from a computer. Now, low-cost digital I/O and multiple channel digital-to-analog converter boards are available as off-the-shelf components from companies such as National Instruments. These cards can be programmed directly in LabView, but most cards have drivers that can be accessed from other languages such as C or Visual Basic.

Receiver Technology

There are a number of approaches to building an NMR receiver, with the primary distinction being where the signal is digitized [5-10]. Ideally, one would directly Nyquist sample the signal directly from the low-noise RF amplifier, but this is rarely practical due to the requirements this places on the digitizer and data throughput. Other approaches range from undersampling the RF signal to a single conversion receiver that directly mixes to audio frequency for digitization. In principle, one would like to digitize as soon as possible, but this can require very fast data transfer rates on the digital side. Commercially available direct digital synthesizers and high speed analog-to-digital converters are available that make the construction of phase stable receivers relatively inexpensive and straightforward. After reviewing the basic NMR receiver, solutions that will be discussed include entire receivers (http://pentek.com), chipsets available from manufacturers such as Analog Devices (http://analog-devices.com) and building receivers from discrete components from companies like Mini-Circuits (http://www.mini-circuits.com).

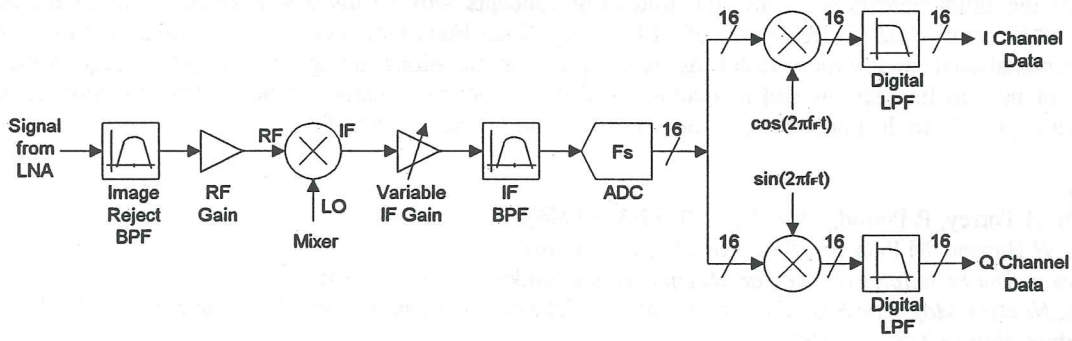

Figure 1. Block diagram of a hybrid digital receiver that can be built from commonly available components. A single analog conversion stage mixes the RF signal to an IF where it is sampled (ADC) and digitally demodulated.

RF Transmitter

Broadband, noise blanked, NMR transmitters are available from a variety of manufacturers. Particularly in the field of microscopy, relatively low power amplifiers are required and it may be desirable and economical to build the RF transmitter. It is reasonably straightforward to build a 10 watt linear RF amplifier using commonly available MOSFETs. Alternatively, a 10-20 watt amplifier can be purchased from Henry Radio for approximately $200. Noise blanking can be added using a simple PIN diode switching circuit.

Magnet

The limiting factor in signal-to-noise ratio for MR microscopy is the magnet, of course, as this determines the available magnetization. However, limitations on size or cost may prevent the use of high-field superconducting magnets. Permanent magnets offer one alternative, with the major disadvantage being their weight and temperature sensitivity. Conventional permanent magnets can be constructed to approximately 1 Tesla, and recently, permanent magnets have been realized with field strengths up to 5 Tesla using Hallbach arrays [11]. Another approach for low-cost NMR hardware is prepolarized systems, in which the higher magnetization field is a relatively inhomogeneous resistive magnet, with a low-field but highly homogeneous magnet surrounding reading out the signal [12].

Fabrication

Printed circuit boards for gradient and RF coils and RF electronics boards can now be fabricated in house with prototypers from LPKF (http://www.lpkfusa.com) and T-Tech (http://www.t-tech.com). Alternatively, quick turnaround of PC boards is available from several sites such as PCB Express (http://www.pcbexpress.com)

Conclusion

Experimental NMR/MRI systems can be designed and assembled for dedicated applications using commercially available subsystems and components. Of course, the more complex and diverse the applications that need to be supported by the system, the more complicated and expensive the design.

References

[1] Eichii Fukushima and Stephen B.W. Roeder, Experimental Pulse NMR A Nuts and Bolts Approach. Addison Wesley Publishing Co., Reading, MA, 1981.

[2] D.I. Hoult, "The NMR Receiver: A Description and Analysis of Design," Progress in NMR Spectroscopy, 12, pp. 41-77, 1978.

[3] S.M. Wright, D.G. Brown, J.R. Porter, D.C. Spence, E. Esparza, D. Cole, F.R. Huson, "A Desktop Magnetic Resonance Imaging System," Magnetic Resonance Materials in Physics, Biology, and Medicine, 13, pp. 177-185, 2002.

[4] K. Kose, T. Haishi, Y. Matsuda, I. Anno, Super-Parallel MR Microscope, Proc. ISMRM, 9, 609, 2001.

[5] G.N. Holland and J.R. MacFall, "An overview of digital spectrometers for MR Imaging," *J. Magn. Reson. Imag.*, 2, pp. 241-246, 1992.

[6] P. Andersen, M. Rosen, P. Erhard, G. Adriany, J. Strupp, R. Salmi, and K. Ugurbil, "Over-sampling digital IF receiver for MRI," in Proc., ISMRM, Apr. 1996, p. 1403.

[7] P. N. Morgan, R.J. Iannuzzelli, F.H. Epstein, R.S. Balaban, "Real-time cardiac MRI using DSP's", IEEE Trans. Med. Imaging, pp. 649-653, July, 1999.

[8] J.C. Hoenninger III, L.E. Crooks, M. Arakawa, "A Floating-Point Digital Receiver for MRI," IEEE Transactions on Biomedical Engineering, 49, No. 7, pp. 689-693, July, 2002.

[9] C.A. Michal, K. Broughton, E. Hansen, "A High Performance Digital Receiver for Home-Built NMR Spectrometers," Review of Scientific Instruments, 73, pp. 453-458, 2002.

[10] H.D. Morris, J.A. Derbyshire, P. Kellerman, A.S. Chesnick, M.A. Guttman, E.R. McVeigh, "A Wide-Bandwidth Multi-channel Digital Receiver and Real-Time Reconstruction Engine for use with a Clinical MR Scanner," Proc. ISMRM, 10, p.61, 20-24 May 2002.

[11] O. Cugat and F. Bloch, The 5 Tesla Sphere, (Mag-net final report), http://mag-net.ee.umist.ac.uk/reports/P14/p14_2.html.

[12] G.C. Scott, B. Chronik, N. Matter, H. Xu, P.N. Morgan, L. Wong, A. Macovski, S. Conolly, "A Prepolarized MRI Scanner, Proc. ISMRM, 9, p. 610, 2001.

Mobile NMR

Bernhard Blümich
Institute of Technical Chemistry and Macromolecular Chemistry, RWTH, D- 52056 Aachen, Germany

Mobile NMR has its origin in inside-out NMR, where NMR spectrometers are lowered into bore holes for analysis of fluids in the surrounding rock matrix [1 - 4]. Such equipment is unique in the sense, that the magnetic fields penetrate the object from one side and that the object can be arbitrarily large. Sensors of this type are referred to as unilateral NMR devices. They can also be used for non-invasive quality control of various products and for medical diagnostics. Although this idea has been formulated about 2 decades ago [5-14], systematic investigations of mobile NMR with unilateral sensors did not proliferate in the scientific literature until the mid nineties with the publication of the NMR-MOUSE® [15 - 19]. The NMR-MOUSE is a small unilateral NMR sensor with highly inhomogeneous fields and a gradient of the polarization field which is about 100 times stronger than that of the down-hole NMR sensors. Despite the strong field gradient, many different NMR parameters can be measured even in imaging mode with a spatial resolution of better than 0.2 mm [20 - 28]. Mobile unilateral NMR sensors are of interest for various applications in industry. This in turn stimulates the development and understanding of NMR in highly inhomogeneous fields [29 - 33]. This tutorial summarizes the development of mobile NMR with emphasis on unilateral NMR, reviews the different designs and characteristics of small NMR sensors like the NMR-MOUSE, the different NMR experiments possible in highly inhomogeneous magnetic fields, and gives an overview over several applications of practical interest.

References

1) E. Woessner, The Early Days of NMR in the Southwest, Concepts in Magnetic Resonance, 13 (2001) 77-102.
2) R.J.S. Brown, R. Chandler, J.A. Jackson, R.L. Kleinberg, M.N. Miller, Z. Paltiel and M.G. Prammer. The History of NMR Well Logging. Concepts in Magn. Reson. 13, 340 - 411, Special Issue (2001).
3) G.R. Coates, L. Xiao , M.G. Prammer, NMR Logging Principles and Applications, Halliburton Energy Services, Houston, 1999.
4) R. L. Kleinberg, Well logging, in: D.M. Grant, R.K. Harris, eds., Encyclopedia of NMR, Wiley-Liss, New York, 1996, pp. 4960 - 4969.
5) A. Nordon, C.A. McGill, D. Littlejohn, Process NMR spectrometry, Analyst 126 (2001) 260 – 272.
6) R.K. Cooper, J.A. Jackson, Remote (Inside-Out) NMR. I., Remote Production of a Region of Homogeneous Magnetic Field, J. Magn. Reson. 41 (1980) 400 – 405.
7) L.J. Burnett, J.A Jackson, Remote (Inside-Out) NMR. II. Sensitivity of NMR Detection for External Samples, J. Magn. Reson. 41 (1980) 406 - 410.
8) J.A. Jackson, L.J. Burnett, F. Harmon, Remote (Inside-Out) NMR. III. Detection of nuclear magnetic resonance in a remotely produced region of homogeneous magnetic field, J. Magn. Reson. 41 (1980) 411 – 421.
9) G.A. Matzkanin, in: P. Höller, V. Hauck, G. Dobmann, C. Ruud, R. Green, eds, Nondestructive Characterization of Materials, Springer, Berlin, 1989, 655–669.
10) R.F. Paetzold, A. De Los Santos, G.A. Matzkanin, Pulse Nuclear Magnetic Resonance Instrument for Soil-Water Content Measurement: Sensor Configurations, Soil Science 51 (1987) 287 – 290.
11) R.F. Paetzold, G.A. Matzkanin, A. De Los Santos, Surface Water Content Measurement Using Pulse Nuclear Magnetic Resonance Techniques, Soil Science 49 (1985) 537 – 540.
12) B.J. Hogan, One-Sided NMR Sensor System Measures Soil/Concrete Moisture, Design News, May 5 (1986).
13) W.L. Rollwitz, Using Radiofrequency Spectroscopy in Agricultural Applications, Agricultural Engineering 66 (1985) 12 – 14.
14) C.I. Nicholls, A. De Los Santos, Drying Technol. 9 (1991) 849.
15) G. Eidmann, R. Savelsberg, P. Blümler, and B. Blümich, The NMR MOUSE: A Mobile Universal Surface Explorer, J. Magn. Reson. A 122 (1996) 104 - 109.
16) B. Blümich, P. Blümler, G. Eidmann, A. Guthausen, R. Haken, U. Schmitz, K. Saito, and G. Zimmer, The NMR MOUSE: Construction, Excitation, and Applications, Magn. Reson. Imag. 16 (1998) 479 - 484.
17) B. Blümich, V. Anferov, S. Anferova, M. Klein, R. Fechete, M. Adams, F. Casanova, A Simple NMR-MOUSE with a Bar Magnet, Magn. Reson. Eng. 15 (2002) 255 – 261.

18) S. Anferova, V. Anferov, M. Adams, P. Blümler, K. Hailu, K. Kupferschläger, M.J. M. Mallett, G. Schroeder, S. Sharma, B. Blümich, Construction of an NMR-MOUSE with short dead time, Concepts in Magn. Reson. 15 (2002) 15 - 25.
19) B. Blümich, V. Anferov, S. Anferova, M. Klein, R. Fechete, A NMR-MOUSE for Analysis of Thin Objects, Polym. Sci. Eng. xx (2003) xxx – xxx.
20) G. Guthausen, A. Guthausen, F. Balibanu, R. Eymael, K. Hailu, U. Schmitz, B. Blümich, Soft-matter analysis by the NMR-MOUSE, Macromol. Mat. Eng. 276/277 (2000) 25 - 37.
21) A. Guthausen, G. Zimmer, R. Eymael, U. Schmitz, P. Blümler, B. Blümich, Soft-Matter Relaxation by the NMR-MOUSE, in: P. Blümler, B. Blümich, R. Botto, E. Fukushima, eds., Spatially Resolved Magnetic Resonance, Wiley-VCH, Weinheim, 1998, pp. 195 – 209.
22) A. Guthausen, G. Zimmer, P. Blümler, and B. Blümich, Analysis of Polymer Materials by Surface NMR via the NMR MOUSE, J. Magn. Reson. 130 (1998) 1 – 7.
23) A. Wiesmath, C. Filip, D.E. Demco, B. Blümich, NMR of Multipolar Spin States Excited in Strongly Inhomogeneous Magnetic Fields, J. Magn. Reson. 154 (2002) 60 - 72.
24) A. Wiesmath, C. Filip, D.E. Demco, and B. Blümich, Double-Quantum-Filtered NMR Signals in Inhomogeneous Magnetic Fields, J. Magn. Reson. 149 (2002) 258-263.
25) M. Klein, R. Fechete, D.E. Demco, B. Blümich, Self-diffusion measurements by a constant-relaxation method in strongly inhomogeneous magnetic fields, J. Magn. Reson. xx (2003) xxx – xxx.
26) P.J. Prado, B. Blümich, U. Schmitz, One dimensional imaging with a palm-size NMR-probe, J. Magn. Reson. 144 (2000) 200 - 206.
27) F. Casanova, J. Perlo, B. Blümich, K. Kremer, 1D multi-echo imaging in highly inhomogeneous magnetic fields, J. Magn. Reson. xx (2003) xxx – xxx.
28) F. Casanova, B. Blümich, Two-Dimensional Imaging with a Single-Sided NMR Probe, J. Magn. Reson. xxx (2003) xxx – xxx.
29) F. Balibanu, K. Hailu, R. Eymael, D.E. Demco, B. Blümich, NMR in inhomogeneous magnetic fields, J. Magn. Reson. 145 (2000) 246 - 258.
30) M.D. Hürlimann, D.D. Griffin, Spin Dynamics of Carr-Purcell-Meiboom-Gill-like Sequences in Grossly Inhomogeneous B_0 and B_1 Fields and Applications to NMR Well Logging, J. Magn. Reson. 143 (2000) 120 – 135.
31) C.A. Meriles, D. Sakellariou, H. Heise, A.J. Moulé, A. Pines, Approach to High-Resolution ex Situ NMR Spectoscopy, Science 293 (2001) 82 - 85.
32) H. Heise, D. Sakellariou, C.A. Meriles, A.J. Moulé, A. Pines, Two-dimensional high-resolution NMR spectra in matched B_0 and B_1 field gradients, J. Magn. Reson. 156 (2001) 146 – 151.
33) C. Meriles, D. Sakellariou, A. Pines, Resolved magic angle spinning of anisotropic samples in inhomogeneous fields, Chem. Phys. Lett. 358 (2002) 391 – 395.

Introduction to Flow and Diffusion via NMR

Joseph D. Seymour
Department of Chemical Engineering, Montana State University, Bozeman, MT 59717-3920, USA

The effects of flow and diffusion have been known since the earliest observations of nuclear magnetic resonance (NMR) phenomena[1]. This lecture will introduce the theoretical and experimental aspects of motion sensitivity in NMR experiments. The material will be covered by following the historical development of the understanding of flow and diffusion effects on the NMR signal. Theoretical approaches to the understanding of translational motion effects using the propagator formalism and cumulant expansion technique[2] will be reviewed and the connections between the approaches made clear through discussion of the equivalent description of dynamic processes using probability distribution functions and random variables. The measurement of mean velocity using time-of-flight and phase contrast methods will be discussed. The measurement of self-diffusion coefficients using static and pulsed field methods will be presented. Discussion of the ability of NMR measurements to refocus motions that are coherent over the displacement measurement time scale and the use of this effect to flow compensate data and study complex dynamics will be undertaken[3]. The interaction of flow and diffusion, Taylor dispersion, is integral to many transport processes and the ability of NMR to characterize these interactions will be reviewed[4]. The lecture will conclude with discussion of multiple pulsed gradient NMR methods to study spatio-temporal dynamics correlations[5] in complex systems. Throughout the lecture nuts and bolts aspects of the experimental implementation and data analysis will be addressed for each topic.

References

1. E. Fukushima, *NMR The Physical Basis*, 1988.
2. P.T. Callaghan, *Principles of Nuclear Magnetic Resonance Microscopy*, New York: Oxford University Press, 1991.
3. E. Fukushima, Nuclear magnetic resonance as a tool to study flow. *Ann. Rev. Fluid Mech.* **31**: 95 (1999).
4. P.T. Callaghan, S.L. Codd, and J.D. Seymour, Spatial coherence phenomena arising from translational spin motion in gradient spin echo experiments. *Concepts Magn.Reson.* **11**: 181 (1999).
5. S. Stapf, S.-I. Han, C. Heine, and B. Bluemich, Spatiotemporal correlations in transport processes determined by multiple pulsed field gradient experiments. *Concepts Magn.Reson.* **14**(3): 172 (2002).

NMR in Gases

Mark S. Conradi
Department of Physics, Washington University, St. Louis MO 63130, USA

Recent developments in MR imaging with hyperpolarized He-3 and Xe-129 gases, for imaging of lungs and porous materials, have brought renewed interest in the NMR of gases. Gas-phase NMR resembles that of liquids in having motionally averaged spin interactions. A major distinction is that while in liquids the correlation time τ_c is determined primarily by temperature, τ_c in gases is mainly a function of density (or pressure). An important distinction is made between monatomic gases, where spin interactions occur only during collisions, and molecular gases, where the collisions serve to modulate the spin interactions. These cases are demonstrated by comparing spin relaxation of Xe-129 and Xe-131 with that of the simplest molecule, H_2. W.N. Hardy's landmark study of H_2 displaying a minimum in τ_1 as a function of density will be covered.

Gases can be hyperpolarized by bringing them into contact with electron spin-polarized, dilute rubidium vapor. In practice, the requirement of long τ_1 limits this to He-3 and Xe-129 noble gases. The process and apparatus will be presented from a user's point of view. Applications of polarized He-3 to lung imaging will be covered, including imaging of ventilation and diffusion. The small airways and alveolar walls restrict the diffusion of gas in lungs, allowing MR measurements of diffusion to report on the integrity of the lung tissue microstructure in each image volume element, particularly as regards emphysema.

An introduction to magnetic resonance imaging

Paul T. Callaghan
MacDiarmid Institute for Advanced Materials and Nanotechnology,
School of Chemical and Physical Sciences
Victoria University of Wellington, New Zealand

The idea that magnetic resonance could be used to obtain a 'picture' of the distribution of molecules inside materials or biological organisms is remarkable both for its practical relevance and for the time it took for the pioneers of NMR to become aware of this possibility.

This lecture will give a simple introduction to magnetic resonance imaging (MRI). The idea of "reciprocal space" will be introduced and used to explain the various different imaging strategies. The talk will range over all the different sorts of "contrasts" which are possible, so that we can image not only where the molecules are, but which molecules, how fast they flow, how fast they diffuse, how fast they tumble, which way they point.

When we want to get the finest spatial resolution, we enter the realm of NMR microscopy. Some limits to resolution will be explored. When we want to image rapidly, we embark on the diverse adventures of echo planar imaging, FLASH and RARE. The limits to speed will be addressed. When we want to measure translational motion, we shift to the scattering universe, where the **q** vector links the techniques of neutron and photon scattering with NMR. The limits to time and space will be revealed.

This lecture is aimed at a graduate student audience, and is designed to introduce a smorgasbord of concepts, sprinkled with a little mathematics, seasoned with physics, and washed down with a wide variety of applications. Suitable references for MRI, NMR Microscopy, or Spatially Resolved NMR are listed below.

1. P. T. Callaghan, *Principles of Nuclear Magnetic Resonance Microscopy* , Clarendon Press, Oxford, 1991.

2. *Spatially Resolved Magnetic Resonance*, eds. P. Bluemler, B. Bluemich, R.E. Botto and E. Fukushima, Wiley-VCH, Weinheim, 1998

3. B. Blümich, *NMR Imaging of Materials* , Oxford University Press, Oxford, 2000.

Biomedical NMR Imaging

Axel Haase
Physics Institute, University of Würzburg, 97074 Würzburg, Germany

NMR imaging has tremendous clinical importance, but it is now well-established that this technique has great potential in all areas of medicine and biology. Compared to other imaging modalities, NMR is non-invasive and has no harmful side-effects. NMR imaging is applicable to human studies, large but also very small animals, embryos, organs and cell cultures. In addition, plant physiology is a further area for biomedical NMR imaging. However, it must be noted that other imaging techniques exhibit a higher spatial resolution (e.g. X-ray), have shorter measuring times (e.g. ultrasound) and provide a deeper investigation of the biochemistry of tissues (e.g. positron emission tomography). The great advantage of NMR compared to other imaging techniques is that many aspects of the live tissue can be investigated using one experiment: characterization of the anatomy, function and biochemistry of the tissue. NMR imaging is a so-called "one-stop-shop".

The spatial resolution in biomedical NMR-imaging is poor compared to other methods although some parameters (NMR relaxation times, chemical shift or J-coupling) in NMR provide very local information on a nanometer scale. The typical volume of an image element (voxel) in (human) medical NMR imaging is 1 mm^3 while for small animals (and plants) it may reach 10^{-5} mm^3. This later regime is the area of "NMR microscopy" which is one of the major topics of this conference. This wide range in spatial resolution is only possible with major hardware changes. Medical NMR imaging is mostly performed using static magnetic field strengths of below 3.0 T and magnetic field gradients of up to 50 mT/m. NMR microscopy on small animals, organs, etc. needs high magnetic field strengths up to 17.5 T and gradient strengths of more than 1000 mT/m. The main limitation in biomedical NMR imaging is the limited signal/noise ratio (note: the NMR signal is linearly dependent on the voxel volume!), technological limits (maximum magnetic field strength and gradient strength is dependent on the present state of magnet technology!) and safety concerns.

The most important topic for the biomedical application of NMR imaging is the image contrast. There exists an intrinsic image contrast due to the interaction of NMR properties of the tissue, image sequences and scan parameters. For the beginner in this field, NMR image contrast is the most confusing issue. The NMR signal intensity depends on intrinsic parameters (e.g., relaxation times T1, T2, spin density, magnetic susceptibility, bulk flow, perfusion, oxygenation, temperature, etc.), on the type of NMR experiment (spin-echo, gradient-echo, stimulated-echo, and their timing parameters), and on the NMR instrument (magnetic field strength, radiofrequency coil, stability, etc.).The dependencies are well understood and should be kept in mind in all biomedical applications. In addition, it is important that true biological information can be obtained, when these parameters are measured quantitatively (e.g. perfusion, oxygenation, temperature, blood flow, etc.). Furthermore extrinsic contrast can be obtained using contrast media. Here abnormal perfusion and tissue-specific information can be detected, like the detection of the breakdown of the blood-brain barrier.

A prerequisite for all biomedical NMR imaging applications is the use of a fast imaging technique. For example, it is needed to "freeze" cardiac motion which can be as fast as 600 beats/min in mice. In many applications, three-dimensional image acquisition, determination of quantitative parameters and functional information is needed. In order to keep the total experimental time as short as possible, some kind of fast acquisition is applied. During the last two decades, a large number of fast NMR imaging techniques was described. The lecture will summarize the important advantages and disadvantages of the different methods. The improvement of fast imaging methods is still going on. Recently, a dramatic decrease of the image acquisition time could be achieved using new hardware developments, e.g. phased-array coil technology and parallel imaging.

Dramatic improvements were described in biomedical NMR imaging in the area of flow imaging and applications to angiography and the determination of perfusion. The method and applications to animal studies will be demonstrated in this talk.

These methods were first described and applied in animal studies and clinical examinations. However, NMR imaging is not only limited to this area. Several groups have successfully applied NMR imaging to the study of plant physiology and function. Important studies, techniques and experimental difficulties for NMR of plants will be summarized in this talk.

Magnetic Resonance Spectroscopy and Microscopy at Variable Distances and Angles

Alexander Pines and Pinenuts
Lawrence Berkeley National Laboratory and
University of California, Berkeley, CA 94720, USA

Over the past decades, developments in magnetic resonance such as multiple-pulse sequences, cross-polarization, time-reversal excitation, multiple-quantum coherence, multidimensional spectroscopy, sample rotation, zero-field resonance, ex-situ spectroscopy, and optical pumping, have enhanced our ability to study molecular structure and dynamics in chemistry, materials science and biomedicine. The present lecture will address recent activities in these areas, in particular solid-state and liquid-crystal NMR, ex-situ NMR, and NMR and MRI with laser-polarized gases, together with examples of their applications over distance scales from nanometers to meters. NMR experiments are typically performed with samples immersed in a magnet shimmed to high homogeneity, in order to provide the greatest possible resolution.

In many circumstances it is impractical or undesirable to transport or insert samples into the gap or bore of a high-field magnet. In such cases it might be useful if spectra could be obtained remotely, for example by means of a magnet scanned over an intact object or subject, in order to acquire magnetic resonance information with compact, portable spectrometers. Developments in this direction are being coupled with the resolution advantages of solid-state coherent averaging and with the sensitivity advantages of laser-polarized xenon "functionalized" for molecular target recognition in materials and biomedicine. In addition, "remotely" detected microscope images of porous samples have been obtained.

Remote Detection of Polarized Xenon in Honeycomb

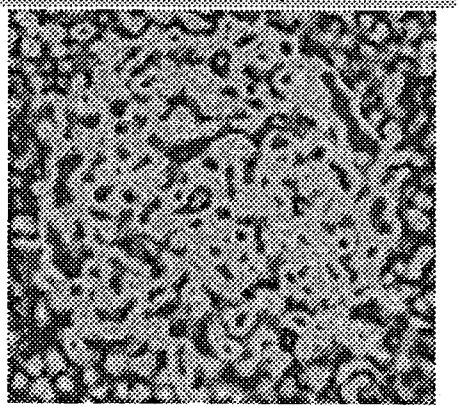

Magic-Angle Turning in Inhomogeneous Field of Ethanol in Rock

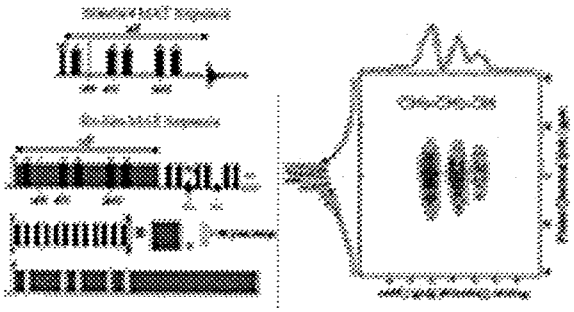

Disorder in BaTiO3 and SrTiO3

R. Blinc and B. Zalar
J. Stefan Institute, Jamova 39, Ljubljana, Slovenia

The ferroelectric phase transitions in BaTiO3 as well as the antiferro distortive transition in SrTiO3 are generally considered to be the classical examples of displacive soft mode type phase transitions taking place in an ordered crystal lattice and describable by anharmonic lattice dynamics. The question of the possible existence of spatial disorder is however still open. The problem to be solved is whether the potential for the Ti motion in the cubic paraelectric phase exhibits a minimum at the center of the oxygen cage or whether the Ti ion is disordered between several off-center sites. Since the electric field gradient (EFG) tensor should be zero by symmetry at the central position and non-zero at the off-center sites, the above problem could be definitely solved by quadrupole perturbed Ti NMR. Here we report on the first observation of a quadrupole coupling induced ^{47}Ti and ^{49}Ti satellite background in the cubic phases of both barium titanate and strontium titanate demonstrating the presence of spatial disorder. The satellite background transforms into well defined satellite lines below T_C. The observation of the satellite background was made possible by the use of a two 90-pulse, four phase "exorcycle" pulse sequence which minimizes the distortions due to antiechoes, transients, ill refocused signals, and piezo resonances. With the standard Hahn or solid echo sequences only the central component can be seen. The ^{49}Ti quadrupole frequency in BaTiO3 is 1.3 kHz above T_C in the cubic phase and 125 kHz below T_C in the tetragonal phase. The local structure is thus different from the average structure. The local displacements of the Ti ions from their cubic sites are along the body diagonals, i.e. the eight (111) directions. The spin-spin relaxation time values demonstrate that the disorder above T_C is dynamic and not static. The NMR technique motionally averages the dynamic hopping on a time scale of 10^{-6} seconds. The angular dependences of the second moments of both BaTiO3 and SrTiO3 demonstrate that we deal in the cubic phases with a tetragonal biasing of the titanium motion between eight off center sites. At the cubic to tetragonal phase transition the tetragonal short range order changes into a long range one. We thus deal here with a peculiar type of a phase transition which incorporates both order-disorder and displacive components.

Optically Pumped NMR of Quantum Wells: Using a "Bottom Up" Approach to Study Electron Spin Physics on Sub-micron Length Scales

Anatoly E. Dementyev[1], Pankaj Khandelwal[1], Nicholas N. Kuzma[1], Sean E. Barrett[1], Loren N. Pfeiffer[2], and Ken W. West[2]

[1]Department of Physics, Yale University, New Haven, Connecticut 06511

[2]Bell Laboratories, Lucent Technologies, Murray Hill, New Jersey 07974

Abstract

In the past decade or so, experiments have suggested that the spin degree of freedom in semiconductors might someday be used in novel solid state devices that would enable entirely new technologies (e.g., spin transistors, spin-based quantum information processors, etc. [1]). While recent progress is encouraging, the full potential of this approach is likely to go unrealized unless experiment and theory are used to develop a detailed understanding of the fundamental physics underlying each application. For example, it is imperative to develop novel experimental probes of spins in semiconductors, which can be used to measure the local electron spin polarization (and dynamics) inside a quantum well, buried deep within a sample. A variety of "top down" probes have been used to study the electron charge degree of freedom in semiconductors (e.g., scanning single electron transistor microscopy, scanning capacitance microscopy, etc.), but local information about the spin degree of freedom has been much more difficult to obtain.

Of course, NMR is the "ultimate local probe", and so it could be used to provide a "bottom up" view of electron spins in semiconductors. Unfortunately, the low sensitivity of NMR has severely limited its application in studies of microscopic samples, such as quantum semiconductor structures, which are often impossible to produce in large quantities. However, a technique called optically pumped nuclear magnetic resonance (OPNMR), which was developed at AT&T Bell Laboratories [2], circumvents this limitation [3]. Optical pumping is used to hyperpolarize nuclear spins in semiconductor quantum wells, enabling the direct detection of the radio-frequency NMR signal from these microscopic structures. A very similar technique is used to produce hyperpolarized noble gases, which will be the subject of another session. The signal boost achieved using OPNMR (e.g., see Fig. 1) makes the study of single interfaces on the interior of samples feasible, which can reveal important, local details about nanoscale structures. In particular, OPNMR experiments have provided many interesting insights into the rich spin physics of two-dimensional electron systems (2DES) in the Quantum Hall Regimes. We will review some of these results in this talk, with a particular emphasis on those experiments which have revealed evidence for the variation of the electron spin magnetization density both across *and along* the plane of the quantum well [4,5]. The connection to other topics at this conference (e.g., MRI), and new experimental directions, will be discussed.

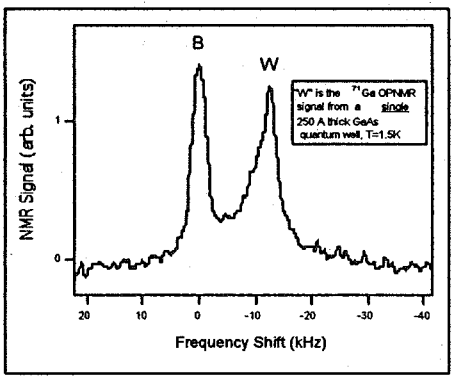

Figure 1: ^{71}Ga OPNMR spectrum of a single Gallium Arsenide quantum well.

References

[1] S. A. Wolf et al., *Science* **294**, 1488-1495 (2001).

[2] S. E. Barrett, R. Tycko, L. N. Pfeiffer, and K. W. West, *Phys. Rev. Lett.* **72**, 1368-1371 (1994).

[3] Optically Pumped NMR of Semiconductors and Two-dimensional Electron Systems, R. Tycko and S. E. Barrett, pp. 711-719 in **The Encyclopedia of Nuclear Magnetic Resonance, Volume 9: Advances in NMR,** edited by D. M. Grant and R. K. Harris, (John Wiley & Sons, Chichester, England, 2002).

[4] P. Khandelwal et al., *Phys. Rev. Lett.* **86**, 5353-5356 (2001).

[5] A. E. Dementyev et al., *Solid State Comm.* **119**, 217-227 (2001).

High resolution atomic magnetometers

M.V. Romalis, I.K Kominis, T.W Kornack, J. J. Heckman, M. P. Ledbetter
Department of Physics, Princeton University, Princeton, NJ 08544, USA

High sensitivity magnetometers find a wide range applications in detecting of weak biological magnetic fields and low-field NMR. Most such applications use SQUID magnetometers operating in liquid helium with a magnetic field sensitivity of about 1 $fT/Hz^{1/2}$ for flux pick-up coils with an area of several cm^2. Atomic magnetometers have achieved similar sensitivities, but only using liter-size volumes. We will describe a new type of atomic magnetometer that has achieved sub-femtotesla magnetic field sensitivity with millimeter spatial resolution [1].

Most sensitive atomic magnetometers use alkali atoms, K, Rb, or Cs. The atoms are spin-polarized, typically with a laser, and their precession in a magnetic field is measured using optical detection methods. The sensitivity of alkali-metal magnetometers is often limited by spin-exchange collisions which cause broadening of the magnetic resonance. However, it is possible to eliminate broadening due to spin-exchange by operating in a very low magnetic field and at high alkali metal density, in a manner similar to motional narrowing in NMR. We have recently developed a zero-field K atomic magnetometer that completely eliminates the spin-exchange broadening as well as a reduction in sensitivity due to the K nuclear spin. The theoretical sensitivity limits for this type of magnetometer are on the order of 10^{18} $T/Hz^{1/2}$, much higher than for other types of magnetic field sensors.

The magnetometer uses separate pump and probe laser beams, to polarize the atoms and to detect their response to the magnetic field. The active region of the magnetometer is defined by the intersection of the two laser beams. By detecting the transmission of the probe beam with a multi-channel photodiode it is possible to simultaneously measure the magnetic field at several different locations. We use high pressure He buffer gas to slow the diffusion of the atoms and enable high resolution magnetic field mapping. Taking linear combinations of different channels allows measurements of first and higher-order gradients of the magnetic field.

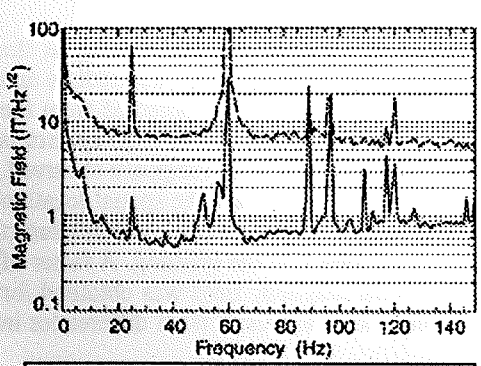

Figure 1: Magnetic field noise floor for a single magnetometer channel (dashed line) and first-order gradiometer (solid line)

Figure 1 shows the magnetic field noise floor for a single magnetometer channel (dashed line) and for a first order gradiometer (solid line). The gradiometer configuration eliminates magnetic field noise generated by Johnson currents flowing in the magnetic shields. Using multi-channel measurements we have also demonstrated localization of magnetic field sources outside of the magnetometer. The spatial resolution of the magnetometer is limited to about 2 mm by diffusion of K atoms.

High sensitivity and spatial resolution as well as absence of cryogenic cooling makes this magnetometry technique attractive for mapping of the magnetic fields produced by brain, heart and other organs. In addition, it can be used to detect magnetic fields generated by nuclear magnetization in low-field NMR.

We have recently demonstrated efficient detection of proton NMR signals enhanced by SPINOE with hyperpolarized liquid ^{129}Xe using high-T_c SQUID magnetometers. Atomic magnetometers would enable detection of such signals with 100 times higher sensitivity. Since atomic and SQUID magnetometers are directly sensitive to the magnetic flux, rather than the rate of change of the flux, then are much more efficient than RF coils at very low fields and allow one to fully utilize the advantages of using SPINOE-enhanced NMR signals.

References

I. K. Kominis, T. W. Kornack, J. C. Allred and M. V. Romalis, Nature **422**, 596 (2003).

^{2}H DQF Spectroscopic MRI as a Tool for the Study of the Microstructure and Biomechanics of Articular Cartilage

Hadassah Shinar, Keren Keinan-Adamsky, Galit Saar and Gil Navon
School of Chemistry, Tel Aviv University, Ramat Aviv, Tel Aviv 69978, Israel

Articular cartilage is a composite material which coats the ends of bones and whose biological function is to provide stress bearing and lubrication. The main constituents of articular cartilage are the oriented collagen fibers, the highly negatively charged proteoglycans (PG) and water. The combination of the swelling power of the proteoglycans as well as the tensile strength of the oriented collagen fibers, provide for the unique characteristics of the tissue.
The two "Gold Standards" for deducing the collagen fiber architecture are scanning electron microscopy (SEM) and polarized light microscopy (PLM). However these methods are very invasive, involving fixation, decalcification, dehydration and sectioning, Spectroscopic MRI offers to obtain information about the structure of the collagen fibers non-invasively on the basis of water proton residual dipolar interaction as well as the residual quadrupolar interaction of water deuterons.
^{1}H is undoubtedly the nucleus of choice for NMR measurements due to its high sensitivity and abundance. However, for the detection of order in biological tissues it has a major disadvantage. The proton chemical exchange between water molecules modulates the dipolar splitting causing it to collapse at room and body temperatures. The residual broadening is the basis of the T_2 weighted MRI images, which display several lamina that have been shown to depend on the orientation of the tissue relative to the magnetic field (1). The ^{2}H splitting is not affected by the chemical exchange since the splitting for the ^{2}H nuclei is caused by quadrupolar interaction which is the same for neighboring water molecules, and thus it is almost independent of the transfer of the deuteron atom from one water molecule to the other. Therefore the quadrupolar splitting is resolved. We thus chose to perform our measurements on ^{2}H for cartilage plugs equilibrated in deuterated saline. An improved resolution is obtained using double quantum filtered (DQF) techniques, since the signal of the isotropic water is eliminated by these techniques and since one can optimize the resolution by a judicial choice of the delay leading to formation of the second rank tensor (the creation time τ) (For a review see ref 2).
By performing DQF spectroscopic imaging one can follow the variation of the ^{2}H quadrupolar splitting in the different layers of the articular cartilage, from the calcified zone near the bone through the radial, intermediate and the superficial zones. An example of such an image is given in Fig. 1 along with some spectra extracted from the image. The x axis is the frequency axis (in Hz) while the y- axis is the spatial axis (in mm). No ^{2}H DQF spectra is observed in the bone. At the bone-cartilage interface, the calcified zone, at least two pairs of splittings are observed. The frequency difference between the satellite transitions as well as their intensity, change with the spatial location on the plug. The splitting depends on both the fibers orientation and the fraction of water molecules which interact with the fibers. Separation between the two effect is obtained by the angular dependence of the splitting. A factor of two between parallel and perpendicular orientations of the cartilage relative to the magnetic field was obtained for the calcified and the radial zones indicating that the differences in the splittings does not result from differences in fiber orientations but from differences in the fiber packing and density.
In the present work we took advantage of the method to investigate the effects of pressure, connection to the bone, and the decalcification on the collagen fibers architecture. Due to the difficulties that people have in investigating the cartilage properties under mechanical pressure, it is customary to apply osmotic pressure instead. In our research we are able to compare effects of these two methods on the structure of the collagen fibers.

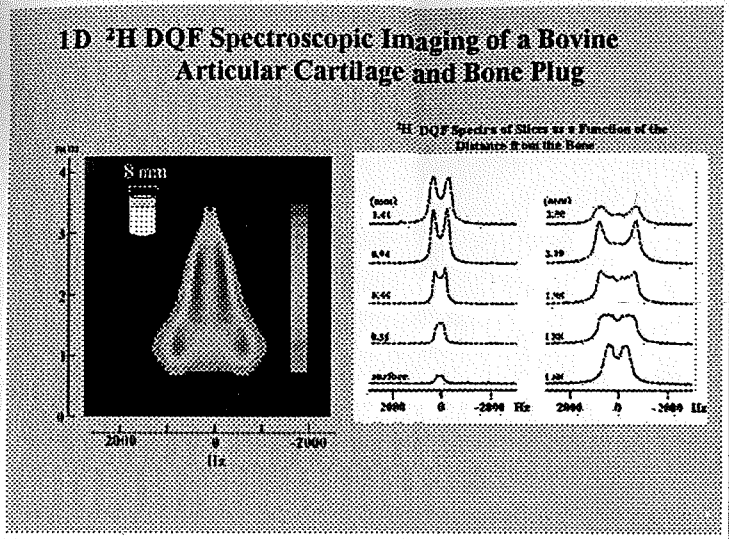

Fig. 1

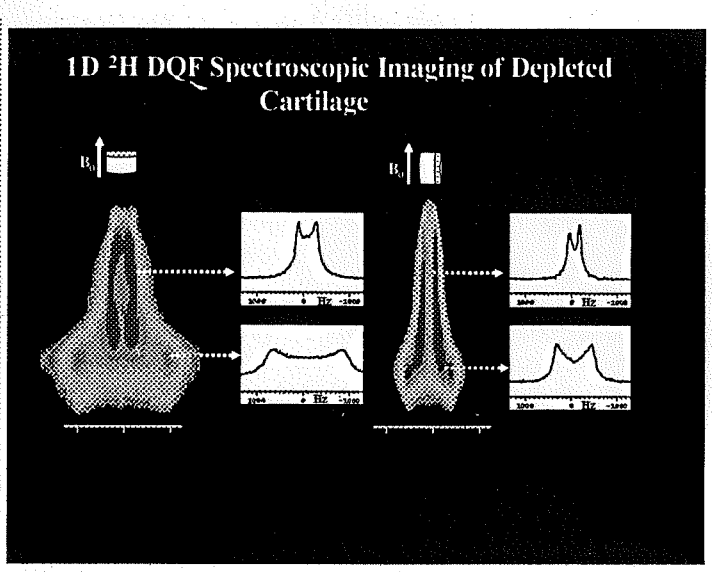

Fig. 2

References

1. Y. Xia, T. Farquhar, N. Burton-Wurster and G. Lust, *J. Magn. Reson. Imaging* **7,** 887-894 (1997).
2. G. Navon, H. Shinar, U. Eliav and Y. Seo, *NMR Biomed.* **14,** 112-132 (2001).

Single-Sided Magnetic Resonance Relaxometry and Elastography of Elastomer Structures

S. W. Sinton[1], E. J. VanderHeiden[2], S. Patil[3], J. Reimer[3]
[1]Lockheed Martin Space Systems Co., Advanced Technology Center, 3251 Hanover St., Palo Alto, CA 94304; [2]Alliant Techsystems, Magna UT; [3]Dept. of Chem. Eng., University of California, Berkeley, CA

Magnetic resonance has great potential as a tool for inspecting organic materials in many applications. Some examples include NMR monitoring of food or polymer processes, evaluating rubber crosslink density in tire manufacture, and the assessment of aging processes and rates of materials for life-cycle prediction. Some important requirements for NMR in these applications are driven by the configuration and characteristics of the process or structure to be inspected. For example, it is often impossible to fit the process or material under inspection within a practical magnet structure, so the "single-sided" approach is adopted. We have developed single-sided NMR to track changes in mechanical properties of elastomers within composite structures using proton relaxometry and elastography techniques. Optimization of pulse sequence settings and data analysis methods for determining T_2 in the inhomogeneous field will be discussed. The ability to determine small changes in crosslink density by single-sided T_2 measurements will be explored. An alternate approach to assessing elastomer mechanical properties based on MR elastography will be presented. An algorithm developed to convert displacements resolved by elastography into spatial information about material modulus will be shown. This algorithm avoids the necessity to solve simultaneous equations with high-order differentials through an integral approach.

Probing Lung Microstructure with Laser-Polarized He-3 Gas Diffusion

Mark S. Conradi, Dmitriy A. Yablonskiy, and Jason C. Leawoods
Washington University, Departments of Physics and Radiology, Saint Louis, MO 63130 USA

The free diffusion of He-3 at 1 atmosphere is remarkably rapid, about 0.88 cm^2/s for dilute He-3 in air or N_2. Thus, even over times of only a few milliseconds, He-3 diffusion is substantially restricted by the alveolar and small-airway walls (typical distances of 0.3 mm). Indeed, in healthy human lungs, the average ADC measured over 2-3 ms is about 0.20 cm^2/s; in rats and mice similar values have been reported. Airway expansion and tissue destruction in emphysema result in reduced restriction. For example, a cohort of patients with severe emphysema have average ADCs of 0.55 cm^2/s. Thus, the combination of He-3 ventilation images and He-3 ADC maps provide a full picture of diseased lungs, revealing the distribution of gas within the lung as well as the local extent of destruction of the lung microstructure.

The average ADC is determined from the ratio of intensities, pixel-by-pixel, of two gradient recalled echo images, one with a diffusion-sensitizing gradient and one without. However, use of a larger number of b-values immediately reveals that a distribution of ADCs exists in each voxel, due to the anisotropy of diffusion. During the experimental timescale of 2-3 ms, He-3 atoms can explore only a single small-airway. Thus, the He-3 Brownian motion will be characterized by a longitudinal diffusion D_L (parallel to the airway) and a transverse diffusion D_T (perpendicular), with $D_L > D_T$. Each voxel contains 1000 or more such airways oriented in all directions, so the anisotropy cannot be determined by rotating the gradient. Instead, the anisotropy results in a non-exponential signal decay versus b-value. The image intensity at each voxel as a function of b is fitted with 3 parameters: initial amplitude, D_L, and D_T. The D_T value is a function of the mean airway radius; the radius determined from He-3 diffusion in healthy lung is in excellent agreement with previous microscopic examinations. Both D_L and D_T increase in emphysema, with substantially reduced anisotropy D_L/D_T.

Measurement of ADC using transverse magnetization are limited to times less than T_2^*. Longer diffusion times and distances can be explored by modulating the longitudinal spin magnetization ($T_1 \sim 20s$). The diffusion over seconds and centimeters involves gas moving from one small-airway to the next, along the maze of the branching network of airways. Thus, while diffusion over milliseconds (D_{msec}) reports on the size of individual small –airways, diffusion over seconds (D_{sec}) reports on airway connectivity. Spatially modulated longitudinal magnetization (striping) is produced with a wavelength of 2-3 cm. The decay of the modulation is monitored with images using small flip angles. The decay from diffusion is readily separated from decay due to T_1 and magnetization consumption by rf pulses; the diffusive decay rate R yields the diffusivity.

In healthy lung, we find D_{sec} to be an order of magnitude smaller than D_{msec}, in keeping with the additional restriction imposed by the airway maze. In emphysema, D_{sec} increases, often by a larger factor than D_{msec} increases. Indeed, the finding of D_{sec} values near the free diffusivity of the gas demonstrates that, in those lungs, the airways are so porous that they are virtually irrelevant to gas transport and diffusion – collateral ventilation has become dominant. Long-range gas diffusivity will be an excellent probe of collateral ventilation.

MR Microscopy for High Throughput Mouse Phenotyping

R. Mark Henkelman, Nicholas A. Bock, Natasa Kovacevic, John G. Sled, F. Stuart Foster, X. Josette Chen
Mouse Imaging Centre, Hospital for Sick Children, University of Toronto,
555 University Avenue, Toronto, Ontario M5G 1X8, Canada

Image-Based Phenotyping
With the completion of the human genome sequence, there is a major challenge to understand how genes give rise to mammalian phenotype. In the human, there is particular interest to understand the relationship between genes and diseases. Much of this understanding will come from work in the mouse, which has a 99% overlap in recognizable genes with the human genome [1]. The mouse has been chosen as the major mammalian model because there are a number of inbred lines, genetic manipulations can be readily carried out, and the rapid generation time minimizes the costs of experiments. Mice also share many of the diseases that are known in humans.

Mouse models of human disease are therefore an important area of current research. Imaging, in turn, has major role to play in the studying of mouse models of disease. Just as imaging is essential for the evaluation of human diseases in the human population, mouse imaging is becoming essential for the evaluation of mouse models of human disease. The objectives of imaging mice can be broadly divided into two categories: 1. time course studies looking at progression of disease and response to treatment in individual mice; and 2. surveys of large numbers of genetically selected mice.

MR Microscopy for Mouse Phenotyping
MRI readily scales from the human to the mouse. Intrinsic loss in SNR can be partially recovered using mouse sized receiver coils, increased field strength, and longer imaging times. The equivalent fractional anatomic definition in the mouse requires voxel sizes of approximately 60 microns. Examples will be given of:

- High resolution isotropic volume images of fixed mice for survey work,
- Cardiac abnormalities in knockout mice,
- Models of growth of brain tumors,
- Use of novel contrast agents.

Multiple Mouse Magnetic Resonance Imaging (MMMRI)
In biological experiments using MR microscopy of mice, there is significant pressure for high throughput either from the desire to study cohorts of equivalent mice or to survey large numbers of mice with individualized genetic changes. This demand has lead us to develop multiple mouse magnetic resonance imaging [2]. We have fitted a 7 Tesla, 40-cm imager with 19 individual transmit/receiver coils (Fig. 1). In its present configuration, this allows for the acquisition of 16 mouse data sets of the same quality and in the same time as it would take to acquire a single mouse on a conventional system. This uses four parallel receivers and four-fold multiplexing. Some of the technical considerations of coil cross talk, gradient homogeneity, image aliasing and pulse sequences will be discussed.

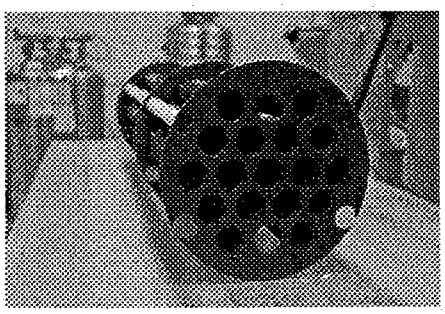

Comparison of MRI with Other Modalities

As in human medical imaging, MRI is not the solution to everything. Similarly in mouse MR microscopy, it is important to compare MR with other imaging modalities. A quick overview of what can be accomplished with the real time aspects of ultrasound, the very high definition of CT and the molecular specificity of optical projection tomography will all be discussed.

Defining a Normal Mouse and Finding a Mutant

Working with genetically identical individuals enables precise anatomical definition of an average mouse phenotype. We have produced an average brain atlas which attempts to capture the range of normal variation in an inbred strain. The variation in brain anatomy within this strain is much tighter than the variation between strains. Thus, it becomes much easier to pick out a variational outlier from the normal population. Inbred strains provide a huge advantage compared with the genetically heterogeneous human population in looking for outliers and will facilitate the identification of vary subtle mutations (Fig. 2).

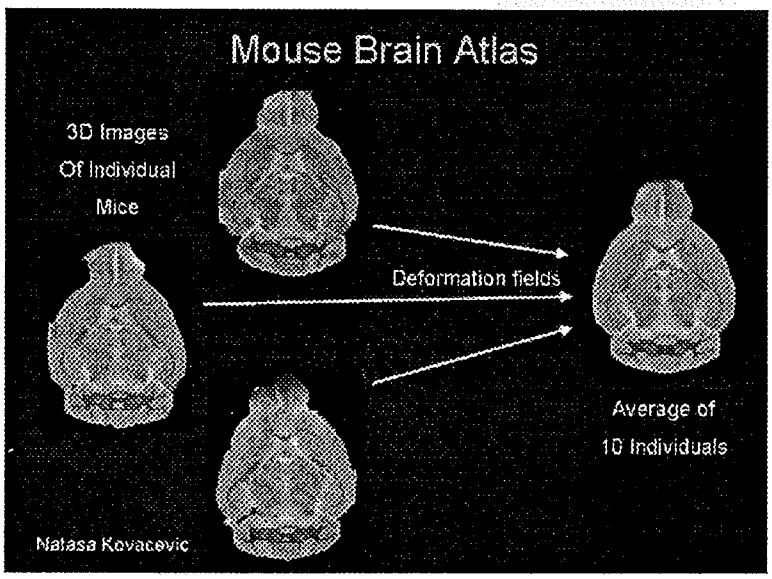

However, there are limitations to the concept of variation of normal anatomy. High definition x-ray CT images of vascular structures show anatomic morphology, which is difficult to compare between individuals. Nevertheless, significant changes in vascular morphology occur with changes in the underlying genome (Fig. 3).

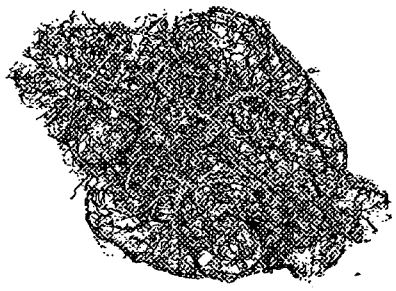

The challenges of image-based phenotyping in the mouse represent an exciting opportunity for scientific innovation.

References

[1] J. H. Nadeau, et al. Functional Annotation of Mouse Genome Sequences. *Science* **291**, 1251-1255 (2001).

[2] Nick A. Bock, Norman B. Konyer, R. Mark Henkelman. Multiple-mouse MRI. *Magnetic Resonance in Medicine.* **49,** 158-167 (2003).

In vivo High-resolution Proton NMR Spectroscopy in a Rotating Mouse

Robert A Wind, Jian Zhi Hu, and Donald N. Rommereim
Pacific Northwest National Laboratory, P. O. Box 999, MS K8-98, Richland, WA 99352

Abstract
In vivo ^{1}H NMR spectroscopy is widely used for investigating metabolic processes in cells, tissues, animals, and humans. However, the spectra often suffer from poor resolution due to variations in the isotropic bulk magnetic susceptibility present in biological objects, resulting in a broadening of the NMR lines. In principle this broadening can be averaged to zero by the technique of magic angle spinning (MAS), where the sample is rotated about an axis making an angle of 54°44' relative to the external magnetic field. However, a problem is that in a standard MAS experiment spinning speeds of a kHz or more are required in order to avoid the occurrence of spinning sidebands (SSBs) in the spectra, which renders analysis of the spectra difficult again. At these spinning speeds the large centrifugal forces cause severe structural damage in larger biological objects, restricting this technique for studies of small cell agglomerates or cell extracts.

In solid state NMR several methods have been developed where slow MAS is combined with special radio frequency pulse sequences to eliminate spinning side bands or separate them from the isotropic spectrum so that a SSB-free high-resolution isotropic spectrum is obtained. It has been shown recently that two methods, phase-adjusted spinning sidebands (PASS) and phase-corrected magic angle turning (PHORMAT), can successfully be modified for applications in biological materials (1, 2), and in excised rat liver with ^{1}H PHORMAT even at a 1 Hz spinning speed a spectral resolution was obtained comparable to that observed with fast MAS (2). Hence it appeared that PHORMAT could potentially be applied in live animals as well, and in this seminar the first results of *in vivo* PHORMAT experiments will be discussed.

The mouse-MAS NMR probe is home-built. The rotor is a cylinder with an I.D. of 20 mm, into which a mouse can be inserted. The rotor is stabilized by non-metallic ball bearings, and is driven by a computer-controlled electrical motor. The ^{1}H NMR experiments were performed using a horizontal wide-bore (30 cm) 2Tesla Oxford magnet, corresponding to a proton Larmor frequency of 85 MHz, and a Varian Unity Plus console. The figure shows the water-suppressed isotropic proton spectra obtained with a stationary BALBc female mouse (A) and with an animal spinning at a speed of 1.5 Hz (B). In the experiments no volume selection was applied, which means that the spectrum originates from the middle section of the mouse body located within the 4 cm long NMR coil. A reduction of about a factor 4 in the line widths of the isotropic lines is obtained in the spinning experiment.

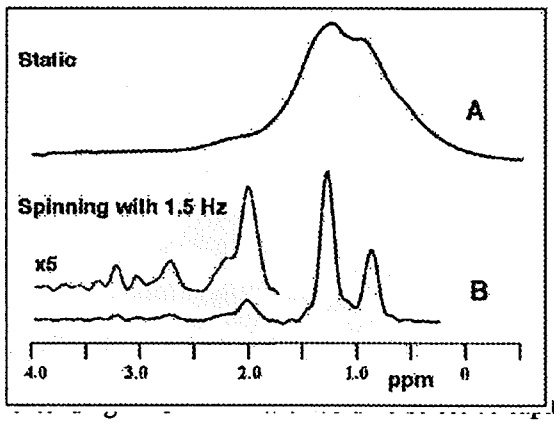

We conclude that even in the relatively low 2T field a significant enhancement in the spectral resolution is obtained, and this will further increase in the 7T or even 9T animal MRI systems available to date. Finally, several technical improvements will be discussed that will increase the utility of *in vivo* PHORMAT as a practical approach, and that are being implemented in our laboratory. Examples are ...bilities, increasing its sensitivity, and reducing its measuring time. It is anticipated that *in vivo* PHORMAT will significantly enhance the utility of proton MR spectroscopy for biomedical research in live animals, and perhaps even in the clinic, in the latter case by rotating the external magnetic field rather than the patient.

References
1. R. A. Wind, J.Z. Hu, and D.N. Rommereim, *Magn. Reson. Med.* **46**, 213-218 (2001).
2. J. Z. Hu, D.N. Rommereim, and R.A. Wind, *Magn. Reson. Med.* **47**, 829-836 (2002).

Image Based Phenotyping

G. Allan Johnson, Ph.D. and Laurence W. Hedlund, Ph.D.
Center for In Vivo Microscopy, Duke University, Durham, N.C. 27710

The successful effort to sequence the human genome has ushered in an entirely new era of medicine. In order to use the information derived from this effort we must now map the genetic information to specific phenotypes. The mouse and rat are the most amendable models for this task. This talk will focus on image-based methods to phenotype the rat and mouse using magnetic resonance and x ray microscopy. The challenges in moving imaging methods from man to mouse are best viewed in the context of the relative volumes. The mouse at 25 gms is nearly 4000 times smaller than the man at ~ 100kGm. The problem in scaling clinical imaging technologies to the mouse is further exacerbated by the temporal scale. The R-R interval in the mouse is ~ 100 ms, nearly ten times shorter than that in the man. No single "trick" will allow one to image the mouse with the necessary temporal and spatial resolution. One must instead use an integrated approach. We have applied this approach in both functional and structural phenotyping using both magnetic resonance microscopy and x ray microscopy. Technical approaches and the applications that can benefit will be included.

Acknowledgements: This work supported by NIH/NCRR P41 05959, NIH/NCI R24 CA092656, NIH/NHLBI RO1 HL 55349-04, DoD DAMD 17-02-2

Looking Deeper into Development Applications of High resolution MRI in Developmental Biology

Russell E. Jacobs and Seth Ruffins
Beckman Institute, California Institute of Technology, Pasadena, CA 91125

The exquisite sensitivity of MRI to the local physical and chemical environment provides a wide range of mechanisms giving rise to intrinsic contrast in the MR experiment, thus providing images with dramatic differences between different tissue types (*e.g.* white versus gray matter, myelinated versus unmyelinated fibers, and brain parenchyma versus ventricles). In this talk we look at two applications of high resolution MRI in developmental biology.

Three-dimensional digital atlases of normal development in the primate, rodent, and avian systems: Real brains and real embryos in the real world exist in 3 dimensions with complex relationships among the various anatomic parts. Print and 2 dimensional web based atlases are extremely useful, but limited tools that describe the various anatomical parts of the animal of interest. We are constructing multidimensional atlases of development of the mouse and quail using high resolution MR imaging. The atlases will not only serve as pedagogical tools, but also present an ideal graphical interface to databases containing non-anatomical information (*e.g.* gene sequences, gene expression domains, literature citations). In this fashion the atlases will serve as the interface for exploring more detailed anatomical findings such as the organization of axonal tracks, maps of cell lineages and regional fate in the developing brain, and patterns of naturally occurring cell death. Gene expression patterns, receptor domains, arrays of innervation in the developing nervous system, cell lineage patterns, and a host of other types of biological processes in embryonic and adult animals take place in three spatial and one temporal dimensions. They occur within the context of anatomy of the specific sample being examined. Digital atlases provide a means to put such specific data within the context of normal specimen anatomy, analyze the information in three (or more) dimensions, and examine relationships between different types of information. We present preliminary information on the mouse and avian systems, but concentrate on the mouse. The atlas discussed here is composed of three different modules: unprocessed μMR images of fixed embryos aged 6.5 to 15.5 days post conception (dpc); an annotated atlas of the anterior portion of a 13.5dpc mouse where anatomical structures in transverse sections of the embryo have been delineated and linked to descriptive files; a three-dimensional model of the 13.5dpc embryo (Figure 1). As an example of how other types of information can be incorporated into this model, we have 'painted' in the gene expression pattern of Dlx5/Dlx6 genes that are involved in the regulation of forebrain development.

Morphometric Cell Movements: The African clawed frog (Xenopus laevis) is an extremely well studied model system in developmental biology. Even so, the fatty nature of the embryo makes it virtually impossible to examine the complexities of cell movements during crucial events in early embryogenesis with optical microscopy. High resolution MRI coupled with single cell contrast agent labeling (Figure 2) have allowed us to follow morphometric movements during gastrulation *in vivo* within individual animals. We find that these movements often do not follow the schematics found in most textbooks. In particular, interactions between mesoderm and neurectoderm in the late blastula and through gastrulation are qualitatively different than current dogma suggests.

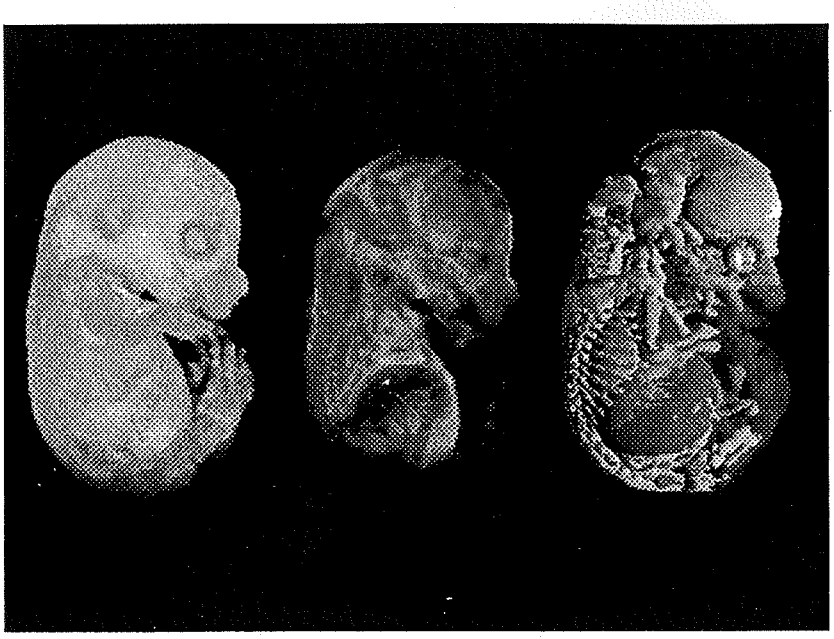

Figure1. μMRI allows internal anatomy of opaque specimens to be imaged nondestructively. μMRI is being used to produce an atlas of mouse development at tissue resolution with high 3D fidelity. The image in the left panel shows a surface rendering of a TS24 mouse embryo; in the middle panel the opacity has been decreased to show internal structures; the right panel shows a volume rendering of delineated anatomical structures.

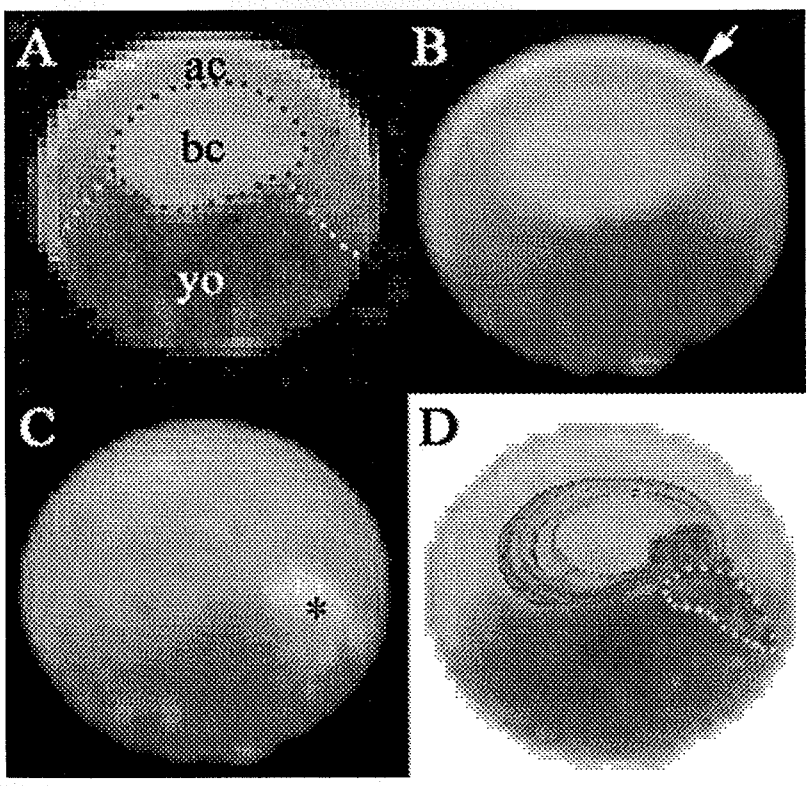

Figure 2. Microscopic MR-images of a live stage 8 *Xenopus laevis* embryo. A single cell (C1 blastomere) was labeled with MR contrast agent at 32 cell stage. A) Single slice from the middle of the sample. The different tissue regions can be distinguished on the basis of their pixel intensities. ac: animal cap; bc: blastocoel; veg: vegetal cell mass. The approximate border between the animal and the vegetal cell mass is highlighted with yellow dots. B) Half the image volume with the front half cut away at the level of the slice in (A) to reveal internal structures. The arrow in A and B points to a bright crescent, which is the liquid-filled cleft between the embryo proper and the vitelline membrane. The magnetite added to the medium does not cross the vitelline membrane and thus cannot eliminate the proton signal from this aqueous moiety. C) Whole image volume. Labeled clone cells (marked with an asterisk) situated in the dorsal marginal zone of the embryo appear as a bright patch. D) Whole image volume in which features of interest have been identified and the opacity lowered to reveal the internal structures. The vegetal cell mass appears dark gray; the animal cap cell is light gray. The blastocoel surface is rendered in lilac. The labeled cells appear greenish-orange. The clone border on the surface and visible in (C) is outlined with white dots.

Magnetic Resonance Microscopy at the Micron Scale, and "DESIRE"

Luisa Ciobanu*, Charles H. Pennington, Joseph A. Martindale
Department of Physics, Ohio State University, Columbus, OH 43210, USA

*Now at Beckman Institute, University of Illinois at Urbana-Champaign, 405 N. Mathews, Urbana, IL 61801

Extending the reach of magnetic resonance imaging (MRI) down to the micron scale, a scale suitable for imaging typically-sized biological cells, requires large improvements in sensitivity, and in gradient strengths, as compared with clinical MRI or even what is currently called MR "microscopy", which usually operates at the resolution of 10's of microns. I will first review some of the hardware tools, such as micro-receiver coils [1-4] and high strength (~10T/m) gradients, [5] that are necessary. I then survey some of the 3D micro-images, with resolution of 3-5 microns (in each dimension), obtained by our group. Representative images are shown in Figures 1 and 2. Figure 1 contains an image of a "phantom" sample consisting of 39□m diameter polymer beads immersed in water, and Figure 2 an image of the *spirogyra* alga cell, in which chloroplast organelles, which are spirally arrayed around the inner cell wall, are resolved. These images, to our knowledge, have the highest raw voxel resolutions reported to date. Other investigators [6-13] have focused on other important issues at the micron or near-micron scale, including diffusion, relaxation times, and localized spectroscopy. A review of recent work is given by Ciobanu *et al.* [14]

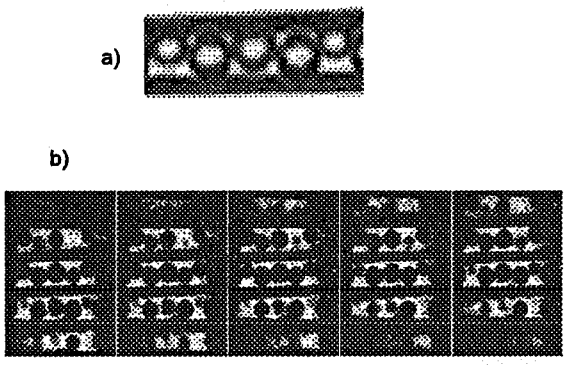

Figure 1 a) Microscope photo of 39□m polymer beads, immersed in water, and sealed in a micro-capillary. **b)** 3D MR image of the sample shown in a). [15, 16] Image has resolution of ~3.5□m in all three dimensions. Image is taken using gradients of ~5T/m, with phase encoding employed for all three directions. Following the phase encode, the echo signal is refocused hundreds of times using a Carr-Purcell or Carr-Purcell-Meiboom-Gill train.

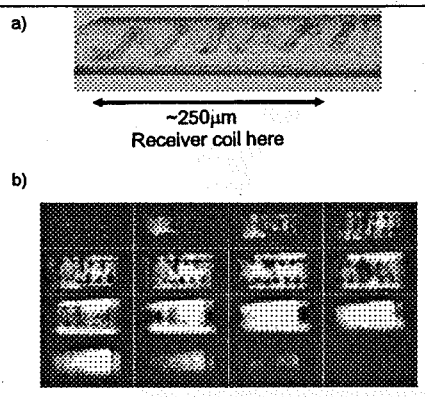

Figure 2 a) Microscope photo of a single *spirogyra* alga cell, immersed in water, and inside a microcapillary, around which a micro-receiver coil (not shown) of length ~250□m is wound. The *spirogyra* has diameter of ~40□m and length of several hundred □m. It features green chloroplasts, which are spirally arrayed around the inner surface of the cell wall. **b)** 3D MR image of the sample displayed in a). [15, 16] Image has resolution of ~5□m in all three dimensions. The chloroplasts are clearly seen piercing the image slices.

While much progress has been made in micron-scale MR microscopy, there are still very imposing limitations. The images of Figures 1 and 2 for example required many hours to acquire. Lauterbur [17-19] has proposed a method, "Diffusion Enhancement of SIgnal and REsolution (DESIRE)" that promises to improve the situation by exploiting molecular diffusion. Using gradient-localized pulses, the nuclear spins are saturated within a micron-scale voxel (1D, 2D, or 3D). Over time, these saturated spins and associated molecules are replaced by new ones, and magnetization is ultimately reduced over a volume region perhaps much greater than the voxel. A tutorial style article by Pennington [20] shows that sensitivity enhancements of 10's to 100's, and perhaps even 1000's, can be attained using DESIRE at the micron scale. I will report on our progress toward DESIRE. Figure 3 shows the first experimental demonstration of the DESIRE concept in 2D. Supported by NSF/DBI9987079.

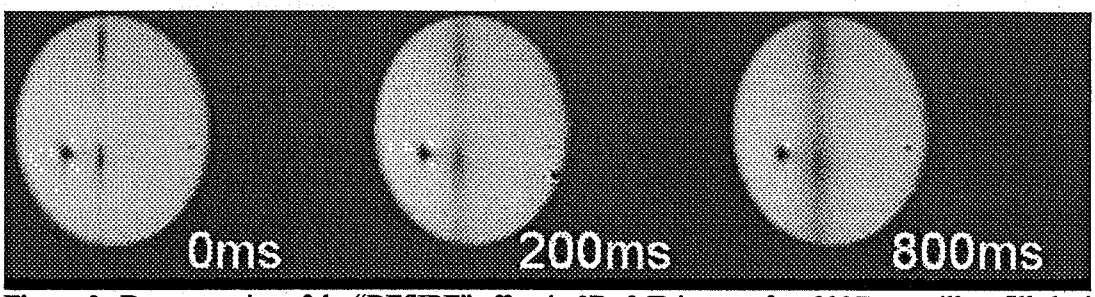

Figure 3. Demonstration of the "DESIRE" effect in 2D. MR image of an 800□m capillary filled with water, with a ~50□m diameter glass fiber inserted for reference. Using trains of 2D gradient-localized rf pulses, nuclear spins are saturated for times 0ms, 200ms, and 800ms within a hole with diameter ~40□m by ~70□m. This figure shows that after 200ms and 800ms, the saturation effect has spread out to cover larger regions of the sample—the DESIRE enhancement effect.

References

1. Webb AG. Radiofrequency microcoils in magnetic resonance. Progress in Nuclear Magnetic Resosance Spectroscopy 1997; 31: 1-42.
2. Minard KR, *et al.* Solenoidal microcoil design. Part I: Optimizing RF homogeneity and coil dimensions. Concepts in Magnetic Resonance 13: (2) 128-142 2001 2001; 13: 128-142.
3. Minard KR, *et al.* Solenoidal microcoil design - Part II: Optimizing winding parameters for maximum signal-to-noise performance. Concepts in Magnetic Resonance 2001; 13: 190-210.
4. Seeber DA, *et al.* Design and testing of high sensitivity micro-receiver coil apparatus for nuclear magnetic resonance and imaging. Review of Scientific Instruments 2001; 72: 2171.
5. Seeber DA, *et al.* Tri-axial magnetic field gradient system for microcoil magnetic resonance imaging. Review of Scientific Instruments 2000; 71: 4263-4272.
6. Minard KR, *et al.* Picoliter ^{1}H NMR Spectroscopy. J. Magn. Res. 2002; 154: 336-343.
7. Wind RA, *et al.* An Integrated Confocal and Magnetic Resonance Microscope for Cellular Research. Journal of Magnetic Resonance 2000; 147: 371-377.
8. Grant SC, *et al.* NMR Spectroscopy of Single Neurons. Magnetic Resonance in Medicine 2000; 44: 19-22.
9. Grant SC, *et al.* MR Microscopy of Multicomponent Diffusion in Single Neurons. Magnetic Resonance in Medicine 2001; 46: 1107-1112.
10. Sehy JV, *et al.* Water and lipid MRI of the Xenopus Oocyte. Magnetic Resonance in Medicine 2001; 46: 900-906.
11. Sehy JV, *et al.* Evidence that both fast and slow water ADC components arise from intracellular space. Magnetic Resonance in Medicine 2002; 48: 765-770.
12. Sehy JV, *et al.* Apparent diffusion of water, ions and small molecules in the Xenopus Oocyte is consistent with Brownian displacement. Magnetic Resonance in Medicine 2002; 48: 42-51.
13. Sehy JV, *et al.* Importance of intracellular water apparent diffusion to the measurement of membrane permeability. Biophysics Journal 2002; 83: 2856-2863.
14. Ciobanu L, *et al.* Magnetic Resonance Microscopy of Biological Cells. Progress in Nuclear Magnetic Resonance Spectroscopy 2003; in press.
15. Ciobanu L, *et al.* 3D MR Microscopy with resolution 3.7mm by 3.3mm by 3.3mm. Journal of Magnetic Resonance 2002; 158: 178-182.
16. Ciobanu L, *et al.* 3D Micron-scale MRI of Biological Cells. Solid State NMR 2003: in press.
17. Lauterbur PC, *et al.* NMR microscopy: old resolutions and new desires. in XI International Society of Magnetic Resonance Conference. 1992. Vancouver, B. C.
18. Lee JJ. PhD Thesis (Chemistry, University of Illinois at Urbana-Champaign, 1998).
19. Hyslop WB. PhD Thesis (Department of Physics, University of Illinois at Urbana-Champaign, 1998).
20. Pennington CH. Prospects for Diffusion Enhancement of Signal and Resolution (DESIRE) in Magnetic Resonance Microscopy. submitted to Concepts in Magnetic Resonance 2003.

Diffusion Tensor Microscopy: From Molecules to Organs

Edward W. Hsu
Department of Biomedical Engineering, Duke University, Durham, NC 27708-0281, USA

Introduction

The translational diffusion of water reflects the geometry and organization of its molecular environment. Diffusion tensor imaging (DTI) has been used to quantify anisotropic diffusion observed by MRI [1]. A key hypothesis of DTI is that the eigenvector corresponding to the largest ranked diffusion tensor eigenvalue (i.e., the direction in which diffusion is the fastest) corresponds to the orientation of the local tissue fibers. This has been supported by the strong correlation reported between fiber orientation angles measured in the myocardium via DTI and conventional histology [2].

In 3D space, a unique solution to the symmetric, 3 x 3 diffusion tensor necessitates diffusion to be quantified in at least 6 non-coplanar directions. Although the minimal DTI experiment would thus consists of 7 image acquisitions (including 1 non-diffusion-weighted image), either or a combination of more diffusion encoding directions or more encoding levels per direction are often added to improve the accuracy. Consequently, the long scan time required by the large dataset and the inherent SNR tradeoff between scan time and resolution present formidable technical challenges for DTI at microscopic resolutions.

Significant methodological advances have been made recently in improving the temporal and spatial resolutions and accuracy of DTI, including (a) reduced encoding and constrained image reconstruction schemes for improving the data acquisition time efficiency, (b) mutual-information based image registration methods to correct for anisotropic image distortions caused by eddy currents accompanying large diffusion encoding gradients, and (c) robust adaptive PDE-based noise removal algorithms to improve fiber orientation mapping accuracy. These techniques are demonstrated in 3D diffusion tensor microscopy of the mouse brain and heart.

Reduced Encoding DTI

Except for the varying diffusion encoding gradient amplitudes, DTI is similar to dynamic MRI where the same object is scanned repeatedly. Since image contrast variations (including diffusion weighting) are primarily low spatial-frequency in nature, k-space data sharing techniques such as the "keyhole" [3] or RIGR (reduced encoding imaging via generalized series reconstruction) [4] may be useful to accelerate DTI scans. We examined the performance (in terms of deviation from "gold standard" tissue fiber angles) of several 50% reduced encoding imaging schemes, including direct replacement keyhole (KD), keyhole with zeroth order correction (KC), and RIGR, against a reduced set of full encoding images of equal scan time (control). Results (Fig. 1) indicate that the combination of reduced encoding acquisition and constrained image reconstruction (e.g., RIGR) can significantly improve the DTI data acquisition efficiency without proportional loss in fiber orientation mapping accuracy.

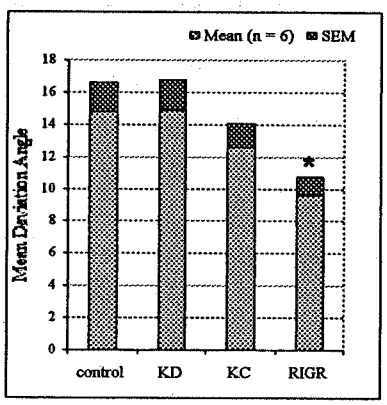

Figure 1: Relative performances of reduced encoding DTI schemes.

DTI Data Noise Removal for Fiber Streamline Tracking

The SNR of DTI is inherently low due to the nature of diffusion encoding (i.e., signal attenuation), inadvertent T2 weighting during the long TE needed by the diffusion encoding pulses, and the tradeoff between SNR, spatial resolution and scan time. Image noise, hence diffusion tensor estimation error, is a major source of error in tracking tissue fiber streamlines. While SNR can be increased by additional scans, post-processing noise removal may be an effective alternative means to enhance DTI accuracy without incurring additional costly acquisition time. We examined selected noise removal techniques such as low-pass and Wiener filtering. To allow better tissue border preservation and fiber streamline tracking, we propose a novel adaptive partial differential equation (PDE, also known as "diffusion" filtering) based algorithm [5]. A key advantage of the technique is that fiber streamline tracking can be selectively weighted to the local diffusion tensor estimation error or diffusion anisotropy parameters such as the fractional anisotropy (FA) index.

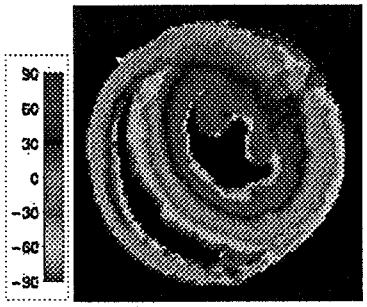

Figure 2. Mid-hemisphere fiber helix angle (essentially inclination angle from the imaging plane) of the mouse heart obtained via 3D reduced encoding diffusion tensor microscopy.

Diffusion Tensor Microscopy of Mouse Hearts

Myocardial fiber orientation plays an important role in the electrophysiological and biomechanical properties of the heart, and changes of the fiber structure has been implicated in injury, diseases, and remodeling in both humans and animal models. Although DTI may be useful in assessing myocardial fiber structure, its SNR constraint may present a formidable challenge in small animal (e.g., mouse) applications. We applied the reduced encoding methodology and noise removal techniques in 3D DTI (78 μm isotropic resolution) of the fixed intact mouse heart. The reduced encoding DTI experiment (1 full-encoding b0 image and 12 diffusion-weighted images encoded in a set of 12 directions) yielded qualitatively similar fiber maps compared to the full encoding-only experiment, but required only 9.1 hr (versus 29.6 hr) scan time.

Diffusion Tensor Microscopy of "Active Stained" Mouse Brains

By providing enhanced SNR and tissue contrast, "active staining" techniques [6] have been useful in rapid MR microscopy-based morphological phenotyping of genetic mouse strains. However, due in part to the complex compartmentation of tissue MR properties including diffusion, the impacts on brain white matter visualization are unclear. We investigated the effects of "active staining" and tissue fixation in 3D DTI (78 μm isotropic resolution) of the C57Bl/6 mouse brain white matter. Results reveal that "active staining" (specifically, transcardiac perfusion fixation with a 1:10 Gd solution) can be used to enhance DTI SNR, leading to improved data acquisition time efficiency and visualization of the brain white matter structure.

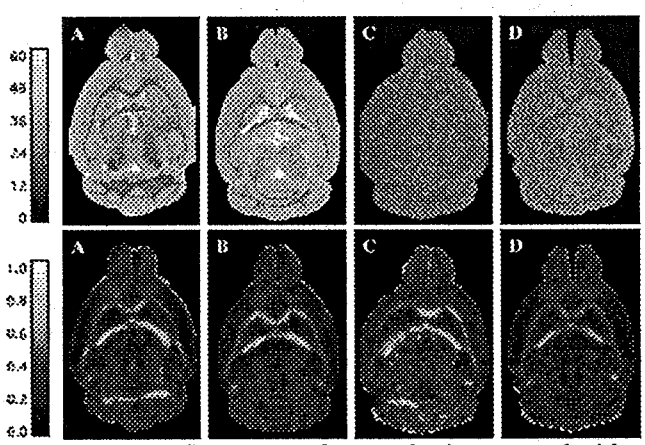

Figure 3. *Top*: SNR maps of mouse brains scanned with (A, B) or without "active staining" (C, D) and fixed for 24 hr (A, C) or 7 days (B, D). *Bottom*: Corresponding diffusion FA maps highlighting the brain white matter structure.

Conclusions

Once constrained by low SNR, methodological advances have allowed DTI to be performed at microscopic resolutions. Highly accurate, 3D fiber structural data of the mouse brain white matter and heart are now obtainable, which paves the way for anatomical atlases of these organs in genetic mouse models.

Acknowledgments

We gratefully acknowledge the technical inputs from staff at the Center for *In Vivo* Microscopy and Dr. Z. P. Liang (RIGR), and grant support from NIH/NCRR (P41-RR05959) and Whitaker Foundation (RG-01-0438).

References

[1] PJ Basser, J Mattiello, D. LeBihan. *Biophys. J.* 66: 259-267 (1994).
[2] EW Hsu, AL Muzikant et al. *Am. J. Physiol.* 274: H2308-H2318 (1998).
[3] RA Jones, O haraldseth et al. *Magn. Reson. Med.* 29: 830-834 (1993).
[4] ZP Liang, PC lauterbur. IEEE Trans. Med. Imaging. 17: 881-892 (1994).
[5] YL You, M Kaveh. IEEE Trans. Image Processing. 9: 1723-1730 (2000).
[6] GA Johnson, GP Cofer et al. *Radiology.* 222: 789-793 (2002).

Probing into Transport of Fluids in Porous Media on Length Scales from Millimeters to Nanometers by NMR

Rainer Kimmich[a], Elmar Fischer[a], Markus Weber[a], Elke Kossel[a], Uwe Beginn[b]
[a]Sektion Kernresonanzspektroskopie, Universität Ulm, 89069 Ulm, Germany,
and [b]ITMC/Tex MC, RWTH Aachen, 52056 Aachen, Germany
(rainer.kimmich@physik.uni-ulm.de)

Confinement effects on hydrodynamic flow and electric current on the one hand and self-diffusion on the other were studied in porous media as coherent and incoherent transport mechanisms, respectively. Coherent transport pathways are visualized with the aid of magnetic resonance microscopy techniques. The physical origins of diffusion anomalies are elucidated. We use the well-known reptation model theory for the determination of pore diameters on a nanometer length scale.

Model objects based on computer generated percolation clusters were milled with a circuit board plotter [1] or were prepared using ultra deep synchrotron ray lithography [2]. The spatial resolutions of these fabrication techniques, 300 □m and 60 □m, respectively, compare with the digital resolution of 26 □m times 37 □m achieved at best in our velocity mapping NMR experiments. Structural information on a nanometer scale was deduced from NMR diffusometry in porous samples prepared by a method based on spinodal decomposition, UV polymerization and cross-linking of the matrix components [3].

The electric current density in percolation clusters was mapped with the aid of an NMR microscopy technique monitoring the spatial distribution of spin precession phase shifts caused by the currents [4,5]. A test structure and quasi two-dimensional random-site percolation model objects filled with an electrolyte solution were examined and compared with numerical calculations based on potential theory. The current density maps permit the evaluation of histograms and of volume-averaged current densities as a function of the probe volume radius as relationships characterizing transport in the clusters. The current density maps are juxtaposed to velocity maps acquired in flow NMR experiments in the same objects. It is demonstrated that electric current and hydrodynamic flow lead to transport patterns deviating in a characteristic way from each other due to the different dependences of the transport resistances on the pore channel width [5].

Diffusion of linear polymers in pores of a solid matrix is sensitive to the diameter of the confinement on a much shorter length scale [6]. Based on the reptation model theory it is shown that the pore diameter can directly be evaluated from echo attenuation curves provided that the appropriate evaluation formalism is employed [7]. With a series of samples with varying pore diameters prepared for this purpose, pore dimensions between 6 and 80 nm were determined.

References

[1] H.-P. Müller, J. Weis, R. Kimmich, *Phys. Rev. E* **52**, 5195 (1995).
[2] E. Kossel, M. Weber, R. Kimmich, *Solid State NMR*, 2003, in press.
[3] U. Beginn, E. Fischer, T. Pieper, F. Mellinger, R. Kimmich, M. Möller, *J. Polym. Sci., A: Polym. Chem.* **38**, 2041 (2000).
[4] G. C. Scott, M. L. G. Joy, R. L. Armstrong, and R. M. Henkelman, *J. Magn. Reson.* **97**, 235 (1992).
[5] M. Weber, R. Kimmich, *Phys. Rev. E* **66**, 026306 (2002).
[6] A. Denissov, M. Kroutieva, N. Fatkullin, R. Kimmich, *J. Chem. Phys.* **116**, 5217 (2002).
[7] R. Kimmich, N. Fatkullin, *Advances in Polymer Science*, 2003, in press.

Unilateral NMR: Concepts and applications of the NMR-MOUSE

Bernhard Blümich, Kai Kremer, Radu Fechete, Sophia Anferova, F. Casanova
Institute of Technical Chemistry and Macromolecular Chemistry, RWTH, D- 52056 Aachen, Germany

Unilateral Nuclear Magnetic Resonance (NMR) [1] has matured into a versatile tool for analysis of elastomer materials and products. The principle of the method is reviewed including the new bar-magnet NMR-MOUSE® (Mobile Universal Surface Explorer, registered trademark of RWTH Aachen) [2], and different applications are addressed. Unilateral NMR sensors like the NMR-MOUSE provide a powerful concept for quality control in combination with rheometry on test rubber samples and non-destructive measurements on the final product.

In unilateral NMR the magnetic field is applied to the sample from one side. Such NMR devices can be built small like the NMR-MOUSE so that they are portable and can be carried to the object [3, 4]. Objects from soft matter can readily be characterized by unilateral NMR of protons in terms of a variety of parameters most notably the effective transverse NMR relaxation time T_{2eff}, which is measured with CPMG-type sequences and correlates with the overall molecular mobility of elastomer materials [5]. In this way information is obtained nondestructively about cross-link density, the state of cure or overcure, the effect of aging, and product heterogeneity. For this reason the NMR-MOUSE can be used to optimize product development, and to monitor rubber product and production quality.

When measuring rubber by unilateral NMR, the sample temperature needs to be well known and stable during the few minutes of measurement time. The temperature-dependent parameters then need to be extrapolated to a reference temperature for comparison with other data. As most technical rubber products are inhomogeneous to NMR, a statistically relevant number of equivalent sections need to be measured to obtain mean values with statistical errors of the order of 1 % and less. The mean value of T_{2eff} describes the average rubber chain stiffness including the effects of additives, and the variance describes the product heterogeneity determined by the processing steps. To facilitate the statistical analysis it is helpful to operate several sensors in parallel. This can be achieved with mobile NMR spectrometers specifically designed for rubber analysis [6].

A particularly important application to elastomer products is quality control. Typically any rubber formulation is tested on a rheometer to assess the material and vulcanization properties by means of the rheometer torque as a function of time with temperature and other parameters as variables. While these tests provide important information for the manufacturers, the final product cannot be probed in this way. For this reason it is desirable to compare the rheometer data with suitable product data in another way. The link between rheometer test sample and final product is the NMR-MOUSE. The NMR properties are measured automatically right after the rheometer measurements and stored in a reference data base (Fig. 1, right). With the mobile NMR equipment the same parameters are monitored at well-defined spots of the final product. Any deviations from the reference values is an indication for a change in compounding, processing, or vulcanization during production. But the rheometer test samples are often found by NMR to be inhomogeneous (Fig. 1, left), so that proper testing should be based on the evaluation of more than one rheometer measurement for each setting.

The nondestructive character of the investigation by unilateral NMR with the NMR-MOUSE is of particular value in on-line monitoring and the analysis of valuable objects. One such class of products is air-springs. Here the positioning of the reinforcement fibers is of interest, which can be monitored by unilateral NMR-tomography, an extension of the NMR-MOUSE principle [7]. A known problem in air springs for rail transportation is water inside the air spring, which may promote corrosion in the presence of temperature cycles. Figure 2 depicts the measured signals (right) in the presence and the absence of water in an air spring bellow (left) of a passenger train car. Although somewhat hidden, the air springs can be inspected by the NMR-MOUSE in most trains without taking the train apart.

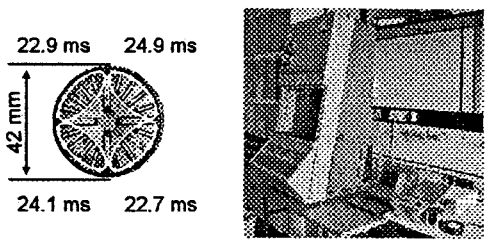

Figure 1. Rheometry and NMR. Left: rheometer test samples are often found to be inhomogeneous according to T_{2eff} from NMR, so that proper testing should be based on the evaluation of more than one rheometer and NMR measurement for each setting. Right: rheometer, notebook, sample preheating unit, NMR-MOUSE and temperature control lid for measuring rheometer test samples.

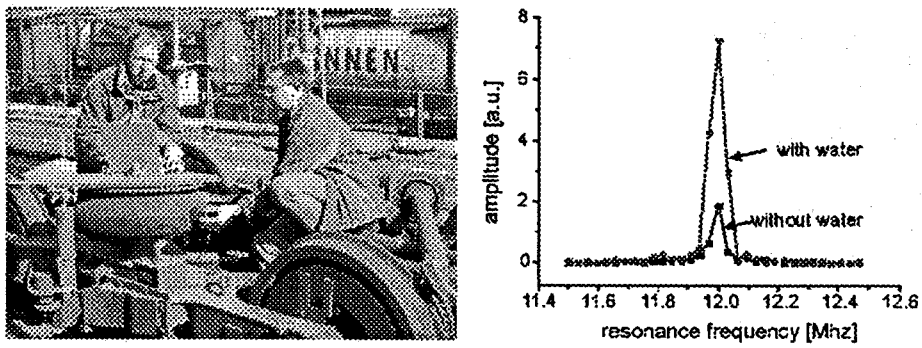

Figure 2. Probing an air spring bellow by mobile NMR. Left: Bernhard Blümich (left) and Kai Kremer (right) testing an air springs in a bogy. Right: signals measured in the laboratory on a Phoenix air spring bellow without and with 0.5 l of water inside. The acquisition time for one signal was less than 30 seconds.

A further topic of interest to rubber quality is thermo-oxydative aging. Thermal aging is known to result in the formation of a thin surface layer structure about 0.2 mm thick which for NR and SBR is harder than the original rubber [8]. A softer layer may follow directly underneath. This layer formation is often ignored in mechanical and chemical analysis of aged rubber samples. The NMR-MOUSE can be optimized for detection of slices less than 0.1 mm thin, and the layer structure can be probed by tuning the sensor to different depth [9]. Figure 3 depicts a comparison of the variation of T_2 measured nondestructively by unilateral NMR and measured on a sample section by conventional NMR imaging. Low values correspond to hard rubber and high values to soft rubber. The variation of the $T_{2\text{eff}}$ with depth into the rubber sheet maps the heterogeneities in the sheet induced by the aging process. The asymmetry of the relaxation time maps is attributed to single sided aging where the samples were lying flat on one side during the temperature treatment, so that the oxygen supply to both sides was different.

Acknowledgments

Work on the NMR-MOUSE has benefited from continuous support by *Deutsche Forschungsgemeinschaft* (DFG) including a project on the evaluation on the electrical degradation of power cable insulation. A comparative evaluation of the use of the NMR-MOUSE in the rubber industry is conducted in cooperation with INTECH-Thüringen GmbH and Alpha Technologies, as well as in a project supported by *Bundesministerium für Bildung und Forschung* (BMBF). Helpful suggestions by Prof. Uwe Weltin are acknowledged.

References

1) G. A. Matzkanin, in: P. Höller, V. Hauck, G. Dobmann, C. Ruud, R. Green, eds, Nondestructive Characterization of Materials, Springer, Berlin, 1989, 655–669.
2) B. Blümich, V. Anferov, S. Anferova, M. Klein, R. Fechete, M. Adams, F. Casanova, Magn. Res. Engin. 15(4) (2002) 255–261
3) B. Blümich, S. Anferova, K. Kremer, S. Sharma, V. Herrmann, A. Segre, Spectroscopy 18 (2003) 24–54.
4) B. Blümich, M. Bruder, Kautschuk, Gummi, Kunststoffe 56 (2003) 90–94.
5) V. Herrmann, K. Unseld, H.-B. Fuchs, B. Blümich, Colloid and Polymer Science 280 (2002) 738–746.
6) Innano Veri, www.mobileNMR.com.
7) P.J. Prado, B. Blümich, U. Schmitz, J. Magn. Reson. 144 (2000) 200–206.
8) P. Blümler, B. Blümich, Macromolecules 24 (1991) 2183-2188.
9) B. Blümich, V. Anferov, S. Anferova, M. Klein, R. Fechete, Polym. Sci. Eng. xx (2003) xxx–xxx.

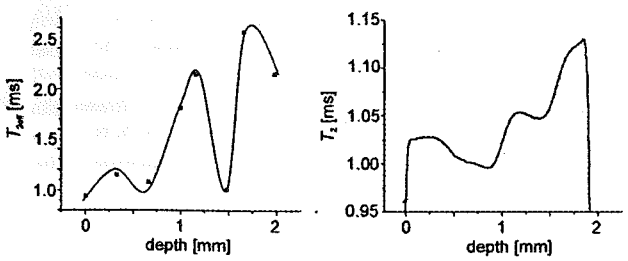

Figure 3. T_2 maps of a 2 mm thick fluorine rubber sheet aged in air for 2 h at 180 °C. The variation in the relaxation time $T_{2\text{eff}}$ measured by the NMR-MOUSE as a function of depth from one side of the sample (left) is reproduced by NMR imaging in high and homogeneous field on a section from the same sample (right).

Advances in Spin-1 NQR for Explosives Detection in the Field: Implications for NQR imaging

Bryan H. Suits,* Allen N. Garroway,† Joel B. Miller,† Karen L. Sauer†‡
*Physics Department, Michigan Technological University, Houghton MI 49931-1295, USA
† Code 6122, Chemistry Div., Naval Research Lab., Washington, D.C., 20375-5342, USA
‡ Physics and Astronomy Dept., George Mason Univ., Fairfax, VA, 22030-4444, USA

Background
It has been estimated that worldwide there are approximately 80 - 100 million landmines in place in about 100 countries resulting in over 800 casualties per month [1]. This on-going threat has created an overwhelming humanitarian problem. In addition, terrorist use of high explosives against people in airplanes and buildings has unfortunately become a fact of life. A reliable explosives detection technique is an essential tool to combat these problems. Unfortunately, the existing technologies are slow and prone to a large number of false positive results and/or have an unacceptable level of false negative results (*i.e.* a failure to detect an explosive which is present).

Nitrogen is present in many explosives and other contraband materials. One technique for the detection of such materials in the field is to use of the magnetic resonance signal from the nearly 100% abundant, spin-1, ^{14}N nuclei. The high chemical-selectivity and the lack of a requirement for a large magnetic field makes nuclear quadrupole resonance (NQR) the magnetic resonance technique of choice. For the sub-kilogram quantities of the materials of concern, detection in a lab environment is relatively straightforward. However, for use as a practical detector in the field one must find ways to deal with severe difficulties which arise including spurious signals from acoustic resonances and radio-frequency (RF) interference combined with generally low signal-to-noise (SNR) levels.

Reported here are details of fundamental studies into multiple RF coil NQR techniques which are less prone to signals from spurious acoustic resonances (without an undo compromise in SNR) and at the same time have potential for future NQR imaging applications.

Circular Polarization
A single RF coil which produces a uniform magnetic field along a single direction is referred to here as a linearly polarized coil. Most magnetic resonance measurements are made using such a coil. Two RF coils which produce magnetic fields in orthogonal directions and which are excited 90° out of phase produce a circularly polarized RF magnetic field.

For an NMR measurement, the resulting RF nuclear magnetization following any RF excitation will be circularly polarized with only one sense of rotation about the applied magnetic field. In contrast, for spin-1 NQR using an oriented single crystal the nuclear magnetization will be linearly polarized following any type of excitation, with the axis of polarization determined by the quadrupole principal axes. However, it was found that for a polycrystalline ("powder") sample, the observed NQR response will always have the same polarization as the excitation used [2]. This latter result arises due to the powder average over a large number of crystallites each of which responds with linear polarization. Since spurious acoustic ringing signals, which are often observed for NQR explosives detection for suitcases or packages, are usually due to a single source which responds with linear polarization, the NQR signal can, in principle, be separated from the interfering signal using this technique. At the same time, an improvement in the SNR is observed.

Three-frequency NQR
Another technique we have explored using multiple coils utilizes the fact that for spin-1 NQR all three of the possible transitions are allowed. Hence, by exciting any two of the transitions, a signal can be observed at the third transition. This is similar to multiple-quantum NMR except in this case the resulting coherence yields an RF nuclear magnetization which can be observed directly.

It was found that for a polycrystalline sample, the resulting signal at the third frequency is optimized using three mutually orthogonal coils, two of which are used for excitation at the frequencies of two of the NQR transitions, and the third used for reception of the signal at the third frequency [3]. We refer to this technique as three-frequency (3f) NQR. For explosive

detection, this technique has the nice feature that the high-power excitations and the weak signal reception are at different frequencies, thus reducing the spectrometer dead time and also spurious acoustic ringing signals occurring within the receiver bandwidth. It is also found that a simple 3f echo sequence can produce a number of different echoes which can be individually selected through phase cycling [4]. The shape and time of occurrence of those echoes can be used to characterize the material being observed.

Prospects for Imaging

NQR imaging is made more difficult than NMR imaging in that all magnetic field components from the gradient coils will contribute rather than just the component along the applied field. In addition, for spin-1 NQR the response to a DC magnetic field is second order. These difficulties suggest that the use of RF gradients might be more fruitful. Both of the techniques mentioned above require the application of orthogonal RF magnetic fields to obtain the desired signal. Using either of those techniques with two non-uniform RF magnetic fields designed to be nearly orthogonal only in a (small) region of interest can be used as unique way to isolate the signal from that region.

References

[1] *Hidden Killers: The Global Landmine Crisis*, Report released by the U.S. Department of State, Bureau of Political-Military Affairs, Office of Humanitarian Demining Programs, Washington, DC, September 1998

[2] J. B. Miller, B. H. Suits, A. N. Garroway, Journal of Magnetic Resonance **151,** 228-234 (2001).

[3] K. L. Sauer, B. H. Suits, A. N. Garroway, J. B. Miller, Chemical Physics Letters **342**, 362-368 (2001).

[4] K. L. Sauer, B. H. Suits, A. N. Garroway, J. B. Miller, Journal of Chemical Physics 118, 5071-5081 (2003).

Compact NMR/MRI systems using Permanent Magnetic circuits

Tomoyuki HAISHI
MRTechnology Inc., Kouya 169-1, Tsukuba, 300-2642, JAPAN

Introduction

In the present study we have developed three NMR/MRI systems using compact MRI consoles and permanent magnetic circuits. These NMR/MRI systems are designed as special systems to which ordinal MRI systems using S.C. magnet hardly can be modeled. Even though permanent magnetic circuits have less field strength than that of a high field S.C magnet, the benefits of the magnet are many like followings: very compact, small fringe field, no cryogen refill, low cost, and good accessibility to imaging area.

Project 1 : Mouse MRI System

Many biologists want to use a small MRI for mice in their own laboratories, which can be worked as a complementary imaging tool against the other measurement modalities; an optical microscope, micro-PET, or micro-CT. However, existing MRI systems used now for mice are very large, expensive, and difficult to be installed into buildings for mice colony where the mice are to be saved from biomedical pollution.

A mouse MRI, which we have developed, consists of a yokeless permanent magnet [1] and compact MRI console [2] (Fig.1-1). The specification of the permanent magnetic circuit is as follows; field strength: 1.0 T, gap: 60 mm, homogeneous volume: 25 mm DSV, size: 30 cm cubed, weight: 210 kg. The installation space is less than 2 m^2. Several solenoid-coil RF probes were developed for this system. A live mouse (adult) was imaged with 3D spin-echo sequences using an internal NMR lock technique to compensate the Larmor frequency drift caused by temperature change of the magnet during a long data-acquisition time [2]. Fig.1-2 shows *in vivo* 2D cross-sectional images of the live mouse selected from a 3D image data set (128 x 128 x 32, 300 micron in plane) acquired a 3D-SE sequence (TR/TE=1500/45). As shown in the figure, detailed anatomical structures are clearly observed. We think the SNR is sufficient for a conventional mouse MRI.

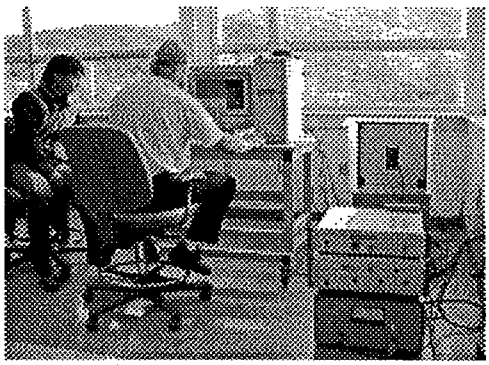

Fig.1-1: Mouse MRI system

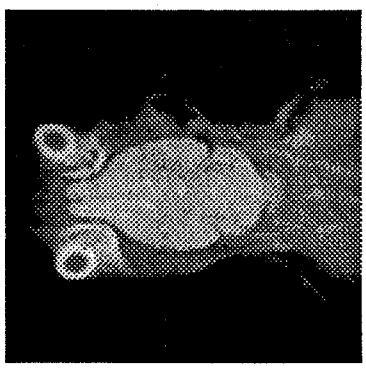

Fig.1-2: Mouse MRI image *in vivo*

Project 2 : MRI observation of gas hydrate formation in a nonmagnetic high-pressure vessel

The purpose of this project is to develop a new monitoring technique of opaque gas hydrate mass, which forms from a guest gas and water at about 3 °C and 0.5 MPa. The utility of gas hydrates as a gas-storage medium is expected to have merits for safety storing and economical transporting natural gas. For the best use of merits of hydrates, it is required to develop a high-rate hydrate-formation procedure and its observation technique for the process of hydrate formation relevant. A nonmagnetic high-pressure vessel with fine-bubble injection and mixing paddles for MRI measurements of hydrate formation has been designed and constructed.

Fig.2-1 shows the schematic of the MRI system with the compact NMR console, 0.3T magnetic circuit (170mm air-gap) and high-pressure vessel made by the cylindrical pyrex glass (I.D.: 70.4 mm). The vessel can be applied to simultaneous measurement with MRI and optical CCD camera. MR and optical images of the gas-hydrate formation consisted of HFC-32 (as a guest gas) and water in the vessel were obtained successfully. Fig.2-2 shows the acquired images. The decrease of NMR signal intensity in the gas-hydrate images was measured as a

function of the ratio related to gas volume (in water) to water volume. The obtained MR images of gas-hydrate indicate the existence of hydrate density distribution in the hydrate mass.

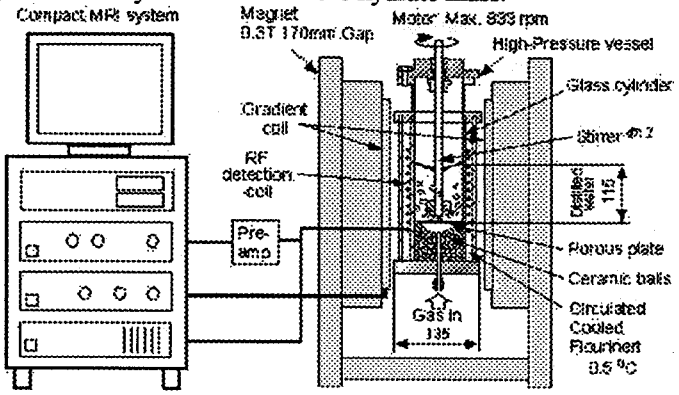

Fig.2-1: Schematics of the high-pressure vessel and the stirrer for forming high-density hydrate

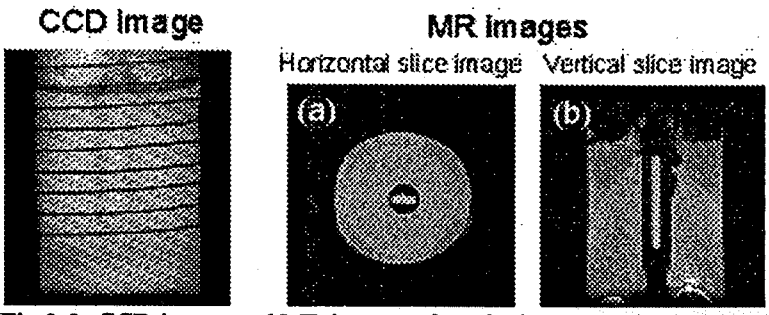

Fig.2-2: CCD image and MR images of gas hydrate mass in the vessel

Project 3 : Mobil NMR/MRI system

Some reports suggest that the diffusion coefficient of liquid decreases under the micro-gravity condition without vibration of measurement systems. NMR measurements of self-diffusion coefficient of the liquid under small acceleration condition were performed with the compact MRI system using a 1.1T permanent magnetic circuit (20mm Gap), which can be used in the airplane for parabolic flights. The advantages of the developed system are compact and mobile features. Diffusion coefficient measurements were successfully done as controlling temperatures of the magnet and room air in the airplane while the vomit comet flights.

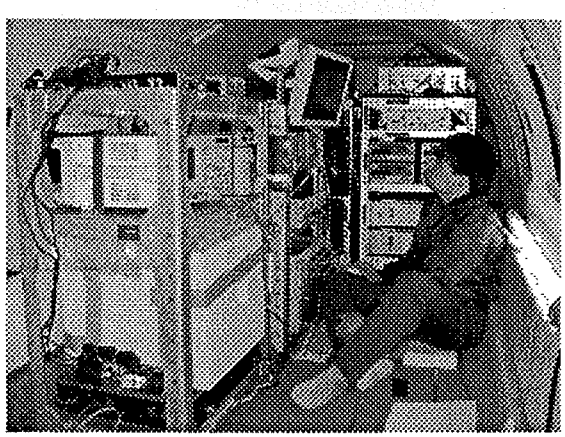

Fig.3-1: Experimental NMR/MRI setup in a jet airplane

Conclusion

The compact MRI systems were developed using the compact MRI consoles and permanent magnetic circuits. The images and/or SNRs are sufficient for the purposes.

Acknowledgements

Project #1 was carried out with New Mexice Resonance and University of Tsukuba. The experimental mouse was prepared by Dr. John B Macauley, Jackson Lab. Projects #2 and #3 were cooperative researchs among MRTechnology, Keio University (Japan) and Sumitomo Special Metals Company (Japan).

References

[1] Akio Nakanishi, *The Transactions of the Institute of Electrical Engineers of Japan*, **D121**, 715 (2001).
[2] Tomoyuki Haishi, Takaaki Uematsu, Yoshimasa Matsuda, Katsumi Kose, *Magnetic Resonance Imaging* **19**, 875-880 (2001).

Industrial Application of NMR imaging to Steel Making Process

Koji Saito
Advanced Technology Research Lab., Nippon Steel Corp., Futtsu City, 293-8511, JAPAN

Introduction

NMR imaging is very powerful tool in order to monitor the chemical reaction and changing phenomena in inhomogeneous systems and we can see many application results in various papers [1]. But there is a few result of NMR imaging application in non-clinical fields which solves real problems and makes a profit in business. In this paper, I would like to show our real four applications which cost down or yield much money for steel making process in our company.

Application to Drying process using STRAF Imaging [2]

Optimization of the drying process conditions in a steel-making converter in a steel work is very critical since the process is off-line and time-consuming. However, it is important to optimize drying process conditions (temperature, surface active agents, etc.), as steam explosion can readily occur with insufficient drying-time. To help understanding, we have demonstrated that we can monitor the drying of real refractory mortar using Stray Field Imaging. We chose this method because of the possibility of detecting short T_2 components. This paper shows the effect of varying water content in different materials on the drying rate. In particular, we find that the free water loss rate is relatively independent of water content. However the bound water loss rate is more affected. It is clear that imaging gives useful information to optimize drying conditions. Using this data, we can adjust and optimize the drying process and time in steel works.

<Drying Process on Materials>

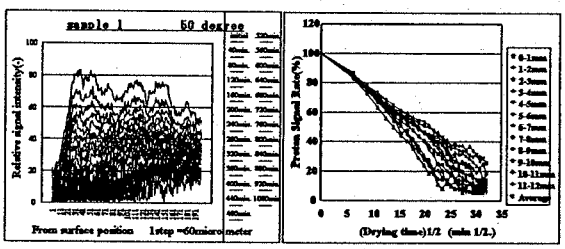

Figure 1 Representative STRAFI echo train profiles recorded at 50 C, every 40 min., during drying of mortar and 12 positions from surface front as a function of root time for as selection of typical drying experiment.

Application to Development of Fuel Cell using Laser-polarized Xenon [3]

The meso size pores of carbon black materials with Pt critically affect catalysts which play an important role for fuel cells of electric vehicles. Time-consuming BET methods are usually used to measure the physisorption enthalpy which determines the characteristics of catalysts. The laser polarized method enhances ^{129}Xe polarization by 4 orders of magnitude, overcoming a low sensitivity, making this measurement technique faster than conventional experiments. In this paper, we first demonstrate Laser-Polarized ^{129} Xe NMR Spectroscopy for studying carbon black materials with Pt of fuel cells of electric vehicles in order to determine the physisorption enthalpy. At the same time, T_1 experiments using Laser-Polarized ^{129} Xe will be discussed in order to clarify the surface condition and adsorption behavior.

<Application of Xe to porous media>

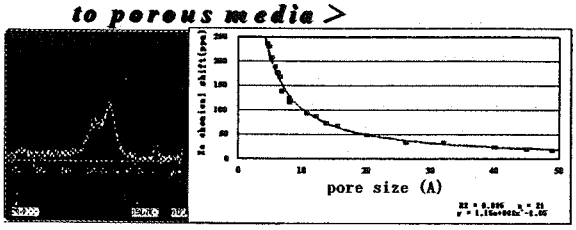

Figure 2 Representative results for ^{129}Xe spectroscopy of absorbed carbon black with meso pore and relationship between pore size and Xe chemical shift

Hp-Xe method → over 50 sample/day
+ another information

Application to Coal science using in-situ Imaging[4-6]

Thermally induced changes in coals are interest from the standpoints of both fundamental and applied research for iron-making process. Furthermore, for very inhomogeneous coals, there is a fascination in the study about the influence of thermal dynamical changes. To monitor the dynamical changes in coals with temperature, an in-situ method must be used, because it is well-known that the properties of coals change dramatically in high temperature range (from 350 to 550 ℃). Therefore, we have carried out the first systematic in-situ high-temperature NMR imaging study of coals between 25 and 550 ℃ with our newly developed high temperature NMR imaging probe with systems to clarify the behavior of mobile component at high temperature in coal specimens.(Figure 3)

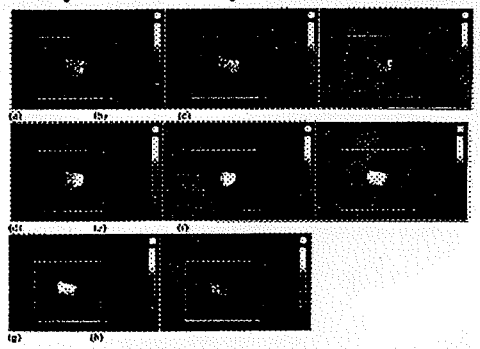

Figure 3 (a) of NMR image of Goonyella coal at 25 ℃, (b) at 350℃, (c) at 375℃,(d) at 400 ℃,(e) at 425℃ (f) at 450℃ , (g) at 475℃,(h) at 500℃

Application to Porous Media using Gas Imaging [7]

The pore structure is very critical and sensitive to react with CO_2 in the case of cokes. But it is very difficult to detect the pore structure of cokes with nondestructive and high resolution because conventional porosimeter method can't detect macro pore (over 400 μ m), and at the same time with destructive. We are at first demonstrating 3D-SPRITE imaging to detect the pore structure using SF_4 gas, before and after CO_2 reaction, (over 1 μ m)with non destructive and the same pores, and then clarify the reaction mechanism. We found that the reaction rate of the cokes with CO_2 depends on the pore size and the critical pore size is over 100 μ m.

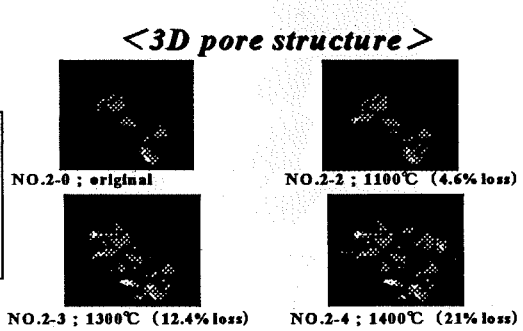

Figure 4 Representative results of 3D pore structure for 4 coke samples
(a) original coke , (b) after reaction at 1100 C ,(c) after reaction 1300 C, (d) after reaction 1400 C

Conclusion

When we understand what is problem in real systems and we can monitor real function of materials using NMR imaging, the results will take us to make a profit in business. I believe NMR imaging has high ability in order to solve real many problems in industries and many applications are waiting for your try.

Acknowledgment

We are grateful to Prof.B.Bluemich (RWTH-Aachen), Porf.P.J.McDonald (University of Surrey), Prof.B.J.Balcom (University of New Brunswick) and Dr.R.E.Botto (Argonne National Laboratory) for their helpful discussion and suggestions

References

[1]Bernhard.Bluemich., Peter.Bluemler. and Koji.Saito, in '*Solid State NMR of Polymers*', I.Ando and T.Asakura Ed. Elseiver, (1998), Bernhard.Bluemich, NMR Imaging of Materials, Oxford, (2000).
[2]Koji.Saito, Koji.Kanehashi, Yoshitoshi.Saito and John.Godward: Appl.Magn.Reson., **2002**, 22, 257
[3]Koji Saito, Atsuomi Kimura and Hideaki Fujiwara, Magn.Reson.Imaging. ,**2003**. in Press
[4]Koji.Saito, Koji Kanehashi. and Ikuo Komaki., *Annual Report on NMR Spectroscopy*, **2001**,44, Academic Press
[5]Koji Saito., Ikuo Komaki., Ken-ichi Hasegawa., and Hisayuki Tsuno., *Fuel*, **2000**, *79*, 405
[6]Koji Saito,and Ikuo Komaki., *EnergyFuel* , **2002**, *16*, 575.
[7]Koji.Saito, Kazuya.Kunitomo, Koich.Fukuda and Kenji.Kato :*Tetsu-to-Hagan* (2002), **88**, 6.

Hyperpolarized Nuclei: Beyond Helium and Xenon

Angelo Bifone
Glaxo Smith-Kline Research Centre, 37100, Verona, Italy

Abstract
Optical pumping methods can be applied to enhance the nuclear spin polarization of ^{129}Xe and ^{3}He by several orders of magnitude, therefore increasing proportionally the sensitivity in NMR detection of these noble gases. Optically polarized ^{3}He and ^{129}Xe have opened up entirely new areas of application of MR imaging and spectroscopy, including lung imaging, surface studies of low surface-area materials, development of biosensors, and the investigation of hydrophobic cavities in proteins. Extension of hyperpolarization methods to other low-sensitivity nuclei would dramatically increase the range of application of NMR methods in medicine, biology and materials science. Among the NMR-sensitive nuclei, ^{13}C is probably the one with the best potential for the application of hyperpolarization methods. Due to its ubiquitous presence in biological and organic molecules, and its rich NMR spectrum, ^{13}C is the nucleus of choice for many *in vitro* NMR studies. However, its low isotopic abundance and low gyromagnetic ratio make it very challenging to detect ^{13}C NMR signals in living organisms, and to image ^{13}C distribution with MRI. The relatively long ^{13}C spin-lattice relaxation times would enable hyperpolarisation methods to be applied and NMR experiments to be performed before the enhanced polarization relaxes back to its equilibrium value. However, the optical methods used for ^{3}He and ^{129}Xe cannot be extended easily to ^{13}C-containing molecules, and a number of other routes has been explored, including Para-Hydrogen Induced Polarization (PHIP) [1], Dynamic Nuclear Polarization (DNP) [2] and polarization transfer from hyperpolarized xenon [3-5]. The physical principles of these methods are presented, and the relative merits and limitations are discussed. Particular emphasis is put on polarization transfer from hyperpolarized ^{129}Xe, both in the liquid and solid phase [6].

References

[1] K. Golman et al, *Magnetic Resonance in Medicine* **46,** 1 (2001).
[2] K. Golman et al. *Acad. Radiol.* **9** (Suppl. 2), S507 (2002).
[3] G. Navon et al., *Science* **271**, 1848 (1996).
[4] R.J. Fitgerald et al., *Chemical Physics Letters* **284**, 87 (1998).
[5] C.R. Bowers et al., *Chemical Physics Letters* **205**, 168 (1993).
[6] A. Cerubini et al., *Chemical Physics Letters* **371**, 640 (2003).

Overview of the Use of Magnetic Resonance to Measure Function *In Vivo*

Harold M. Swartz
Department of Radiology, Dartmouth Medical School, Hanover, NH 03755, USA

This symposium will focus on one of the most promising and important new areas of magnetic resonance in biology—the use of these techniques to obtain physiological information *in vivo*. While some of the earliest uses of magnetic resonance *in vivo* promised such potential (especially the use of phosphorus and proton NMR spectroscopy to follow metabolism), until recently the actual achievements have been disappointingly limited. But in the last few years, as techniques and understanding have progressed, many new areas of productive measurements have been developing rapidly. The central theme in the recent progress and in this symposium is the use of magnetic resonance *in vivo* to obtain information about function. While the well-known "functional MRI" (fMRI) applied to studies of brain function is an important part of the new capabilities, it is only a part and we will emphasize other aspects, including the use of electron paramagnetic resonance (EPR, ESR). The NMR techniques already are widely applied in biological systems ranging from cells to human subjects. The *in vivo* EPR techniques have developed much later than for NMR and have been applied principally in small animals and only recently have been extended to human subjects.

Both spectroscopy and imaging have important roles in the new set of applications of NMR and EPR. The value of imaging is well known, providing spatial distributions of functional aspects such as diffusion and perfusion. Less appreciated but equally important, are the spectroscopic capabilities. Both magnetic resonance techniques can provide spectroscopic information on parameters that are difficult or impossible to measure with other techniques. For example, NMR spectroscopy can provide data on biochemistry *in vivo* with unique specificity. For many problems of interest, it is not essential that this information to be highly resolved spatially. EPR provides unique capabilities for measuring free radicals but the most important aspects are likely to be its capability to measure environmental parameters such as oxygen, molecular motion, redox metabolism, and specific and sensitive measurements of classes of biochemicals such as thiol groups.

The prototypic functional magnetic resonance technique, fMRI, is based on the paramagnetic state of deoxyhemoglobin, which alters relaxation times of protons; this often is termed the "BOLD" effect. It has proven to be immensely powerful for detecting the small changes in blood volume and/or hemoglobin saturation that occur with neuronal activation. For this type of application, the most important aspect is that there is a detectable change associated with the activation, although clearly understanding the mechanism involved could add additional information and avoid some potential artifacts. But because the BOLD signal reflects changes in the amount of deoxyhemoglobin in the volume of interest and these changes can occur through several different mechanisms (e.g. increase in blood volume without a change in saturation of the hemoglobin or a change in the saturation of hemoglobin without a change in blood volume), it is difficult to interpret BOLD effects in terms of physiological changes. This has not prevented some innovative experiments in which BOLD is used to try to probe oxygenation in hypoxic areas such as tumors, but it has limited the interpretations that can be made.

While the needs of following gene activation *in vivo* has one of the driving forces for the development of methods to make measurements *in vivo*, direct measurement of gene activation and cell signaling probably will not be the main use of magnetic resonance techniques. This is because of the small numbers of molecules that are involved in these processes combined with limitations in the sensitivity of magnetic resonance techniques (on a molar basis). But magnetic resonance techniques will be very important in the study *in vivo* of cell signaling because of their capability to follow the consequences of the molecular events at higher levels of function, measuring changes in important parameters such as oxygenation, perfusion, and metabolism. For these types of measurements, it is likely that the magnetic resonance techniques will have a dominant role because of the widespread availability of NMR and the power of the techniques.

The measurement of oxygen directly and through related processes such as perfusion is often the dominant theme in many of these functional magnetic resonance techniques. EPR has especially useful characteristics for the direct measurement of oxygen, including making repeated measurements non-invasively once the oxygen sensitive paramagnetic materials are placed in the tissues at the sites of interest. EPR also has been used to provide images of oxygen, using soluble oxygen sensitive paramagnetic molecules. Direct measurement of oxygen by NMR is more

difficult to do with sufficient sensitivity, but some impressive results have been obtained by the direct injection of suitable fluorine containing compounds into the sites of interest. The greatest contribution of NMR, however, is in its ability to measure related processes such as perfusion, diffusion, and key components of oxygen related metabolism (e.g. lactate, high-energy phosphorus containing compounds).

The symposium will highlight some of the areas of greatest scientific interest and potential. We anticipate that the audience will become convinced of our overall conclusion that the use of magnetic resonance to measure function *in vivo* is an area of great value already and has high potential for even greater contributions for both experimental and clinical applications.

Physiological MRI (pMRI): Current Capabilities and Future Possibilities

Jeff F. Dunn
Department of Radiology, Dartmouth Medical School, Hanover, NH 03755, USA

INTRODUCTION

In vivo NMR has become successful both in basic science and in the clinic due to its capability to image soft tissue structure. At the same time, *in vivo* biochemical analysis was made possible through the introduction of *in vivo* spectroscopy, and this has been extensively used in animals, and used with some success clinically. Now, the study of physiological processes is growing in both capability and application. This presentation will provide an overview of this important area.

DISCUSSION

The capabilities of *in vivo* NMR often are applied to the study of oxygenation *in vivo*. I will use this subject to provide a framework for this presentation as many NMR related methods, both direct and indirect, can be used to study tissue oxygenation.

The utilization of oxygen in the body occurs largely within the mitochondria. This process generates energy in the form of ATP. ATP is in equilibrium with phosphocreatine (PCr), another energy storage metabolite. One can use ^{31}P-NMR to follow intracellular pH (which will change with the utilization of PCr) as well as phosphorus containing metabolites. The pH also will decline if there is an accumulation of lactate, an intracellular metabolite which is produced in some tissues in the absence of oxygen—providing an indirect assessment of oxygen availability. Of course, lactate can be monitored directly using ^{1}H-NMR spectroscopy. The oxidation state of the mitochondria is influenced by the concentration of substrates, and will decline if oxygen becomes limiting for energy production. It has been shown that the ratio of PCR/Pi provides a reasonable index of the mitochondrial oxidation state.

^{13}C NMR is a powerful tool used to track the movement of metabolites in energy metabolism. Pulse-chase studies, where metabolites labeled with ^{13}C are injected and then the resulting ^{13}C containing metabolites are monitored over time, provide unique information about intracellular metabolic regulation. One of the exciting theories arising from this type of study is the possibility that intermediary metabolism is compartmentalized between the glia and neurons in the brain.

If energy metabolism is limited by a lack of oxygen, then other energy requiring functions will be influenced by the lack of energy. One such process is ion regulation, which influences water balance. Ion regulation is a key component to the theory behind the changes in the apparent diffusion constant (ADC) after the onset of hypoxia/ischemia in the brain. The ADC is now recognized as being one of the earliest indices of hypoxic/ischemic damage. It will change under conditions where the cell water balance is changing. Current theories suggest that energy limitation causes impaired osmotic regulation. This osmotic impairment is an indication of impaired ion regulation and is associated with cell swelling which influences the ADC. The energy requiring step is the Na/K ATPase, which uses ATP contained energy to pump Na out of the cell to maintain ion balance. Ion balance studies also can be undertaken with Na and Rb NMR. The former has been used successfully to monitor Na in a range of tissues. Na imaging of lesions *in vivo* now has become possible, and is showing promise as a method of imaging damaged or cancerous regions in brain. Rb is transported in K channels, and so can be used to follow the kinetics of K transport in cells. One of the "bread and butter" sequences of NMR imaging is the T2 weighted MRI. Although contrast from this image is sensitive to many pathophysiological conditions, one of the most useful is the fact that the T2 image becomes brighter with edema. When this edema is caused by cell swelling, it is called cytotoxic edema and is associated with impaired water balance. When the edema is caused by increased leakiness across the vessel wall, it is called vasogenic edema.

The transport of oxygen involves oxygen carrying pigments, the hemoglobin and the myoglobin. When these are deoxygenated, the internal Fe becomes paramagnetic. This alters the relaxation rate of the surrounding protons and forms the basis of "functional imaging" or fMRI. Such paramagnetic effects of deoxyhemoglobin were described by Pauling and now are used almost routinely in MR studies of cognitive function. The imaging method "BOLD" (Blood Oxygen Level Dependent imaging) can be used to observe regions of brain function because the saturation of

the blood increases in areas near the activation site. This causes a brightening of the image. BOLD imaging now is used to study normal brain function, responses to hypoxia in brain, and tumor biology. In combination with modern modeling methods and an assessment of flow, BOLD imaging has been used to estimate regional metabolic rate or oxygen utilization rates in brain. Spectroscopy also has been used successfully to monitor changes in the myoglobin oxidation state during activation of muscles, which contain this oxygen carrying pigment.

Oxygen delivery also is heavily influenced by flow and perfusion. This is an area of rapid growth in MR imaging. Perfusion sensitive sequences often involve some aspect of T_1 saturation. In NMR angiography without contrast, the theory is that the slowly moving spins will become saturated and moving blood will be relatively bright. Contrast also can be added to reduce the T_1 of blood, again making it brighter than the surrounding tissues. Gadolinium (Gd) infusion with rapid imaging also can be used effectively for angiography. Bolus injections of Gd, in conjunction with rapid T_1 imaging, also are used in dynamic imaging to study blood flow and blood volume. The method of arterial spin tagging also uses T_1 based imaging, but utilizes a T1 based spin-tag as a perfusion marker, thus eliminating the need for injection of contrast. Blood volume in brain increases with flow. Thus, blood volume measurements, with dynamic contrast or steady-state imaging of contrast agents with long plasma ½ lives, are useful for measuring flow. They are also used to study the growth and regression of blood vessels.

The absolute concentration of oxygen in liquids has been measured by relying on the effect of oxygen on relaxation rates of other nuclei. In particular, the T1 of fluorine is shortened in the presence of oxygen. This characteristic has been used effectively to obtain images of the oxygen partial pressure in living organisms. Oxygen NMR itself has been used in exciting new studies of both oxygen concentration and utilization.

If one follows the flow of oxygen, it begins with transport into the lungs. Lung imaging has become possible with sequences that reduce motion. Hyperpolarized gas imaging, especially of Xe, also has been used effectively to image the structure of the lung.

This talk is intended to provide an overview of physiological imaging through presentations of specific examples and to stimulate thought about the directions that physiological imaging is taking and possible directions for future work.

Molecular Imaging with MRI: Making Contrast the "Old Fashioned" Way

Robert Weisskoff
EPIX Medical, Inc., 71 Rogers Avenue, Cambridge, MA 02142, USA

While long recognized as an outstanding anatomic imaging modality, MRI has in the last decade been increasingly recognized as an outstanding research tool for functional imaging as well. *In vivo* functional imaging has long been the province of specifically targeted nuclear medicine agents. MRI's most effective tools for human work in this area have been quite different: either intrinsic MR effects due to changes in blood oxygenation or dynamic changes in signal due to general-purpose extracellular MRI agents.

Recent inventions continue to push novel mechanisms of action for new chemical compounds that affect MRI signal *in vivo* [1-3], and have created unique, potentially responsive contrast agents. Nevertheless, the compounds closest to clinical implementation for molecular imaging using MRI currently target disease-specific receptors or proteins in order to generate useful contrast. MRI already provides exquisite anatomic information, and the challenge for researchers trying to provide molecularly-specific data is to overcome the intrinsic lack of sensitivity of MRI. The two general methods to produce the necessary MRI signal are a) using large molecular weight constructs (Gd-laden liposomes, iron oxide particles, etc.); and b) using more traditionally-defined chemical entities with enhanced relaxivity. The advantages and challenges of biologically-directed MR imaging will be illustrated using molecular imaging of thrombus ([4-5], and recent work from EPIX) by targeting of various sites uniquely available in thrombus. These techniques demonstrate that when targets at the end of a biological cascade (such as the clotting cascade, in the case of thrombus) can be targeted, MR contrast agents can be designed with sufficient sensitively and specifically in order to provide useful enhancement both for medical and basic research applications.

References

[1] K. Ward, A. Aletras, R. Balaban, *J Magn Reson* **143,** 79-87 (2000).
[2] A.Y. Louie, et al, *Nat Biotechnol* **18,** 321-325 (2000).
[3] A. Moore et al, *Radiology* **221,** 244-250 (2001).
[4] L.O. Johansson et al, *J Magn Reson Imaging* **13,** 615-618 (2001).
[5] S. Flacke et al, *Circulation* **104,** 1280-1285 (2001).

Functional EPR imaging: Tissue redox status & oxygenation

Periannan Kuppusamy
Center for Biomedical EPR spectroscopy and Imaging, Davis Heart & Lung Research Institute, Department of Medicine, The Ohio State University, Columbus, Ohio *(Supported by NIH Grant CA 78886)*

Electron paramagnetic resonance imaging (EPRI) enables visualization of the distribution of electron spins (free radicals) in tissues. It can directly detect and image relatively stable free radicals as well as labile radicals such as oxygen-derived superoxide and hydroxyl radicals that are implicated in the pathogenesis of oxidant injury. In addition, spin probes can be used to image cellular radical metabolism, redox state, membrane structure and fluidity, oxygen, pH, temperature, protein structure, and cell death. With spin labeling of molecules and cells, noninvasive mapping of their localization in tissues can be performed.

A major power of EPR technology is its ability to precisely measure oxygen (O_2) in tissues. The 'EPR oximetry' uses spin probes whose EPR line-widths are sensitive to O_2 concentration. It enables precise and accurate measurements of O_2 concentrations in tissues, noninvasively and repeatedly over periods of months in the same site. This approach uses fine crystals of phthalocyanine-based radical molecules that are stacked producing a very strongly exchanged-narrowed EPR line-shape, that is highly sensitive to local O_2 concentration [1-3]. These probes are biocompatible and stable in tissues. They can be implanted at the desired site or with a suitable coating can be infused into the vasculature for targeted delivery to tissues. In addition, these probes can be internalized in cells enabling measurement of intracellular pO_2 with milliTorr accuracy.

The redox status of cells and tissue are governed by several independent factors including perfusion, oxygenation, levels of antioxidants, and a network of enzymatic systems. A variety of intracellular molecules contribute to the overall redox status in tissues including glutathione (GSH), thioredoxins, NADPH, flavins, ascorbate, and others. Oxidative or reductive stress and alterations in the endogenous/exogenous antioxidant levels cause an imbalance in the redox homeostasis of the cells. The cells then revert to the normal redox status by mounting a stress response using various signaling pathways and enzymatic systems. For example, tumor cells are known to have significant alterations in the redox status. The tumor redox status is an important determinant in the response of the tumor to certain chemotherapeutic agents, radiation, and bioreductive hypoxic cell cytotoxins. Therefore, a noninvasive assessment of such information will be useful for tumor treatment planning.

Magnetic resonance spectroscopy and positron emission tomography (PET) are some radiologic methods which are capable of providing tissue redox information. More recently, EPR imaging has been developed to provide such information in small animals [4]. The EPR methods, however, require the use of exogenously infused redox sensitive spin probes such as nitroxyls. Two critical properties of nitroxyls provide such capability: (i) Nitroxyl radicals participate in redox-reactions where the nitroxyl (paramagnetic, EPR detectable) are reduced to the corresponding hydroxylamine (diamagnetic, EPR silent) and the hydroxylamine can undergo reoxidation back to the nitroxyl; (ii) In cells nitroxyls undergo reduction to the corresponding hydroxylamines more efficiently under hypoxic conditions than under aerobic conditions via intracellular enzymatic processes. When nitroxyls are administered *in vivo*, a rapid equilibrium is established between the levels of nitroxyl and hydroxylamine. A variety of nitroxyl molecules capable of reporting cellular redox levels including total redox, thiols, and glutathione can be used. These molecules are nontoxic and are converted to nonradical species and cleared from the system within hours after infusion.

We have previously used *in vivo* EPR spectroscopy and imaging techniques and shown that tumor tissues (subcutaneously implanted RIF-1 tumor in the upper hind leg of C3H mice) are highly reducing and hypoxic compared to normal tissues [5]. We further developed techniques to obtain spatially-resolved redox data from normal and tumor tissues of RIF-1 tumor-bearing mice and examined the role of intracellular glutathione on the tissue redox status [4-7]. Experiments were performed using a redox sensitive nitroxyl probe, 3-CP. L-buthionine-S,R-sulfoximine (BSO), an inhibitor of GSH synthesis, diethylmaleimide (DEM), or carbogen-breathing was used to modulate tissue GSH or redox levels. The results showed the existence of significant heterogeneity of redox status in the tumor tissue. Figures 1 shows a typical EPR image of the distribution of redox probe, which was administered *in vivo*, and redox image (distribution of reducing equivalents/thiols) under air- and carbogen (95% O_2/5% CO_2)-breathing mice. The results demonstrate the spatially-resolved effect of oxygenation on the redox status of the tumor microenvironment. The distribution of the rate constants seen in the frequency plot of Figure 1 reveals that the tumor

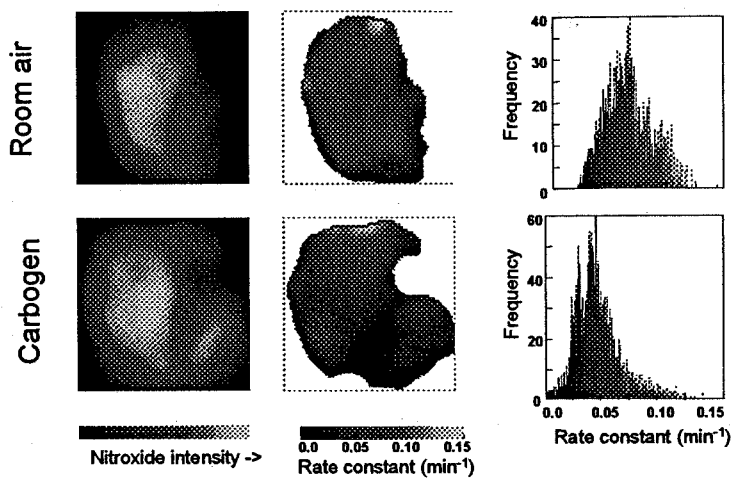

Figure 1. Redox mapping of tumor, *in vivo*. Following tail vein infusion of a nitroxyl redox probe (3-CP), a series of 2D images of the nitroxide from tumors (RIF-1) of air or carbogen-breathing mice was measured using L-band EPR imaging method. 2-D spatial mapping (10x10 mm^2) of the probe distribution (left), redox map (middle) and frequency plot of the reduction rate constant (right) in the tumor tissue of room air-breathing (TOP) and carbogen-breathing (BOTTOM) mice are shown.

has heterogeneity in terms of the redox status. This heterogeneity in the redox status may arise due to either the heterogeneity in perfusion or in the oxygen concentration in the tumor. On the other hand, the frequency plot of the carbogen-administered animal shows a relatively narrow distribution of rate constants. The higher values noticed in the former, have been considerably decreased and the higher frequencies of rate constants are shifted to the left. The diminished heterogeneity of the tumor redox status in the case of carbogen-breathing may be due to elimination of diffusion-limited hypoxia, thus rendering the tumor more homogeneously oxygenated. Thus the heterogeneity in the redox values of tumor at normal air-breathing animal may also come from the heterogeneity of oxygen distribution.

References

1. Liu, K. J.; Gast, P.; Moussavi, M.; Norby, S. W.; Vahidi, N.; Walczak, T.; Wu, M.; Swartz, H. M. Lithium phthalocyanine: a probe for electron paramagnetic resonance oximetry in viable biological systems. *Proc. Natl. Acad. Sci. USA* **90:**5438-5442; 1993.
2. Ilangovan, G.; Li, H.; Zweier, J. L.; Kuppusamy, P. Electrochemical preparation and EPR studies of lithium phthalocyanine. 3. Measurements of oxygen concentration in tissues and biochemical reactions. *J. Phys. Chem. B* **105:**5323-5330; 2001.
3. Ilangovan, G.; Manivannan, A.; Li, H.; Yanagi, H.; Zweier, J. L.; Kuppusamy, P. A naphthalocyanine-based EPR probe for localized measurements of tissue oxygenation. *Free Radic. Biol. Med.* **32:**139-147; 2002.
4. Kuppusamy, P.; Li, H.; Ilangovan, G.; Cardounel, A. J.; Zweier, J. L.; Yamada, K.; Krishna, M. C.; Mitchell, J. B. Noninvasive imaging of tumor redox status and its modification by tissue glutathione levels. *Cancer Res* **62:**307-312; 2002.
5. Kuppusamy, P.; Afeworki, M.; Shankar, R. A.; Coffin, D.; Krishna, M. C.; Hahn, S. M.; Mitchell, J. B.; Zweier, J. L. In vivo electron paramagnetic resonance imaging of tumor heterogeneity and oxygenation in a murine model. *Cancer Res* **58:**1562-1568; 1998.
6. Ilangovan, G.; Li, H.; Zweier, J. L.; Krishna, M. C.; Mitchell, J. B.; Kuppusamy, P. In vivo measurement of regional oxygenation and imaging of redox status in RIF-1 murine tumor: effect of carbogen-breathing. *Magn Reson Med* **48:**723-730; 2002.
7. Yamada, K. I.; Kuppusamy, P.; English, S.; Yoo, J.; Irie, A.; Subramanian, S.; Mitchell, J. B.; Krishna, M. C. Feasibility and assessment of non-invasive in vivo redox status using electron paramagnetic resonance imaging. *Acta Radiol* **43:**433-440; 2002.

Rheo-NMR-microscopy: localising the physics of soft matter

Paul T. Callaghan
MacDiarmid Institute for Advanced Materials and Nanotechnology,
School of Chemical and Physical Sciences
Victoria University of Wellington, New Zealand

A central problem in the physics of soft matter concerns the molecular basis of complex mechanical properties, and especially the response of the material to deformation and deformational flow. The study of such macroscopic constitutive mechanics is known as *rheology*. The key to addressing central questions concerning the role of molecular organisation and dynamics in macroscopic constitutive behaviour, lies in the use of spectroscopic techniques that are capable of accessing information at the molecular level during deformational flow. Examples include optical birefringence and dichroism measurements, neutron and X-ray scattering, and most recently, nuclear magnetic resonance.

With rheology, magnetic resonance has formed a useful partnership. In the rheology of complex fluids and soft materials, nuclear magnetic resonance (NMR) is a nice tool for the elucidation of molecular dynamics, alignment and organisation. But when coupled with the use of magnetic field gradients NMR allows these molecular properties to be spatially localised, so that we can select any part of the flow field for analysis. Furthermore gradients enable NMR velocimetry, which in turn gives us access to the fluid mechanics. As will be shown in this lecture, these two approaches are highly complementary.

An overview of the NMR methods will be given, along with some examples of flow measurement in different deformation geometries. Velocity tubeless siphon flow, the "spurt effect", shear banding, fracture, yield stress phenomena, polymer demixing and shear-induced polymer chain alignment while spectroscopy is answering new questions about molecular organisation and ordering.

Already Rheo-NMR has thrown up some interesting effects. These include anomalous polymer deformation under shear, dynamics of shear-induced isotropic to nematic phase transitions in wormlike micelles, and correlations between stress fluctuations, shear banding fluctuations, and fluctuations in the orientational order of surfactant molecules.

Novel techniques for porous media research

Yi-Qiao Song
Schlumberger-Doll Research, Ridgefield, CT 06877 USA

Diffusion in porous media has been used as a probe of pore geometry in various NMR techniques. Diffusion in the susceptibility-contrast induced internal field is discussed as a means to probe pore size and pore shape. In addition, we present the general concept of two-dimensional relaxation-type experiments for the study of molecules, fluids, materials and their dynamics that are characterized by spin relaxation and diffusion.

Internal magnetic field and DDIF

When a sample is placed in a uniform magnetic field, a spatially varying field and its gradients appear naturally inside the pore space due to the magnetic susceptibility contrast between the host solid material and the pore-filling fluid [1]. This field is called the internal field, B^i, and it is often characterized by a very wide distribution of its gradient in materials including rocks and biological tissues [2-4], reflecting its complex spatial dependence. Since B^i is determined by the spatial distribution of pores, it is speculated that some properties of B^i may be used to study the detailed pore structure.

Recently, an NMR method was introduced [5] to characterize the internal field in order to obtain the pore sizes. A stimulated echo sequence [6] was used to modulate the magnetization during the encoding period to create a spatial pattern within individual pores. The decay time constant of such modulation was found to be directly related to pore sizes [5]. The method is dubbed as Decay due to Diffusion in Internal Field (DDIF). It was shown to be capable of identifying pores of different sizes even when they were spatially near each other so that the spin relaxation exhibited single-exponential decay [5,7]. DDIF technique has been used to examine other types of rocks [8] and the geological evolution of pore space in rocks [9,10]. DDIF is also potentially useful as a probe of the internal structure of other materials, such as in biological tissues.

Pore shape

Pore shape is a characteristic of pore geometry that is important for fluid flow and especially multi-phase flow. It can be studied by analyzing three-dimensional images of the pore space [11,12]. Also, the long-time diffusion coefficient measurements on rocks have been used to argue that the shape of pores in many rocks are sheet-like and tube-like [13]. We recently reported [14] that the combination of DDIF, mercury intrusion experiment, and a simple analysis of two-dimensional thin-section images provides a characterization of pore shape from only geometric properties.

DDIF was performed on a Berea sandstone sample and the pore size distribution was obtained [14] showing a peak in pore size at 85 micron. We also performed a mercury (Hg) intrusion experiment with a constant injection rate by regulating the intrusion pressure [15]. This is different from the conventional mercury intrusion experiment where the intrusion pressure is kept constant to record the mercury intrusion volume. From the Hg experiment, we obtained the distribution of the pore body volumes showing a pronounced peak at around 20 nl for the Berea sample. The usual assumption of spherical pores will give a pore diameter of 340 um, which is inconsistent with the thin-section micrograph and the DDIF result that the pore body size is about 85 um in this sample. This clearly indicates that the pore body is far from a spherical shape. Addition information comes from the thin-section micrograph images showing that the majority of the pore cross-sections are not extensively elongated and have a small aspect ratio. Thus, we conclude that the pores in this sample are very much elongated and tube-like.

Two-dimensional NMR using relaxation and diffusion as parameters

Diffusion and spin dynamics are sensitive probes of electronic and molecular structure and dynamics. These parameters are often measured by NMR experiments such as, for example, CPMG to measure T_2, inversion recovery for T_1, and pulsed field gradients for the diffusion coefficient. Such experiments are an analog of the one-dimensional Fourier spectroscopy in that the signal is measured as a function of one variable. Extension to two-dimensional and multi-dimensional Fourier spectroscopy has greatly enhanced the ability of NMR to identify and characterize molecules, their structures and dynamics.

Experiments to determine correlation of relaxation time constants, such as T_1 and T_2, and diffusion coefficient, are conceptually similar to the multi-dimensional Fourier spectroscopy in that the spin system is characterized by two independent variables. This technique is potentially most useful for the study of heterogeneous materials, such as polymers, natural materials, and biological materials. The main difference compared to Fourier spectroscopy is that the time dependence of the signal is described by exponential functions, instead of oscillatory functions. Thus, a spectrum of T_1, for example, is obtained by the inverse Laplace transform. Thus, these experiments may be called Laplace NMR spectroscopy. The primary difficulty to perform this type of 2D experiments is due to the absence of an efficient multi-dimensional Laplace inversion program. For example, a supercomputer had to be used to perform two-dimensional Laplace inversion of a relatively small data set [16], because of the enormous demand on memory and speed for the inversion. Recently, a new computer algorithm has been developed for 2D Laplace inversion that has significantly reduced the requirement on computer memory and speed and that can be used on standard PCs and workstations. The details of the algorithm and applications have been presented in Ref. 17-19.

A two-dimensional experiment and its pulse sequence, in general, can be separated into two parts and the spin dynamics is governed by two different processes, respectively. For example, the T_1-T_2 correlation experiment can be performed using the inversion recovery sequence as the first part, and the CPMG as the second part:

$$\underbrace{\pi - \tau_1}_{\text{first part}} \quad \underbrace{-\frac{\pi}{2} - t_e/2 - [\pi - t_e]_N}_{\text{second part}}$$

where N is the echo number. The first time variable is τ_1 and the second one is τ_2 = Nte. During the first part, the spin dynamics is governed by T_1 processes and in the second part by T_2 processes. T_1 and T_2 may be sensitive to different aspects of the molecular dynamics, for instance. The first part may be replaced by a diffusion-sensitive segment, such as a stimulated echo with pulsed field gradient [20]. Then the experiment can be used to determine a diffusion coefficient-T_2 correlation. DDIF can be used as one of the dimensions in such a 2D experiment for probing the connectivity of pores.

Acknowledgement
The author is indebted to collaboration and discussions with D. F. Allen, W. E. Kenyon, M. D. Hurlimann, C. Flaum, and R. L. Kleinberg on the properties of rocks and NMR applications, L. J. Zielinski, S. Ryu, P. N. Sen on theory, L. Venkataramanan on mathematics, Q. Chen on mercury experiments, N. V. Lisitza, W. S. Warren, T. Brown and E. Guo on biological applications. Many of them co-authored the work reviewed here.

References

1. R. J. S.Brown, *Phys. Rev.* **121**,1379 (1961).
2. R. J. S. Brown and P. Fantazzini, *Phys. Rev. B* **47**,14823, 1993.
3. R. M. Weisskoff, C. S. Zuo, J. L. Boxerman, and B. R. Rosen, *Magn. Reson. Med.* **31**, 601(1994).
4. M. D. Hurlimann, *J. Magn. Reson.* **131**, 232(1998).
5. Y. Song, S. Ryu, and P. N. Sen, *Nature* (London) **406**, 178 (2000).
6. E. L. Hahn, *Phys. Rev.* **80**, 580 (1950).
7. L. J. Zielinski, Y. Song, S. Ryu, and P. N. Sen, *J. Chem. Phys.* **117**, 5361 (2002).
8. Y. Song, *Magn. Reson. Imaging* **19**, 417 (2001).
9. Y. Song, N. V. Lisitza, D. F. Allen, and W. E. Kenyon, *Petrophysics* **43**, 420-424(2002).
10. W. E. Kenyon, D. F. Allen, N. V. Lisitza, and Y. Song, SPWLA 43 ann. meeting (2002).
11. Q. Chen and Y. Song, *J. Chem. Phys.* **116**, 8247 (2002).
12. B. P. Flannery, H. W. Deckman, W. G. Roberge, and K. L. D'Amico, *Science* **237**, 1439 (1987).
13. J. T. Fredrich, B. Menendex, and T. F. Wong, *Science* **268**, 276 (1995).
14. R. L. Kleinberg, *Magn. Reson. Imaging* **12**, 271(1994).
15. H. H. Yuan and B. F. Swanson, *SPE Formation Evaluatio*, **17** (1989).
16. A.E. English, et al, *Magn. Reson. Medicine* **22**, 425(1991).
17. L. Venkataramanan, Y. Song, and M. D. Hurlimann, *IEEE Trans. Signal Proc.* **50**, 1017 (2002).
18. Y. Song, et al, *J. Magn. Reson.* **154**, 261(2002).
19. M. D. Hurlimann and L. Venkataramanan, *J. Magn. Reson.* **157**, 31(2002).
20. E. O. Stejskal and J. E. Tanner, *J. Chem. Phys.* **42**, 288 (1965).

Investigation of the microstructure of the heart: Comparison between T2*, diffusion tensor and SSFP imaging

Sascha Köhler, Karl-Heinz Hiller, Wolfgang R. Bauer, Axel Haase, Peter M. Jakob
Physikalisches Institut, Universität Würzburg, Am Hubland, 97074 Würzburg, Germany

Introduction
The myofiber structure of the heart plays a critical role in force production and contraction of the heart and is known to be modified in different cardiac diseases. The purpose of the present study was to provide a detailed insight into the microstructure of isolated hearts with MRI techniques. In particular, the fiber structure of isolated beating hearts was visualized with T2* imaging [1] and a quantitative description of the T2* based myocardial fiber contrast was given. Furthermore, the fiber structure obtained with T2* imaging was compared to high-resolution diffusion tensor imaging (DTI) and to the results of steady-state free precession techniques (SSFP: TrueFISP, FIESTA, Balanced-FFE).

Methods
MR imaging was performed on a Bruker AMX-500 microscopy system at 11.75T. Hearts of male Wistar rats were excised and perfused in the Langendorff mode with Krebs-Henseleit buffer. In case of diffusion experiments, the heart was arrested by perfusing with a cardioplegic solution.

• T2* imaging:
For T2* imaging a 2D gradient-recalled multiecho pulse sequence was used (FOV: 20 x 20 mm, matrix: 256 x 256, spatial resolution 78 μm in plane, slice thickness: 500 μm).

• Quantification of T2* based fiber contrast:
In the presence of mesoscopic field inhomogeneities, the T2* relaxation rate is influenced by the *static* and *dynamic* dephasing regime. Experimentally, T2'(static) can be quantified with an adapted two-point Dixon method [2,3]. This method was developed to quantify susceptibility effects and makes use of data from two spin echo acquisitions with the same echo time but with the position of the 180° time reversal pulse moved by a small amount ΔT in the second acquisition. The two acquisitions provide information which can be used to calculate a susceptibility loss (A') image. For estimation of the internal diffusion effects caused by mesoscopic magnetic field gradients (dynamic dephasing), an additional acquisition of a Carr-Purcell-Meiboom-Gill (CPMG) sequence with the same echo time but with additional refocusing pulses was acquired (D').

• Diffusion tensor imaging:
Diffusion-weighted imaging was performed using a pulsed field gradient, spin echo sequence (PGSE) with diffusion weighting in seven directions (x, y, z, xy, xz, yz, and zero). For SNR efficiency, a multiple echo readout was performed collecting the spin echo and several gradient echos placed symmetrically around the spin echo position. Colored trace maps were constructed to highlight both isotropic and anisotropic diffusion in the same image [4].

• SSFP imaging:
For SSFP imaging a TR/TE = 4.0/2.0 ms was achieved with a matrix of 256 x 256. Using different phase cycles of the RF excitation pulse, the spectral profile of the SSFP sequence [5] and consequently the image contrast behavior was modified.

Results
Figure 1a shows a magnification of a region of a T2* map. The variation in the myocardial fiber orientation is clearly visible. In comparison to histology (Fig. 1b), the T2* map shows an excellent spatial correspondence of myocardial fiber structure. Figure 2 shows a magnification of a region of a susceptibility loss image (A'), a diffusion-weighted image (D') due to internal field gradients and a T2* image of the isolated rat heart in the long axis view. The D' image shows no significant signal attenuation due to internal diffusion effects caused by tissue specific field inhomogeneities (dynamic dephasing), whereas the A' image shows significant signal attenuation due to static dephasing. Dark pixels in Figure 2a represent short T2' values between 5 ms and 20 ms, whereby light pixels indicate longer T2' values. Figure 3 shows a comparison between a colored trace map of the diffusion tensor

and a T2* map. SSFP images with different phase cycles and consequently different contrast on myocardial fiber structure are shown in Figure 4.

Discussion

From the results shown in Figure 2 it is evident that the static dephasing regime is responsible for visualization of myocardial microstructure with T2* imaging and internal diffusion effects can be neglected in terms of their effect on the T2* relaxation time. The comparison of fiber structure obtained with T2* imaging and DTI showed not only a macroscopic analogy of diffusion anisotropy and fiber orientation, but also a correspondence in visualization of anatomical details such as muscle layers and microvasculature system. The main direction of the fibers can be seen from the color in the color trace map. Some areas appear predominately green, which indicates that D_{yy} is considerably larger than the other trace elements and the main fiber orientation is defined in this direction in space. However, the colored trace map showed also white areas, which indicates areas of free diffusion. These areas appear also light in the T2* map, which corresponds to long T2* values, because these areas consists mainly of fluid.
Figure 4 demonstrates that SSFP sequences can be used to investigate and visualize the fiber structure of the heart. The high SNR and short TR of SSFP sequences allow faster acquisition times and/or an improvement in spatial resolution as compared to T2* experiments. Furthermore, tissue contrast can be modified in SSFP sequences using different phase cycles of the RF pulses.

Conclusion

The present study demonstrates that the complex architecture of heart musculature can be visualized with different imaging techniques. T2*, diffusion tensor and SSFP experiments provided almost equivalent information about myocardial fiber structure. Because T2* mapping and SSFP experiments visualizes directly the anatomical details, and due to shorter acquisition times as compared to DTI, T2* and SSFP techniques could become a useful tool for investigation of myocardial fiber structure and might replace DTI in certain applications. Furthermore, T2* and SSFP sequences could be applied on beating hearts without any limitations.

Acknowledgements

This work was funded by the SFB 355/A7.

References:

[1] S Köhler et al, Magnetic Resonance in Medicine **49**, 371-375 (2003)
[2] WT Dixon et al, Radiology **153**, 189-194 (1984)
[3] JC Bergin et al, Radiology **180**, 845-848 (1991)
[4] BA Inglis et al, Magnetic Resonance Imaging **15**, 441-450 (1997)
[5] SS Vasanawala et al, Magnetic Resonance in Medicine **43**, 82-90 (2000)

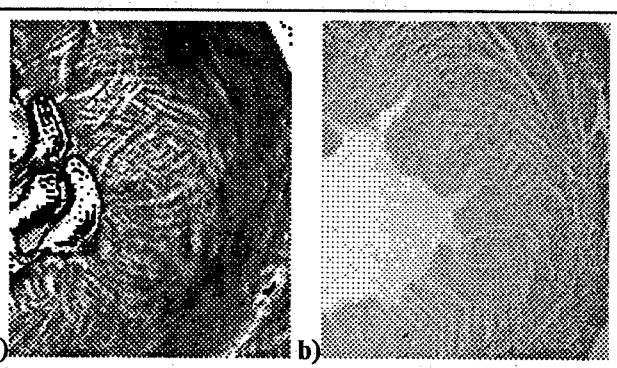

Figure 1: a) Magnification of a region of a T2* map and b) corresponding part of histological section.

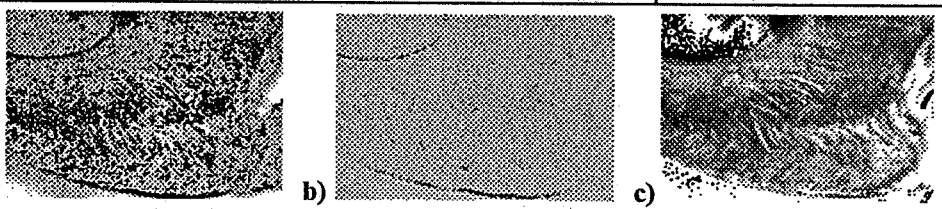

Figure 2: Magnification of a region of a susceptibility loss A' (a), a diffusion-weighted D' (b) and a T2* image (c) of the isolated rat heart in the long axis view (resolution: 78 μm in-plane, 500 μm slice thickness).

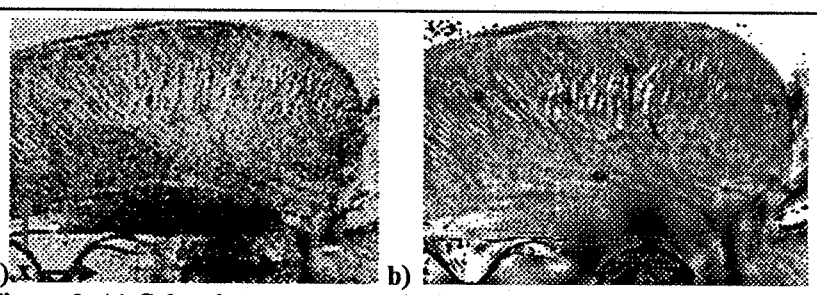

Figure 3: (a) Colored trace map was obtained by summing the D_{xx} (blue), D_{yy} (green) and D_{zz} (red) maps. (b) Corresponding T2* map.
resolution: 78x78x500 μm, T_{ACQ}(DTI) = 80 min, T_{ACQ}(T2*) = 7 min

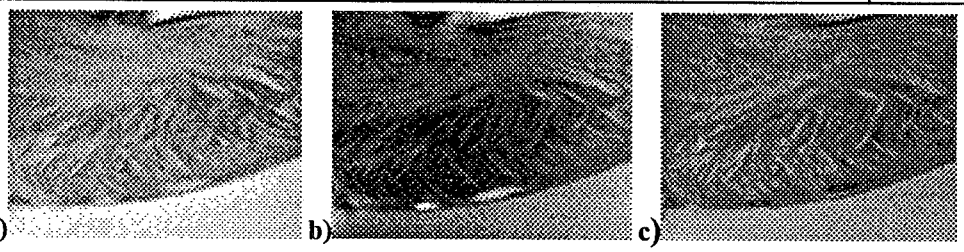

Figure 4: SSFP images with different phase cycles of RF pulse:
a) 0-180
b) 0-0
c) 0-90-180-270
resolution: 78x78x500 μm, T_{ACQ} = 51s

Flow measurements below 50 μm: NMR microscopy experiments in lithographic model pore spaces

Elke Kossel, Rainer Kimmich
Sektion Kernresonanzspektroskopie, Universität Ulm, 89069 Ulm, Germany

Investigating spatially resolved transport through porous media is a challenging task: On the one hand, the detailed structure of the pore space must be known and transport parameters have to be determined with sufficiently good spatial resolution. On the other hand, the usually extremely complex pore space geometry has to be implemented into the theoretical models used to predict the transport behavior.

Our approach to simplify this scenario is the introduction of percolation clusters as model porous media [1]. Percolation clusters are generated by occupying sites on a specific lattice with a probability p. If p is increased starting from zero, clusters of occupied sites begin to form. Above a certain probability p_c, the so-called percolation threshold, an 'infinite' cluster appears. On a finite lattice, the infinite cluster is a cluster that connects opposite edges of the grid. If the occupied sites can be considered as conducting sites, e.g. pores in a solid material or a conductor on an insulator, transport across the sample becomes possible. When p is further increased, a geometrical phase transition occurs. Geometrical properties of the structure and therefore also transport properties can be described by elementary power laws. While this fascinating feature attracted numerous theorists to investigate percolation clusters [2], there has been little experimental work covering this subject.

For providing ourselves with appropriate samples, we have been realizing the computer-generated clusters as artificially created pore spaces in solid polymer materials. This has primarily been done by using a circuit plotter for milling the structure into polystyrene sheets. The fabricated samples were quasi-two- or three-dimensional and based on site-percolation- or so-called swiss-cheese-models. The smallest obtainable pore size of 400 μm depended on the resolution of the circuit board plotter. For a series of MRI experiments, these pore spaces have been flooded with liquids and used to investigate different transport phenomena like flow, diffusion, thermal convection and ionic current [3,4,5,6]. The obtained results were successfully related to theoretical predictions.

However, the generated pore spaces were still macroscopic compared to most natural porous media. If the size of the pores and therefore the diameter of the flow channels for a percolating liquid is decreased to be smaller than about 100 μm, the microfluidic flow regime is entered. Microfluidic flow often differs significantly from macrofluidic flow [7]. This is, on the one hand, caused by the increasing influence of friction. On the other hand, effects like no-slip-boundary-conditions and micro inertia are discussed to contribute to the flow characteristics [7,8].

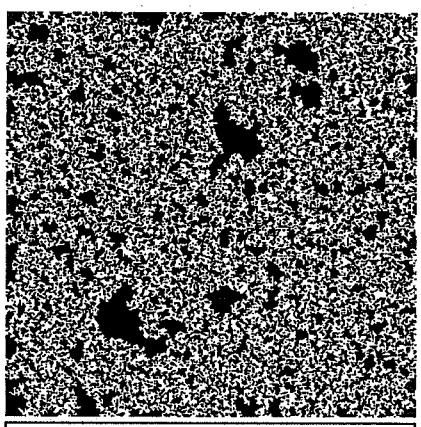

Figure 1: Percolation cluster, generated on a 300 times 300 sites square lattice, that was used as a template for the fabrication of model pore spaces. Only the infinite cluster is shown. p=0.62

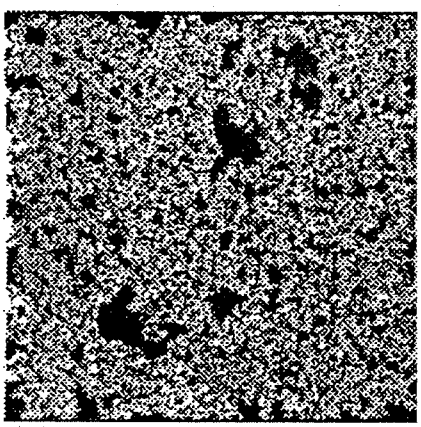

Figure 2: A spin density map of the lithographically fabricated pore space. Minimum pore size: 60 μm
Nominal s patial resolution:
z: 26 μm , x: 37 μm

Our objective was to fabricate quasi-two-dimensional pore spaces based on site percolation models with a minimum in-plane pore size in the order of the best achievable resolution of our microimaging system. In order to still get a reasonable signal from one voxel, the pores have to contain as much liquid as possible. With fixed in-plane pore sizes it is the depth of the pores that has to be increased to enlarge the voxel volume. Therefore a fabrication technique providing an extremely high aspect ratio is needed. We found Deep X-ray Lithography (DXRL) to compete best with these requirements. In DXRL a polymer, in most cases PMMA, is irradiated with x-rays originating from a synchrotron radiation source. A part of the rays is blocked by a gold-patterned mask. Where the x-rays hit the PMMA-sheet, some of the polymer bonds are cracked and the polymer becomes soluble under certain environmental conditions [9].
We employed this technique at the National Synchrotron Light Source's beamline X27b to fabricate pore spaces with minimum pore diameters of 50, 60 and 80 μm, respectively, and a depth of 1 mm [10]. Figure 1 shows the template used for designing the mask. A spin density map of a pore space with a minimum pore size of 60 μm is shown in figure 2. The pores were filled with an aqueous solution of $CuSO_4$. The nominal spatial resolution was set to be 26 μm in the frequency encoded z-direction (right/left-direction in this picture) and 37 μm in the phase encoded x-direction (up/down-direction). To overcome susceptibility related distortions originating at the solid/liquid interfaces, very high gradient pulses of up to 0.9 T/m have been used. It can be clearly seen that the resolution is sufficient to resolve the cluster in all details.
A pressure gradient was applied for driving liquid flow through the cluster and a FEVI pulse sequence has been used to visualize the flow velocities. Four-dimensional data sets (x,z,v_x,v_z) have been measured for both a macroscopic pore space with a minimum pore size of 400 μm and a total sample size of 12 cm, and a microscopic pore space with a minimum pore size of 60 μm and a total sample size of 18 mm. The data set for the larger sample was measured at a 4.7 T Bruker Biospec 47/40 tomograph while the smaller sample has been investigated at a 9.4 T Bruker DSX 400 spectrometer which is equipped with a microimaging unit. Flow paths obtained from the velocity maps are shown in figures 3 and 5, respectively. The nominal spatial resolution of the macro-flow map is 290 μm times 290 μm while the nominal spatial resolution of the micro-flow map is the same as for the spin density image shown in figure 2. Figure 5 shows only a section of the obtained flow-path-map. The size of this section is 18mm times 4.7mm. Additionally, a map of the magnitude of the flow velocity obtained from finite volume simulations is shown in figure 4. While the simulated data match the experimental data from the macro-pore sample exceptionally well, the quality of the micro-pore data is still not good enough to allow a quantitative comparison of the data sets. Nevertheless, the flow paths in the lower region of the sample coincide well, maybe even better than the macroscopic flow paths, with the flow paths predicted by the simulation as can be seen in figure 5.
As a concluding remark it can be stated that it is possible to investigate microfluidic flow through artificially created pore spaces based on percolation clusters, although some future work has to be done to improve the resolution.

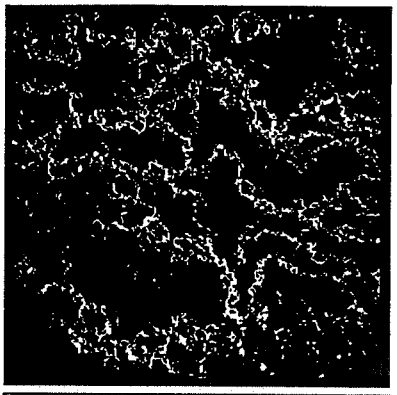

Figure 3: Flow paths of pressure gradient driven flow through the macroscopic model cluster measured with a FEVI pulse sequence. The liquid enters at the right side and leaves the pore space at the left side.

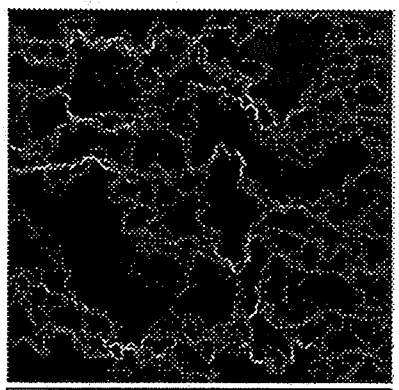

Figure 4: Flow paths of pressure gradient driven flow through the model cluster obtained from finite volume simulations. The brighter the color, the higher the magnitude of the flow velocity.

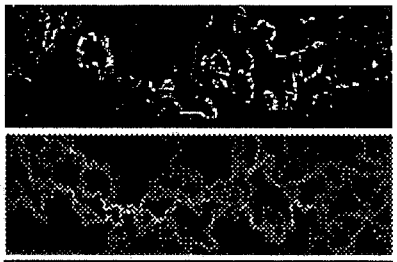

Figure 5: Selected flow paths obtained from FEVI experiments on micro-clusters (upper half) compared to flow paths derived by finite volume simulations (lower half).

Acknowledgements
The experiments involving the macroscopic percolation clusters and the finite volume simulations shown above have been performed by Andreas Klemm.

This research was carried out in part at the National Synchrotron Light Source, Brookhaven National Laboratory, which is supported by the U.S. Department of Energy, Division of Materials Sciences and Division of Chemical Sciences, under Contract No. DE-AC02-98CH10886.

References

[1]A. Bunde, S. Havlin (Eds.), Fractals and Disordered Systems, Springer-Verlag, Berlin (1996)
[2] H.E. Stanley, *J. Phys. A* **10,** L211, (1977)
[3] A. Klemm, R. Kimmich, and M. Weber, *Phys. Rev. E*, **63**, 041514, (2001)
[4] A. Klemm, R. Metzler, R. Kimmich, *Phys. Rev. E* **65,** (2002) 021112-1 -- 021112-11
[5] M. Weber, R. Kimmich, *Phys. Rev. E* **66,** (2002) 056301-1 – 056301-13
[6] M. Weber, R. Kimmich, *Phys. Rev. E* **66,** (2002) 026306-1 - 026306-9
[7] I. Papautsky, J. Brazzle, T.A. Ameel, A.B. Frazier, *Sensors and Actuators A*, **73 no.2**, 101-108, (1999).
[8] E. Bonaccurso, H.-J. Butt, V.S.J. Craig, *Phys. Rev. Lett.* **90,** 144501-1, (2003)
[9]Marc Madou, Fundamentals of Microfabrication, CRC Press, (1997)
[10] E. Kossel, M. Weber, R. Kimmich, *Solid State NMR,* in press

Amplification of Xenon NMR and MRI by Remote Detection

Song-I Han, Juliette A. Seeley, Alex Pines
Materials Science Division, Lawrence Berkeley National laboratory and
Department of Chemistry, University of California, Berkeley, CA 94720, USA.

Abstract
A novel technique will be presented in which a nuclear magnetic resonance (NMR) spectrum or magnetic resonance image (MRI) is encoded and stored as spin polarization and is subsequently moved to a different physical location to be detected. Remote detection allows the separate optimization of the encoding and detection steps, permitting the independent choice of experimental conditions, and excitation and detection methodologies. Furthermore, remote detection allows the utilization of ultra-sensitive optical or superconducting detection techniques, which broadens the horizon of NMR experimentation.

Introduction
In a conventional NMR experiment, a series of radio frequency (rf) and gradient pulses are applied to the information carrying sample nuclei immersed in a strong magnetic field in order to encode information about the local atomic environment, physical interactions between the nuclei, and the macroscopic position and motion of the nuclei of interest. The encoded information is then detected through the observation of the resulting frequencies and amplitudes. A single rf coil is commonly used for both the encoding and detection of the NMR signal, so that only one aspect can be optimized to the detriment of the other. So, conventional NMR employs a compromise that is a trade-off between encoding and detection efficiency, resulting in conditions that are not necessarily optimal for either mode. NMR remote detection separates the encoding and detection steps both spatially and temporally. The NMR information is carried by means of longitudinal magnetization from one location to the other. NMR remote detection capitalizes on the extraordinary strength of NMR, the myriad of encoding possibilities, and suggests new experimental paths to circumvent the inherent weak point of NMR, the low sensitivity.

Experimental details and methods
Pulse scheme The remote detection pulse sequence is based on the principle of indirect detection, and generally consists of three segments, the encoding period (t_1), the travel period (t_t), and the detection period (t_2). In the simplest case, the encoding step is a $\pi/2$ excitation pulse followed by an evolution period t_1 and a $\pi/2$ storage pulse. The stored longitudinal magnetization is transferred to the detection coil by physically moving the stored magnetization between locations. The amplitude of the stored magnetization is determined using a $\pi/2$ pulse in the detection coil. By incrementing the t_1 evolution time, the NMR time domain signal is modulated along the indirect dimension. The spectrum or image that is encoded in the first coil is reconstructed in the second coil using point-by-point detection. The principle of remote detection is generally applicable to NMR experiments where coherence carries the NMR information. One drawback is that this indirect acquisition inherently adds one dimension to the remote experiment.
Sensor nuclei The carrier of remote information can be any NMR sensitive nuclei, provided that the longitudinal polarization survives the travel from the encoding location to the detection location. Various biological fluids or gases could be used as carriers of remote information, but the ideal carrier medium is hyper-polarized Xe^{129}. The combination of high SNR, extremely long T_1 relaxation time, broad chemical shift range, and chemical inertness make Xe^{129} atoms information carriers and model sensors of local environment.
Travel time The NMR signal transfer step necessitates the controlled flow of the encoded xenon nuclei during the course of each single NMR scan. Given that, the travel time (t_t) between the encoding and detection locations, and the characteristic transport distribution of the signal must be determined. This has been measured by inverting the Xe^{129} magnetization in the encoding coil, and then measuring the signal amplitude as it arrives in the detection coil after a certain incremented flow time. Examples of such travel time curves are presented in Fig. 1. The timescale of t_t depends on the travel distance between two locations and the flow rate; Fig. 1 corresponds to a travel distance of about 4 cm between two coils within one probe, whereas travel distances up to 6 m between two different magnets (and coils) have been successfully covered. The minimum amplitude in each travel time curve corresponds to t_b, the time at which the greatest percentage of encoded signal has reached and occupied the detection cell. The broad dip around the minimum gives us information about the spread of encoded spins during the travel time.

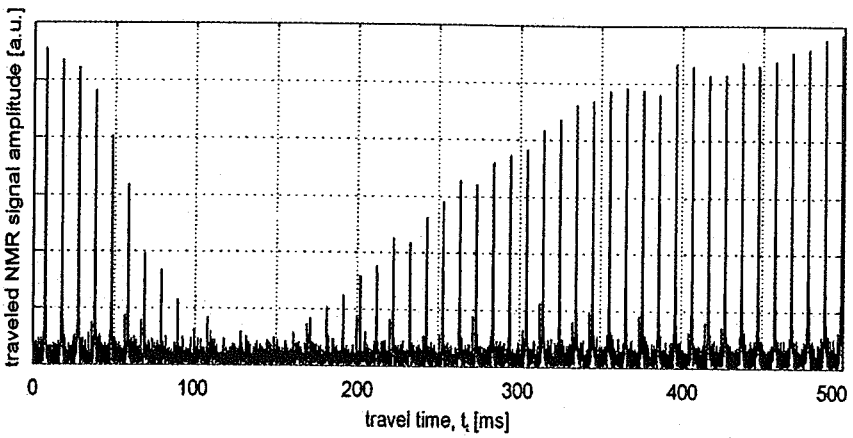

Figure 1: Xe^{129} signal after traveling (t_t) as it arrives in the detection coil. Only positive amplitudes are observed because the inverted magnetization mixes with un-encoded magnetization due to diffusion and turbulence while traveling.

Results, discussion and outlook

Remote detection spectroscopy In the first experimental demonstration of this technique, we show that NMR signal can be amplified by taking dilute Xe^{129} from a porous sample placed inside a large encoding coil and concentrating it into a smaller detection coil (Fig. 2a) [1]. The first remote spectrum reconstructs the chemical shift of Xe^{129} within aerogel crystal fragments, whereby the 1D remote spectrum (Fig. 2d) is a slice taken from the indirect dimension of the 2D NMR spectrum (Fig. 2c). Because only pure xenon gas is transported (not the aerogel sample itself) to the detection coil, the direct dimension shows a single xenon gas peak at 0 ppm (Fig. 2b), whereas the modulation of this direct peak (Fig.2c, inset) measures the chemical shift of xenon gas inside the aerogel fragments. The direct dimension represents the spectrum in the detection cell, and the indirect dimension the encoding cell. The remote spectrum shows a higher SNR than the directly detected spectrum from the encoding coil, reflecting their filling factor difference of ~10. This experiment demonstrates the signal amplification potential of remote detection, where information is read out in a more efficient way by transporting long living polarization to an optimized detector.

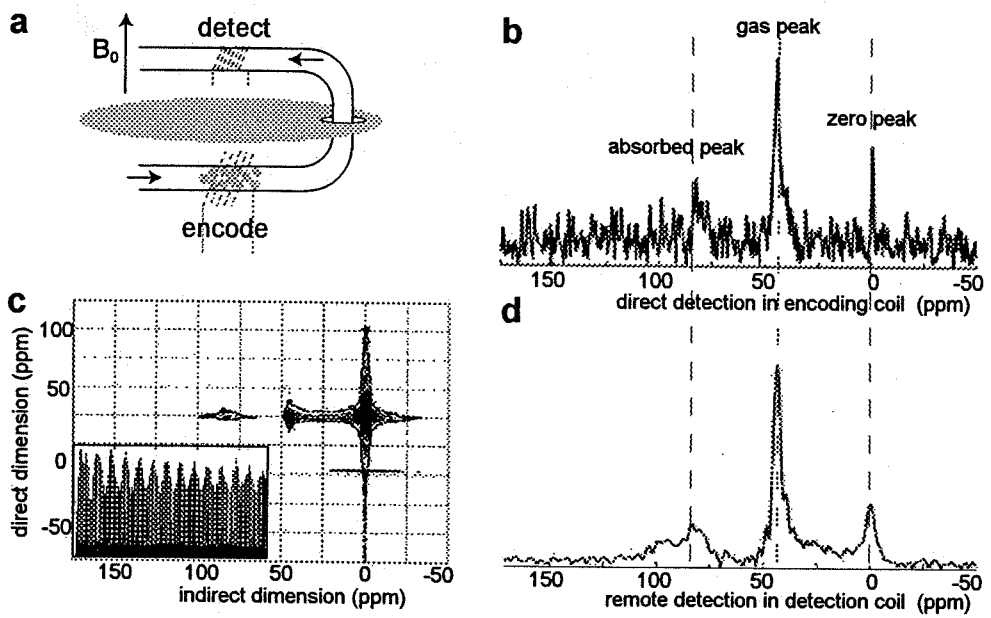

Figure 2: (a) setup. (b) direct spectra of Xe^{129} in aerogel. (c) 2D remote spectroscopy experiment and corresponding time signal (inset). (d) 1D remote spectrum. The three peaks in the spectrum correspond to the free Xe^{129} gas peak, the bound gas peak and a reference peak which appears at zero on the figure scale. This reference peak arises due to un-encoded Xe^{129} gas arriving at the detection coil, which leads to an offset in addition to the remote signal that cannot simply be corrected for because minute variations in the total Xe^{129} polarization between each remote scan.

Remote detection imaging The second experimental demonstration of remote detection extends the basic idea in two senses. The acquisition of remote 2D images demonstrates that the relocation of a more complex information structure than a one dimensional spectrum is possible. Also, it shows that improvements, derived from the NMR conditions that exist at both low and high fields by encoding and detecting the signal at different magnetic fields, can be made. The first remote imaging experiments were performed using a low field magnet (4-7 mT) for the encoding site and a high field magnet (4.2 T) for the detection site. The travel distance for the remote signal was about 5 m. Typical travel times were 7-10 s for flow rates of 4-7 ml/s. 2D remote images representing the expected length proportions and density distribution of the sample cell were obtained [1].

The third experiment demonstrates the application of remote detection imaging to structured porous media and the feasibility of high quality void space images utilizing superior detection quality. 2D images of arranged glass channels of 1mm inner diameter (Fig. 3b,c) and even smaller void space structures (Fig. 3a) could be remotely reconstructed, whereby both rf coils were placed within the same high field (7T) magnet equipped with micro-imaging hardware.

It is remarkable that NMR images, clearly representing the sample structure, can be reconstructed at all, after traveling a long distance under conditions where the spatial order of spin positions is lost. Remote imaging is possible because the encoded *k*-space data travels pixel by pixel after being stored as longitudinal magnetization, not its Fourier transformed data, which is the direct image information. Reconstruction of a full representation of position dependent spin densities requires that all the spins encoded in each remote scan, corresponding to one pixel in *k*-space, are relocated to the detection coil regardless of their macroscopic order. This "collection" is realized by multiple acquisitions. In remote imaging, blurring occurs mainly during the encoding period when the gas atoms diffuse and swap positions, as is also true for conventional gas phase imaging.

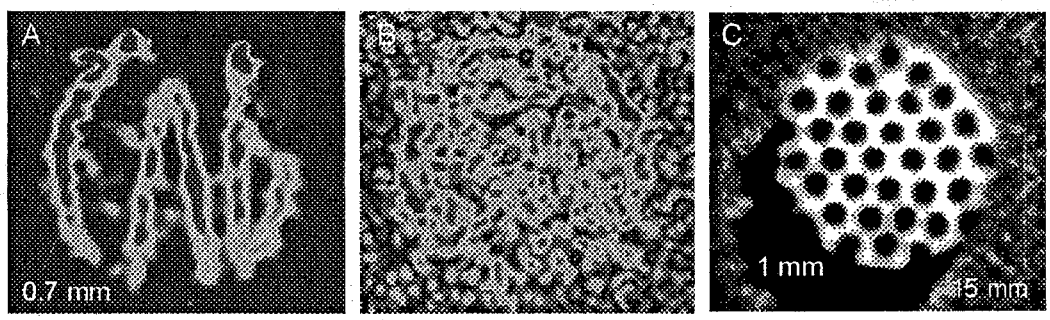

Figure 3: Remotely detected 2D Xe^{129} NMR images of a void space structure "CAL" (A), and parallel arranged glass channels (B) are presented. A conventional void space imaging can be challenging due to the low concentration of the gas phase within the pores, requiring time-intensive signal averaging. This remote experiment, consisting of 128x128 phase encoding steps and 256 points in the direct dimension, was acquired in less than two hours.

Solution state remote detection A challenging, but very promising research goal which we are pursuing at the moment is the realization of solution state remote detection. Here, the xenon sensor is being dissolved into the solution of interest, and after the NMR encoding step, extracted out and collected as pure gas phase in order to be detected with much higher efficiency. At each NMR scan, the insertion and extraction of the NMR spins must be realized in a reproducible fashion. We are utilizing pressure differences, directed by pneumatically controlled valves, pressure regulator and check valves, whereby all devices are triggerable, miniaturized and non-metallic. The xenon biosensor is one of the few means to explore proteins and other biomolecules in solution under native conditions [2], but even with laser-polarization of xenon, this still suffers from low signal to noise. Remote detection first allows us to extract only the information carrying laser-polarized xenon sensor out of the dilute medium into a smaller detection location. The physical concentration of the NMR signal in combination with sensitive detection technique show us a new way to access NMR and MRI information of low concentration NMR active nuclei with special emphasis in biomolecular binding events and porous media study.

References

[1] Moulé, A.J., Spence, M.M., Han, S., Seeley, J.A., Pierce, K.L., Saxena, S., Pines, A., "Amplification of Xenon NMR and MRI by Remote Detection", *Proc. Nat. Acad. Sci.*, submitted.

[2] Spence, M.M., Rubin, S.M., Dimitrov, I.E., Janette Ruiz, E., Wemmer, D.E., Pines, A., Shao, Y., Tian, F., Schultz, P.G., "Functionalized xenon as a biosensor", *Proc. Nat. Acad. Sci.* **98** (19), 10654 (2001).

3D multi-echo imaging in highly inhomogeneous magnetic fields.

J. Perlo, F. Casanova, and B. Blümich
Institute for Technical Chemistry and Macromolecular Chemistry,
Aachen University of Technology, RWTH, D-52056 Aachen, Germany

Introduction

Inside-out NMR uses single-sided sensors that positioned on the surface of unrestricted-size objects define a sensitive volume inside the sample with a shape and a dimension determined by the size and geometry of the device [1]. A simple design of a unilateral sensor is the so-called NMR-MOUSE® (mobile universal surface explorer). It uses two permanent magnets with anti-parallel polarization forming a magnet in the classical U-shaped geometry [2].

The development of imaging methods to be used in the presence of the strongly inhomogeneous magnetic fields generated by the open magnet geometries of these sensors have made possible to assess the heterogeneity degree of samples across the sensitive volume with high spatial resolution [3]. Recently it was reported that 1D profiles can be obtained in the highly inhomogeneous fields of the NMR-MOUSE. Spatial resolution along one space coordinate has been achieved by implementing a single-point imaging method on a U-shaped NMR-MOUSE equipped with a dedicated gradient coil system [1]. It combines the use of a Hahn-echo sequence to refocus the magnetization spread due to the static gradient with the application of a pulsed magnetic field gradient to encode position in the phase of the spin-echo signal. Using this single-point imaging method a spatial resolution of about a few hundred of microns was achieved in a time of about 1 hour. The reported imaging methods can also be used to spatially resolve the relaxation time T_2 or the self-diffusion coefficient D along one space coordinate. The procedure demands the repetition of a set of independent imaging experiments increasing parametrically the evolution period of the Hahn-Echo sequence in order to sample the local magnetization decay, making the total experimental time extremely long and limiting the application of this method.

The first aim of this work is to demonstrate that 3D spatial resolution can be achieved in a single-sided probe, and the second one is to present a new multi-echo acquisition sequence to fully exploit the echo formation reducing the experimental time in a imaging experiment. A new MOUSE including a gradient coil system producing two perpendicular pulsed gradients was built. A new U-shaped magnet with an optimized geometry was used to provide, in contrast with the original one, a static magnetic field with a highly constant gradient of about 2 T/m along the depth direction. This new configuration defines rather flat slices of constant frequency parallel to the *x-z* plane in a region going from the surface up to 20 mm depth (*y* direction). Under this strong static gradient hard RF pulses produce selective excitation of thin flat slices making it possible to select different depth into the object by changing the excitation frequency. In the next sections it is shown that implementing a two-dimensional phase encoding method 2D space resolution across the selected slice can be obtained.

The echo time (T_E) used in the single-point imaging method is mainly determined by the gradient pulse length applied for spatial encoding during the free evolution intervals. Usually T_E is much shorter than T_2 and several echoes can be generated by applying further refocusing RF pulses like in a CPMG sequence. This was fully exploited in conventional NMR imaging, where both the static magnetic field and RF field are homogeneous, to obtain an important experimental time reduction. Either the echo signals can be added before image reconstruction to obtain a sensitivity enhancement or separated images can be reconstructed from each single echo to obtain the complete relaxation decay for each pixel in a single imaging experiment.

The implementation of a CPMG sequence for multi-echo imaging in inhomogeneous magnetic fields has not been previously reported. The extension from a single- to a multi-echo imaging experiment is not direct because the non-uniform plane rotations defined by the RF pulses, as a consequence of the off-resonance excitation, introduce dramatic distortions in the phase encoding defined by the gradient pulse. The spin dynamics during the application of a CPMG-like sequence in the presence of a grossly inhomogeneous B_0 and B_1 fields has been extensively analyzed by Hurlimann et. al. [4]. They have demonstrated that applying a CPMG sequence composed by a nominal first $(\square/2)_x$ pulse followed by a train of nominal $(\square_y$ pulses, the component along the y-axis of the magnetization tipped by the first RF pulse is locked, while the x component goes to zero after a transient period. In an imaging experiment the loss of the x-component (quadrature detection) introduces a mirroring of the spectrum hindering the use of the echo train for sensitivity enhancement.

In this work we have combined the application of a CPMG sequence to sample the *y* component of the magnetization with the application of a CP sequence to sample the *x* component. The pulse sequence is depicted in Fig. 1. The gradient pulses are applied in the first free evolution interval and define the echo time of the first echo. In order to

generate as many echoes as possible a train of refocusing pulses is applied with an echo time T_E shorter than the first one and limited by the dead time of the probe.

The new multi-echo imaging technique was firstly applied to improve the signal-to-noise of the imaging experiment by adding the echoes obtained during the application of the CPMG-like sequence making possible to obtain a complete 2D projection in a single scan. As a second application the sequence was applied to obtain the value of T_2 spatially resolved along two directions of an inhomogeneous object.

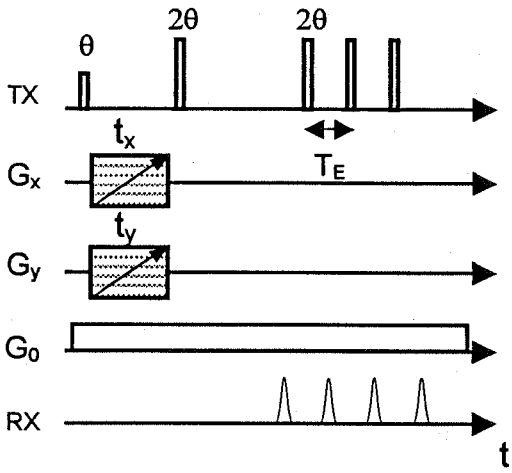

Figure 1: CPMG sequence applied to improve the S/N. The gradient pulses are both applied simultaneously after the first RF pulse determining the first echo time. To maximize the number of echoes that can be acquired the echo time T_E is reduced after the first echo being finally limited by the dead time of the probe.

Finally, the method was used to obtain a set of 2D images selecting slices at different depth positions, showing 3D spatial localization can be obtained using a single-sided probe.

Results

The experimental time reduction that can be achieved using this technique instead of the Hahn-echo sequence becomes really important for samples having long T_2. To show the contrast between the two sequences a silicone rubber sample with T_1 = 330 ms and T_2 = 90 ms was chosen. The simple object geometry shown in Fig. 2a was positioned on the top of the RF sensor and a slice at 5 mm depth was selected. The sequence of Fig. 1 was implemented applying both gradient pulses 0.37 ms long, and an echo time for the detection period of 0.11 ms . The gradient amplitude was increased in 32 steps sampling the k-space from negative to positive values, and with the field-of-view (FoV) set to 32 mm a spatial resolution of about 1 mm was obtained. A single scan was used per gradient amplitude and 800 echoes were acquired and averaged to improve the signal-to-noise ratio. It is important to point out that, as described before, actually two experiments are needed per gradient amplitude. A CP and a CPMG sequence were applied to obtain both components of the echo signal. A recycling delay of 0.45 seconds was used between experiments defining a total experimental time needed to obtain a 2D image of 15 minutes. Figure 2b shows the cross section obtained using the new pulse sequence, the images reproduces a fair structure of the object without appreciable distortions demonstrating that 2D spatial localization can be obtained across the selected slice.

To obtain a 2D cross-section with the same signal-to-noise ratio but using a Hahn-echo sequence a experimental time of about 43 hours would be required. It shows for this sample a time reduction by a factor of 175 can be obtained using the multi-echo acquisition method instead of the original single-echo technique.

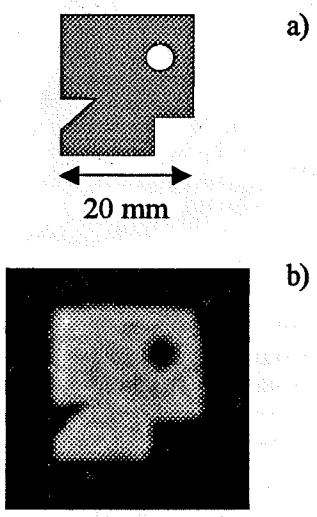

Figure 2: a) Test object geometry made of silicon rubber. b) 2D image obtained applying the new multi-echo acquisition scheme.

To show that spatially resolved T_2 measurements can be done using the multi-echo imaging sequence, a sample with a spatially dependent T_2 was used. Three different rubber sample with different relaxation times were used to build the object shown in Fig 3a. From dark to light gray the relaxation times measured using a CPMG sequence are 1.2 ms, 6 ms, and 34 ms. A slice at 5 mm from the surface and inside the object was selected and the multi-echo sequence was applied using 1000 echoes to correctly sample the longest decay present in the object. The gradient amplitude was increased in 24 steps and with the FoV set to 32 mm a spatial resolution of about 1.3 mm was obtained. The repetition time was set to 0.3 seconds, 3 times the

longest T_1 to avoid any T_1 weight in the image. Averaging 16 experiments, 8 scans for the CP and 8 for the CPMG, a complete 2D image was reconstructed from each echo. Figure 3 shows different T_2 contrasted images obtained adding the echoes b) 8 to 32, c) 32 to 200, and d) 200 to 400. Normalizing the intensity of each image to one, Fig. 3b shows the shortest T_2 region with half of the maximum intensity, Fig. 3c shows the shortest T_2 with zero intensity, the second with the half, and the longest with full intensity, and in Fig. 3d only the region with the longest T_2 is visible.

Finally, combining the 2D phase encoding method with the slice selection, 3D spatial resolution has been achieved. Figure 4 shows an object with 3D structure built stacking a set of letters forming the word MOUSE cut from a sheet of 2 mm thick natural rubber. Having no spacer between each letter an object of 1 cm along the depth direction is obtained. For a better view Fig. 4b shows the letters separated one from the other. After calibrating the frequency dependence with the position along the depth direction different slices 1 mm thick were selected one inside each letter.

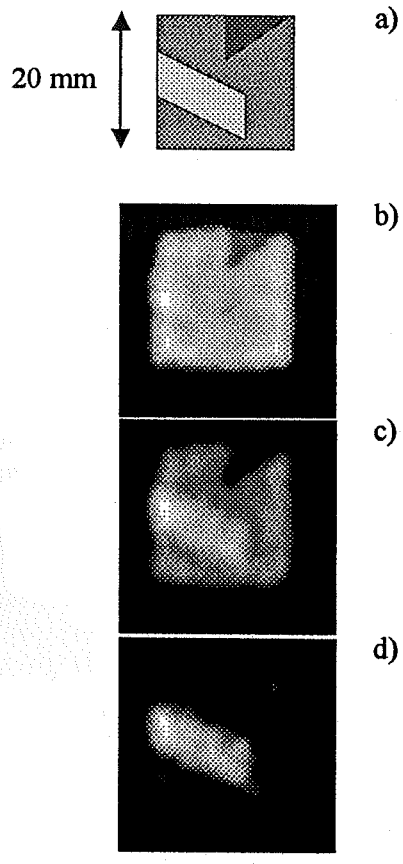

Figure 3: a) Object geometry composed of three different kinds of rubber with different relaxation times shown in different color. The images obtained by adding b) the echoes 8 to 32, c) 100 to 200 and d) 200 to 400 are depicted showing different contrast.

The new multi-echo acquisition scheme was applied using 20 gradient steps and a FoV of 32 mm, giving a spatial resolution of about 1.6 mm. To have the same field-of view at different depth both gradient intensities were calibrated. For this rubber sample a maximum of 96 echoes were added for sensitivity improvement, and an increasing number of scans was used to compensate the dependence of the B_1 as a function of the depth. Using a recycling delay of 30 milliseconds and 4 scans (2 CP and 2 CPMG experiments) a experimental time of 48 seconds was needed for the first letter. For the last letter 4 times more scans were averaged. The 2D image of each letter can be observed in Fig. 4c. The flatness of the sensitive volume is good enough to observe no superposition of consecutive letters.

Conclusion

A multi-echo imaging method to be used in the presence of a strongly inhomogeneous field was presented. The new sequence was implemented in a single-sided NMR sensor equipped with a gradient coil system to produce pulsed gradients along two perpendicular spatial direction. The technique was applied to obtain a complete spatially resolved T_2 map in a single imaging experiment and to improve the signal to noise adding the complete echo train.

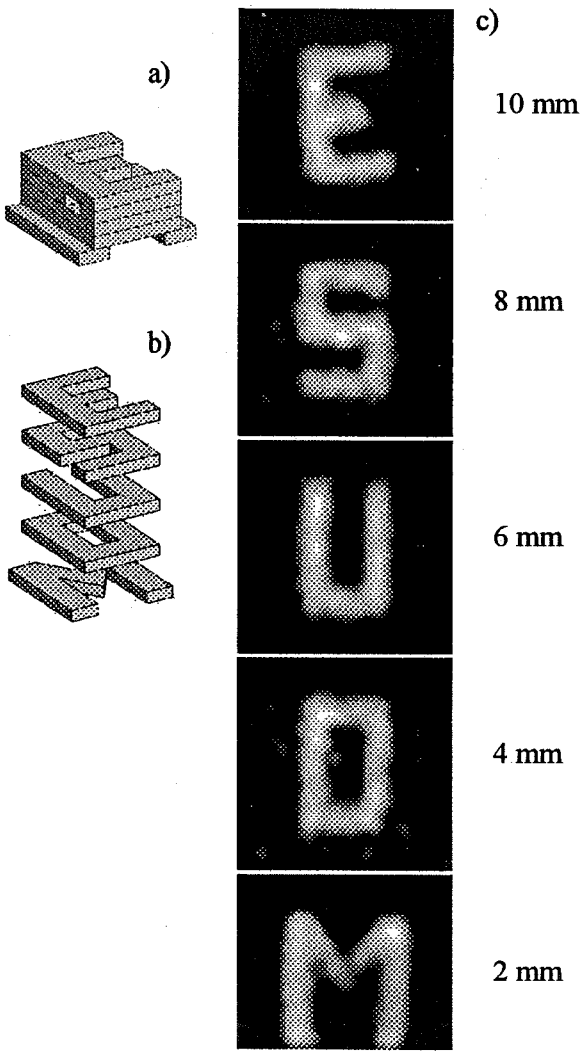

Figure 4: a) Object made staking the letters of the word MOUSE. b) View of the object drawing the letters separated one from the next one to see the object structure. c) Images of each letter obtained applying the multi-echo imaging method.

References

1. G. A. Matzkanin in:, "Nondestructive Characterization of Materials", Springer, Berlin (1992).
2. Eidmann G, Salvelsberg R, Blümler P, Blümich B. J. Magn. Reson., A122: 104-109 (1996).
3. P. Prado, B. Blümich, and U. Schmitz, J. Magn. Reson., 144, 200-206 (2000).
4. M.D. Hürlimann, and D.D. Griffin, J. Magn. Reson., 143, 120-135 (2000).

Continuous Wave NMR Imaging of Short T_2 Materials

A.J. Fagan, G.R. Davies, J.M.S. Hutchison, D.J. Lurie
Dept. of Biomedical Physics and Bioengineering, University of Aberdeen, Foresterhill, Aberdeen AB25 2ZD, UK

Introduction

The study of materials in the solid state and liquids in confined geometries poses considerable technical difficulties to traditional NMR imaging techniques due to the broad NMR lines and very short T_2 spin-spin relaxation times typically encountered. Over the years, several approaches to tackling this problem have been developed, including the use of line-narrowing techniques, very large magnetic field gradients and pure phase encoding. Although these techniques have met with considerable success in application-specific areas [1], no one technique has emerged as an all-round gold standard, and imaging of very short (~10 μs) T_2 components has not been reported in the literature. Over the past number of years, we have been developing a technique for studying broad-line materials using continuous-wave (CW) NMR detection with moderately-strong, continuously-applied magnetic field gradients [2]. We report here on-going developments of the instrument and examples of its application to some short T_2 material systems.

Experimental

The CW-MRI apparatus is based around a 7 T 183 mm horizontal bore superconducting magnet. The home-built coil assembly consists of an 8-rung birdcage resonator, X and Z gradient coil sets (maximum gradient strengths: 250 mT/m), and an additional split solenoidal coil co-axial with the 7 T magnet which provides a magnetic field sweep (up to ± 7 mT). Continuous RF is applied to the resonator via a quadrature hybrid, through which changes in the electrical characteristics of the resonator as the magnetic field is swept through resonance are recorded. Field modulation at 1 kHz superimposed on the magnetic field sweep allows for lock-in detection. 1D projection data are acquired in the direction of the applied gradient, from which 2D images are produced by filtered back-projection reconstruction. The experiment is run by a PC, with sequence control and data acquisition software written in LabVIEW and image reconstruction carried out using IDL.

Results

1D profiles and 2D images with good SNR have been recorded from samples containing ^{1}H protons exhibiting T_2^* values in the region of 10 μs in a variety of materials. Sample sizes of up to 45 mm in diameter and 60 mm in length can be accommodated in the current system. Sub-millimetre spatial resolution was achieved on a PMMA (Plexiglas) phantom (principal T_2^* components of approximately 14 and 40 μs) using a gradient strength of 200 mT/m and an acquisition time of 30 minutes. The technique has also been used to study the hydration, drying and subsequent water penetration into a range of cementitious materials; inhomogeneities arising from the cure conditions were observed. Water penetration into oil reservoir sandstone rock samples was found to be sensitive to the naturally-occurring layering structure within these materials. Preliminary experiments have been carried out to introduce relaxation time contrast into the images by varying acquisition parameters such as the RF power, the modulation frequency and amplitude.

(a) 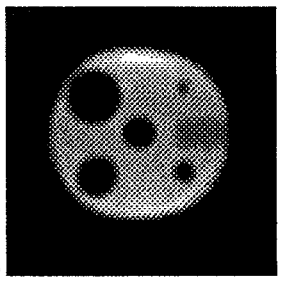 (b) 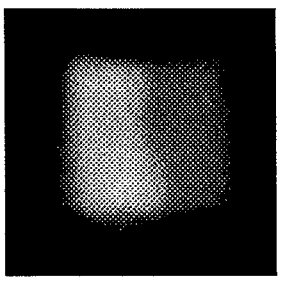

(a) PMMA (Plexiglas/Perspex) resolution phantom (principal T_2^* components: ~ 14 and 40 μs) – the hole on the top right side is 2 mm in diameter; (b) Water penetration into a cement sample (left side of sample immersed in water for 15 minutes) - the signal on the right side is from chemically combined water in the cement structure, with a T_2^* of ~ 10 μs.

References

[1] D.E. Demco and B. Blumich, *Concepts in Magnetic Resonance*, **12**, 188-206 (2000).
[2] A.J. Fagan et al., *Journal of Magnetic Resonance*, in press (2003).

Quadrupole Resonance: A Different "Spin" on Nondestructive Inspection of Polymeric Fiber-Reinforced Composite Structures

Stephanie A. Vierkötter, Catherine Ward, David Gregory.
Quantum Magnetics, Inc., 15175 Innovation Dr., San Diego, CA 92128, USA.

Abstract
The discipline of nuclear magnetic resonance (NMR) spectroscopy has seen an impressive growth of capabilities and applications since its discovery now more than 50 years ago. From simple characterization of molecules that previously were analyzed by chemists via tedious wet-chemical approaches we have come to conduct complex, high-resolution NMR experiments that reveal the structure and function of biological molecules of ever-increasing size. Solid-state NMR spectroscopy, once almost impossible, has long since become a strong field in its own right. In addition to laboratory-based research NMR is also used for applications such inspecting oil boreholes, on-line quality control, etc. But what about NMR's relative, Nuclear Quadrupole Resonance (NQR) or "zero-field NMR"?

In terms of "real-world" applications that require NQR measurements outside of the laboratory several applications have been realized, e.g., explosives detection for aviation/homeland security purposes and land mine detection, drug/contraband detection, etc. However, the bandwidth of applications appears to be much smaller for NQR than for NMR. Are the requirements we need a material to satisfy (crystallinity, nuclei with appropriate spin) too restricting to apply QR more broadly?

This paper describes the use of Nuclear Quadrupole Resonance for the nondestructive inspection of polymeric fiber-reinforced composites structures. Interestingly, the technique straddles the area of nondestructive inspection of composite materials and that of smart materials. Tiny crystals of a suitable additive are either embedded into the composite at the time of the manufacture or are applied as part of a surface coating. Stresses acting on the composite lead to strains in the composite matrix, which in turn are transferred to the additive crystals. The strains in the crystals can be read out via Nuclear Quadrupole Resonance spectroscopy since the NQR frequency shifts as a function of strain.

The paper describes studies of the NQR responses of fiberglass/epoxy coupons under tensile loads are compared to simultaneous measurements of strain via an extensometer. The NQR responses were found to be quite sensitive to strain. Hysteretic behavior of the NQR frequency when load cycles are applied is discussed. The paper also describes the investigation of residual strains in composites, i.e., strains that formed during the manufacturing process rather than through stresses acting on the composite during use.

In developing an NQR-based composite inspection method it is critical to produce an instrument that can actually function in a real-world environment. For the measurement (and mapping) of the strain in the additive crystals and hence in the composite a lightweight NQR coil is used as detector head. The result obtained during a recent first field-test of our QR composite inspection prototype are promising. A 75-foot long composite pole was placed under various bending loads. Using surface-applied coatings with QR active additive changes in strain of the pole were detected. The NQR based composite inspection technology technique has the advantage of being a nondestructive and non-contacting inspection method that requires no attached cables, embedded fiber optics, etc. Furthermore, strains can be measured anywhere on the structure, as long as QR active crystals were applied to that location.

Water distribution and skin formation in semi-crystalline polymer layers cast from solution: a magnetic resonance imaging study

E.Ciampi and P. J. McDonald
School of Electronics and Physical Sciences, University of Surrey, Guildford, Surrey, UK;

Introduction

The drying of polymer layers is an important step in many industrial production processes. Polymers such as poly (vinyl alcohol), PVOH, are glassy at room temperature but become rubbery in the presence of sufficient solvent, in this case water. As the drying of a polymer solution proceeds, water evaporation induces a rubber to glass transition. In the case of drying layers, the question arises as to whether the polymer concentration remains uniform throughout the layer depth. If the evaporation leads initially to a more concentrated solution at the layer surface, then a skin is predicted to form at the air interface. In turn, this skin can hinder evaporation and slow the drying. With PVOH, there is the additional complication of whether the skin is entirely amorphous or whether crystalline regions develop within it. Crystalline regions potentially create a greater barrier to water transport than amorphous regions and can therefore further inhibit drying. In recent studies, Ngui and Mallapragada [1,2] examined the drying of semi-crystalline PVOH using a combination of bulk techniques, such as thermogravimetric measurements, differential scanning calorimetry and Fourier transform infrared spectroscopy. The same authors also developed a mathematical model to predict the skin formation and the water loss rate from the polymer films. We take this work further with the first studies using MRI. MRI allows us to directly visualise the water distribution in drying layers.

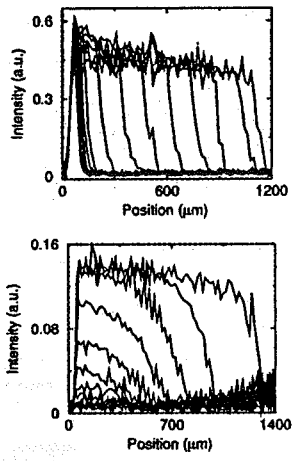

Figure 1. Very different water concentration drying profiles are observed for PVOH layers dried slowly (top, data over 7 days) and quickly (bottom, data over 12 hours). The former develops a crystalline skin which seriously slows water loss in the later stages of drying.

Experimental

Magnetic resonance microscopy using GARField, [3], is used to measure the water distribution as a function of time in layers of PVOH cast from aqueous solution. It is shown that the water distribution remains uniform in thin layers dried slowly but is non-uniform in thicker layers dried more quickly. Moreover, it is shown that layers dried slowly in comparison to a time characteristic of the amorphous – crystalline transition develop a crystalline skin whereas other layers do not. In a new theoretical approach, these results are described in terms of a parameter space defined by a (dimensionless) Peclet number for the layer and a dimensionless drying time. The Peclet number links the layer thickness and evaporation rate with the polymer diffusivity which seeks to maintain a uniform concentration. The dimensionless time compares the drying and crystallisation rates. The initial position of the layer in this space can be used to broadly predict the drying profiles and characteristics of the dried layer. The magnetic resonance imaging results and interpretation are supported by pulsed field gradient measurements of polymer and water diffusion coefficients and by differential scanning calorimetry (DSC) measurements of dried layers as well as by experiments using FLASH MRI which investigate re-wetting of dried layers.

References

[1] Ngui M. O. and Mallapragada S. K., *J. Polym. Sci., Polym. Phys.*, **36**, 2771 (1998)
[2] Ngui M. O. and Mallapragada S. K., *Polymer* **40**, 5393 (1999)
[3] Glover P.M., Aptaker P.S., Bowler J.R., Ciampi E. and McDonald P.J. , *J. Magn. Res.* **90**, 139 (1999).

Centric Scan SPRITE (Single Point Ramped Imaging with T_1 Enhancement) Magnetic Resonance Imaging

Bruce J. Balcom, Meghan Halse, Bryce MacMillan
Department of Physics, MRI Center, University of New Brunswick, Fredericton, NB E3B5A3, Canada

The standard SPRITE (Single Point Ramped Imaging with T_1 enhancement) imaging technique has proven, over the last six years, to be a very flexible and robust methodology for MRI of materials. As a pure phase encode imaging method it is largely immune to image artifacts arising from inhomogeneous magnetic fields. Repetitive RF excitation, as a function of stepped or ramped phase encode gradients, with gradient switching prior to excitation, ensures that MR systems with T_2* lifetimes as short as tens of microseconds may be successful visualized. The SPRITE methodology, largely immune to image artifacts, yields a geometrically correct image which is therefore implicitly more quantitative than MRI methods which suffer from systematic geometric distortion.

The standard SPRITE methodology, while yielding geometrically correct images, is a longitudinal steady state imaging method which ensures two significant deleterious features. (1) The local image intensity will depend on a longitudinal steady state which can only reduce the observed local signal intensity. Removing this dependency requires reducing the RF flip angle which is not ideal since this reduces the observable signal intensity or increasing the repetition time. The later is not satisfactory since this carries a significant gradient duty cycle penalty. (2) The image signal equation for standard SPRITE depends on too many parameters for ready quantification. These include the repetition time, flip angle and spin lattice relaxation time as well as the proton density, phase encoding time and effective spin-spin relaxation time.

A centric scan approach to SPRITE imaging will remove the longitudinal steady state from the local signal equation increasing the inherent MR image intensity while at the same time simplifying the image signal equation. This presentation will outline two rapid centric scan SPRITE experiments. The Spiral-SPRITE method utilizes a modified Archimedean spiral k-space trajectory. The Conical-SPRITE method utilizes a system of spirals mapped to conical surfaces to sample the k-space cube. The sampled k-space points are naturally Cartesian grid points, eliminating the requirement of a re-gridding procedure prior to image reconstruction. In addition, each experiment features a dramatically reduced gradient duty cycle, at both short and long time scales, when compared to standard SPRITE experiments. The impact of movement to a longitudinal steady state on the practical image resolution will be discussed in terms of point spread functions and a systematic procedure for optimizing the experiments described. Finally a methodology for sampling multiple FID data points, yielding multiple image data sets, will be described. The reconstructed image data sets naturally possess different fields of view which may be recombined to a common field of view using the chirp Z transform. The separate image data sets may then be recombined for T_2* mapping purposes or SNR improvement.

MR Microscopy of flow dynamics in porous structure

Janez Stepišnik,
Department of Physics, FMF, University of Ljubljana, 1000 Ljubljana, Slovenia

The Gaussian phase approximation (GPA) [1] provides a way to describe the gradient spin echo measurements of diffusion and flow in the static or the generalized modulated magnetic field gradient. Resulting techniques makes possible to extract information not only about the macroscopic self-diffusion coefficient, but also about the details of the molecular velocity correlation spectrum [4]. In the case of short-pulse-gradient-spin-echo, it gives the spin echo signal related to an averaged propagator [3], $E(q,\tau)=\sum_i e^{iq.\Delta\mathbf{r}_i(\tau)-\frac{1}{2}q^2\langle\Delta\mathbf{r}_i^2(\tau)\rangle}=\int P(\mathbf{r},\tau)\,e^{i\mathbf{q}.\mathbf{r}}d\mathbf{r}$, which is a sum of the normal probability as

$$P(\mathbf{r},\tau)=\sum_i \frac{1}{\sqrt{2\pi\langle\Delta\mathbf{r}_i^2(\tau)\rangle}}\exp\left[-\frac{(r-\Delta\mathbf{r}_i(\tau))^2}{2\langle\Delta\mathbf{r}_i^2(\tau)\rangle}\right]$$

Here the mean, $\Delta\mathbf{r}_i(\tau)=\mathbf{r}_i-\langle\mathbf{r}_i\rangle$ and the variance, $\langle\Delta\mathbf{r}_i^{\,2}(\tau)\rangle=\langle(\mathbf{r}_i-\langle\mathbf{r}_i\rangle)^2\rangle$ are the mean displacement and to the mean squared displacement of spins from the mean location $\langle\mathbf{r}_i\rangle$

The method is applicable to describe the spin echo measurement of diffusion and flow in complex media. In the case of flow through the porous structure, Taylor's diffusion-dispersion equations provide the displacement and the squared displacement due to the flow and dispersion as

$$\Delta\mathbf{r}_j(\tau)=\mathbf{v}_j\tau+\sum_k \mathbf{b}_k\sin(\mathbf{k}\mathbf{v}_j\tau)e^{-\frac{\tau}{\tau_k}}$$

$$\langle\Delta\mathbf{r}_j^2(\tau)\rangle\approx 2K_j\tau+\sum_k c_k\left(1-\cos(\mathbf{k}\mathbf{v}_j\tau)e^{-\frac{\tau}{\tau_k}}\right)$$

Here $\mathbf{b}_k$ and c_k are structure factors, while $\mathbf{v}_j$ is the local mean velocity and K_j is the dispersion coefficient. Resulting evolution of the flow dispersion propagator exhibits a kind of early time oscillation that is developing into a spreading distribution, which is shifting in the direction of flow. The measurement of the spin echo phase shift and attenuation makes possible to visualize the flow dispersion as shown on fig. 1, as well as to determine the microscopic details of structure from the short time dependence on time [3] or the flow dispersion spectrum [4] obtained by the modulated gradient method.

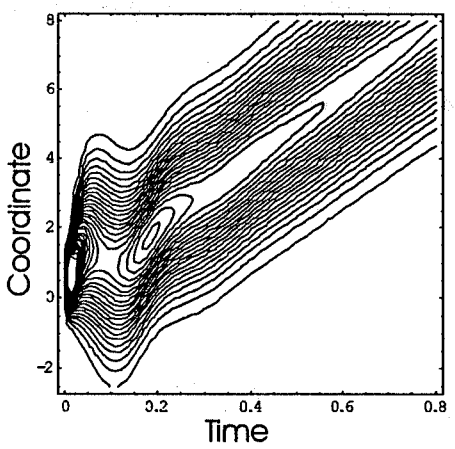

Figure 1: Contours of flow dispersion propagator in porous structure as it evolves with time

This analysis opens an access to the space-time correlations of motion, closing a gap between so-called NMR diffusometry and q-space NMR. The approximations beyond the GPA expansion have no significant effect to the basic understanding of spin echo evolution, giving only small corrections to the spin echo-phase and attenuation [5].

References

[1] J.Stepišnik, Physica B, 104, 350-64, 1981
[2] J.Stepišnik, Europhysics Letters, 60/3, 453-59, (2002
[2] M. Holz, S. R. Heil., I. A. Schwab, Mag. Res, Imaging 19 (2001) 457–463
[4] P.T. Callaghan, J. Stepišnik, J. of Mag. Res. A 117, 118-122(1995)
[5] J.Stepišnik, to be published in Physica B

Non-Destructive Microstructural Characterization of Ceramics: Spatially Resolved Gas Adsorption using NMRI

Steven D. Beyea, S. Jill Glass[§] and Andrew McDowell
New Mexico Resonance, 2301 Yale Blvd. SE, Albuquerque, New Mexico, 87106, USA
[§] Sandia National Laboratories, Albuquerque, New Mexico, 87185, USA

Characterization of the structural parameters and morphology of porous ceramics is essential to the development of new nanoscale materials. One specific area of interest is sintering processes in multilayered and functionally graded materials, particularly in ceramics created using nanocrystalline powders. The development of pore microstructure during sintering is highly complex.

Gas-phase NMR imaging is a powerful non-destructive evaluation method for porous materials created to exhibit gradients in morphology or composition [1-3]. These non-destructive measurements permit spatially resolved studies of pore variables such as porosity, pore size, specific surface area, pore shape, and gas/substrate adsorption energy [4]. Results of validation experiments performed on a phantom containing a variety of uniform materials (nanocrystalline powders, porous glass, partially sintered nanoporous ceramics) will be shown. Spatially extracted microstructural parameters are shown to agree with those obtained in bulk using conventional methods such as N_2 BET [5], as shown in Table 1.

Initial results from gas-phase NMRI studies of next-generation ceramics designed to exhibit microstructural/morphological gradients, developed by the Materials & Process Sciences Centre at Sandia National Laboratories, will be shown. Space resolved measurements of adsorbate fractional surface coverage, NMR relaxation rate (a function of molecular collision frequency) and diffusion coefficient reveal internal variations in the microstructure, obtained non-destructively and non-invasively.

Table 1: Comparison of Local Microstructural Parameters Extracted from NMR Images with Conventional Bulk BET Measurements

Materials	Conventional BET Specific Surface Area (m^2/g)	NMRI Specific Surface Area (m^2/g)	NMRI Adsorption Energy (kJ/mol)
ZnO Powder	19	17 ± 2	8.7 ± 0.7
ZnO Ceramic	7	7.5 ± 0.6	8.5 ± 0.5
□-Al_2O_3 Powder	41	42 ± 1	5.8 ± 0.9
□-Al_2O_3 Ceramic	34	35 ± 2	5.6 ± 0.9
Porous Glass	112	119 ± 6	3.5 ± 0.4

Sandia is a multiprogram laboratory operated by Sandia Corporation, a Lockheed Martin Company, for the United States Department of Energy under Contract DE-ACO4-94AL85000.

References:

[1] A. Caprihan *et al* "Characterization of Partially Sintered Ceramic Powder Compacts Using Fluorinated Gas NMR Imaging", *Mag. Res. Imaging* **19**, 311 (2001).
[2] S.D. Beyea *et al* "Spatially Resolved Adsorption Isotherms of Thermally Polarized Perfluorinated Gases in Y-TZP Ceramic Materials using NMR Imaging" *Appl. Magn. Res.* **22** (2), 175 (2002).
[3] S.D. Beyea *et al* "Studies of Porous Media by Thermally Polarized Gas NMR: Current Status" *Mag. Reson. Imaging* **21**, in press (2003).
[4] S.D. Beyea *et al* "Non-Destructive Characterization of Nanopore Microstructure: Space Resolved BET Isotherms using NMRI" *J. Appl. Phys.*, in press (2003).
[5] S. Brunauer, P.H. Emmett and E. Teller, *J. Am. Chem. Soc.* **60**, 309 (1938).

Kinetics and Mechanism of Mixing in Concentrated, Oil-in-Water Emulsions

Nina C. Shapley, Marcos A. d'Avila, Jeffrey H. Walton*, Ronald J. Phillips, Stephanie R. Dungan and Robert L. Powell**

Department of Chemical Engineering and Materials Science, University of California, Davis, CA 95616, USA

* NMR Facility, University of California, Davis, CA 95616, USA

** Department of Chemical Engineering, Columbia University, New York, NY 10027, USA

In most emulsions, a density difference between the dispersed and the continuous phases leads to separation of the components by gravity, known as "creaming." Typically, a uniform emulsion is desirable, and hence it is important to examine the kinetics and mechanism of emulsion mixing required to achieve this uniform state. In addition, previous mixing research has focused on the evolution of the microstructure of a system under known flow fields, where the developing microstructure does not modify the flow field in the process. In contrast, in the case of concentrated emulsions, it is shown here that the evolution of the nonuniform droplet concentration profile has a major impact on the observed flow field.

Mixing of concentrated oil-in-water emulsions in a horizontal, concentric-cylinder geometry was studied using nuclear magnetic resonance imaging (NMRI). An initial nonuniform concentration profile was established by creaming over several hours of a homogeneous emulsion of isooctane and water stabilized with nonionic surfactant. Then, the time-dependent effect of slow shear flow on the concentration and velocity profiles was quantified. Time-of-flight and chemical shift imaging methods were used to measure velocity profiles and oil droplet concentration maps, respectively, during the mixing process.

The results revealed detailed information about mixing in concentrated emulsions. In the initial state, before mixing, the emulsion system formed three layers: an upper, oil-rich, "creamed" layer; a lower, water-rich layer; and a bulk concentration layer in between. It was found that the thickness of the creamed layer remained constant during mixing, while the oil concentration in that layer decayed exponentially as a function of time. It was also observed that most of the emulsion is quiescent while mixing progresses; the only motion detected occurs in a thin layer close to the rotating, outer cylinder. The velocity profile only begins to transform into its steady state configuration after the emulsion becomes well-mixed. Several of these effects are apparent in Figure 1. A simple model is introduced that gives a plausible explanation of these experimental observations. In addition, supporting measurements of the droplet size distribution in the creamed layer will be presented. These results indicate that the mixing mechanism in concentrated emulsions is significantly different from that in single-phase liquids.

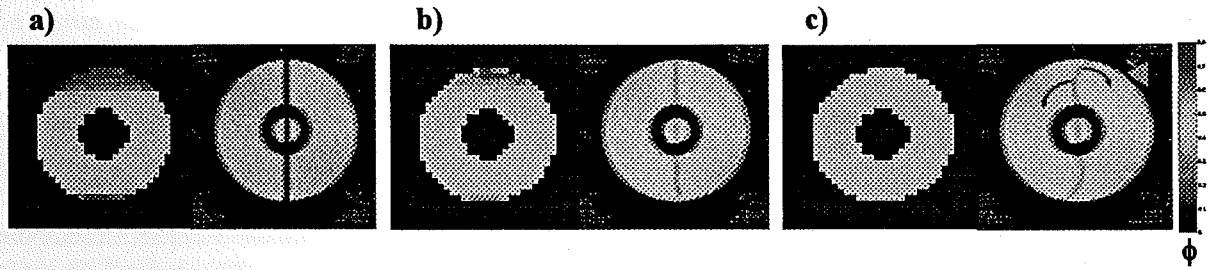

Figure 1: Side by side oil concentration maps and time-of-flight images for an emulsion with □ = 0.5 and V = 0.05 cm/s, after 3 hours of creaming. The series of images shows the progression of mixing.
a) immediately before mixing, b) after an average of 8.5 minutes of mixing, c) steady state.

Long-Time Scale Molecular Dynamics of Ordered Fluids[1]

Farida Grinberg and Günter Majer
Max-Planck Institute for Metals Research, Heisenbergstr. 3, 70569 Stuttgart, Germany

Complex fluids like liquid crystals, polymers, colloids, etc. are characteristic of the orientational molecular order on the meso- and macroscopic length scales. Individual or collective molecular motions in these substances tend to range over many time decades. This in turn gives rise to extremely slow spin relaxation mechanisms in the range of milliseconds and longer. Usually, several different mechanisms contribute simultaneously to spin relaxation in the same frequency or time ranges. The most illustrative examples can be found with the confined liquid crystals widely used in the electro-optical devices. Another example is given by elastomers where ultra-slow chain relaxation modes are associated with the presence of chemical cross-links.

Addressing molecular dynamics of oriented fluids by the NMR techniques raise a problem of decomposing numerous overlapping stochastic processes. Naturally, the relaxation studies must be extended to the longest possible time scale as provided by the field-cycling relaxometry [1] or by the three 90^0-pulse sequence. In this work we demonstrate the experimental results obtained for liquid crystals constrained in nanostructured materials by several NMR techniques: stimulated echo studies [2,3], 2D-exchange spectroscopy [4,5], temperature and frequency dependent measurements of the relaxation rates [4,5], Pulsed Field Gradient diffusion measurements. Experimental data are supported by the Monte-Carlo simulations. Cavity constraints are found to strongly affect molecular collective and non-collective orientational fluctuations both below and above the nematic-isotropic transition. The correlation length of the surface-induced order is determined.

In elastomers, ultraslow chain relaxation modes with correlation times of the order of a few milliseconds were monitored by measuring the dipolar-correlation effect on the stimulated echo. The mean squared fluctuation (MSDF) of the residual dipolar coupling constant shows a strong dependence on the cross-link density of natural rubber studied in dry and swollen states. Cross-link density of rubber materials can be determined on this basis. The MSDF suggests a new contrast parameter for NMR mapping. The MSDF-maps of certain composite samples were evaluated from the attenuation curves of the stimulated and the primary echo measured under the application of the standard scheme of the magnetic field gradients providing a spatial resolution [6]. The advantages of employing this kind of mapping for characterization of materials are discussed.

References

[1] R. Kimmich. *NMR: Tomography, Diffusometry, Relaxometry* (Springer-Verlag, Heidelberg, 1997).
[2] F. Grinberg, M. Vilfan, E. Anoardo. In *NMR of ordered liquids*, edited by E. E. Burnell and C. A. de Lange, Kluver Academic Publishers (Boston, Dordrecht, London), in press, (2003)
[3] F. Grinberg and R. Kimmich. *J. Chem. Phys.* **105**, 3301-3306 (1996).
[4] F. Grinberg. In NATO SCIENCE SERIES "Magnetic Resonance in Colloid and Interface Science", edited by J. Fraissard and O. Lapina, Kluver Academic Publishers, Dordrecht, (2002)
[5] F. Grinberg and R. Kimmich. *Magn. Reson. Imaging*, **19**, 401-404, (2001).
[6] F. Grinberg, M. Heidenreich and W. Kuhn, *J. Magn. Reson.*, **159**, 87-91, (2002)

Acknowledgements
F.G. cordially thanks Prof. Dr. R. Kimmich for the most fruitful co-operation and the excellent research conditions during my multi-year stay in his laboratory. My warmest thanks go to Prof. M. Vilfan for many valuable discussions on relaxation mechanisms in liquid crystals.

[1] A big part of the materials demonstrated in this work was obtained in the Sektion Kernresonanz-spektroskopie (Universität Ulm, 89069 Ulm, Germany) headed by Professor Dr. R. Kimmich. Pulsed Field Gradient diffusion experiments are performed at Max-Planck Institute for Metals Research.

3D MR microscopy of trabecular bone: architecture parameters by reference to high resolution microtomography (synchrotron radiation) on matched ROIs

David Last (1), Ludovic De Rochefort (1), Françoise Peyrin (2), Geneviève Guillot (1)
(1) U2R2M CNRS UMR8081 Bât 220; Université Paris-Sud 91505 Orsay France
(2) CREATIS-ESRF BP 220 38043 Grenoble France

Scope
As a non invasive 3D method, micro MRI (μMR) should be a useful tool for the analysis of trabecular bone microarchitecture. To estimate whether MR images correctly represent the trabecular network, the same parameters should be evaluated from μMR and from data obtained with a "Gold Standard" technique such as high resolution x-ray tomography (μCT), as far as possible on the same ROIs. However it is difficult to ensure the recovery of identical ROIs in different 3D acquisitions, due to different resolution and sample position in each image frame. The purpose of this work was to show the interest of performing parameter evaluation on ROIs matched between the two modalities, and to compare architecture parameters (bone volume fraction BV/TV, topology, orientation) at identical voxel size.

Materials and Methods
29 defatted and dried cylindrical samples (7 mm diameter, 15 mm height) were taken from 15 human calcaneus. μCT images were acquired at ESRF (European Synchrotron Radiation Facility) with a 10μm cubic voxel size, yielding 660^3 matrices with a signal to noise (SNR) of 150. Simple thresholding could be unambiguously used for segmentation, thus providing a gold standard bone volume fraction (BV/TV_0). 3D μMR images were acquired in a 8.5 T MRI prototype, with the samples filled with water. A 3DFT spin-echo sequence (TE/TR 8/200ms) and a bandwidth of 50kHz were used to avoid the problem of magnetic susceptibility difference between bone and water. Zero-filling (by a factor 2 in each dimension) yielded a 128x128x256 matrix with a cubic voxel size of 66μm and a SNR of 17. A ROI matching algorithm based on the three major differences between the two modalities (resolution, sample position and field of view) was applied on each pair of images [1]. Segmentation was performed by thresholding for the resampled μCT images, with a threshold leading to $BV/TV=BV/TV_0$, and with a labeling method developed in the laboratory for the 3D μMR images [2]. BV/TV, connectivity (Euler-Poincaré characteristic CN_3 [3]) and orientation (the 3 Euler angles □,□,□ found from the fit of the Mean Intercept Length to an ellipsoid surface [4]) were computed on matched and non-matched ROIs.

Results
Automatic repositioning was successfully achieved for all samples with an excellent accuracy. Comparison on matched ROIs decreased the differences between the modalities by as far as 70%. Connectivity and orientation measures were highly reliable on μMR. For BV/TV, although the measure was very precise, there was a bias (7%) corresponding to its systematic overestimation by μMR.

Conclusions
ROI matching is a critical issue for comparison of trabecular bone parameters, especially for network orientation. Our study shows that the general organization of trabecular bone can be reliably assessed by μMR at 66μm voxel size. The recovery of bone volume fraction was precise but strongly biased causing a systematic BV/TV overestimation by μMR; it corresponded to a 150% BV/TV error at the lowest BV/TV_0s of the samples examined in this study. Analysis of μMR in vivo images of the middle finger (acquired at 7T with 156μm cubic voxel size) is currently in progress.

References
[1] David Last, Ludovic de Rochefort et al, *Magma* **15**,219 (2002).
[2] Theocharis Antoniadis, Jean-Pierre Scarpelli et al, *Medical Image Analysis* **3**,119-128 (1998).
[3] Hans-Jorg Vogel, *Acta Stereologica* **16/2**:97-104 (1997).
[4] TP Harrigan, RW Mann, *Journal of Materials Science* **19**, 761-767 (1984).
[5] Geneviève Guillot, David Last et al, 9th ISMRM Proceedings 928 (2001).

Hyperpolarized ^{3}He Detection of Radiation-Induced Lung Injury in Rats

L. Hedlund[1], Z. Vujaskovic[2], E. Ward[2], W. Kurylo[1], C. Wheeler[1], G. Cofer[1], G.A. Johnson[1]
[1]Center for In Vivo Microscopy and [2]Department of Radiation Oncology,
Duke University Medical Center, Durham, NC 27710, USA

Introduction

The apparent diffusion coefficient (ADC) of hyperpolarized (HP) helium in the lung reflects the restricted diffusion of ^{3}He in the gas space compartments. As this restriction is lessened by increased alveolar size, the ADC of ^{3}He increases and vice versa. In an elastase model of emphysema, we found a smaller difference in ADC from full inspiration to end-expiration than in controls, and this was consistent with a persistent enlargement of alveolar spaces due to loss of elasticity [1]. This suggests that ADC of ^{3}He in the lung is a sensitive index of changes in the micro-architecture of the lung's gas exchange regions. In the present study, we use ADC of ^{3}He to evaluate micro-structual changes in the lung after fractionated radiation.

Materials and Methods

Adult rats were exposed to right, hemithoracic radiation with fractionated doses (5 x 8 Gy) totaling 40 Gy (4 MV photons). Proton (^{1}H) and helium (^{3}He) imaging was performed in vivo 12–30 weeks after irradiation. ^{3}He was polarized by spin-exchange [1]. Rats were imaged in a dual-frequency birdcage coil at 2 Telsa. Breathing gas and HP ^{3}He were delivered with an MR-compatible ventilator [2]. Images were acquired during brief (400 ms) periods of held-breath after full inspiration and during end-expiration. A radial projection sequence was used (TE = 900 micro-sec, TR = 20 ms, and 20 views per breath). For the diffusion images, the sequence cycled through a series of 5 bipolar gradients from 0 to 16 Gauss/cm (weighting 0 to 9.4 s/cm^2). ADC maps were calculated pixel-by-pixel using a non-linear, least-squares fitting routine. Finally, lungs were fixed for histology.

Results

After right, hemithoracic radiation, proton signal intensities were greater in the right lung, suggesting an overall lower gas density than in the left lung related to the presence of fibrosis in the right lung [3]. Fibrosis was confirmed present in the lung by conventional histology. The graph shows left to right lung differences in ADCs. In controls (N=4), the difference is close to zero, while at more than 20 weeks post-radiation (N=4), the differences at both lung volumes were significantly different from controls (HB, P = 0.04; End-Ex, P = 0.01). At both lung volumes, ADCs in the injured lungs were smaller than the left lung. The greater restriction of diffusion in the right lung reflects the reduced alveolar volumes related to fibrosis.

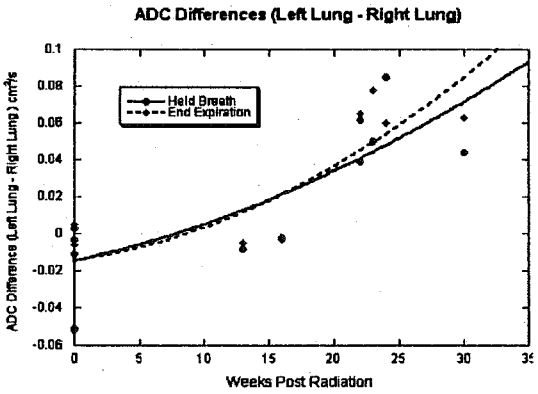

Discussion

On proton images, there were slight increases in signal intensity in the right lung without clear morphologic defects. In contrast, ADC maps generally showed the injured lung to have smaller ADCs than the uninjured lung. This finding is consistent with the reduced alveolar volumes associated with fibrosis in the radiated lung and is in contrast to the generally elevated ADC in the emphysematous lung associated with enlarged gas spaces. The results demonstrate that hyperpolarized ^{3}He imaging is a useful tool to study lung injury in small animal models.

References

[1] X. Josette Chen, Laurence Hedlund et al., *PNAS* **97**, 11478-11481 (2000).
[2] Laurence Hedlund & G. Allan Johnson, *ILAR Journal* **43**, 159-174 (2002).
[3] Zeljko Vujaskovic, I. Batinic-Haberle et al., *Free Radical Biology & Medicine* **33**, 857-863, (2002).

Acknowledgements Funding from: NIH/NCRR P41 05959, NIH/NCI/SAIRP R24-CA92656, and Varian Medical Systems

Simultaneous MRI of Hyper-Polarised ^{3}He and ^{129}Xe in Lungs

R.H. Acosta[1], S. Han[1], P. Blümler[1], S. Appelt[2], H. W. Spiess[1]
[1] Max Planck Institute for Polymer Research, 55128 Mainz, Germany
[2] Research Center Jülich, Zentrallabor für Elektronik, 52425 Jülich, Germany

In the last years there is a growing interest in the application of LASER-polarised noble gases in clinical imaging, particularly for the study of the otherwise 'invisible' air spaces in the lung. Different authors use ^{3}He or ^{129}Xe for this purpose. Even though both nuclei are suitable for this studies, they posses unique characteristics that makes them very different in their applications. ^{3}He has a high gyromagnetic ratio, thus providing high sensitivity. Polarization up to 90% can be achieved and it has no physiological effect [1]. On the other hand, ^{129}Xe has a low diffusion coefficient and is lipophilic, it perfuses and dissolves in the blood and even acts as an anesthetic and has a large chemical shift range [2]. From the clinical point of view ^{3}He is ideal for detailed observation of the anatomy of the lung, pore size determination (via self diffusion) and O_2 concentration (via paramagnetic relaxation). ^{129}Xe is suited for functionality and perfusion studies, the gas absorbers in blood, a process which can be accurately monitored through it's chemical shift. The very different gyromagnetic ratio of both gases easily allow double-resonance experiments and hence simultaneous excitation and detection, in this way the information provided by each nuclei can be obtained in a single experiment. In this work we report first attempt to image both isotopes in a gas mixture simultaneously in a phantom and in animal lungs. For this purpose both gases have to be hyper-polarised [3,4] and suitable partial pressures have to be chosen to compensate the very different signal-to-noise ratios.

The investigation of lungs with MRI methods require extensive procedures when performed on living animals (anesthesia, triggering of heart and breathing rate). On the other hand it is unlikely that one inhalation is exactly identical with the next. For sequence development one wishes to have a simple, static and reproducible model of a lung, which has an almost identical fractal morphology down to the size of the alveolae. We also present the procedures for the fixation of entire lungs of small rodents up to pigs. Therefore the lung/heart complex is excorporated and filled with various liquids for fixation using a lower pressure on the outside. Finally it is dried and can be stored in a non-collapsed state of inhalation. Light-, SEM-Microscopy and MRI techniques using hyperpolarised ^{3}He were employed to verify the intact state of the alveolae on a microscopic level and the morphology of the entire lung.

References

[1] M. Ebert, T. Grossmann, W. Heil, W. E. Otten, R. Surkau, M. Leduc, P. Bachert, M. V. Knopp, L. R. Schad, M. Thelen, *Lancet* **347**(9011) (1996) 1297-1299.
[2] M. S. Albert, G. D. Cates, B. Driehuys, W. Happer, B. Saam, C. S. Springer, A. Wishnia, *Nature* **370** (1994) 199-201
[3] J. Becker, W. Heil, B. Krug et al., *Nucl. Instr. and Meth. A* **346** (1994) 45
[4] S. Appelt, A. B. Baranga, C. J. Erickson, M. V. Romalis, A. R. Young, W. Happer, *Phys. Rev.* A **58**(2) (1998) 1412-1439.

Imaging Lung Tissue is not so Difficult

Dean O. Kuethe, Rebecca Montaño, Natalie Adolphi
New Mexico Resonance, Albuquerque, NM, USA

Introduction

Presentations about imaging lungs with NMR often begin with a statement like, "Lungs are difficult to image because of low proton spin density and inhomogeneous magnetic fields due to water-air interfaces." We don't believe it anymore. Lungs are a broadband sample, and when we use a broadband technique to image them, the remaining problem is not lack of signal, but lack of receiver dynamic range. Computers have improved, so that making large 3D Fourier projection images is now within the capabilities of a personal computer, and a reasonable approach to imaging lungs is to make a detailed 3D image of the entire thorax using FID-projection imaging.

Our immediate purpose is to study models of inflammatory lung diseases in small rodents, but there appear to be applications to pulmonary medicine. Small airway inflammation has been implicated in the etiology of chronic severe asthma, but there is currently no way to locate it in patients. X-ray CT can image the lungs spectacularly, but can not tell inflamed tissue from healthy. NMR imaging is usually good at this distinction. Likewise, MRI may outperform X-ray CT at telling whether a lung nodule is cancerous or benign.

Methods

Our pulse sequence is a modification of the one we use to image SF_6 gas ($T_2 = T_2^* = T_1$, about 1 ms) in lungs of rats and uses hard RF pulses, in the presence of 45 mT/m imaging gradients. For each FID, we sample 512 data at 1 MHz, which is sufficient brevity to image whatever has a T_2^* of 100 μs or longer, and sufficient oversampling to compute projections with an appropriate Fourier-like transform, despite incomplete data due to RF dead time. A 6.7 ms repetition time allows for spoiling gradient pulses. One degree flip angles provide a spin density image. Twelve degree flip angles provide a T_1-weighted image. Because of programming limitations of our Tecmag Libra console, it takes us 30 minutes, rather than five to obtain the 14308 independent gradient directions for a 150-cubed pixel Fourier projection image of a rat thorax. We collect data during the 40% of the respiratory cycle when the lungs are full. With an echo time of zero, the pulse sequence is inherently motion-compensated, and at our current resolution of 0.5 mm, cardiac gating is not necessary. This imaging technique could be implemented on a clinical scanner with minor changes in hardware and software.

Results

Figure **1a** shows four planes of the 56 by 64 by 88 pixel, lung-containing subsection of a 150-cubed pixel T_1-weighted image of the thorax of a 630 g rat with acute inflammation caused by instilling lipopolysacharide from pseudomonas bacteria into its trachea 2 days prior to imaging. Figure **1b** shows the corresponding frames of the spin-density image. Figure **2** shows similar frames of similar images of a healthy rat for comparison. Note that the lung tissue and ribs have substantial signal compared to the gas space in the trachea and major bronchi, indicating we are indeed imaging tissues with short T_2^*. The comparison of spin density and T_1-weighting may be effective at differentiating diseased tissue.

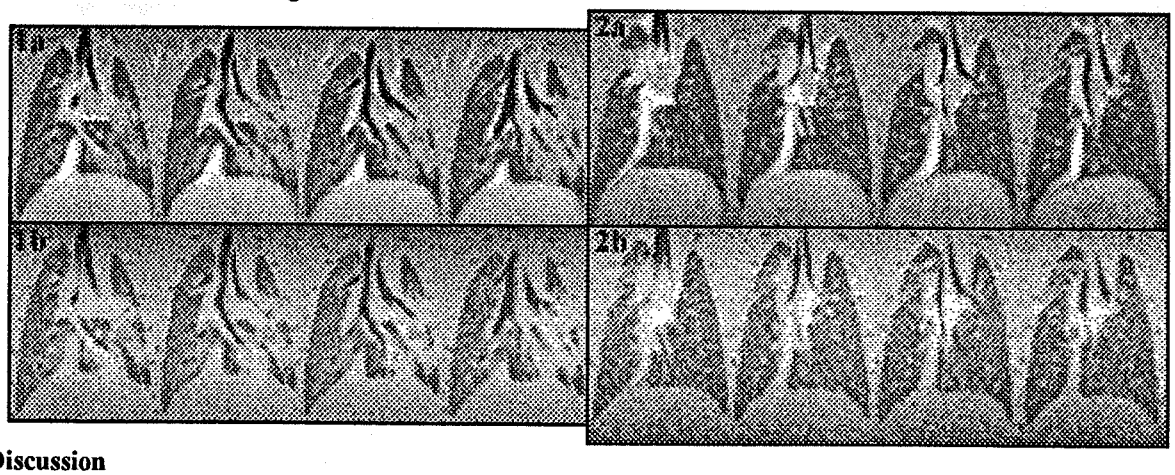

Discussion

Not too bad, eh?

First T_1 Images of Inert Fluorinated Gases in Lungs

Natalie Adolphi,*# Dean Kuethe#
*Knox College, Galesburg IL 61401, USA
and #New Mexico Resonance, Albuquerque NM 87106, USA

Introduction
The T_1s of some inert fluorinated gases (e.g. SF_6, CF_4, C_2F_6) are dominated by the spin-rotation interaction, mediated by molecular collisions, and are very predictable. Among other things, the T_1s can measure gas composition, because collisions with less massive molecules, like O_2 and CO_2, are less effective mediators. One application is that the T_1 of C_2F_6 or SF_6 in lungs will be a monotonic function of ventilation-to-perfusion ratios (V/Q), and imaging T_1 would thus provide map of gas exchange in lungs. One advantage over our prior method of mapping V/Q with spin density images of SF_6 [1] is that the T_1 imaging method allows the subject to breath an O_2 rich gas mixture during the entire procedure. The spin density method requires a reference image made while breathing a normal O_2 concentration, which would be most unpleasant for some pulmonary patients.

Methods
We set out to develop a modified Look and Locker [2] T_1 imaging sequence, in which a series of low angle pulses, following an inversion pulse, monitors the recovery. With the aid of a computer simulation, the pulse sequence parameters (number of pulses, tipangles, lengths of delays, etc.) were adjusted to yield the lowest standard deviations of the T_1s using the least experimental time. We find that because our sample (a gas) has inherently low S/N, the most effective "low angle" pulses are actually not very low (~ 45°), and their depletion of longitudinal magnetization **M** must be entered into the calculation of the recovery curve (which no longer has the shape of a standard inversion-recovery curve). In a sense, our pulse sequence falls somewhere between a Look-Locker sequence with very low-angle pulses (which inspects **M** without changing it) and a traditional Inversion-Recovery sequence (which *completely* alters **M** prior to each inspection pulse). Additionally, the simulations demonstrate that using medium-angle inspection pulses is most effective in conjunction with relatively long delays (comparable to T_1) between pulses. In our T_1 sequence, information is gleaned not only from the recovery from inversion, but also from the recovery from the inspection pulses themselves. Thus we obtain useful information from delays that are longer than would be optimal if **M** were recovering only from inversion. Most important, longer delays mean that there is enough time between pulses to collect good quality data from the faster-relaxing SF_6 (with T_1s in lung of ~0.9-1.6 ms). Imaging the T_1 of SF_6 reduces the experimental time by a factor of ~3 compared to imaging C_2F_6 (with T_1s in lung of ~4-7 ms).

Results
We have obtained a number of T_1 images of C_2F_6 and SF_6 mixtures in bundles of sealed test tubes and in rat lungs demonstrating the effectiveness of the pulse sequence. To our knowledge, the latter are the first T_1 images of inert fluorinated gases in a porous medium. We discovered an interesting feature of the T_1 sequence from our first T_1 image of C_2F_6 in lung. For this image, the rat breathed an 80% C_2F_6-20% O_2 mixture in order to have the *same* T_1 for all lung pixels.[1] We were surprised to find that the noisiest pixels in the T_1 image had a higher average T_1 than the least noisy pixels. Through further simulations, we confirmed that recovery data with insufficient S/N biases the T_1 results. Evidently, noisy recovery curves look "flatter" to the curve-fitting program and tend to yield higher T_1s. The simulations further indicate there is a threshold S/N level necessary to avoid the bias problem.

References
[1] D.O. Kuethe et al, 'Imaging obstructed ventilation with NMR using inert fluorinated gases,' *J. Appl. Physiol.* 88:2279-86 (2000).
[2] D.C. Look and D. R. Locker, 'Time saving in measurement of NMR and EPR relaxation times,' *Rev. Sci. Instrum.* 41:250-1 (1970).

MR Microscopy of an Exogenous ALS-PDC Mouse Model: High-Resolution T_2^*- and Diffusion-Weighted Imaging at 17.6 T

S.C. Grant[1], J.M. Wilson[2], M.S. Petrik[2], S.J. Blackband[1] & C.A. Shaw[2]
[1]Department of Neuroscience, University of Florida, Gainesville, FL 32610, USA
[2]Department of Ophthalmology & Neuroscience Programme, University of British Columbia, Vancouver, BC V5Z1L8, Canada

Introduction

The progressive human neurological disease Amyotrophic Lateral Sclerosis-Parkinsonism-Dementia Complex (ALS-PDC) has been linked to the consumption of seeds from the cycad palm tree (*Cycas micronesica K.D. Hill*), particularly in the populace of Guam [1]. Recently, similar *in vivo* neurodegeneration has been induced in an animal model through cycad feeding [2]. Specific cortical and subcortical cell losses were measured with histologically stained two-dimensional sections. In this study, ^{1}H MR images of intact, excised brains and spinal cords were acquired at resolutions of at least 50 microns through the use of optimally constructed RF coils and a 17.6-T microimaging system. Using T_2^* and diffusion contrast, these three-dimensional images were used to examine the effects of ALS-PDC induced anatomical changes in a mouse model.

Methods

Adult CD-1 mice were fed washed cycad as part of their normal diet for two months and showed behavioral deficits resembling those seen in ALS-PDC patients. Following their two-month diet, animals were perfusion-fixed and sacrificed. Intact brains and spinal cords were excised and maintained in 4% paraformaldehyde until examination. Tissue was scanned at the University of Florida using an optimally constructed split-ring resonator interfaced with a Bruker 17.6-T magnet and Micro2.5 imaging system. T_2^* scans were acquired using a true 3D gradient echo sequence at an isotropic resolution of 41 microns in five hours. T_2 and diffusion-weighted images were acquired using multi-slice, 2D spin echo sequences at resolutions of better than 50x50x300 microns in less than 2.25 hours. Datasets then were analyzed using 3D visualization and processing software packages (Amira 3.0 and IDL), allowing select areas of interest to be measured with respect to volumetric and contrast changes. In total, 4 groups of animals (n=4 per group) were examined: flour-fed; cycad-fed; flour-fed, stem cell-treated; and cycad-fed, stem cell-treated.

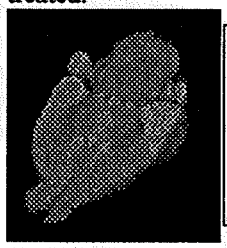

Figure 1: 3D GE image of cycad brain acquired in five hrs at $(41\text{-}\mu m)^3$ resolution.

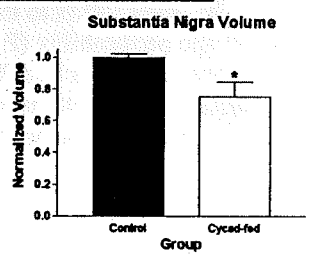

Figure 2: Example comparison of the volume differences in the substantia nigra between control and cycad groups (*$p<0.001$)

Results

Cycad-fed mice showed significantly decreased substantia nigra, striatum and olfactory bulb volumes. Cycad-fed mice also showed decreased cortical thickness. Additionally, diffusion results (including tensor analysis) demonstrate changes in white matter regions of the brains and spinal cords of cycad-fed mice, which may indicate an alteration in axonal tracts resulting from ALS-PDC pathology.

Conclusions

MR microscopy is easily sensitive enough to measure degeneration in an early stage model of this progressive neurological disease. Additionally, volumetrics and diffusion analysis demonstrate great potential in tracking the progression of ALS-PDC. In future investigations, these MR microscopic techniques will be used as a diagnostic tool for *in vivo* examinations of ALS-PDC in animal models.

References

[1] L.T. Kurland, *Trends Neurosci.* **11**, 51-53 (1988).
[2] J.M.B. Wilson, et al, *NeuroMolecular Med.* **1**, 207-221 (2002).

Water permeability of capillaries in the SFO of rats determined by T_1 relaxation time measured by ^{1}H MRI.

Y. Seo[1], A. Takamata[2], T. Ogino[3], H. Morita[4], M. Murakami[5]
[1]Department of Physiology, Kyoto Prefectural University of Medicine, Kyoto 602-0841, Japan; [2]Department of Environmental Health, Nara Women's University, Nara 630-8506, [3]Department of Biochemistry and Cellular Biology, National Institute of Neurosciences, NCNP, Kodaira, 187-8502, [4]Department of Physiology, School of Medicine, Gifu University, Gifu 500-8705, Japan; [5]Department of Molecular Physiology, National Institute for Physiological Sciences, Okazaki 444-8585, Japan

Introduction: The subfornical organ (SFO), one of the circumventricular organs (CVO), has been characterized as a region of the brain with permeable capillaries, and it might be a part of the sensory system involved in the body fluid homeostasis especially on the osmolarity of serum. However, no direct observations on the water permeability of capillaries in the SFO have been reported. In order to measure the water permeability in the SFO in situ, we applied ^{1}H MRI and a relaxation reagent: Gd-DTPA^{2-}.

Materials and Methods: ^{1}H MR images of anesthetized Wister rats were obtained by a Bruker BioSpec spectrometer (ABX-4.7/40) with a home-built surface coil. T_1-weighted gradient-echo image (TR/TE = 100/4.2 ms) and an inversion-recovery fast-image (Fast-T_1 MRI) with RARE factor of 16 were obtained before and after Gd-DTPA^{2-} infusion (1.5 - 2.0 mmol/kg body weight).

Results and Discussion: 1) Detection of water permeable sites: Typical sagittal T_1-weighted MR images before and under the steady state of Gd-DTPA^{2-} intravascular infusion are shown in Figs. a and b, respectively. The SFO area was clearly imaged as high signal intensity (arrowhead) under the Gd-DTPA^{2-} infusion. As shown in the mid sagittal section of a 3D-angiography with a vascular contrast reagent, AMI-227 (Fig. c), arteries and veins were clearly depicted in high signal intensity, but there are no detectable vessels in the SFO area. These results suggested that the capillaries in the SFO have higher permeability compared with the blood-brain barrier (BBB) in the cortex and thalamus. **2) Capillary permeability of Gd-DTPA^{2-}:** The anatomical compartment of Gd-DTPA^{2-} is essential for determining the water permeability: whether or not Gd-DTPA^{2-} could cross the capillaries in the SFO. The intensity of the T_1-weighted images of the SFO, cortex and thalamus were measured sequentially. After the Gd-DTPA^{2-} injection the image intensity in the SFO increased by 60%. When the BBB was broken by the bolus injection of 25% of mannitol via ICA, the image intensity in the SFO increased again, and this increase was continued after the transient changes induced by the mannitol injection. Image intensities in the cortex and thalamus were maintained at their original intensities before the BBB breakdown, but they were also increased very sharply by the mannitol injection. The breakdown of the BBB allows the Gd-DTPA^{2-} leaked out into the extravascular space in the cortex, thalamus and SFO. If the capillaries in the SFO were permeable to the Gd-DTPA^{2-}, we should not observe this additional increase in the image intensity in the SFO. Therefore, we concluded that Gd-DTPA^{2-} stays in capillaries in the SFO. **3) Estimation of water permeability:** The $1/T_1$ before and after Gd-DTPA^{2-} infusion were 0.70 ± 0.02 s^{-1} (mean ± SEM, n=9) and 1.53 ± 0.11 s^{-1} (n=9), respectively. The rate constant for water influx to the capillaries was estimated to be 0.84 ± 0.11 s^{-1} (n=9) which corresponds with a diffusive membrane permeability (P_d) of $3.7 \cdot 10^{-3}$ cm s^{-1} on an assumption of the two-compartment exchange model. This P_d value of the capillaries in SFO was the same order as that of transmembrane permeability of water of the vasa recta, and it may be 10 - 100 times larger than that of the BBB in the cortex. From these results, we conclude that the capillaries in SFO have one of the highest water permeability values among all of the capillaries in the brain.

Figure 1: a, b) T_1-weighted MRI of rat brain. The arrow-head points the SFO. c) 3D-angiography.

MR microscopy of a large human embryo collection (Kyoto collection) using a four-channel super-parallel MR microscope at 2.34 T

Yoshimasa Matsuda[1], Shinya Ono[1], Tomoyuki Haishi[2], Katsumi Kose[1]
[1]Institute of Applied Physics, University of Tsukuba, Tsukuba, 305-8573, Japan,
[2]MRTechnology Inc, Tsukuba, 305-2642, Japan

Introduction

Kyoto University has a large human embryo collection (~50,000), which were collected from 1961 to 1974 [1]. Since such a collection will never be obtained again, their nondestructive measurements are highly desired. Thus, Kyoto University and Tsukuba University have stared to take 3D MR microscopic images of about 4,000 embryos in two years to make an anatomical database of human embryos (the Kyoto 4,000 Human Embryo 3D Visualization Project). To acquire a large number of MR microscopic images efficiently, we have developed four- channel super-parallel MR microscope using a 2.34T/40cm superconducting magnet [2].

Four channel super-parallel MR microscope

The four-channel super-parallel MR microscope consists of a four-channel array probe and four-channel 100 MHz MRI console (Figure.1). The array probe consists of four gradient probe units. The RF probes are exchangeable and 16 mm inner diameter solenoid RF coils were used for the present experiments. The four-channel MRI console consists of an industrial PC for digital control and data acquisition, four-channel 100 MHz transceiver, gradient driver, and eight-channel wideband (10-200 MHz) class AB gated transmitter.

Experiments

Experiments were performed using a 2.34T/40cm superconducting magnet (homogeneous region: 16 cm dsv). Four 3D images human embryos (21st Carnegie stage) were simultaneously acquired using a 3D spin echo sequence (TR=100ms, TE=10ms, NEX=16).

Results and discussion

Figure 2 shows 2D cross-sectional images selected from 3D image data sets of the human embryos. The image matrix is 128 x 128 x 256 and the voxel size is 120 micron cubed. By optimizing the diameter of the RF coil, much higher spatial resolution could be obtained for smaller embryos. Because we are now measuring eight embryos every day, 4,000 embryos can be measured in 500 days (two years).

Conclusion

A four-channel super-parallel MR microscope was developed for 3D MR microscope of 4,000 human embryos in two years. It was demonstrated that the system had a sufficient performance for the two years' project.

References

[1] Hideo Nishimura, Kiichi Takano, et al. *Teratology*, 1 281-290(1968).
[2] Yoshimasa Matsuda, Shin Utzuzawa, et al., A Super-parallel MR microscope, *Magnetic Resonance in Medicine*, in press, (2003).

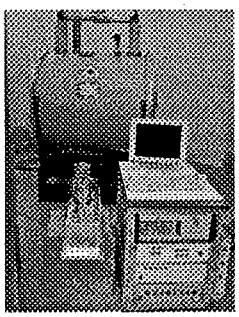

Figure 1: Overview of 4CH SPMRM.

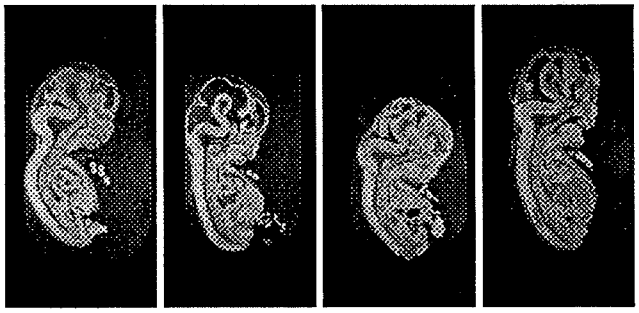

Figure 2: 2D Cross sectional images selected from 3D image data sets of 21st stage human embryos

Central nervous system in vivo MR microscopy at 17.6 T

T. Weber[1,2], T. Neuberger[1], V. Behr[1], I. Wieland[1], U. Bogdahn[2], A. Haase[1], A. Steinbrecher[2] and C. Faber[1]

[1] Experimentelle Physik 5, Institute of Physics, University of Würzburg

[2] Department of Neurology, University of Regensburg

Introduction

The most limiting parameter in MR imaging is the signal-to-noise ratio (SNR). For this reason imaging is performed at increasingly high field strengths. A higher B0 field strength is also accompanied by other effects as longer T1 relaxation times and decreased T2 and T2* relaxation times which reduce the SNR improvements. The quantification of these in vivo relaxation times is necessary for optimal sequence design.

Objects and Methods

MR imaging general

Imaging experiments were conducted on a Bruker Avance 750WB system at 17.6 Tesla. The maximum gradient strength in the animal gradient system was 200 mT/m with a rise time of 180 µs.

Brain

For brain imaging a 38 mm birdcage resonator was used. After initial tests two sequences were selected for imaging. Best contrast could be achieved with a Turbo Spin Echo method with an effective echo time of 20 ms and repetition time of 5 s. The spatial resolution was 117 µm in-plane at a slice thickness of 500 µm. T1, T2 and T2* relaxation times were quantified with an Inversion Recovery Snapshot Flash, a multi spin echo sequence, and with a multi gradient echo sequence, respectively.

Spinal cord

For the acquisition of spinal cord data a surface coil was used. To avoid artefacts caused by blood flow and respiratory motion both ECG triggering and breath gating were applied. A multi-slice 2D gradient echo was used with an echo time of 3.5 ms and a repetition time of approximately 200 ms depending on the heart rate. After each heart beat signal was detected for all slices acquired, i.e., every slice had a different trigger delay. During breathing periods no signal was detected.

Animal preparation

Female Fisher and DA rats, for brain and spinal cord imaging, respectively, were anesthetized with 2% isofluorane with Carbogen (95 % oxygen and 5 % carbon dioxide) as respiratory gas.

Results

Multi-Slice Turbo Spin Echo images with an in-plane resolution of 117 µm and 500 µm slice thickness allowed identification of fine structures within the brain. Data on in vivo relaxation time measurements are presented for the first time at this field strength.

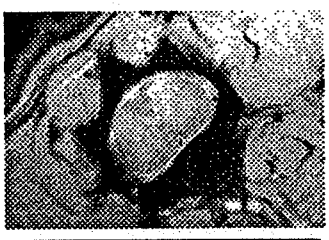

Figure: 2D gradient echo of *in vivo* rat spinal cord

MR images of the lumbar part of the spinal cord could be acquired without motion artefacts at an in-plane resolution of 69x69 µm² and a slice thickness of 500 µm. Gray and white matter can be clearly distinguished with an SNR of approximately 17 in gray matter and approximately 12 in white matter, respectively.

Discussion

With the achieved spatial resolution in both brain and spinal cord imaging it will be possible to do time course studies of most central nervous system disease models. Relaxation time measurements allow an optimization of the pulse sequences in order to achieve a better CNR. Especially the detections of spinal cord lesions will be greatly eased due to resolution improvements – as compared to studies performed at lower fiefld strengths.

Diffusion and displacement analysis in heterogeneous, multicompartment, (bio-)systems by PFG-Multi-Echo NMR/MRI

Henk Van As, Daniel Polders, P. Adrie de Jager, Frank J. Vergeldt.
Department of Biophysics and Wageningen NMR Centre, Wageningen University, 6703 HA Wageningen, The Netherlands

Introduction
^{1}H NMR and MRI relaxometry and diffusometry are commonly used to investigate the physical properties of water in biological tissues and in many other heterogeneous systems and materials of practical importance. Most of these studies attempt to assign the experimentally observed diffusion- or relaxation components to different (sub-)cellular compartments within such tissue. From these parameters one can extract valuable information on the diffusion constant in the compartments, the (relative) water fractions, the compartment dimensions, and the water membrane permeability of the membranes separating the compartments. The interpretation of these diffusion measurements in such heterogeneous (bio)systems strongly depends on the discrimination of (homogeneous) fluid fractions. Combined PFG and Multi-Echo sequences have been used for this purpose, both experimentally in non-imaging and imaging mode and via simulations. A two-dimensional data set is obtained which can be analyzed in different ways.

Different analysis approaches
In non-imaging mode differences in relaxation time behaviour can be used for Diffusion or Displacement Analysis by Relaxation Time Separation (DARTS) [1]. The amplitude of a fraction corresponding to a specific relaxation time can now be analyzed as a function of b-factor or in a q-space spectrum to obtain the self-diffusion coefficient, D, or information based on the displacement spectrum. T_2 analysis is either based on CONTIN or SPLMOD. CONTIN results are very sensitive to S/N, which is a problem in PFG experiments. SPLMOD is a problem in heterogeneous systems, due to the spreading of T_2 values.
Recently an efficient and stable Fast Laplace Inversion (FLI) algorithm has been introduced to transfer correlated diffusion and T_2 measurements into a 2D correlation plot [2,3]. No *a priori* knowledge about the number or distribution of fractions is necessary.
PFG-ME simulations have been performed to investigate the effect of exchange in a realistic concentric cylindrical two compartment model for both plant and animal tissue. The resulting 2D data sets were used to solve the question in what way the observed parameters $T_{2,app}$, D_{app} (CONTIN, SPLMOD and FLI as a function of G, Δ and S/N) and the intensities of the different echoes or the amplitude of a fraction corresponding to a specific relaxation time as a function of b-factor or in a q-space spectrum are affected and in how far (and in what way) combined diffusion and relaxation time measurements allow to separate signals into a set of multi-compartment sources. FLI resulted in very promising results, even at a low S/N in the order of 10, a realistic value for a single pixel in an image. This is illustrated by PFG-ME imaging results of plants.
At increasing diffusion labeling time restricted or hindered diffusion has been observed in these systems. If exchange between fractions is present one observes that at sufficient long labeling time the differences in diffusion between the compartments average out to a certain amount due to exchange. On the other hand, if fast exchange with respect to T_2 is present, resulting in averaging out the T_2 over the system, the different D values can still be observed at short Δ values. Increasing Δ results again in observation of restiction effects, which are diffently manifest in q-space and FLI correlation plots.

References
[1] van Dusschoten D, et al, *Jornal of Magnetic Resonance A* **116**, 22-28 (1995).
[2] Venkataramanan, L, et al, *IEEE Transaction on Signal Procession* **50**, 1017-1026 (2002)
[3] Hürlimann, M.D., et al, *Journal of Chemical Physics* **117**, 10223-10232 (2002).
[4] van der Weerd L, et al, *Journal of Magnetic Resonance* **156**, 213-221 (2002).

Improving the spatial point spread function in magnetic resonance microscopy using variable-time phase encoding

A.G.Webb
Physikalisches Institut EPV, Universität Würzburg, Am Hubland, Germany

The acquisition of extremely high spatial resolution in magnetic resonance microscopy requires both high sensitivity RF microcoil detectors and very large magnetic field gradients. For such experiments multi-dimensional phase-encoding is often used since it has signal-to-noise advantages over frequency encoding due to the small associated acquisition bandwidth [1]. For a 1-D phase encoding sequence, the signal S(G) can be expressed by:

$$S(G_y,t_{enc}) = \iiint \rho(x,y,z)\exp(-jyG_y yt_{enc})\exp\left(-\gamma^2 DG^2 t_{enc}^3/3\right)\exp(-TE/T_2^*)dxdydz$$

where t_{enc} is the phase encoding time, and D is the diffusion coefficient. The term from diffusional attenuation corresponds to a blurring in the spatial domain given by the point spread function (PSF) H(x) [2]:

$$H(x) = \exp\left(-3x^2/4Dt_{enc}\right)$$

with spatial full-width-at-half-maximum (FWHM) given by $\Delta x = 1.92\sqrt{Dt_{enc}}$. Smaller values of t_{enc} result in higher spatial resolution, but the minimum value of t_{enc} for a given spatial resolution is limited by the value of G_{max}. The use of a variable phase encoding time, using a constant gradient value of G_{max} for each step, reduces the blurring function for the data acquired at the center of k-space. Preliminary simulation results are shown below for a linear decrease in encoding time as a function of phase encoding step. Data acquisition corresponds essentially to that of the original Fourier imaging sequence proposed by Kumar et al. [3], but the effects of t_{enc} on spatial resolution are only apparent for high resolution microimaging. The sequence is also constant-time, in that a variable delay is included after phase-encoding before data acquisition. Both gradient- and spin-echo versions of the sequence can be run. Although small side-lobes are introduced into the spatial PSF due to a convolution with a sinc-squared function, the reduction in the FWHM more than compensates for this effect.

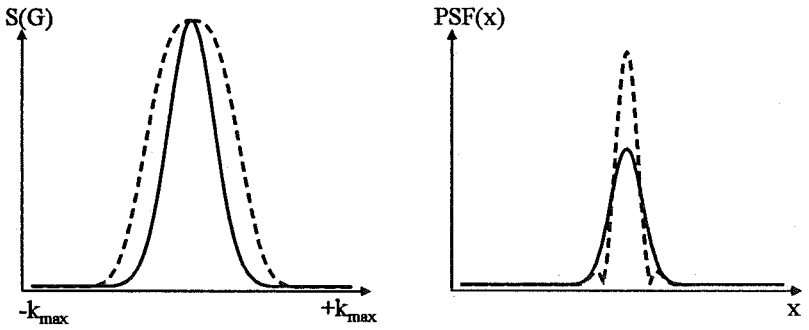

(left) Signal attenuation from diffusion as a function of k-space during the phase encoding gradient. The solid line corresponds to conventional phase encoding, and the dotted line to keeping the gradient value fixed at G_{max} and adjusting the encoding time to cover the same Cartesian k-space matrix. (right) Corresponding point spread functions in the spatial domain. Simulation parameters: field-of-view 500 μm, 256 data points, G_{max} 2 T/m.

References.

[1] L.Ciobanu, A.G.Webb and C.Pennington, *Prog.NMR.Spectroscopy,* in press 2003.
[2] E.W.McFarland and A.Mortara, *Magn.Reson.Imaging*, **10**, 279-88 (1992).
[3] A.Kumar, D.Welti and R.R.Ernst, *J.Magn.Reson.* **18**, 69 (1975).

Exo-MRI

Pablo J Prado, Serge Bobroff
Quantum Magnetics, 15175 Innovation Dr, San Diego, CA 92128, USA

Single Sided MRI Probe Head

MR measurements are currently carried out with mobile single-sided probes [1,2]. Rendering three-dimensional images from a sensitive volume entirely outside an MRI scanner facilitates non-invasive testing and diagnosis.

A small single-sided MRI probe head has been developed at Quantum Magnetics. The new MRI probe features a tailored Neodymium Iron Boron permanent magnet array, producing flat surfaces of constant magnetic field (Figure 1). Depth resolution is achieved by automatically shifting the resonance frequency of a dedicated RF coil over a wide range. Both the RF coil and the receiver protection circuit (quarter lambda) are retunable in few milliseconds.

The open-face MRI device [3] was designed using a light probing head and a reduced stray field configuration. The single-channel probe is connected to a control unit using a flexible shielded multi-conductor cable.

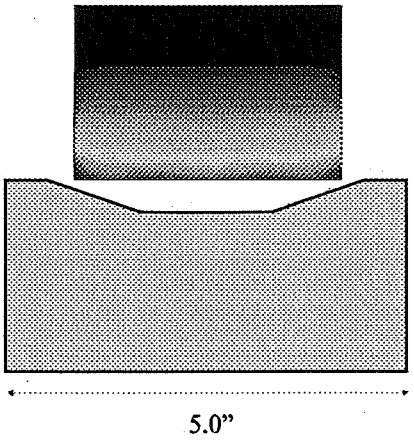

Figure 1: Permanent magnet array. Static field distribution. Field drops to 20% in 40 mm

Imaging with a Single Sided MR Scanner

The MR probe unit has been designed to house gradient sets (Figure 2) to further extend the image capabilities for in-plane spatial resolution [4].

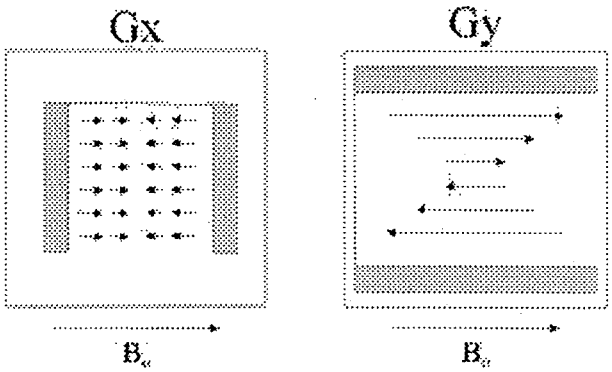

Figure 2: Sketch of the field generated by the two sets of gradient coils.

3D images are rendered with a series of 2D images, corresponding to the selected depths.

The local gradient, inherent from the magnet array, varies from 1400 G/cm to 260 G/cm in the first 40 mm away from the coil. A single sided MRI laboratory prototype system has been tested; automatically rendering depth profiles down to 20 mm. Depth resolution of about 100 microns is achieved by slice selection using the controlled frequency shifting circuit.

The in-plane spatial resolution is achieved with phase encoding methods, using two sets of gradient coils. A standard 2D FT is then applied at each depth.

<u>References</u>

[1] Rollwitz WL. *Agricultural Engineering*, **66**, 12 (1985).

[2] B. Blümich, et al., *Magn. Reson. Imaging*, **16**, 479 (1998).

[3] P.J. Prado. *Magn. Reson. Imaging* (2003)

[4] P.J. Prado, B. Blümich, and U. Schmitz. *J. Magn. Reson.* **144**, 200 (2000).

Optimisation of indirect detected ^{13}C spectroscopy and micro imaging experiments for *in vivo* applications in plants

Davide Santoro, Walter Köckenberger
Magnetic Resonance Centre, School of Physics and Astronomy, University of Nottingham, Nottingham, NG7 2RD, UK

Abstract
The use of the stable isotope ^{13}C in *in vivo* NMR experiments has great potential for studies of metabolic pathways and metabolic conversion rates in biological systems. However, these studies are frequently limited by the low NMR sensitivity of direct ^{13}C detection. A possible solution to this is the use of indirect detection schemes, such as cyclic cross polarisation (CYCLCROP [1]) where polarisation is transferred in two modules: from the protons to the ^{13}C nuclei and then, after a module that saturates all the residual ^{1}H resonance lines, from these ^{13}C nuclei back to the protons. Such technique allows the detection of ^{13}C nuclei with a sensitivity comparable to that of conventional proton- NMR experiments and therefore combines the high sensitivity of ^{1}H NMR with a high chemical selectivity due to the high chemical shift dispersion of ^{13}C nuclei .

Here we present a detailed analysis of the detection efficiency for three possible polarisation transfer modules under *in vivo* conditions: a) INEPT (Insensitive Nuclei Enhanced by Polarisation Transfer [2]) b) CP (Hartmann-Hahn Cross Polarisation experiment [3]) c) PRAWN (Pulse Rotating frame trAnsfer sequence with WiNdows [4]) .

We performed computer simulations (based on the Spin-Operator formalism and random walk models) of the three sequences to estimate the attenuation of the transfer induced by diffusion through strong B_o field gradients. In plant tissue such gradients are generated by susceptibility differences between the intercellular spaces filled with air and the water within the cells. Our simulations also estimate the attenuation induced by a mismatch of the H-H condition for the sequences based on polarisation transfer in the rotating frame. The predictions of the simulations were verified on phantom samples with polystyrene micro-spheres.
On the basis of the simulation results and of the *in vitro* experiments we have chosen the PRAWN sequence, optimizing its parameters for the best transfer efficiency, for the editing part of our imaging experiments on castor bean seedlings [5] .

In order to improve further the SNR, a multi-echo acquisition scheme has been implemented in the imaging module. Such CPMG-likes scheme consist of a train of π-pulses in which consecutive echoes are acquired. The spin-echo signal is selected through phase cycling, without the need of spoiling gradients which would attenuate the signal intensity.
In order to reduce the experimental time of the *in vivo* images a k-space weighted acquisition by a Hanning function has been applied: this allowed the acquisition of an image of the plant with a matrix size 64 by 64 and a nominal resolution of $\sim$ 110 μm within $\sim$ 48 mins, averaging at the centre of k-space up to 256 acquisitions, with no substantial artifacts introduced by the windowing.
Adding a Pulsed Gradient Spin Echo module after the polarisation transfer allowed us to measure the mobility of the sucrose molecules within the plant *in vivo*.

References
[1] C. Kunze and R. Kimmich, *JMR* B **105,** 38 (1998).
[2] G. A. Morris and R. Freeman, *J. Am Chem. Soc.* **101,** 760 (1979).
[3] S. R. Hartmann and E. L. Hanh, *Phys. Rev.* **128,** 2042 (1962).
[4] N. Chandrakumar and R. Kimmich, *JMR* **137,** 100 (1999).
[5] M. Heidenreich et al., *JMR* **132,** 109 (1998).

In vivo ^{31}P MRI monitoring of gene expression in yeast cells

Buntoku Sugihara, Hidehito Tochio, Masahito Morita, Sewon Ki, Azusa Okada,
Tetsuro Kokubo, Masahiro Shirakawa
Graduate School of Integrated Science, Yokohama City University, Tsurumi, Yokohama 230-0045, Japan

Introduction

Whole genome sequencing of many organisms is providing a vast number of sequence information. To expand our understanding of gene functions beyond sequence, profiling of gene expressions is necessary to be made. We developed a novel method to monitor gene expression in yeast cells using ^{31}P MRI. Yeast cells are known to accumulate large amount of polyphosphate (PolyP), about 120mM, in its vacuole, although its biological relevance has not been well understood. A gene group called *phm*, comprised of *phm1-5*, has been shown to control PolyP accumulation in yeast [1]. We employed *phm* as a reporter (marker) gene and examined its availability for monitoring gene expression in yeast cells. In our approach, target gene expression is coupled with the amount of PolyP accumulation via *phm*, so that ^{31}P NMR detects and assesses the expression level by monitoring PolyP NMR signal. The method was also shown to be applicable to high throughput analysis of genetic interaction such as promoter mapping.

Materials & Methods

Wild type and various recombinant *Saccharomyces cerevisiae* strains of yeast were used for the study. MRI experiments were carried out on Bruker DRX 500MHz equipped with Micro5 probehead. Yeast cells were grown up on YPD agarose plates at 30C. Cells were harvested when in the logarithmic growth phase and packed in 3.5 mm (radius) x 2 mm (depth) wells. The wells were inserted in 8mm NMR tube and spin echo MR Microscopy was performed.

Results & Discussion

Sample wells containing wild type and *phm4* disrupted (*Δphm4*) yeast cells were placed in the order of wild–*Δphm4* from the bottom of NMR tube. PolyP selected ^{31}P chemical shift microscopy showed high contrast images reflecting PolyP level in wild type and *Δphm4* yeast cells (see images below). For further assessing the availability of the method, various other recombinant yeast strains were prepared and tested. Whereas no PolyP ^{31}P NMR signal was detected in *Δphm4*, deriving *phm4* gene expressing constitutively into the cells by certain plasmid vectors recovered the PolyP level up to observed in wild type strain. The correlation between PolyP amount and *phm4* expression level was also examined with strains in which *phm4* expression was regulated by temperature or galactose concentration change. The results showed that PolyP accumulation can be controlled by *phm4* gene expression, hence indicating that *phm4*–PolyP reporter system is utilized for monitoring gene expression. Furthermore, high sensitivity and small requirement of yeast cells allow us to analyze many different yeast strains simultaneously, making our approach a unique *in vivo* high throughput method to study genetic interaction.

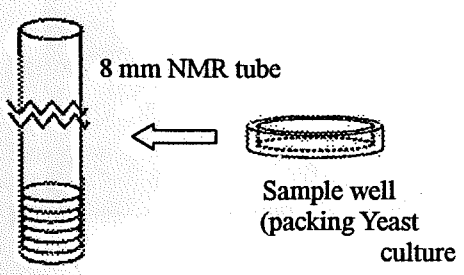

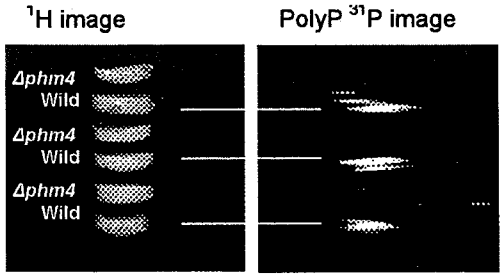

^{1}H (Left) and PolyP chemical shift selective image (Right). Wild type of yeast contains PolyP, whereas no PolyP in *phm4* disrupted yeast.

References

[1] Ogawa N. et al, *Mol. Biol. Cell*, **11**, 4309-4321 (2000).

3D NMR microscopy of intact plant root systems

Ilja Kaufmann*, Lars Wegner[1], Ulrich Zimmermann[1], Axel Haase*
* Physikalisches Institut Universitaet Wuerzburg, Germany
[1] Institut fuer Biotechnologie, Universitaet Wuerzburg, Germany

Introduction
NMR microscopy is an ideal method for studying plant roots in vivo, since it is non-invasive and does not require direct contact with the sample. As such, roots can be studied while surrounded by a known medium to investigate their internal structure, development and functionality.

Subjects and Methods
The experiments were performed at a vertical Bruker 11.75T AMX500 spectrometer with a home-built probehead. A dedicated root-NMR-glass-tube with a narrowed examination area, together with a Helmholtz coil (R=5mm) provides a good filling factor to optimize the SNR. The root of a Zea mays plant was allowed to grow into the glas tube for 10 days after germination. A small capillary was used to refill the sourrounding media, a 4.0mmol NO_3 nutrient solution.
Inhomogeneities due to air supplying tissues (Aerenchym) led to very short T2*. Therefore we used a Turbo Spin Echo sequence (TSE) [1] with an 8 echo train in the second spatial (phase encoding) dimension. To gain maximum intensity, the first echoes were used for the center k-space lines.
Another plain phase encoding loop was added for the third dimension. Echo time and Inter-echo time were both 10.9ms, with TR of 1s. Averaging a phasecycle (x,-x) for the 90° excitation puls, the acquision of a 3D data set (128^3 points, FOV=(5mm)^3) took about 70 minutes.

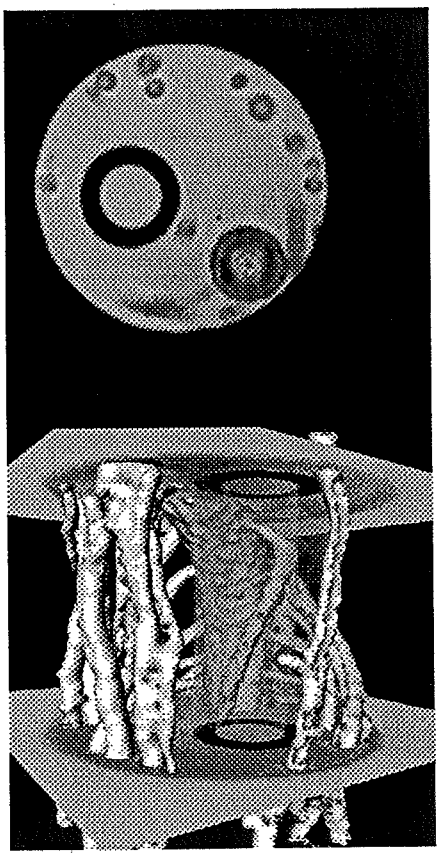

Results
The figure shows a center slice of the 3D dataset. The resolution and the contrast were sufficient to perform a surface reconstruction of the root system within the taken FOV. To distinguish the root from the capillary and the glas tube, a rough segmentation of the different areas was done before.

Discussion
This first 3D NMR microscopy of an intact plant root system shows that NMR is a viable means to observe and reconstruct root systems within their sourrounding media. The TSE sequence provides good spatial resolution and sufficient time resolution, and will be of great utility in future studies of the internal tissue developement of root systems during their growth.

References
[1] J. Hennig, A. Nauerth, H. Friedburg, *Magnetic Resonance in Medicine* 3, 823-833 (1986).

Fast Magnetic Resonance Characterisation of Multi-Phase Liquids

K.G. Hollingsworth, J.P. Hindmarsh, A.J. Sederman, L.F. Gladden and M.L. Johns
Department of Chemical Engineering, University of Cambridge, Cambridge, U.K., CB2 3RA

Various immiscible liquid dispersions have been investigated using magnetic resonance (MR) techniques, with the intention of quantifying their evolving microstructure as they are processed in a variety of ways. This has necessitated the application and development of various fast MR techniques for rapid imaging and measurement of restricted self-diffusion. The following specific projects in this general theme, will be discussed in detail:m

On-line Emulsification
Difftrain [1], a pulse sequence that acquires self-diffusion data in less than 5 s whilst retaining spectral information, has been applied to the sizing of emulsion droplets [2], based on the restrictions placed on self-diffusion of the discontinuous phase molecules by the edges of the droplets. Traditional MR techniques required several minutes to make such measurements. The limits of applicability of this pulse sequence for emulsion droplet sizing will be described, as will its robust implementation. Its use to follow and quantify various emulsification processes in-situ in a completely non-invasive manner will be discussed. The application of Area-based Regularisation techniques to interpret the acquired experimental data and hence produce a droplet size distribution for the emulsion, without assumption regards the distribution shape, will also be described [3].

Droplet Migration in Sheared fields
Droplet migration, in the shear direction produced by a wide-gap couette cell, of both individual and small groups of droplets in an immiscible continuous liquid phase has been followed using imaging techniques, based on the application of the Rapid Acquisition of Re-focussed Echoes (RARE) pulse sequence [4]. This has necessitated the application of rotational compensation to the imaging magnetic field gradients in order to accurately register the shape of the rotating droplets. This consequently produces a *k-space raster* that rotates in phase with the droplet of interest. This has been further exploited in order to determine the dynamic interfacial tension between the two phases, based on an analysis of droplet shape. MR imaging techniques, employing a variety of phase-contrast mechanisms, have also been used to follow the migration of multiple droplets (emulsions) in various sheared environments (couette and capillary flow). Migration of the emulsion droplets away from the edges of the respective device was observed and compared favourably with relevant theory.

RARE pulse sequence applied to droplet freezing
Droplets of various water/sucrose compositions have been suspended and frozen in a super-cooled flowing air stream, in-situ. The application of this research is to better understand spray freezing/drying processes and the droplet microstructure they produce. RARE imaging has been used to image the rapid solidification of the droplets as they freeze. The location of nucleation is identified as is the subsequent freezing stages of the droplet (recalescence and heat-transfer limited cooling). The size domains of resultant unfrozen supersaturated regions is determined based on MR restricted self-diffusion measurements. Trends will be reported based on sucrose concentration and the degree of super-cooling employed.

References
[1] Stamps, J.P., Ottink, B., Visser, J.M., Van Duynhoven, J.P.M. and Hulst, R., *J. Magn. Reson.* **151**, 28 (2001)
[2] Buckley, C., Hollingsworth, K.G., Sederman, A.J., Holland, D.J., Johns, M.L. and Gladden, L.F., *J. Magn. Reson.*, **161**, 112-117 (2003).
[3] Hollingsworth, K.G. and Johns, M.L., *J. Colloid Interface Sci.*, **258**(2), 383-389 (2003)
[4] Hennig, J., Nauerth, A. and Friedburg, H., *Magnetic Resonance in Medicine*, **3**, 823-833 (1986).

Statistical Approach in the Theory of Diffusion Attenuated MR Signal in Biological Systems

Dmitriy A. Yablonskiy, G. Larry Bretthorst, and Joseph J.H. Ackerman
Washington University, One Brookings Drive, St. Louis, MO 63130

Introduction Numerous studies of the diffusion of water and/or other metabolites in brain tissue and other biological systems have documented a non-mono-exponential behavior of the MR signal S as a function of the b-value at fixed diffusion times in a Stejskal-Tanner pulsed gradient spin echo (PGSE) experiment (see for example [1]). Most authors report that their data can be fit well by a bi-exponential function with two different diffusion coefficients (large/fast and small/slow) and some have ascribed the two exponential components to two physical compartments (extra- and intra-cellular) in a tissue. While the two compartment model is conceptually appealing, in most cases the origin of fast- and slow-diffusion pools has not been elucidated. Herein we propose a rather general phenomenological model (as an alternative to model derived from bi-exponential signal behavior) that can describe a rather large number of experimental results related to the structure of PGSE diffusion attenuated MR signal in biological systems.

Theory Our model relies on the following assumptions: (a) The MR signal from a given voxel containing a variety of cells and intercellular spaces can be described as a sum of signals from individual spin packets originating from different positions within the voxel; (b) Because spin packets originate from different positions, travel through different displacement trajectories, and are confronted with different restrictions and hindrances to displacement, their apparent diffusion coefficients, *ADCs*, are, generally speaking, different; (c) The total MR signal can be described in terms of a distribution function, $P(ADC)$, that gives the fraction of spin packets with a given *ADC*.

In the case of signal from a biological system, if the diffusion time Δ is much longer than the average time required for molecules to travel across cells, then all spin packets sample similar trajectories and environments. This results in a peak-shaped distribution function. The exact shape depends on the details of the cellular structure within the voxel. However, under a realistic assumption that a large number of "similar" cells reside in a voxel, the width of distribution should be rather small and the "tails" of the distribution should decay rather fast. Obviously, these assumptions can be satisfied by a Gaussian-type function that is characterized by two parameters – the position of distribution maximum (*ADC*) and the distribution width - (σ).

Methods MR brain data from a human volunteer were obtained on a whole body 1.5 T Siemens Magnetom Sonata. The human study was approved by the institutional review board. Fifteen axial 2D spin echo EPI images with b=0.15, 0.3, ..., 2.25 ms/μm^2 were taken for each of three orthogonal directions of the diffusion-sensitizing gradients. Data were analyzed using Bayesian probability theory to estimate the model parameters for the signal intensity (magnitude images) on a pixel-by-pixel basis.

Results For practically all human brain regions, the diffusion attenuated MR signal shows non-mono-exponential behavior, which was well represented by the above described model ($R^2 > 0.99$). Examples of *ADC* and σ maps obtained from the head of one volunteer are shown below.

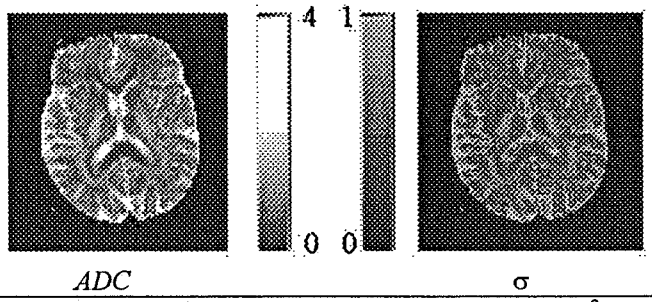

Figure *ADC* and σ maps corresponding to diffusion sensitizing gradient direction perpendicular to slice plane. The scale bars provide references for *ADC* (from 0 to 4 μm^2/ms) and σ (from 0 to 1 μm^2/ms).

The brightest regions in the *ADC* map correspond to CSF in ventricles and subarachnoid spaces. On the σ map, CSF in ventricles is dark but remains bright at the ventricular edges and in subarachnoid spaces. The latter is most likely due to the partial volume effect.

The average *ADC* across all ROIs was 0.90±0.27 μm^2/ms and the average σ was 0.31±0.07 μm^2/ms or 36±9 % if calculated on a per voxel basis as a percentage of corresponding *ADC*.

We conclude that the proposed approach based on a statistical model with a Gaussian-type distribution function for tissue *ADC* models multiple b-value data well and provides a consistent method for quantification of PGSE MR signal in biological systems.

1. Diffusion tensor imaging and axonal mapping - state of the art. Special Issue. NMR Biomed 2002;15.

From Porous Media to Fluidised Beds – the Next Step of the Complex Fluid Dynamic Investigations

Alexandre A. Khrapitchev[1,2], Siegfried Stapf[1], Paul T. Callaghan[2], Bernhard Blümich[1]
[1]Lehrstuhl für Makromolekulare Chemie ITMC, RWTH Aachen, Worringerweg 1, D-52074 Aachen, Germany
[2]The MacDiarmid Institute for Advanced Materials and Nanotechnology, Victoria University, PO Box 600, Wellington, New Zealand

Porous and granular media are two typical objects for investigations of complex dynamic processes of molecular interactions. A bead pack represents the easiest example of porous media. The pack of highly monodisperse spherical particles has well defined geometry of structure therefore allows to make theoretical predictions and computer simulations of processes. On the other hand, granular media is a model of molecular motion on large scale, where interacting molecules are replaced by the macroscopic particles of the medium.

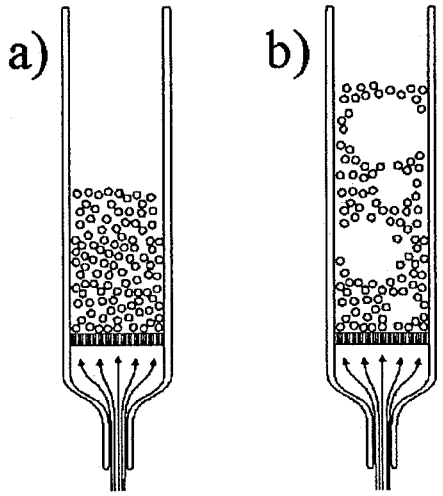

Figure 1: Different stages of granular media a) fluidised phase; b) slugging phase.

The dynamics of granular media has recently attracted considerable interest as an additional physical state by comparison to the "classical" liquids. In granular media, the investigated liquids are replaced by macroscopic particles, which undergo motion introduced by permanent external excitation. A particularly interesting case of granular media is the gas-fluidised bed, where a constant gas flow is provided from the bottom of a container filled with macroscopic particles. A schematic diagram of the different phases of a fluidised bed is shown in Figure 1. However, performance of experiments to investigate these dynamic properties of gas-fluidised beds quantitatively is a difficult task [1].

The use of Pulsed Gradient Spin Echo (PGSE) NMR to investigate dynamic processes is well established [2,3]. Using two pairs of position-encoding pulses in the Double PGSE experiment gives the possibility of examining velocity fluctuations by comparing displacements during the two encoding intervals and can be used to directly measure the Velocity Auto-correlation Function (VACF) [4]. The shape of the fluctuation distribution depends on the ratio of the mixing and the correlation time. For sufficiently long mixing, each particle has experienced a history of velocity changes so that its encoded velocities before and after the mixing time interval are no longer correlated.

This work presents a detailed investigation of the VACF for both radial and axial directions and for different flow rates so that the Péclet number scaling effects can be seen. We also present a new interpretation of previous experimental results and demonstrate that it can be used to provide new information about flow and dispersion in porous media. The application of these NMR techniques to investigate motion in a fluidised bed is discussed in the part devoted to granular media. The transitions towards fluidisation, bubbling phase, and slugging phase are visualised. The onset of these transitions is shown as a function of the particle sizes for a given cell geometry. The effective diffusion coefficients are measured and the distributions of particle displacements are demonstrated.

References

[1] R. Savelsberg, D.E. Demco, B. Blümich and S. Stapf, *Phys. Rev. E* **65**,020301 (2002).
[2] P.T. Callaghan, "Principles of NMR Microscopy", *Oxford: Clarendon Press*, (1991).
[3] B. Blümich, "NMR Imaging for Materials", *Oxford Science Publications*, (2000).
[4] A.A. Khrapitchev and P.T. Callaghan, *Phys. Fluids*, submitted (2003).

Velocity fields during the contraction flow of viscoelastic fluids.

Galina E. Pavlovskaya
Department of Chemistry, Colorado State University, Fort Collins, CO 80526

The divergence of velocity fields during the contraction flow of viscoelastic fluids occurs in abrupt contraction with the ratio of upstream /downstream radii of 3. As the fluid approaches to the contraction entry plane, the divergence influences the shape of the radial profiles of axial velocities leading to the appearance of off-centered maxima.

The axial positions of the divergence area can be easily mapped if another joint velocity probability function ($P(v_z,Z,X)$ is used to quantify the flow. When the slice selection is made in the direction of flow then all the spins with locations defined by a pair of (z,x) coordinates are labeled. The flow of these particles is let to evolve during the time between two field gradients applied in the flow direction. As a result of this spatial encoding, the displacements of spins that acquired a non zero transverse component of velocity during flow evolution are detected. The spatial boundaries where this phenomenon occurs can also be determined in this type of flow experiments.

We have applied this technique to measure a fully developed flow of a shear–thinning viscoelastic fluid (0.5% Xanthan in 0.1M NaCl aqueous solution) in a 3:1 abrupt contraction. The surface plot of velocities shows a measurable off plane flow in the area near to the contraction entrance, while the rest of velocities are at around zero value. The divergence area is determined very clearly. These studies can be very important in the explanation of the nature of elastic instabilities occurring in contraction flows.

Imaging the Tubeless Siphon by NMR Microscopy

Yang Xia[1], Paul T Callaghan[2]
[1]Department of Physics, Oakland University, Rochester, MI 48309, USA
[2]School of Chem and Phys Sciences, Victoria University of Wellington, New Zealand

Introduction

Highly elastic polymer fluids can exhibit some unusual flow phenomena [1], one of them being the tubeless siphon (Fano flow) where a fluid column can be drawn upward out of a container by a pipette, even when the pipette is completely above the fluid container [2,3]. The driving force for a tubeless siphon in polymeric fluid is the elastic energy stored within the polymer molecules: the stretching of the polymer molecules along the flow direction releases the elastic energy that acts to pull additional fluid out of the container.

Material and Methods

The flow system comprises a pump with its inlet and outlet connected to a reservoir (12.5mm id) and a glass pipette, respectively. The pipette tip (1.2mm id) is inserted into the reservoir to form a close loop. The flow system is filled with ~600 ml of 0.5% w/v polyethylene oxide in water. The inserted portion of the reservoir and pipette tip is located within the 15mm rf coil of a Bruker AMX300 spectrometer. 2D velocity mapping [4] was performed using a PGSE spin-warp imaging sequence, at 16 different heights along the siphon column. The slice thickness was 1mm (transverse to the column) and the in-plane resolution was 31.25 μm. At each siphon height, eight images were acquired with q-gradient pulses of duration 1 ms, separation 5 ms and maximum gradient 0.21 T/m. The flow rate was 125 ml/hr.

Results

We were able to establish a tubeless siphon with a column heigl of about 6 mm inside the magnet, stable over several hours (Fi 1). Velocity images were obtained at various heights along th column. Fig 2 shows a sample of the succession of 16 velocit maps taken at 0.5mm spaced vertical displacements with respec to the pipe entrance at z=0, negative distances referring to level below the pipette entrance and within the Fano column. Th velocity images show successive changes in velocity patterr with vertical displacement. Just inside the pipette, a non-sli boundary condition is nearly achieved. Outside the pipette, in th column, a finite velocity is seen at the free surface, with tendency towards a low outer surface shear rate becoming mor apparent. The arrows in Fig 2 point to stationary fluid.

Fig 1

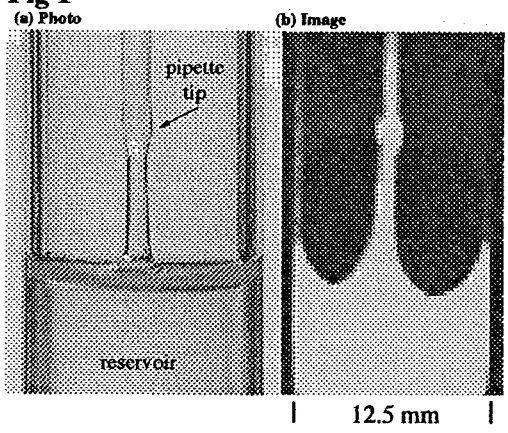

Fig 2

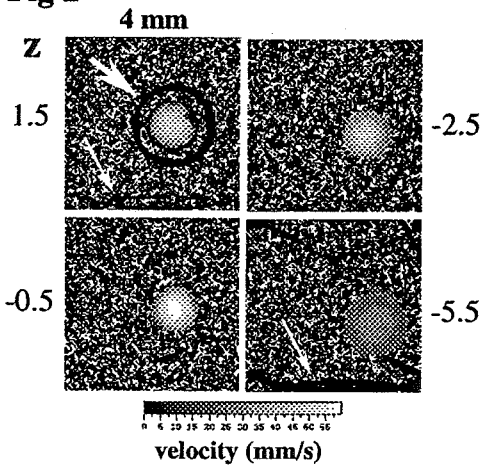

Conclusions

To our knowledge, the results reported here constitute the fir quantitative and direct measurement of velocity profiles in Fan flow. More than just a peculiar flow phenomenon, the tubeles siphon offers an unique opportunity to measure extensiona viscosity in elastic liquids.

References

[1] Y Xia and PT Callaghan, *Macromolecules* **24**(17), 477 4786 (1991). [2] E Matthys, *J Rheol* **32**, 773-788 (1988). [3] E Stejskal and JE Tanner, *J Chem Phys* **42**, 288-292 (1965). [4] P Callaghan and Y Xia, *J Magn Reson* **91**, 326-352 (1991).

Acknowledgement: YX: OU REF Biotech, Bennett NM Facility, NIH (R01 AR 45172); PTC: the Royal Society of NZ Marsden Fund, Centres of Research Excellence Fund.

NMR velocity studies on a falling liquid film

Markus Küppers, Siegfried Stapf, Bernhard Blümich
Lehrstuhl für Makromolekulare Chemie, Magnetic Resonance Center,
RWTH Aachen University, Aachen, Worringer Weg 1 52072, Aachen, Germany

Within the collaborative research center 540 at the RWTH Aachen, different methods of measuring the velocity of falling liquid films are used. The cooperation partners use methods like Laser-Doppler-Anemometry (LDA), Particle-Imaging-Velocimetry (PIV), phosphorescence, and fluorescence to measure the film thickness, wavelength, velocity, and amplitude of the waves. All of these methods have a much better time resolution than NMR can provide. But none of these methods can detect more than one information in the same measurement at the same data point like NMR can do. Also these engineering methods are restricted to optically transparent films and apparatus, which is not the case for NMR.

Earlier research in this project [1] had shown that NMR can provide velocity [2,3] and propagator [4] measurements on a falling liquid film [5]. These results led to a modification of the design of the apparatus. The new design allows to change the distance between the generation of the film and the measurement area. It also allows to induce waves on the film by the use of a speaker. A further advantage is the modified geometry of the plate. This modification provides a nearly undisturbed film even close to the edges of the film. Because of these changes it is now possible to measure the waves at a certain state of its periodicity.

A further improvement is the use of a new pulse sequence. This new sequence is using two slice selections [6] along different axes. This selects a small square in the film, so that the full information about the velocity profile in the film can be obtained from one-dimensional measurement. The results of these NMR measurements are combined together with the results obtained by the engineers in the other projects of the collaborative research center to discriminate different models to describe the motions in a falling liquid film.

In future experiments all cooperation partners will use the same conditions for the liquid film characterized by the hydrodynamical quantities: Reynolds number (Re_F), Prandtel number (Pr), Froude number (Fr), Film number (Fi), and Strouhal number (Sr), so that all results are directly comparable to each other.

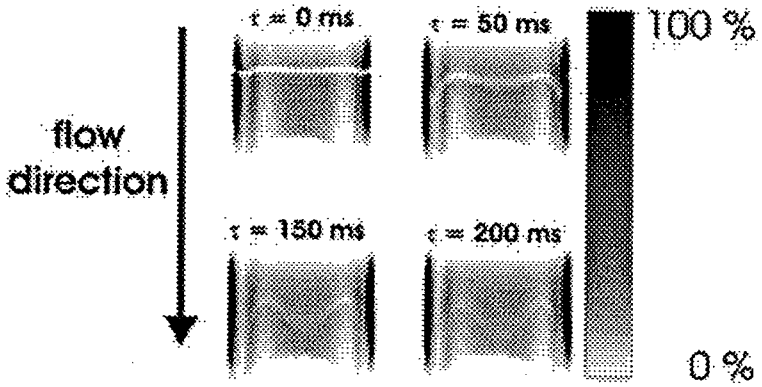

Figure 1: Four images of a silicone oil film at $Re_F = 1.0$ with a tagging sequence with different delay times between the tagging and the imaging part [1].

References
[1] Heine, C., *NMR von rotatorischer und translatorischer Dynamik*, Dissertation RWTH Aachen 2001
[2] Fukushima, E., *Annu. Rev. Fluid Mech.* **31**, 95 (1999)
[3] Caprihan, A., Seymour, J. D., J. Magn. Reson. **144**, 96 (2000)
[4] Callaghan, P.T., *Principles of Nuclear Magnetic Resonance Microscopy*, Clarendon Press, Oxford (1993)
[5] C. Heine, K. Kupferschläger, S. Stapf, and B. Blümich. NMR velocimetry of falling liquid films, *J. Magn. Reson.*, **154**, 311 (2002)
[6] Blümich, B., *NMR imaging of materials*, Clarendon Press, Oxford (2000).

Industry Trends and New Product Development for Hyperpolarization of Noble Gases

Stephen R. McComb
Market Development Manager, Coherent Semiconductor
5100 Patrick Henry Drive, Santa Clara, CA 95054

Abstract

The applications associated with optically pumping to hyperpolarize noble gases continue to expand. In addition the industry and companies focused on commercializing the technology continue to emerge and mature. For these trends to continue, cost effective solutions must keep on being developed. Semiconductor Laser Diodes have allowed techniques that were acceptable only in research settings to become widely applied.

Applications in physics, material science, high-resolution medical imaging have given semiconductor laser diode suppliers the impetus to develop products focused for these applications. Devices and systems now exist that allow investigators and industrial users to access techniques utilizing systems employing various noble gases (3HE and 129Xe) and alkali metals (Rb, K, Cs).

Today there is a broad spectrum of product available to meet the needs of this emerging industry. Products are available from low power, less than 1 watt, to high power greater than 80 watts. Devices can be simple stand-alone devices to fully integrated systems. A variety of optical delivery options exist.

Coherent Semiconductor has lead the way in supporting the commercialization of this industry. We offer a broad spectrum of devices with varying wavelengths, 670nm, 770 nm and 795 nm. Powers vary from 1 watt to 80 watts. Optical delivery options include non-lensed highly divergent sources to systems incorporating circular polarizing optics. Plug and play turnkey systems are available for the laboratory user. The key is "Focussed Solutions", easy to use, easy to maintain, cost effective and robust.

Development of a Compact MRI for Bone Volume Density Measurements

Katsumi Kose[1], Yoshimasa Matsuda[1], Takeaki Kurimoto[1], Sadanori Tomiha[1], Seitarou Hashimoto[1], Yukako Yamazaki[1], Tomoyuki Haishi[2], Shin Utsuzawa[2]
[1]Institute of Applied Physics, University of Tsukuba, Tsukuba, 305-8573, Japan,
[2]MR Technology Inc., Tsukuba, 305-2642, Japan

Introduction

Bone density measurements are indispensable to diagnosis of several diseases such as osteoporosis. In this field, MRI has definite advantages over conventional modalities such as DXA and QUS, because MRI can safely measure "volume density" of trabecular bone [1]. However, use of a whole body MRI for this purpose is not appropriate in viewpoints of space and cost. In the present study, we have developed a compact MRI for heel imaging and measured trabecular bone volume fraction (TBVF) of the calcaneus for female volunteer groups.

Compact MRI

Figure 1 shows the overview of the compact MRI (installation space: 2m x 2m) developed in this study. The MRI utilizes a permanent magnet, of which specification is as follows; field strength: 0.21T, gap: 16cm, homogeneity: 50ppm over 12cm dsv, weight: ~500kg. The RF probe is a seven-turn solenoid with an oval aperture (14cm x 8.2cm). The coil was fixed in a RF shield box with plant oil phantoms used as a proton density standard. Figure 2 shows a sagittal cross-section of a heel measured with a 2D SE sequence.

Method for Bone Density Measurements

TBVF was quantified using two sagittal cross-sectional images of the calcaneus and plant oil phantoms acquired with conventional SE sequences (TR/TE=1200ms/12ms, 1200ms/96ms). T_1 saturation was eliminated using the long TR. T_2 decay and J-coupling effect was corrected using the nearly J-refocused spin echoes. The absolute proton density of the bone marrow was calculated using image intensities of the external standard plant oil phantoms, and that of an oil phantom measured instead of the heel.

Experiments

Two healthy female volunteer groups (group A; 22 students, age: 18~23, mean 19.8. group B; 47 women, age 24~58, mean 40.0) were recruited from our university. After the informed consent was obtained, MRI TBVF and QUS measurements were performed for the right calcaneus.

Results and Discussion

Figures 3 shows the TBVF plotted against the stiffness measured with the QUS for the group A. R^2 values were 0.3939 and 0.2846 for the group A and B. These results show that the TBVF measured with the compact MRI has a high correlation with the stiffness measured with QUS. This means that considerable part of the stiffness is determined by the TBVF.

Conclusion

A compact MRI for bone density measurements was developed. Bone volume density was measured using the compact MRI for healthy female volunteer groups and high positive correlations with QUS were observed. The future plan is to improve the reproducibility of the TBVF value and to measure a large number of volunteers.

References

[1] Maria A. Fernandez-Seara et al. *Magnetic Resonance in Medicine* **46**, 103-113, (2001).

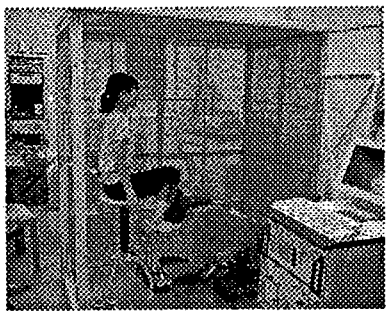

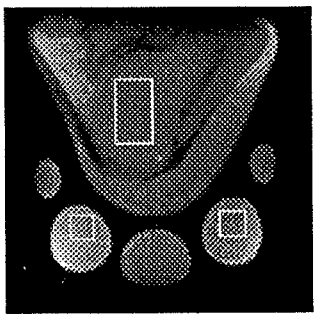

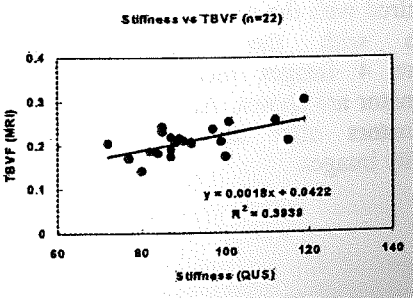

Fig.1 System overview Fig.2 SE image of the calcaneus Fig.3 Correlation between QUS and MRI

First Evaluation of Very High Field Multi-Channel Probes for Double-Resonant- and Quadrature-Detection at 17.6 T

Volker C. Behr, M. Oechsner, D. Gareis, I. Wieland, T. Neuberger, A. Haase, C. Faber
Department of Physics, EP5 (Biophysics), University of Würzburg, Würzburg, Germany

Synopsis
High field spectrometers operating at 17.6 T for small animal imaging have recently become available. Microscopic imaging as well as spectroscopic experiments benefit from improved SNR and increased chemical shifts yielded by these field strengths. Not only methods had to be adapted to frequencies of 750 MHz, the larmor frequency of ^{1}H at 17.6 T, but also hardware requires new considerations and designs. In this abstract we present the results of our preliminary studies with double-resonant and quadrature resonators for ^{1}H, ^{19}F and ^{23}Na MR imaging and spectroscopy.

Setup
At our site a Bruker Avance wide bore magnet at 17.6 T is available for high field experiments. This system can be equipped with either a 1 T/m gradient unit with an inner diameter of 40 mm or one with 200 mT/m and 56.5 mm inner diameter, depending on the experiment. Furthermore a choice of transmitters is available allowing ^{1}H and X-nuclei studies.

Hardware
Two resonators built for multi-channel applications are shown in figure 1. Both resonators were designed for the 200 mT/m in-vivo gradient system and have an inner diameter of 38 mm. The quadrature birdcage is an eight-legged high-pass birdcage with a height of 42 mm. During its assembly special care had to be taken to use capacitors of exactly the same values (down to ±0.1 pF) since at a frequency of 750 MHz only very small capacitances of a few pF are used and even minor deviations lead to major imbalances in the current distribution and, as a result, in the B_1 field. The double-tuned saddle coil pair is optimized for ^{23}Na imaging with saddles of approximately 40 by 40 mm^2 while the ^{1}H saddles are about 30 by 40 mm^2 and primarily intended for positioning of the sample and shimming. For this resonator the coupling between the overlapping saddles proved to be the main issue to overcome. In figure 2 an optimized layout for a double-tuned four-legged birdcage resonator is shown. For the second channel the feeds as well as tuning and matching capacitors (C_T and C_M) are located 90° rotated with respect to the first (not shown). The common ground-ring is designed for stabilizing and decoupling of the two channels.

Figure 1: *left:* ^{1}H quadrature birdcage *right:* ^{23}Na-^{1}H double-tuned saddle coil pair

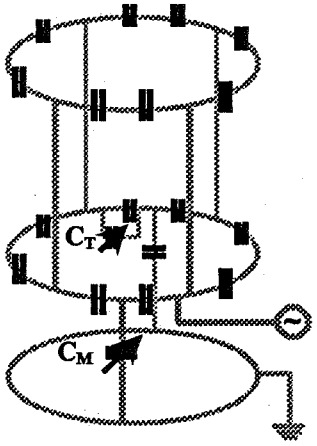

Figure 2: Design for an optimized birdcage

Experiments and Conclusions
Preliminary studies were performed to evaluate the function of the resonators described above. Figure 3 shows a well resolved sodium image after positioning and shimming was acquired with the saddle coil resonance (images not shown). In done with the proton simultaneously with the two quadrature modes of the birdcage figure 4 images recorded be seen both channels yield good signal over the entire sample. Both resonator are shown. As can decoupling of their modes and B_1 homogeneity to acquire highest resonators offer sufficient quality images.

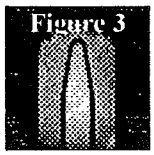

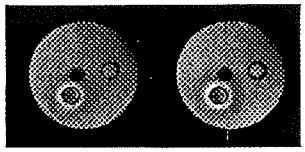

High Density Xenon-129 Optical Pumping for In-Situ NMR Spectroscopy of Methane Combustion.

Satyanarayana Anala, Galina E. Pavlovskaya, Prakash Pichumani, Todd J. Dieken, Michael D. Olsen and Thomas Meersmann
Department of Chemistry, Colorado State University, Fort Collins, CO 80526

In situ nuclear magnetic resonance spectroscopy (NMR) of high temperature reactions is of potential value for the investigation of catalytic combustion and other high temperature applications of catalysts such as partial oxidation of hydrocarbons and steam reforming. Unlike open flames where reactions take place within an optically transparent region, the reaction zone in catalytic processes is located within an opaque medium. Non-invasive measurements that study gas and reaction dynamics within the interior of a combustor are therefore challenging, however the radiofrequency regime provides a previously unused opportunity to investigate reaction processes in these optically non-transparent systems. 129Xe NMR spectroscopy can provide valuable information about reaction heat in various regions (or combustion stages) within an opaque medium.

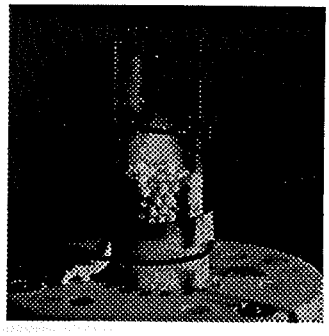

Figure 1: Photograph of the NMR coil region during methane combustion. The upper surface of the Na-Y zeolite pellets may participate as a catalyst in the reaction.

The feasibility of in-situ combustion NMR and the effect of temperature on the sensitive chemical shift of xenon are demonstrated. The long relaxation times of ^{129}Xe (even in the presence of paramagnetic molecular oxygen) are utilized for studies of the gas flow dynamics within a combustion process. Reasonable signal intensity is obtained for ^{129}Xe-NMR using hyper-polarized (hp)-xenon produced by spin-exchange optical pumping procedures. Of particular value is the high-density optical pumping technique [1] for these studies. It is also discussed how specific regions or zones within the combustion process can be identified by chemical shift selective hp-129Xe magnetic resonance imaging (MRI).

References

[1] M.G. Mortuza, S. Anala, G.E. Pavlovskaya, T.J. Dieken, T. Meersmann, *J. Chem. Phys.* **118**, 1581-1584 (2003).

NMR Imaging of Swollen Superabsorbent Polymers

Ruediger Voelkel, Rudolf Berg, Samantha Champ
BASF Aktiengesellschaft, Polymer Research Division, D67056 Ludwigshafen, Germany

Introduction
Superabsorbent polymers are produced at a scale of more than 1 million tons per year and are thus of considerable commercial importance. Their ability to absorb liquid up to 100 times their own weight makes them the active ingredient of many articles of hygiene. The polymer itself is usually based on poly(acrylic acid) which is cross-linked to some extent and partially converted into its sodium salt. The characterisation of such swollen polymer gels by NMR microscopy provides additional details of their structure and morphology [1] and furthermore helps to improve these materials as well as develop new products.

Imaging swollen gels
We can choose the concentration of water, relaxation (T_1 or T_2^*) and diffusion as contrast. T_2 maps generated by a slice-selective single echo Hahn-spin-echo sequence look very similar to published images [2] which have been interpreted as an indication of a gradient in cross link density due to surface cross linking. The latter is used to prevent "gel-blocking" of the particles. T_2 maps based on multi-slice-multi-echo experiments are very useful in order to construct 3D images which characterise the internal structure of commercial superabsorbent particles [3] even if these are of irregular shape due to grinding of the gel during production. We can easily decide whether a spot of long T_2^* and slowed diffusion is located inside the particle or on its surface and therefore distinguish surface cross-linking from structure induced by gel polymerisation itself.

New morphologies for improved performance
One new line of development tries to reduce the volume of diapers by using less fluff. This in turn requires that the active absorbent itself distributes the liquid effectively. An open pore foam made from superabsorbent material will do so and indeed responds much faster to any liquid. NMR images of such a material, partly saturated with water, allow to distinguish the filled paths from the empty ones, although the concentration of water is practically the same in the channels as in the swollen gel itself. Imaging sequences are even fast enough to enable some "life" experiments following the swelling in real time.

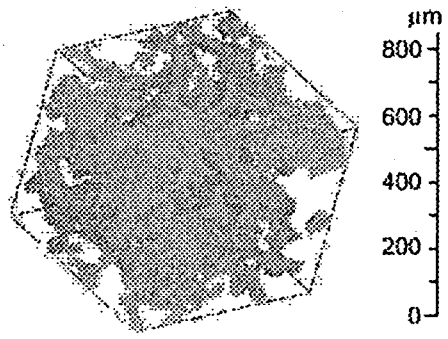

Figure 1: Fully swollen poly (sodium acrylate) foam submersed into water. Contrast is based on T_1.

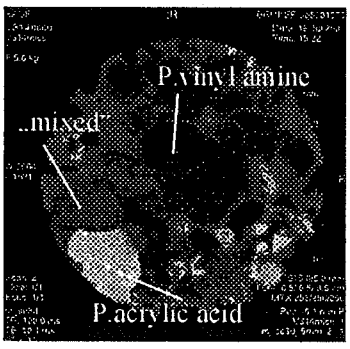

Figure 2: Imaging chemistry in an MDC superabsorbent.

Imaging Chemistry
Another development in the field of superabsorbents tries to avoid one of the drawbacks of the existing materials: Micro domain composite (MDC) superabsorbents which consist of a "mixture" of a cationic and an anionic polymer are known to be less sensitive to salt in the liquid than the standard material in use today. NMR microscopy reveals segregation into domains of different chemical composition inside this new superabsorbent and thus provides an explanation of its swelling.

References
[1] Malgorzata Szayna, Rudolf Berg, RuedigerVoelkel, *39th ENC Asilomar CA (USA)* 1998
[2] B. Traub, T. Fritzhanns, S. Hafner, H.W. Spiess, *Colloid Polym Sci* **278**, 547 (2000)
[3] Ruediger Voelkel, Rudolf Berg, Sergey Evsyukov, H.-Joachim Haehnle, *6th ICMRM, Nottingham (UK)* 2001.

Applications of NMR to the study of travelling waves and convection in autocatalytic reactions

Melanie M. Britton
Magnetic Resonance Research Centre, Department of Chemical Engineering, University of Cambridge, New Museums Site, Pembroke Street, Cambridge, CB2 3RA, UK.

Experiments on systems, whose heterogeneity is produced through the coupling of non-linear kinetics and diffusion, are presented. There are a number of reactions that can produce such heterogeneity, forming travelling waves or stationary patterns[1], and examples are found throughout chemistry and biology. In this study Nuclear Magnetic Resonance (NMR) imaging and spectroscopy techniques have been used to investigate the 1,4-cyclohexanedione-bromate-acid (CHD) oscillatory reaction[2]. This system is an analogue of the famous Belousov-Zhabotinsky reaction[3], and exhibits a similar wealth of spatio-temporal behaviour, but has some key differences. Firstly patterns tend to be longer lasting and more importantly no CO_2 bubbles are formed. Visual observation of the waves comes from the inclusion of a transition metal ion. During key feedback processes the metal ion is periodically oxidized then reduced, so producing periodic colour changes. NMR visualisation of the waves is made possible through a relaxation time difference for water molecules surrounding either the oxidized or reduced transition metal ions. This makes it an excellent system to study using NMR imaging techniques, as has been previously found, in similar studies, by Armstrong *et al*[4], who imaged the BZ reaction. In this study the fast imaging technique, RARE[5], has been used to image pattern formation. Using this technique images take approximately 4 s to acquire, allowing the development of patterns to be observed.

In this system, however, NMR can provide far more than an alternative means of visualising the wave and there is a greater opportunity to understand the processes which underpin pattern formation and development. The chemistry and oscillatory nature of this system is based on 1,4-cyclohexanedione and its derivatives. These are 'NMR observable' molecules and so can be studied using NMR spectroscopic methods. By following the rate of change of concentration of key organic species, with concurrent imaging, independent verification[2] of key steps in the proposed reaction mechanism[6] has been possible.

While understanding of pattern formation in chemical systems is of interest in its own right, it is the ability to apply these systems as models for pattern formation in biological systems that has been a great spur for research in this field. The presence of convection, considered a major factor in pattern formation in biological systems, has been studied in the CHD reaction. Convection arises through density differences between fluid inside and outside waves. NMR measurements of mass transport, based on Pulsed Gradient Spin Echo (PGSE) experiments, have been used to measure convection in the CHD oscillator. Factors influencing the manifestation of convection are investigated.

References

[1] Steve K. Scott, *Oscillations, waves, and chaos in chemical kinetics* (Oxford University Press, Oxford, 1994).
[2] Melanie M. Britton, *Journal of Physical Chemistry A* **in press** (2003)
[3] A. N. Zaikin and A. M. Zhabotinsky *Nature* **225**, 535-537 (1970)
[4] Robin Armstrong and A. Tzalmona et al in *Magnetic Resonance Microscopy: methods and application in materials science, agriculture and biomedicine*; ed. B. Blümich and W. Kuhn; VCH: Weinheim, 1992
[5] J. Hennig *Journal of Magnetic Resonance* **78** 397-407 (1988)
[6] Istvan Szalai and Endre Körös *Journal of Physical Chemistry A* **102**, 6892-6897 (1998)

Magnetic Field Induced Antiferromagnetic Order in the Vortex Core of HTSC Studied by Spatially-Resolved NMR

K. Kumagai[a], K. Kakuyanagi[a], M. Matsuda[b], and M. Hasegawa[c]
[a)]Division of Physics, Graduate School of Science, Hokkaido University, Sapporo 060-0810, Japan
[b)]Institute of Solid State Ohysics, University of Tokyo, Kashiwa 277-8581, Japan
[c)]Institute for Materials Research, Tohoku University, Sendai 980-8577, Japan

The microscopic structure of vortex core turns out to be a very interesting subject of High-T_c superconductors (HTSC), since many unexpected behaviors have been observed so far. A new class of theories based on the t-J and SO(5) models have pointed out that the antiferromagnetism arising from the strong electron correlations is very important for accounting the vortex core structure, and that the enhanced antiferromagnetism can appear in the vortex core. Therefore, spatially-resolved probes which are sensitive to the magnetic excitations in the vortex state is strongly desired. Recent experimental and theoretical NMR studies have established that the spatial dependence of nuclear spin-lattice relaxation rate, T_1^{-1} in the vortex state serves as a probe for the spatially different low energy excitation spectrum in HTSC. We have reported the spatially-resolved NMR of underdoped ^{17}O in $YBa_2Cu_4O_8$ (T_c=85K). [1]

Here, we will report spatially-resolved $^{205}T_1^{-1}$ of nearly optimal-doped $Tl_2Ba_2CuO_6$ (T_c=85K). T_1^{-1} at the Tl site can monitor AF fluctuations sensitively, because the Tl atoms are located just above the Cu atom, and hence there exist large transferred hyperfine interactions between the Tl and the Cu site through apical oxygen. $^{205}T_1^{-1}$ in the vortex core is enhanced almost by two orders larger than that of the superconducting region. Together with the characteristic behavior of the recovery curve of nuclear magnetization and anomalous spectrum broadening at low temperature, we show clearly evidences of the antiferromagnetic vortex core in $Tl_2Ba_2CuO_6$. [2] We will present also results of the external field dependence of the antiferromagnetism in the vortex core of HTSC.

[1] K. Kakuyanagi, K. Kumagai, and Y. Matsuda, Phys. Rev.B65, 60503 (2002).
[2] K. Kakuyanagi, K. Kumagai, Y. Matsuda, and M. Hasegawa, Cond-mat/0206362 (2002), and to be published in Phys. Rev. Lett. (2003).

Atomic Resolution Magnetic Resonance "Diffraction"

Mladen Barbic, Axel Scherer
Applied Physics and Electrical Engineering, Caltech 200-36, Pasadena, CA 91125

We will present our recent proposal [1] for the observation of sharp spectral peaks in the magnetic resonance signal for the case of a crystal in close proximity of a ferromagnetic nanosphere, as shown in Figure 1. The appearance of the peaks shown in Figure 2 is a ***direct signature of the discrete atomic sites*** in the crystal lattice, and the positions of the spectral peaks are sensitive to the crystal unit cell size thereby providing a magnetic resonance diffraction method for determination of the basic parameters of the crystal at the atomic scale. Therefore, the technique provides a magnetic resonance alternative to the other three well-known atomic resolution crystallography techniques of x-ray, electron, and neutron diffraction. Applications to the studies and imaging of crystals, thin films, and crystallites will be discussed, and potential measurement methods for the confirmation of the diffraction theory will be proposed [2]. The technique significantly relaxes the magnetic resonance sensitivity requirements compared to single spin imaging proposals by allowing many spins to coherently contribute to the signal while still providing atomic scale information. The analysis suggests that the long desired goal of detecting atomic resolution magnetic resonance diffraction [3] is well within reach of current experimental techniques such as Magnetic Resonance Force Microscopy [4]. We will also describe our experimental efforts towards realization of atomic resolution magnetic resonance "diffraction" that include fabrication and characterization of composite magnetic/plasmonic nanowire based NEMS sensors, as well as integrated ultra-high magnetic field gradient sources and micro-coil detectors shown in Figure 3.

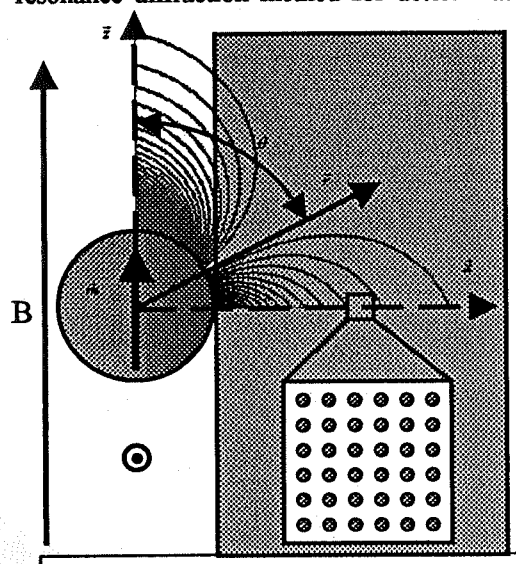

Figure 1. Model system for atomic resolution magnetic resonance diffraction.

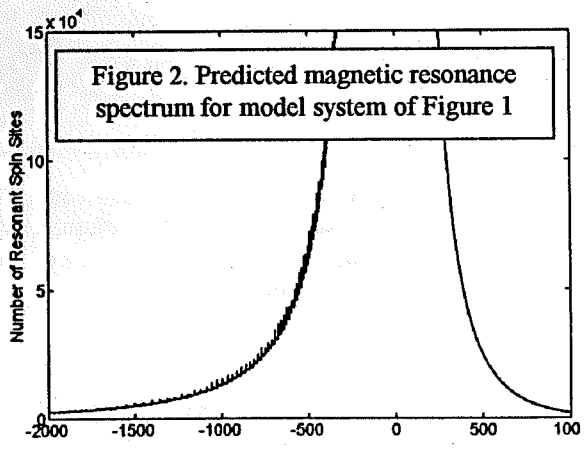

Figure 2. Predicted magnetic resonance spectrum for model system of Figure 1

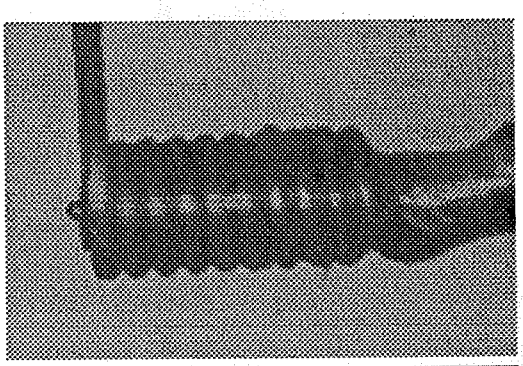

Figure 3. Integrated magnetic micro-sphere and micro-coil for scanning probe MRI.

References

[1] M. Barbic *Journal of Applied Physics* **91**, 9987-9994 (2002).
[2] M. Barbic and A. Scherer *Journal of Applied Physics* **92**, 7345-7354 (2002).
[3] P. Mansfield and P. K. Grannell *Journal of Phyics C: Solid State Physics* **6**, L422 (1973).
[4] Sidles J. A. et al. *Reviews of Modern Physics* **67**, 249 (1995).

High field *in vivo* quantitative 3D motion mapping of murine myocardium with phase contrast MRI

Philipp Mörchel, Volker Herold, Cornelius Faber, Eberhard Rommel, Axel Haase
Physikalisches Institut EP5, Universität Würzburg, Am Hubland, 97074 Würzburg, Germany

Introduction
Characterization of myocardial movement delivers a direct measure of the function and viability of the heart. The aim of this work was to assess high temporal and spatial resolution cine-sequences with 3D phase contrast motion encoding [1] of the murine myocardium on a 17.6T MR-system.

Methods
All measurements were performed on a Bruker Avance 750 spectrometer with a maximum gradient strength of 1.0T/m and a 20mm Bruker birdcage coil. Mice with body weights between 10 and 20g were anesthetized via 1.0 – 1.5 vol.% isoflurane inhalation. Images were acquired using a segmented FLASH sequence with velocity compensation in all gradient directions (TE 2.7ms, TR 8.0ms, resolution 78x78µm, slice thickness 0.5mm, 2 averages). Motion encoding was done by preparing the spin phase using a bipolar gradient which causes the moving spins to accumulate a velocity-dependent net phase with respect to stationary spins. The 3D velocity vectors of each cine frame were computed from separate acquisitions of motion encoding in read-, phase-, and slice-directions. The acquisition was ECG and respiratory gated using a home-build ECG unit [2]. 15 frames of midventricular short axis and long axis views were obtained over the RR-interval (130ms) to cover a heart cycle. To acquire all information for computing the 3D velocity, 7 cine data sets were recorded in about 30min.

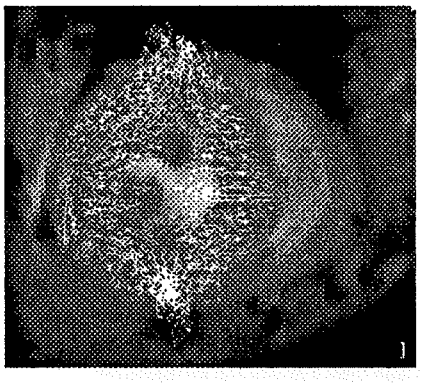

Results
The measuring methods were validated on a rotating and a tube-phantom yielding deviations of only 1.5 %. Figure 1 and 2 show one frame of the midventricular myocardium short axis and long axis, respectively. For comparison, the pictures were recorded at the same position of the heart cycle. Each arrow represents the velocity magnitude and direction in the corresponding image voxel (size: 78x78x500µm³) with a temporal resolution of about 5 ms. We were able to measure absolute myocardial velocities ranging from 0.5 to 3.5cm/s over the heart cycle. These velocities are higher than planar motion measurements [3] reflecting the contribution of the third dimension.

Conclusion
High field phase contrast MRI provides high resolution motion maps. We have demonstrated that this method delivers accurate quantification of the velocity in read-, phase- and slice-directions at a spatial resolution of 78µm in plane and a temporal resolution of about 5ms.

References
[1] P van Dijk, JCAT, 8(3):429-436, 1984.
[2] E. Rommel et al, Proc ESMRMB, Paris, 568, 2000.
[3] J. Streif et al, MRM 49:315-321, 2003

NMR Studies of Xenon Gas Flow in Porous and Granular Media

R. W. Mair[1,2], R. Wang[1,2], M. S. Rosen[1], D. Candela[3] and R. L. Walsworth[1]
[1] Harvard-Smithsonian Center for Astrophysics, Cambridge, MA, USA
[2] Nuclear Engineering Dept., Massachusetts Institute of Technology, Cambridge, MA, USA
[3] Dept. of Physics, University of Massachusetts, Amherst, MA, USA

PGSE-based NMR techniques can be used, either spectroscopically or in combination with imaging, to measure fluid velocity and/or acceleration, in addition to diffusion [1]. The recent advances in spin-exchange optical pumping [2] have made laser-polarized noble gas MRI a powerful tool, not only for spin density imaging but also for gas diffusion studies [3]. However, very few attempts have been made to study gas flow by NMR [4] - despite indications that such studies may also prove useful in biomedical and materials science studies.

After optical pumping [4], the polarization chamber was opened to an evacuated sample in the NMR magnet, connected by thin teflon tubing. Xenon flowed continuously from the supply bottle through the polarization chamber, then to the sample in the NMR magnet, under the influence of a pump and moderated by a mass flow controller, both downstream of the NMR instrument. In Figure 1, a classic diffusive diffraction pattern is shown, obtained from polarized xenon gas flowing through a static 2 mm glass bead pack at different flow rates. At the highest flow rates, when spins are traversing multiple void spaces between beads, a diffraction minimum is seen at $0.7b^{-1}$, where b is the bead diameter. In Figure 2, we show initial results from studies of laser polarized gas fluidizing a sample of small glass beads in a column. The xenon intensity decreases at the point where the particle density is greatest. Localized PGSE-based measurements on the gas flow are now underway.

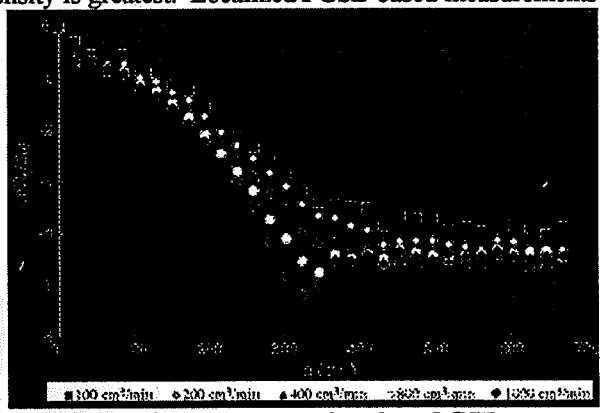

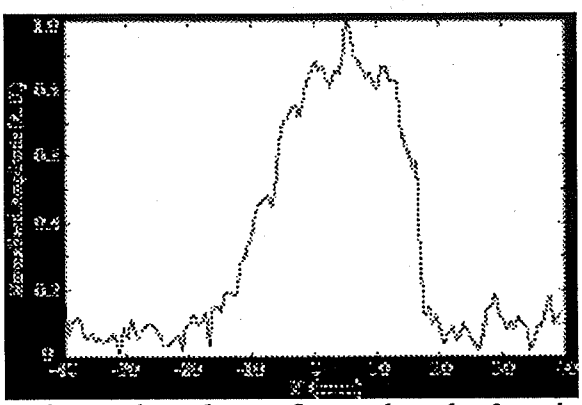

Fig. 1 (left). *Echo attenuation plots from PGSE experiments on laser-polarized xenon flowing through a 2 mm bead pack.* ***Fig. 2 (right).*** *Lengthwise 1-D profile of laser-polarized xenon flowing through a granular medium.*

The use of PGSE techniques allows the study laser-polarized xenon gas at high flow rates. In porous media studies, the high gaseous diffusion coefficient, and ability to control high flow rates allows structural characterization on larger length scales than are possible in liquid state NMR, while requiring less gradient strength. In granular media, the behavior of the interstitial gas can, for the first time, be probed.

References

1. P. T. Callaghan, *Principles of Nuclear Magnetic Resonance Microscopy*, Oxford University Press (1991).
2. T. G. Walker and W. Happer, *Rev. Mod. Phys.*, **69**, 629 (1997).
3. H. E. Moller, X. J. Chem, B. Saam, K. D. Hagspiel, et al., *Magn. Reson. Med.*, **47**, 1029 (2002).
4. R. W. Mair, C.-H. Tseng, G. P. Wong, D. G. Cory and R. L. Walsworth, *Phys. Rev. E* **61**, 2741 (2000).

Modified Behaviour on a Nanoscopic Level of Materials Confined in Porous Systems

Jonathan Mitchell, Sue C. Stark, and John H. Strange
School of Physical Sciences, University of Kent, Canterbury, Kent, UK, CT2 7NR

The properties of materials are altered on a nanoscopic level when confined in pores only a few angstroms in diameter. This modification of molecular behaviour is of interest due its potential use in chemical and catalytic reactions. Using a suite of nuclear magnetic resonance techniques, the behaviour can be studied and characterised. Ideal porous systems of silica glasses and sol-gel silicas have been used to allow systematic studies to be performed over a range of pore sizes without the complications of chemical interactions between the absorbate and the absorbent. The behaviour of water and cyclohexane has been explored in great depth and new discoveries are still being made. To further the understanding of these systems, naphthalene and various n-alkanes are being explored.

Using relaxation time measurements, diffusion studies, and field-cycling experiments, numerous behavioural phenomena have been observed, related to the confining geometry. The most notable result is the Gibbs-Thomson reduction in melting point of the confined material. The freezing point is also reduced and super cooling of the samples is possible. The sample will remain liquid well below even the depressed melting point before suddenly snap-freezing. The mechanism behind this process is not yet comprehensively understood. A secondary phase has also been noted, only one or two molecular diameters in depth, located at the interface between the confined materials and the pore wall. This has been termed the 'non-frozen surface layer' from studies of water ice at the interface. Although this phenomena has been observed in all the systems studied, the term 'non-frozen' is sometimes misleading. In naphthalene, for example, the surface layer is an irregular solid. The regular solid lattice has a transverse relaxation time of 10□s, whereas the surface layer has an increased relaxation time of ~100□s in pores ranging from 60Å to 200Å in diameter. This behaviour is indicative of an irregular crystal lattice, not a liquid in this material. Exchange between the regular solid and the surface layer has been observed in both water and naphthalene using the Goldman-Shen experiment for studying magnetisation transfer. There is also a critical pore diameter below which none of the confined material freezes into a regular state. For cyclohexane this is approximately 25Å and for naphthalene (having four times the molecular radius of cyclohexane) this diameter is 50Å. In pores below this critical size, the organic materials appear to enter an amorphous glassy state. Studies of cyclohexane have revealed metastable phases forming in the pores if the sample is quenched, but not on regular cooling. This was first observed in 20nm thin films of cyclohexane.

Even in relatively unreactive porous silicas, surface interactions can be significant. This is most obvious in water where the molecules in the liquid can interact and exchange with hydroxyl groups on the silica surface. The mobility of water molecules on the pore surface was reduced, whilst in non-polar organics the mobility increased in the surface layer. This difference is due to the increased residence time of polar molecules on the pore wall, caused by hydrogen bonding with the silica surface hydroxyl groups. These surface interactions have been shown to influence results from NMR relaxometry experiments. Another influence on the NMR results for materials confined in sol-gel silicas comes from the presence of paramagnetic impurities in the silica. This effect has been characterised by the technique of NMR cryo-relaxometry and high-resolution relaxation time measurements of the silicon in the gels. This has been shown to be the dominant relaxation mechanism for T1 and T1□, and to some degree, T2 in narrow-line systems in the porous media.

Pore filling mechanism of spontaneous imbibition in porous media determined by internal field effect and Conical-SPRITE MRI

Quan Chen[a], Murray K. Gingras[b], and Bruce J. Balcom[a]

[a]MRI centre, Department of Physics, [b]Department of Geology, P.O. Box 4400, University of New Brunswick, Fredericton, New Brunswick, E3B 5A3, Canada

Abstract

Spontaneous imbibition is the process by which a wetting fluid is drawn into a porous medium by capillary action. The imbibition effect is critical to oil recovery from sedimentary reservoirs, especially those reservoirs which are fractured. Ground-water flow in unsaturated layers is also related to the imbibition effect. Thus, studies of imbibition have received considerable attention. From previous investigations, different mechanisms of imbibition have been proposed. However, in the absence of direct measurements of pore- and throat- filling processes during imbibition in real porous media, it has not been possible to verify suggested pore-level mechanisms.

When a fluid-filled porous medium is subjected to a uniform magnetic field, a spatially varying field and its gradients appear inside the pore space due to susceptibility differences between the solid and the pore-filling fluid. The internal field depends on the geometry of the pore space. So, variations of the internal field in the pore space reflect pore size changes in media.

In this work, a new magnetic resonance technique, DDIF (the decay of magnetization due to diffusion in the internal field)[1], combined with mercury porosimetry, to investigate pore geometry[2], including pore- and throat-size distribution, and pore connectivity. Unlike relaxation time distributions, DDIF is less sensitive to surface relaxivity and diffusive coupling effects between interconnected pores and depends primarily on pore size.

As the mechanism of fluid displacement in porous media with centrifugation is well known, a comparison of DDIF spectra for fully saturated Berea sandstone with the partially saturated sample (centrifugation in air) at indicated that DDIF can be used for the measurement of water filled pore size distributions in partially saturated porous media.

Conical-SPRITE is a rapid, 3D, centric scanning, spin-density weighted single point imaging technique. Compared with the standard SPRITE (single-point ramped imaging with T_1 enhancement)[3] technique, Conical-SPRITE has many advantages, such as fast acquisition speed, low duty cycle and reduced sensitivity to spin-lattice relaxation time. It shows great advantages for solid materials with very short relaxation time.

Dynamic water imbibition into air-filled Berea sandstone was investigated using a DDIF water filled pore- and throat- size distribution measurement technique. In-situ 3D saturation and capillary driven water penetration were monitored using Conical-SPRITE. These measurements provide direct evidence for differences in the pore filling mechanisms for co-current imbibition and counter-current imbibition in Berea sandstone.

During spontaneous co-current imbibition, water flows through the pores and connected throats with a piston-type mechanism. Air is displaced from the sample by the leading edge of the waterfront, resulting in a macroscopic piston-like flow through the entire sample.

During spontaneous counter-current imbibition, water flows through the pores and connected throats with a film-like structure along the corners and surfaces of the pore space. Air escapes from the sample by flowing through the center of the pores and pore throats, in the opposite direction. Once the penetrating waterfronts meet, at the sample center, there is a global, uniform increase in water content.

This study has for the first time combined the DDIF water-filled pore size distribution method in partially saturated porous media with Conical-SPRITE imaging.

References

[1] Yi-Qiao Song, Seungoh Ryu et al, *Nature* **406**, 178-181 (2000).

[2] Quan Chen and Yi-Qiao Song, *Journal of Chemical Physics* **116**, 8247-8250 (2002).

[3] Bruce J. Balcom, Rod P. MacGregor et al, *Journal of Magnetic Resonance Series A* **123,** 131-134 (1996).

Magnetic resonance imaging and spectroscopy of catalytic reactions

I.V. Koptyug, A.A. Lysova, A.V. Kulikov, V.A. Kirillov, V.N. Parmon, R.Z. Sagdeev
International Tomography Center, Boreskov Institute of Catalysis, and Novosibirsk State University, Novosibirsk 630090, Russia

An important problem in chemical engineering and catalysis is the influence of mass and heat transport on a chemical reaction, and in particular the possible coupling of the transport processes with the chemical transformation. These issues are directly related to the efficiency of large-scale reactors and the safety of their operation. One of the striking examples of a coupling of mass transport and the chemical reaction is the Belousov-Zhabotinsky (BZ) oscillator. We have employed the MRI technique to study the propagation of chemical waves in the BZ reaction carried out in model porous media. The reduction of the wave front velocity is shown to be related to the reduction of the effective diffusivity in porous media as compared to bulk liquids. For given concentrations of the key reactants, a critical pore size value exists below which the propagation of concentration wave fronts is not observed. The most interesting behavior is found when the reaction mixture flows in a porous medium. The measured velocity of the downstream propagating front is much larger than the sum of the average flow velocity and the front velocity in a static system. The front which travels in the opposite direction can be made stationary relative to the bed by appropriately adjusting the liquid flow rate. It is shown, however, that it can remain stationary if the flow velocity is further increased by an order of magnitude. Such an exciting behavior is caused by the dispersion phenomena upon filtration of fluids in porous media [1].

Heterogeneous catalytic hydrogenation is one of the model reactions widely used in the studies aimed at a better understanding and the optimization of large-scale catalytic processes, and is also of practical importance for chemical industry. We have employed a combination of NMR imaging and spectroscopy to visualize the processes in an operating single catalyst pellet or in a granular catalyst bed. During the experiments, the catalyst (1% Pd/γ-Al_2O_3) is residing inside the rf coil of the NMR instrument, and the H_2 gas and the liquid reactant (α-methylstyrene) preheated to 68-80 ^{0}C are supplied to the reaction volume. The catalyst temperature can be as high as 170-190 ^{0}C due to the exothermic nature of the reaction. A slice-selective spin-echo sequence was used to obtain 2D images of the liquid distribution with the spatial resolution of 230×140 μm^2 (pellet) or 230×310 μm^2 (bed) within a 2 mm slice. To reduce the T_1 times of the liquids, the catalyst was impregnated with Mn ions. This allowed us to acquire the 2D images in 34 s and to obtain a detailed picture of the redistribution of the liquid phase within the pellet or the bed in the course of the reaction. These studies have revealed the existence of the oscillating regimes of the process caused by the oscillations of the catalyst temperature and directly demonstrated the existence of the coupling of mass and heat transport with the chemical reaction itself.

In order to determine the composition of the liquid phase with spatial resolution, free induction decays were phase encoded along one or two spatial coordinates within a vertical slice of a cylindrical catalyst bed. Despite a substantial linewidth, the spatially resolved NMR spectra clearly indicate the increase in the relative amount of product (cumene) towards the lower (downstream) edge of the catalyst bed. We have shown earlier [2] that substantial line broadening and distortions in the NMR spectra of liquids permeating porous solids can be somewhat reduced if the NMR spectra are detected with spatial resolution. Our latest results show that the linewidths are further reduced at elevated temperatures (ca. 800 Hz at 20 ^{0}C; ca. 300 Hz at 130 ^{0}C). Note that these preliminary spectroscopic experiments were performed under highly unfavorable conditions, i.e., with the catalyst impregnated with paramagnetic Mn ions. Without them the lines should be appreciably narrower, and an accurate quantification of the mixture composition throughout the catalyst pellet or bed should be possible.

This work was supported by RFBR (grants ## 02-03-32770, 03-03-06020), and the Russian President's program of support of the leading scientific schools (grant # NSch-2298.2003.3). A.A. Lysova acknowledges a scholarship awarded by the Zamaraev Charitable Scientific Foundation.

References

[1] I.V. Koptyug, A.V. Matveev et al, *Appl. Magn. Reson.* **22,** 187-200 (2002).
[2] I.V. Koptyug, A.V. Kulikov et al, *J. Amer. Chem. Soc.* **124,** 9684-9685 (2002).

On-Line Monitoring with the NMR-MOUSE® during Tire Production

Kai Kremer, Nicolae Goga, Bernhard Blümich
Institut für Technische Chemie und Makromolekulare Chemie, RWTH-Aachen, D-52074 Aachen

Analysis of elastomer materials and products can be done with mobile nuclear magnetic resonance. Unilateral NMR sensors like the NMR-MOUSE provides a new and powerful concept for on-line quality control in combination with rheometry on test samples and nondestructive measurements on the final product.

A particular application of the NMR-MOUSE is measuring rubber test samples of a rubber process analyzer (RPA) in order to obtain reference NMR-parameter for nondestruvtive product and quality control. Usually the formulation of a technical rubber product is tested on a rheometer, where a test sample is vulcanized, undergoing small oscillatory shear deformation. During curing, the torque increases to a maximum and decreases on further curing following reversion of the cross-linking reaction. From the theory of rubber elasticity, it is known that the torque at small deformation is a direct measure of the crosslink density. NMR relaxation measurements have turned out to be extremely useful for quality control of elastomer products in connection with a database of reference values for different formulations and curing parameters. In this project we followed the complete production process of a tire to investigate dispersions in the raw polymer, at all intermediate processing steps and before and after the vulkanisation of a tire. We made non-invasive on-line measurements of T_2 with the NMR-MOUSE at all steps of the production and compared the data with those of standard RPA and MDR rheometer tests. The skillful use of the NMR-MOUSE can help to replace some of the expensive tests on the racetrack by measurements in the laboratory.

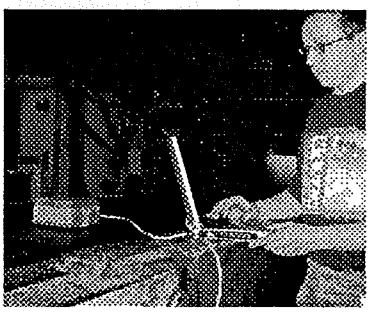

Figure 1: On-Line measurements at a tire factory.

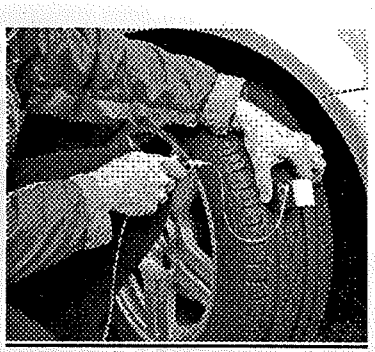

Figure 2: NMR-MOUSE testing a tire.

References

[1] G. Eidmann, R. Savelsberg, P. Blümler, B. Blümich, *The NMR MOUSE: A Mobile Universal Surface Explorer*, **J. Magn. Reson.** A 122, 104-109 (1996).

[2] B. Blümich, V. Anferov, S. Anferova, M. Klein, R. Fechete, M. Adams, F. Casanova, *A Simple NMR-MOUSE® with a Bar Magnet*, **Magn. Reson. Eng.** 15 (4), 255-261 (2002).

[3] B. Blümich, S. Anferova, K. Kremer, S. Sharma, V. Herrmann, A. Segre, *Unilateral NMR for Quality Control: The NMR-MOUSE®*, **Spectroscopy** 18(2), 18-32 (2003).

Flow Characterization Using a Single-Sided NMR Probe

Federico Casanova, Juan Perlo, and Bernhard Blümich
ITMC - RWTH-Aachen Worringerweg 1, D52056 Aachen, Germany

Nuclear Magnetic Resonance has proved to be a powerful tool to study motion at a microscopic and macroscopic scale. A large number of methods have been proposed to measure, for example, vascular flow in steams an petioles at various stages of plant development, as well as vascular blood flow at various stages in the cardiac cycle [1,2]. Also numerous applications in porous materials as natural sandstone have made possible the elucidation of models that describe the transport of fluids within the porous structure [3]. Diffusion and velocities measurements are predominantly carried out using PFG-SSE (pulsed field gradient stimulated spin echo) sequences [1]. Different modifications to this pulse sequence have been proposed with good success to reduce distortions introduced by static background gradients due to susceptibility variations across the object or spatial variation of the polarizing magnetic field [4].

These sequences have been tested using conventional NMR magnets having small static gradients but never using single-sided probes. Inside-out NMR uses unilateral sensors for near-surface studies of arbitrarily large objects and due to the open geometry of these magnets the magnetic field possess a strong static gradient [5].

In this work we implemented an alternating-pulsed-gradient stimulated-echo sequence to measure one-dimensional velocity profiles using a NMR-MOUSE (mobile universal surface explorer) unilateral sensor. The NMR-MOUSE combines two permanent magnets positioned on an iron yoke in an anti-parallel way forming a U-shaped geometry, and for exitation and detection it uses a surface RF coil positioned in the gap between the magnets [6]. In this work an optimized U-shaped magnet was used. It provides a static magnetic field with a uniform gradient of 2.5 T/m along the depth direction. This constant gradient defines a rather flat sensitive volume at a depth position that can be selected by retunning the probe frequency. An appropriated coil system to supply the pulsed gradient field along a lateral direction (gap direction) necessary for displacement encoding was built and positioned in the gap between the magnets.

To test the method one-dimensional velocity propagators have been measured for different pipe geometries with a velocity resolution better than 1 mm/s. To improve the signal-to-noise-ratio a multi-echo sequence was implemented during the detection period. Taking advantage of the large number of echoes that can be generated in liquid samples a large sensitivity enhancement has been obtained by adding the echoes of the train. Finally, using the slice selection provided by the strong static gradient velocity profiles at different depth have been measured obtaining 1D spatially resolved velocity profiles along the depth direction and up to 15 mm deep in experimental times of some minutes. Experimental results have been compared with calculated velocity profiles showing good agreement and demonstrating a PFG-SSE sequence can be implemented in the inhomogeneous magnetic fields of single-sided probes to determine fluid transport properties inside the sensitive volume defined by these sensor.

References

[1] P. T. Callaghan, *Principles of NMR Microscopy*, Clarendon Press, Oxford, (1991).
[2] B. Blümich, *NMR Imaging of Materials*, Clarendon Press, Oxford, (2000).
[3] K.J. Packer, and J. Tessier, *Molecular Physics*, **87**, 267, (1996).
[4] R.M. Cotts, M.J.R. Hoch, T. Sun, J. T. Markert, *J. Magn. Reson.*, **83**, 252 (1989).
[5]G. A . Matzkanin, Non-Destructive Characterization of Materials, Springer-Verlag (1989).
[6] G. Eidmann, R. Savelsberg, P. Blümer, and B. Blümich, *J. Magn. Reson.* A 122, 104 (1996).

NMR Study of Changing Morphology of Porous Al_2O_3 during Deactivation and Regeneration

Xiaohong Ren, Siegfried Stapf, Bernhard Blümich
Institute of Technical Chemistry and Macromolecular Chemistry, RWTH Aachen,
D-52074 Aachen, Germany
Dahai Tang, Andreas Jess
Lehrstuhl für Chemische Verfahrenstechnik, University Bayreuth,
D-95440 Bayreuth, Germany

In catalytic hydrocarbon conversion processes, the reversible deactivation of the catalysts has been mainly associated with the carbonaceous residues (coke) formed on the catalyst surface, which block the active sites and inhibit the molecular transport. Therefore the interest in these catalysts lies not only in their high catalytic activity and selectivity, but also in the possibility of regenerating them several times so that their "lifetime" is compatible with the cost of their production. However, due to the complex mechanism of the deactivation, the understanding of the fundamental mechanisms of the regeneration processes remains poor or inconsistent which has restrained the simulation and optimization for both procedures.

Compared to the NMR study on a naphtha reforming catalyst Pt/Re-Al_2O_3 [1], the porous support Al_2O_3 was selected as a model system in this work in order to simplify the mechanism of the deactivation. Different NMR techniques were applied for characterizing the changing morphology of Al_2O_3 during the deactivation and regeneration processes on length scales not accessible directly by conventional NMR imaging.

The self-diffusion of pure fluids (n-heptane) as well as the diffusion of fluids in the Al_2O_3 support were measured. Due to the short transverse relaxation time of protons of liquids adsorbed in the catalyst samples, the measurement of the self-diffusion coefficient is performed using an echo-recalled PGSTE procedure [2]. Based on these measurements, the tortuosity was evaluated from the ratio of the diffusion coefficient of the confined and bulk liquid [3]. The relationship between tortuosity and the coke content for both deactivation and regeneration processes is discussed.

Based on the NMR measurements of the freezing point depression of cyclohexane in the pores[4], the change of the pore size distribution of the support during both processes was investigated. The results were compared with those obtained from the BET method and corroborate the findings obtained from the tortuosity measurements. Moreover, the diffusion and relaxation properties of freezing cyclohexane at different temperatures have been investigated and were connected with the coke distribution.

Furthermore, the influence of the coke content on the relaxation properties of different adsorbed molecules as a function of Larmor frequency [5] was studied. Combining the results from these different techniques, a model for the kinetics of deactivation and regeneration was derived.

References

[1] X.-H. Ren, M. Bertmer, S. Stapf, D. E. Demco, B. Blümich, C. Kern, A. Jess, *Appl. Catal. A: General*, **228**, 39 (2002).
[2] B. Blümich, *NMR Imaging of Material*, Clarendon Press, Oxford (2000).
[3] R. W. Mair, G. P. Wong, D. Hoffmann, M. D. Hürlimann, S. Patz, L. M. Schwartz, R. L. Walsworth, *Phys. Rev. Lett.*, **83**, 3324 (1999).
[4] J. H. Strange, M. Rahman, E. G. Smith, *Phys. Rev. Lett.*, **71**, 3589 (1993).
[5] X.-H. Ren, S. Stapf, H. Kühn, D. E. Demco, B. Blümich, *Magn. Reson. Imaging, in press*

Dynamic microscopy of flow in model fixed-bed reactors

Xiaohong Ren, Siegfried Stapf, Bernhard Blümich
Institut für Technische Chemie und Makromolekulare Chemie ITMC, RWTH Aachen,
Worringerweg 1, D-52074 Aachen, Germany

The design of fixed-bed reactors, consisting of randomly packed porous particles which act as catalytic reaction sites and are subjected to flow of a fluid containing reactants, depends vitally on a thorough understanding of flow processes. Most classic techniques access only integral quantities such as the long-time limit of the dispersion coefficient, residence-time distributions or averaged conversion factors which quantify the efficiency of the reactions taking place in the reactor. PFG-NMR allows not only to determine the temporal evolution of the dispersion process in the preasymptotic regime, but also to provide spatial information such as maps of the spin density or the relaxation time, and to correlate motional with spatial parameters by suitable combinations of ***k*** space and ***q*** space microscopy.

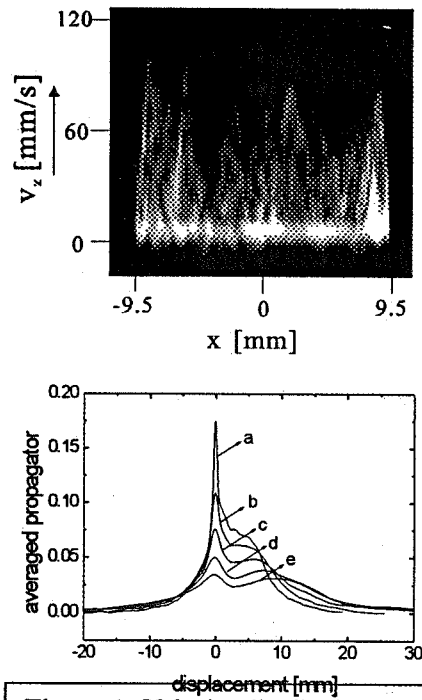

Figure 1: Velocity distribution for a cross-section of a fixed bed with 4 mm diameter glass beads for 7 ms encoding time (top) and volume-averaged over increasing encoding times from 250 to 750 ms (bottom).

In this study, different techniques to obtain velocity information were combined for a systematic investigation of fixed beds as a function of particle size, shape and material. The beds were generated from random packings of spherical glass beads and commercial, metal-containing porous catalyst pellets of spherical and cylindrical shape of different sizes d_p inside cylindrical tubes of diameter d_t. Flow investigations were performed for reduced dimensionless tube diameter d_t/d_p in the range 1.3 to 32. The influence of pellet ordering effects on the distribution of flow channels is demonstrated employing static and velocity encoded spin density images. The velocity distribution averaged over the radial coordinate in the tube follows an oscillatory pattern which largely reflects the ordering of the particles themselves, being accessible by determining the density distribution of the interparticle fluid [1,2]. Both the ordering of the pellets and the flow channels persist, although less pronounced, for irregularly-shaped catalyst particles. In all cases, flow occurs mainly along a few backbone branches [3], constituting a small fraction of the total cross-section of the reactor. The time-dependence of axial displacements is discussed by applying either volume-averaged long-time propagator techniques (see Fig. 1, bottom) or combining one- and two-dimensional ***k*** space imaging with velocity measurements over short encoding times (Fig. 1, top) to provide a connection between local and space-averaged transport properties. Based on these statistical descriptions obtained from comparing displacement distributions for different flow rates, times and particle morphologies, the evolution of the relative fractions of flowing and stagnant fluid (the latter predominantly comprising liquid trapped in the interparticle voids) is discussed [4], providing an indirect measure of the reactor efficiency.

References

[1] J.N. Papageorgiou, G.F. Froment, *Chem.Eng.Sci.* **50**, 3043 (1995).
[2] J.Götz, K.Zick, C. Heinen, T.König, *Chem.Eng.Process.* **41**, 611 (2002).
[3] L.F.Gladden, *Topics in Catalysis* **8**, 87 (1999).
[4] U.Tallarek, D.van Dusschoten, H.Van As, E.Bayer, G.Guiochon, *J.Phys.Chem.B* **102**, 3486 (1998).

Imaging of Materials with Multiple NMR-MOUSE Sensors and Caterpillar

L.Grunin[1], M.Bruder[1], B.Blümich[2], D.Karasev[3], I.Ivanov[3], I.Nikolaev[3]
[1]INTECH Thüringen GmbH, Germany; [2]RWTH Aachen, Germany,
[3]Mari State Technical University, Yoshkar-Ola, Russia

For investigation of internal structure of closed-loop samples it was built the NMR-based imaging device, containing one 18 MHz NMR spectrometer that controlled several NMR-MOUSE sensors, gradient amplifier and the mechanical caterpillar system for moving a sample. It was constructed the specialized software for simulation of an experiment and simultaneous acquisition of multiple images.

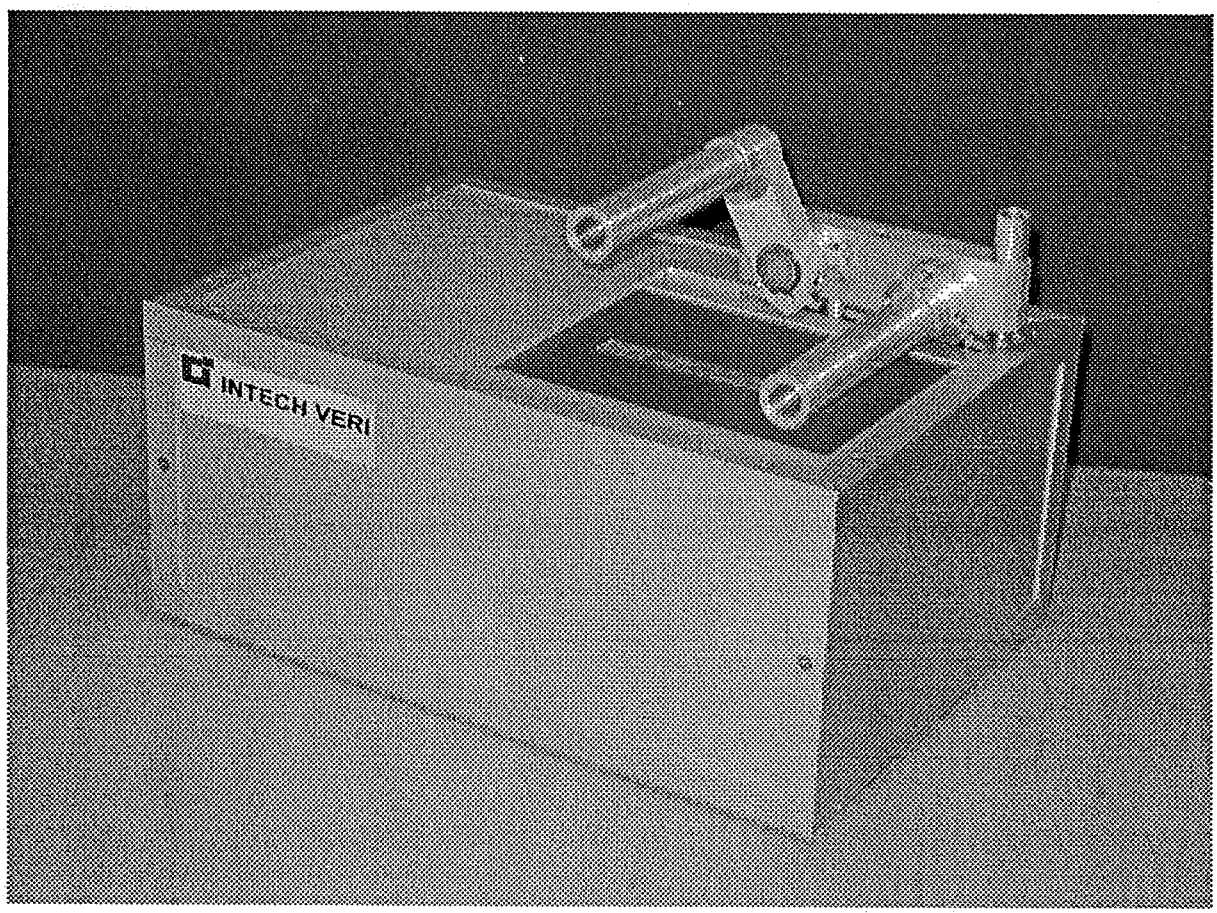

Figure 1: INTECH VERI Sensor

To reach the highest spatial resolution up to 0.1 mm and maximum speed of an experiment the multi-solid-echo sequence was used. The amount of echoes in the sequence was reduced because of the inhomogenity of the magnetic field across the gap of NMR-MOUSE.
Both the results of test measurements and numerical calculation and surface multi-channel MRI simulating software are presented.

Investigation of artificial paper aging by the NMR-MOUSE

C. Blümich,[a] S. Anferova,[a,b] V. Anferov,[a,b] A.L. Segre,[c] C. Federici[d] and B. Blümich[a]

[a] Institute of Technical Chemistry and Macromolecular Chemistry, RWTH, D-52056 Aachen, Germany

[b] Kaliningrad State University, 236041 Kaliningrad, Russia

[c] Institute of Chemical Methodologies of CNR, M. B. 10, 00016 Monterotondo Stazione, Rome, Italy

[d] Instituto centrale di patologia del libro, Via Milano 76, 00184 Rome, Italy

The NMR–MOUSE is a mobile sensor for single-sided NMR inspection of organic materials [1]. It was successfully used for nondestructive discrimination of different degrees of paper degradation of historical books using the Hahn echo sequence [2]. An improved NMR-MOUSE with a meander coil was constructed to aim at very shallow penetration depth (Fig. 1a). The meander coil produces an effective alternating magnetic field at a small distance from the surface of the coil and enables NMR measurements from the surface of samples and from the thin samples of 0.1-0.3 mm thickness. The meander coil is manufactured on glass and fixed by a small amount of glue, which gives a low background signal. The short dead time of the NMR-MOUSE with the meander coil (about 15 μs) permits the measurement of rapidly relaxating signals using the CPMG sequence. The measurement time was reduced from 24 hours with the Hahn echo sequence to 45 minutes using CPMG method. The static magnetic field is generated by two antiparallel permanent magnets positioned on an iron yoke in the horseshoe geometry. Both magnets are widened at the ends to reduce the homogenity of the magnetic field along the gap from 10% to 5%.

Two series of unaged and artificially aged sheets of watman paper with the thickness of 0.3 mm were investigated using the CPMG sequence with a very short echo time of 30 μs (Fig. 1b). From the logarithmic presentation it is obvious, that the decays are bi-exponential. The fast decaying exponent with T_{2short} values in the range of 0.11-0.14 ms corresponds to the cellulose protons and is not influenced by the aging process. The long component T_{2long}, which is known to be characteristic of the state of paper, corresponds to water protons. With increasing degradation of paper it is decreasing because of water loss.

All sheets of watman paper which were treated with different types of biological glue have higher values of T_{2short} and T_{2long} in comparison with the untreated material. The aging process of the treated sheets with biological glue (food gelatin and fish glue) gives rise to lower T_{2long} values in comparison with the same unaged sample. For aged sheets treated by synthetical glue aging process is not noticed. It is conducted, that the aging process is less effective in the treated sheets.

References

[1]B. Blümich, S. Anferova et al, Spectroscopy, **18**, 18-33 (2003).

[2] B. Blümich, S. Anferova et al, *Journal of Magnetic Resonance* **161,** 204-209 (2003).

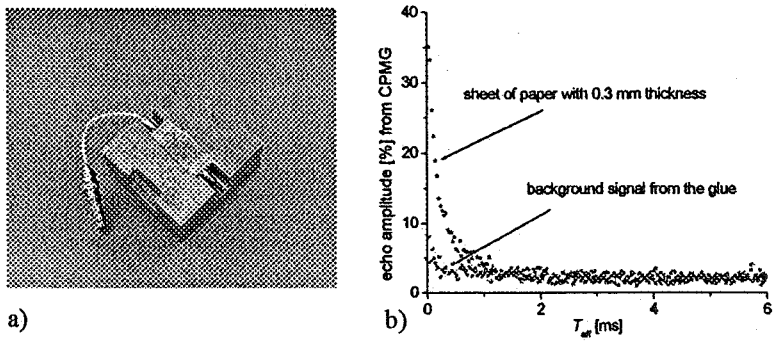

Figure 1:a) NMR-MOUSE with the meander coil on a glass support. b) CPMG echo decays from one sheet of paper and empty probe.

Design and Construction of a Portable One-Sided Access NMR Probe

Mark W. Hunter[1], Paul T.Callaghan[1], Robin Dykstra[2] and Craig D. Eccles[2]
[1]Macdiarmid Institute for Advanced Materials and Nanotechnology,
Victoria University of Wellington, Wellington, New Zealand.
[2]Institute of Fundamental Sciences,
Massey University, Palmerston North, New Zealand.

The distribution of moisture in concrete during the curing process gives important information about its strength, possible crack formation and readiness to accept coverings. A non-destructive method to measure moisture profiles is of particular interest in the case of floor slabs. A one-sided access nuclear magnetic resonance (OSA-NMR) probe provides a useful solution.

Conventional NMR has the sample inserted in a large magnet with a homogenous field from a super conducting solenoid. In this case we are limited to access from one side of the sample only, therefore a homogenous region needs to be produced remotely from the probe. A region 55mm deep, of field strength 10mT with a volume of approximately $10^{-6}m^3$ is achieved using an array of permanent magnets.

The design of the field involved numerical simulations of the magnets using a Biot-Savart calculation in MATLAB. The required field was defined in terms of its Taylor coefficients. The positions of the magnets were adjusted using Newton's method until the desired coefficients were found. This proved to be a simple and robust technique to solve the problem of generated the required field. The array was constructed and the design verified using field mapping techniques. A simple B_1 surface coil was designed and built to try and optimize signal-to-noise.

References

NMR Apparatus. New Zealand patent application 520114

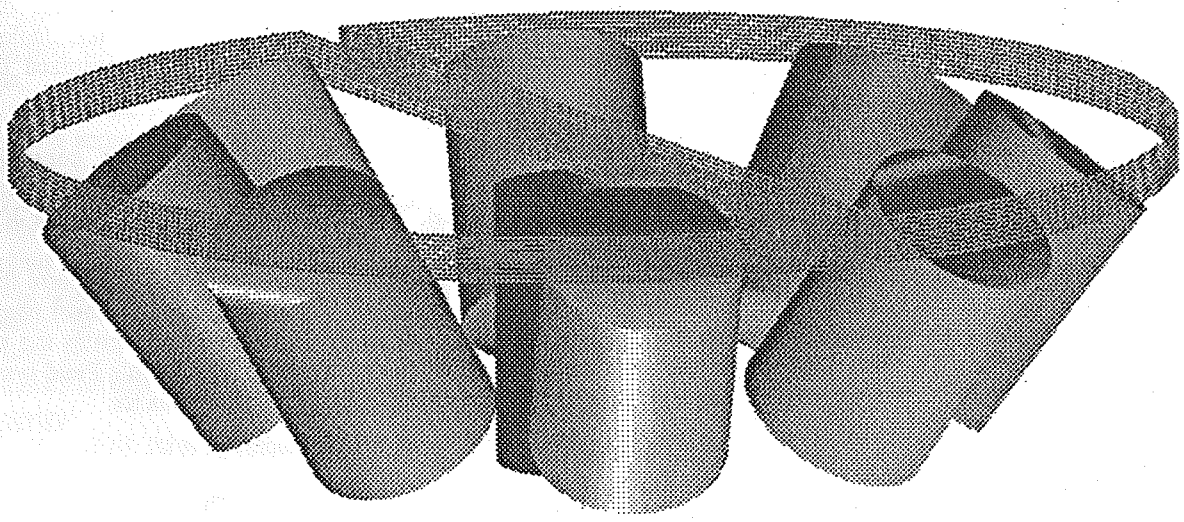

A schematic diagram of the magnet array and B_1 coil

A Portable NMR System for Remote Measurements

Robin Dykstra[1], Paul T. Callaghan[2], Craig D. Eccles[1] & Mark W. Hunter[2]
[1] Institute of Fundamental Science, Massey University, Palmerston North, New Zealand.
[2] MacDiarmid Institute of Advanced Materials and Nanotechnology, School of Chemical and Physical Sciences, Victoria University of Wellington, Wellington, New Zealand.

A portable NMR system has been developed to enable measurements to be performed at remotes sites. The central part, known as the "system core", consists of a Digital Signal Processor (DSP) based pulse programmer and data acquisition board and uses a Universal Serial Bus (USB) interface to communicate with a host laptop computer [1]. A graphical user interface is provided by an application running on Windows XP. This interface is fully configurable and scriptable through the use of a macro language and a set of standard commands. Pulse programs can be generated using the built-in language provided by the user interface or by using a C compiler/assembler to generate code for the DSP itself. The DSP runs at 100 MHz and therefore provides a pulse program timing resolution of 10 ns.

A RF transceiver board has also been developed that uses digital signal processing techniques to sample the FID, immediately after the IF stage or the preamp, with a 14-bit, 50 MHz digitizer. The FID is then mixed digitally with synthesized sine and cosine functions to generate the lower frequency quadrature outputs. This technique guarantees gain matching and zero DC offsets of the quadrature channels. This eliminates the need for the phase cycling techniques that are usually required to overcome these problems. The bandwidth of the receiver can be up to 1 MHz and its output is fed to the DSP for further processing and storage. Another matched synthesizer is used to generate any required B_1 signals. Both synthesizers have phase and frequency hopping capabilities and are phase locked to each other and the DSP. The synthesizer frequencies are determined by the user and can be set between 0 and 25 MHz with a frequency resolution of less than 0.02 Hz. The analog input to the receiver has a 250 MHz bandwidth, allowing undersampling techniques to be used for input signals with frequency components greater than 25 MHz. A 100 MHz, 14-bit digitizer version of the transceiver is planned for the near future.

The DSP and RF transceiver are built on standard Euro-card sized multi-layer PCBs and connect to each other via a back plane. This enables a system to be built up in a standard rack mount case. The RF amplifier, duplexor and preamp requirements are determined by the NMR probe and are therefore designed and optimized for each application.

One of our main applications is the moisture profiling of curing concrete. Here a surface probe, consisting of a permanent magnet array, generates a relatively homogenous B_0 field 50 mm below the surface. Mobile protons in this region are then excited by a B_1 pulse generated by a butterfly coil. The ^1H resonant frequency is about 400 kHz.

Another application is Earth's Field NMR. Here a lower speed digitizer board was developed to capture the audio frequency FID at an oversampled rate. The DSP performs all the necessary digital filtering and down conversion. This method is very flexible and allows for the quick modification of the filter response, eliminates the need for complicated anti-aliasing filters and reduces the amount of noise due to quantization. The Earth's Field system has been used extensively in Antarctica to perform brine content and mobility measurements on sea ice.

References

[1] R. Dykstra, *Proceedings of the Ninth Electronics New Zealand Conference*, 6-11 (2002).

STUDY OF THE BEHAVIOUR OF AN L_3-PHASE UNDER SHEAR USING RHEO-NMR

Antoine Lutti and Paul T. Callaghan
MacDiarmid Institute for Advanced Materials and Nanotechnology
Victoria University of Wellington, New Zealand

Surfactants in solution lead to various self-aggregates, the structure of which depends on the intrinsic properties of the surfactants and on some space-filling constraints. The objective of this work is to study the dynamics of the transition induced by shearing on an L_3-phase. This so-called sponge phase is a lyotropic, thermodynamically stable, optically isotropic, bicontinuous phase (fig.1). The shear-induced transitions of this system have been the subject of intense study using various methods (neutron [3] and X-ray [4] scatterings, measurement of the birefringence [3,5], rheology [5]) and various surfactant systems. All of them lead to the same conclusion at high dilution of the phase: the sponge phase transforms into a lamellar phase above a threshold value of the shear rate, which is proportional to the dilution of the phase. However, the dynamics of the transition (namely the formation and the orientation of the subsequent lamellar phases), as well as the dependence on the dilution is still an open issue [3]. Indeed, an absence of a transition below a precise value of the dilution has been noticed, without the occurrence of a sudden change in the structural properties of the phase.

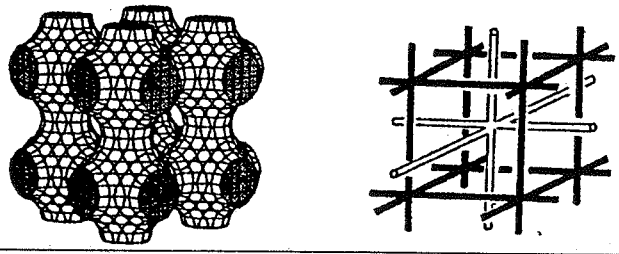

Fig.1 Minimal surface over which an L_3 phase is draped and topology of the two struts corresponding to the bicontinuous solvent phases.

The aim of this work is to study this phenomenon using a Nuclear Magnetic Resonance (NMR) device as well as rheometry. In the NMR-experiment, the shear is applied using a Couette cell located inside a Bruker micro-imaging coil that applies the radio frequency field. The cell and the probe are then placed in a superconducting magnet producing a magnetic field of 7 Tesla (Fig.2). The whole device is such that the applied shear rate as well as the temperature of the sample is tunable.

NMR enables the measurement of anisotropic diffusion, the velocity distribution across the gap of the Couette cell, the variation of the order parameters and of the chemical shifts [6]. These are crucial parameters in the determination of the structure and orientation of the sample under study. The rheology experiments are performed using an ARES Rheometrics controlled strain-rate rheometer. They allow the rheological response of the resulting phase to be obtained for several types of shearing mode. The association of NMR and rheology will supply a new understanding of the transition, which will improve the comprehension of the dynamics and the dependence on dilution of the phenomenon.

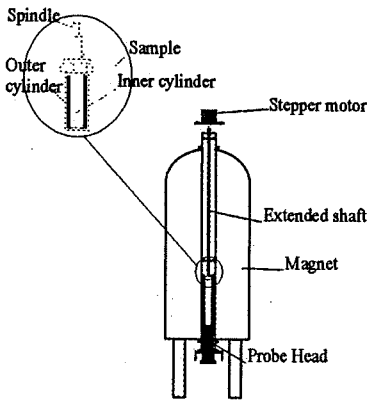

Fig.2 Experimental setup

References

[1] M.L Foo, J.M. Jarvis, Princeton University, Ceramic Materials Laboratory, 2001
[2] R.G. Larson, *The structure and rheology of complex fluids*, Oxford, 1999.
[3] O. Diat and D. Roux, *Langmuir*, 11 (1995) 1392.
[4] H.F. Mahjoub, C. Bourgaux, P.Sergot, M.Kleman, *Phys.Rev.Lett*, 81 (1998) 2076.
[5] M. Kleman, Pramana, *J. Phys*, 53 (1999) 107.
[6] P.T Callaghan *"Principles of NMR Microscopy"*, Oxford: Clarendon Press, 1991.

NMR Imaging of Microbial Transport in Porous Media

Justin P. Gage, Joseph P. Seymour, Sara Codd, Robin Gerlach
Department of Chemical Engineering, Montana State University, Bozeman, MT 59717, USA

Abstract
Biofilms are heterogeneous structures which form on solid surfaces exposed to aqueous environments under physiological conditions. Biofilms consist of bacterial cell clusters held together in an extracellular polysaccharide (EPS) matrix [1]. The presence of biofilms can cause biofouling resulting in reduced heat exchanger and pump efficiencies, infections associated with the use of medical implant devices, and contamination in water distribution systems as well as in the food processing industry. In addition, bacteria in the biofilms state are found in the subsurface and play an integral role in the biotransformation and transport of contaminant compounds. The study of the impacts of biofilms on the transport properties of porous media systems is of interest in many fields such as packed-bed reactor design and operation, enhanced oil recovery, in situ bioremediation, and the modeling of contaminant transport in geological media. The rate of biofilm growth in porous media systems, and therefore the biotransformation rate, is strongly influenced by transport properties such as pore velocity distribution, dispersivity, and molecular diffusivity [2]. Therefore, the processes of subsurface mass transport, biotransformation and biofilm growth are all closely related. The use of nuclear magnetic resonance (NMR) imaging technology provides a non-invasive technique capable of resolving transport properties over different spatial and temporal scales under a variety of experimental conditions. Recent work in our group has demonstrated the ability of NMR imaging to image biofilms in flow systems. A model porous media system comprised of 240 μm monodispersed polystyrene beads is used in this study. NMR imaging techniques such as Pulsed Gradient Spin Echo (PGSE) methods were performed to gather diffusion and velocity data in the sterile porous media column. In addition, similar experiments were conducted with biofilms present within the porous media column and transport properties were evaluated over large times to monitor for processes such as biofilm growth and decay.

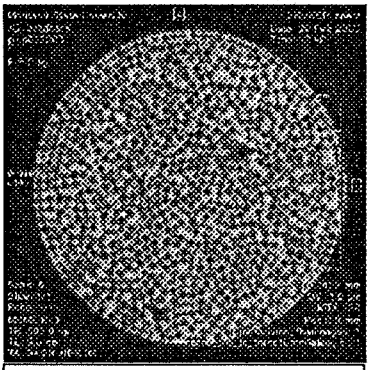

Figure 1: Porous media column consisting of 240 μm polystyrene beads.

References
[1] J. William Costerton, Zbigniew Lewandowski, Douglas E. Caldwell, Darren R. Korber, and Hilary M. Lappin-Scott. Microbial Biofilms. Annu. Rev. Microbiol. 49: 711-745 (1995).
[2] A. B. Cunningham, E. J. Bouwer, W. G. Characklis. *Biofilms*; W. G. Characklis, K. C. Marshall, Eds.; New York, 1990; Chapter 18, pp 697-732.

Microfluidics of Colloidal Particles by NMR PGSE Measurements

Jennifer R. Brown, Joseph D. Seymour and Sarah L. Codd
Department of Chemical Engineering, Montana State University, Bozeman, MT 59715, USA

Microfluidics, the process of fluids moving in small channels[1], is being investigated in the context of colloidal particle suspensions. Multi-dimension PGSE experiments[2] will be used to study the motion and mixing of colloidal particles in small channels with eventual applications to porous media. NMR techniques are a useful tool in studying colloidal systems since they are generally opaque. In addition, microstructure and diffusion can be measured directly. The colloidal particles used in the majority of these experiments are 214 nm diameter positively charged, monodisperse polystyrene latex spheres from IDC Latex, Portland Oregon. The particles are suspended in distilled water with the volume fraction at 4.2%. A slug of these particles was injected into a 1.9 mm diameter PTFE tube that was then sealed at one end and covered at the other to reduce water evaporation from the sample. During a two-month time period NMR diffusion, T_2 and density maps are being used to analyze the process of drying and particle volume fraction heterogeneity in the sample. There are many complex interactions of forces in the suspension microstructure and the results sought here have the potential to generate a better understanding of these types of systems. Other possibilities include looking at the sedimentation of red blood cells in blood and the behavior of a colloidal particle suspension in various rheometric and micro-scale flows.

References:

[1] H.A. Stone and S. Kim, *AIChE Journal* **47**, 1250 (2001)
[2] P.P. Mitra, *Phys. Rev. B* **51**, 15074 (1995).

MR microscopy of water distribution and dynamics in Polymer Electrolyte Membranes (PEMs)

James C. Mabry[1], Sarah L. Codd[1], Scott C. Busse[2] and Joseph D. Seymour[1]
[1]Department of Chemical Engineering, Montana State University, Bozeman MT
[2]Department of Chemistry, Montana State University, Bozeman MT

Broad application of hydrogen fuel cells is limited in part by failures of the ion conducting membranes central to their operation. The polymer electrolytic membrane (PEM) used in this study was Nafion® 117 (N-117). N-117 is a perfluorosulfonic acid (PFSA) polymer that is fabricated from a copolymer of tetrafluoroethylene and perfluorinated monomers containing sulfonic acid groups. The N-117 has the chemical and thermal stability of DuPont™ Teflon® fluoropolymer resins. While Teflon® is one of the most hydrophobic substances known, N-117 is one of the most hydrophilic. It will absorb water and some polar organics rapidly, even at room temperatures, depending upon the number of sulfonic acid groups. Whereas Teflon® resin is chemically inert, N-117 is a strong polymeric acid that reacts with organic and inorganic bases. However, the sulfonic acid groups in the polymer are essentially immobile and immersed in a fluoropolymer matrix. Hydronium ions are transported through the membrane from the anode side of a fuel cell to the cathode side where the H^+ reacts with oxygen to generate current across the fuel cell. One of the problems with using PEMs in fuel cells is their high mechanical failure rate, which may be due to inhomogeneity in the membrane structure.

Magnetic resonance microscopy (MRM) can be used to noninvasively spatially resolve information about the heterogeneity of the membranes by probing the water molecules and hydronium ions within the membrane. This will help to determine to what extent heterogeneity is responsible for the PEMs failure. Electrophoretic NMR (ENMR) has been used to study to study the electroosmotic drag in a stack of PEMs [1]. In the experiments reported here single 177 □m dry thickness membranes are imaged. Spatially resolved magnetic relaxation time, T_1 and T_2, and time dependent diffusion measurements were taken to supply information on the dynamics of the water within the PEMs. These measurements provide a method to explore water exchange among sites within the membrane and transfer into and out of the PEMs. Two methods of pre-treating the PEMs by boiling or soaking in acid solutions were followed according to previous NMR work [1, 2]. In one method there is a step to remove paramagnetic contaminants from the samples to ensure they do not interfere with the NMR experiment [2].

MRM T_1 weighted images with spatial resolution of 19.5 □m/pixel in the vertical and 78.1 □m/pixel in the horizontal over a 1mm slice are shown in Figure 1. The images shown demonstrate the redistribution of water T_1 relaxation time within the PEM after several days of soaking in water after the acid treatment. This phenomenon may be due to either an uptake of paramagnetics or association of the water in the interior of the membrane with sulfonic groups. The long T_1 water in Fig. 1 b) at the membrane water bath interface is likely undergoing exchange. T_1, T_2 and diffusion measurements will be presented to further understanding of these effects.

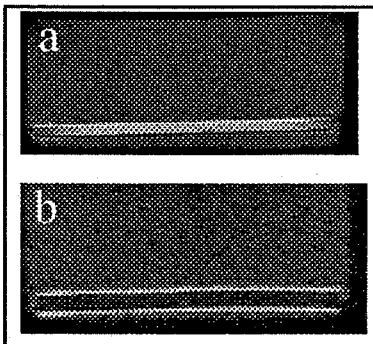

Figure 1: T_1 weighted images of N-117 after treatment according to [1]. a) Several hours after acid treatment and b) after 8 days soaking in distilled water.

References

[1] M. Ise, K.D. Kreuer, J. Maier, *Solid State Ionics* **125**, 213-223 (1999).

[2] B. MacMillan, A.R. Sharp, R.L. Armstrong, *Polymer* **40**, 2471-2480 (1999).

NMR Microscopy of Biofilm Structure and Bioreactor Fluid Dynamics

Erica L. Gjersing, Sarah L. Codd, Phil S. Stewart, and Joseph D. Seymour
Department of Chemical Engineering and Center for Biofilm Engineering, Montana State University, Bozeman, MT 59717

Biofilms are multi-cellular communities of microorganisms, which are attached to surfaces and surrounded in a polysaccharide hydrogel matrix known as EPS. They are encountered ubiquitously with some being a mere nuisance, like toilet bowl scum, while others are involved in life threatening infections in cystic fibrosis patients and on medical implants [1]. Internal structures of biofilms are impossible to see with ordinary light microscopes and the major tool for imaging them is the confocal laser microscope that is limited to about 100 □m depth penetration [2]. Additional techniques to corroborate confocal images and elucidate more information about biofilm systems are needed. NMR techniques are ideally suited for studying biofilms since they are non-destructive and non-invasive. A major advantage of NMR is the ability to look at any depth in the biofilm structure, a point on which other microscopy methods fail due to light or laser penetration barriers. The current focus of this research is to apply NMR techniques to biofilm systems to image biofilm structure, map bulk flow patterns around them and to measure diffusion within the EPS. Understanding how biofilms interact with bulk flow will contribute to better models of nutrient and anti-microbial transport and to the overall knowledge of biofilm behavior.

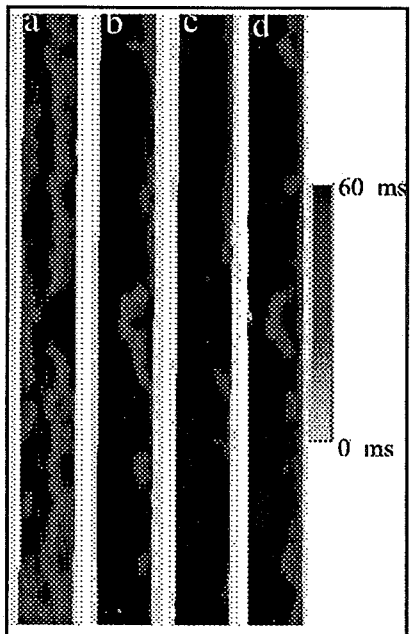

Figure 1. T_2 maps of biofilm structure. Maps a)-c) are contiguous 300 μm slices across the square bioreactor. Map d) is a slice perpendicular to the center slice b).

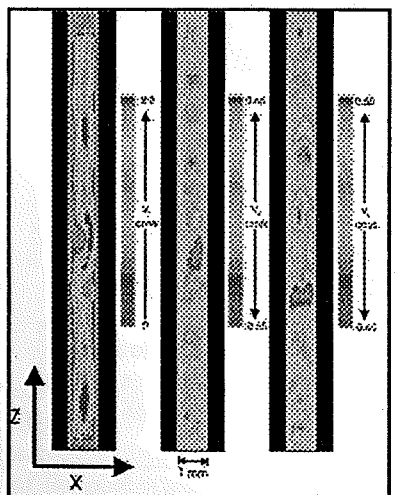

Figure 2. MRM velocity maps of axial and non-axial velocity for laminar flow in a 1mm bioreactor

Relaxation time weighting was used to image biofilm structure while pulsed gradient spin echo (PGSE) techniques [3] were used to image the flow around biofilms and the diffusion within them in 1mm square glass capillary bioreactors. Figure 1 shows T_2 maps of the biofilm structure of a *Staphylococcus epidermidis* biofilm with 19.5 □m/pixel resolution across the bioreactor and 156 □m/pixel resolution along the bioreactor length. Laminar flows in a clean capillary have no x or y components of velocity, while the z direction velocity is both uniform and symmetrical. Figure 2 shows velocity profiles in the z, x and y-directions (left to right in figure) for flow around a biofilm. In contrast to a clean capillary, a biofilm fouled capillary displays irregular flow patterns in the z direction along with distinct x and y flow perturbations. These results show that biofilm fouling has a significant impact on bulk flow, generating higher dimensional flows, which lead to chaotic mixing in transport models. Future experiments will examine how flow patterns change over the course of biofilm growth in addition to characterizing molecular diffusion and hydrodynamic dispersion in this system.

References

[1] P.S. Stewart and J.W. Costerton, *The Lancet* **358** 135-138 (2001).
[2] J.W. Costerton and P.S. Stewart, *Scientific American* **285** 61-67 (2001).
[3] P. T. Callaghan, "Principles of Nuclear Magnetic Resonance Microscopy". Oxford University Press, Oxford (1991).

NMR Study of the Flowing Layer in a Granular Media in a Rotating Drum

James E. Maneval[1], Braunen E. Smith[2], Eiichi Fukushima[2]
[1]Department of Chemical Engineering, Bucknell University, Lewisburg, PA 17837, USA
[2]New Mexico Resonance, Albuquerque, NM 87106, USA

Introduction

We report NMR imaging and velocity measurements for the flow of granular material in a half-filled horizontal rotating cylinder. We focus attention on shear layer in the upper portion of the system, measuring concentration and velocity profiles for pure and mixed granular systems of different-sized particles. Proton phase-encoded velocity and time-of-flight tagging images were made in a horizontal bore magnet with a field of 1.89T. The particles contained an NMR-observable oil and had diameters from 1 to 4mm. The rotation rate of the 70mm diameter drum varied between 5 and 60 rpm.

Pure systems

Systems containing single-sized particles have been extensively studied but mostly by methods that looked at flows through clear end plates. So, the primary reason for applying NMR methods to these systems is to make spatially resolved measurements that are not influenced by cylinder end-caps. Velocity-profile measurements along the perpendicular bisector to the flowing surface show that the model used by Yamane, et al. [1] fits very well, validating a parabolic velocity profile rather than the linear profile that is usually assumed for modeling [2]. Measurement of velocity profiles near the cylinder end-caps were found to be significantly different from profiles measured in the central region of the cylinder. Generally, these end-cap velocity profiles have lower maximum velocities for a given drum rotation rate and are more linear, as opposed to parabolic, in shape. These findings suggest that past measurements from systems where the cylinder length is only a few multiples of the particle diameter (for example, [3] and [4]) may be significantly influenced by end-wall-particle effects.

Binary Systems

Measurements of velocity profiles for binary mixtures reveal a range of interesting phenomena as a function of composition and rotation speed. The well known process of radial segregation (where smaller particles form a core surrounded by larger particles) is clearly observed along with segregation within the flowing layer. The velocity profiles for mixed systems do not have the same shape as the profiles found for pure systems. Rather, the mixed systems show the formation of a relatively low-shear layer of larger particles at the surface of the flow (Figure 1). The characteristics of the flowing layer are a function of the composition as well as the cylinder rotation rate and may provide some insight into a mechanism of axial segregation in these flows [5].

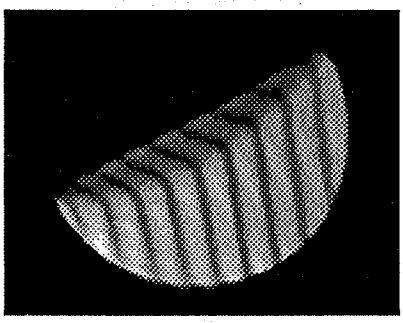

Figure 1. Deformation profile for flow in a mixed system. Thin, bright layer at the upper surface is due to a low-shear region of larger particles.

References

[1]Yamane, K., M. Nakagawa, S.A. Altobelli, T. Tanaka and Y. Tsuji, *Physics of Fluids*, **10**, 1419-1427 (1998).

[2] Khakhar, D.V., A.V. Orpe, P. Andresén and J.M. Ottino, *Journal of Fluid Mechanics*, **441**, 255-264 (2001).

[3] Jain, N., J.M. Ottino and R.M. Lueptow, *Physics of Fluids*, **14**, 572-582 (2002).

[4] Bonamy, D., F. Daviaud and L. Laurent, *Physics of Fluids*, **14**, 1666-1673 (2002).

[5] Aranson, I.S., L.S. Tsimring and V.M. Vinokur, *Physical Review E*, **60**, 1975-1987 (1999).

Probing Pore-Scale Velocity Fields During Fluid Flow in Porous Media: Displacement Propagators of Non-Newtonian Fluids in Sedimentary Rocks

Silke Sheppard[1], Andy J. Sederman[2], Dimitris A. Verganelakis[2], Mike L. Johns[2], Mick D. Mantle[2], Lynn F. Gladden[2]

[1] Schlumberger Cambridge Research, High Cross, Madingley Road, Cambridge, CB3 OEL

[2]Department of Chemical Engineering, University of Cambridge, Pembroke Street, Cambridge CB2 3RA, UK

Abstract

Complex fluids used in oilfield applications, such as polymeric and surfactant solutions, are often of non-Newtonian rheology. Examples of such fluids are water-soluble polymer solutions used during water flooding to provide more stable oil displacements. In oil production wells, polymeric solutions are employed to permanently seal high-permeability zones and so prevent excessive water production. Visco-elastic surfactant solutions (VES) in the form of rod-like micellar solutions can be used for hydraulic fracturing, a reservoir stimulation process to overcome limitations in well productivity.

The shear-flow properties of these polymeric and surfactant solutions are commonly investigated in the bulk, and steady shear-viscosity versus shear-rate curves exhibit shear-thinning (pseudoplastic) behaviour. The flow behaviour of these fluids through topologically complex porous media, i.e. the sedimentary rocks of oil and gas bearing formations is commonly described by macroscopically averaged transport properties, such as volumetric flow rates and differential pressures. However, the use of bulk rheological properties of complex fluids in continuum models of flow in porous media, is insufficient in providing accurate predictions of macroscopic transport properties [1]. The aim of this work is to study how the different microstructural characteristics of the investigated porous structures, such as porosity and permeability affect the rheological characteristics of the infiltrating complex fluids.

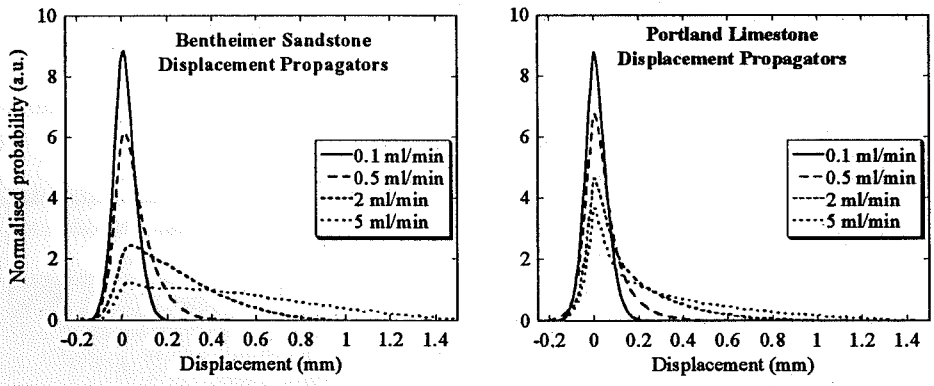

Figure 1 Experimental propagators acquired for 3 % KCl brine solution in Bentheimer sandstone and Portland Limestone rock cores at increasing flow rates (□ = 825 ms)

An experimental way of determining the microscopic, i.e. pore-scale transport properties of fluids in sedimentary rocks exists in the propagator measurement in Pulsed Field Gradient (PFG) NMR [2]. The propagator P(□,t) is the ensemble density distribution of molecular displacements in a chosen direction, □, in a given time interval, t. By varying the displacement time, t, an increasingly wider domain of the pore-scale velocity field within the porous medium can be probed directly. In this study we have used PFG NMR to follow the porous media flow of an array of complex fluids ranging from water soluble polymers such as partially hydrolysed poly(acrylamide) and Xanthan to VES solutions. The behaviour of these fluids was compared to that of simple Newtonian fluids, e.g. brine. Two different types sedimentary rocks, Bentheimer sandstone and Portland limestone, were used to investigate Stokes-flow with diffusion (see figure 1). Propagator results P(□,t) and its first three cumulants were analysed in terms of the bulk shear rheology of the fluids and the microstructure of the rocks. A discussion of the inherent differences in terms of rock core microstructure will be presented.

References

[1] J.R.A. Pearson and P.M.J Tardy, *Journal of Non-Newtonian Fluid Mechanics* **102**, 447-473 (2002).

[2] J.J. Tessier, K.J. Packer, J.F. Thovert and P.M. Adler, *AIChE Journal* **43**(7), 1653-1661 (1997).

MRI Measurements of Local Flow Velocities and Structure in Biofilm Systems

Bertram Manz*, Frank Volke*, Daniel Goll, Harald Horn****
* Fraunhofer-Institut für Biomedizinische Technik, Ensheimer Str. 48, 66386 St. Ingbert, Germany
** Hydrochemistry, Hochschule Magdeburg-Stendal (FH), 39114 Magdeburg, Germany

The characterisation of substrate transport in the bulk phase and in the biofilm matrix is one of the problems which has to be solved for the verification of biofilm models. MRI techniques were employed to study structure and transport phenomena in biofilm systems. The investigations were carried out for defined heterotrophic biofilms which were cultivated in a tube reactor at a Reynolds number of 2000 and 8000 and a substrate load of 6 and 4 g/m²d glucose.
It has been shown that relaxation time values of water hydrogens are reduced in biofilms [1]. In this contribution we use relaxation time maps to spatially resolve the biofilm surface and study flow behaviour near the biofilm/bulk water interface and particularly in the hydrodynamic boundary layer. Structure parameters, such as biofilm thickness, surface enlargement and roughness are presented for different biofilms [2].
The local shear stress is calculated from the measured velocity images. This information is important to develop models for biofilm detachment.

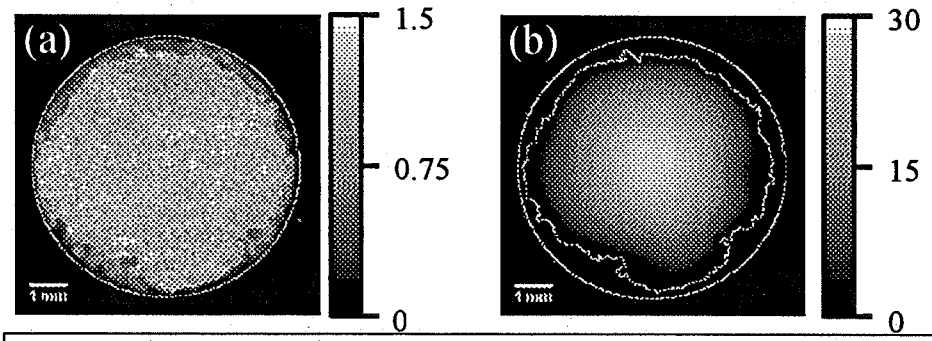

Figure 1: (a) A spatially resolved map of T_2 values through a tube segment grown with a biofilm. The grayscale gives the value of T_2 in s. The contour lines indicate the inner and outer walls of the biofilm (b) A velocity image of the same slice. The velocities are given in mm s^{-1}.

References
[1] Hoskins, B C, Fevang, L, Majors, P D, Sharma, M M, Georgiou, G., *J. Magn. Reson.* **139**, 67-73 (1999).
[2] Manz, B., Volke, F., Goll, D., Horn, H., *Biotechnol. Bioeng.* (submitted)

Crack Detection in Porous Materials

Joshua J. Young[a,b], Bruce J. Balcom[a], Theodore W. Bremner[b], Pavol Szomolanyi[a]
[a]MRI Centre, Department of Physics and [b]Civil Engineering, University of New Brunswick, P.O. Box 4400, Fredericton, NB, Canada, E3B 5A3

A Magnetic Resonance Imaging (MRI) methodology was developed to spatially resolve cracking in cement based materials [1]. The method uses spin echo imaging to distinguish water held within cracks and water held within the pore structure of hydrated cement paste. The methodology is based on the "relatively" long spin-lattice and spin-spin relaxation times of water filled cracks. Water held within the pore structure of hydrated cement paste has shorter relaxation times.

Hydrated cement paste is a porous material containing a distribution of pore sizes from the nanometer scale up to the micrometer scale [2]. NMR has been used to measure this distribution by exploiting the dependence of T_1 and T_2 on the surface to volume ratio of the water filled pores [3]. Bulk T_1 and T_2 of the liquid water phase in hydrated cement paste is generally multiexponential and on the order of a few milliseconds and hundreds of microseconds respectively [4]. Water filled cracks have different surface to volume ratios than the water occupied pore structure and thus significantly longer relaxation times.

Spin Echo imaging, due the short relaxation times of water occupied pores, is not well suited to the study of water movement. However, the cracking problem manifests itself as a "long" T_1 and T_2 contrast problem, spin echo imaging combined with an inversion recovery component is able to distinguish water filled cracks from the surrounding paste in three dimensions.

Figure 1 is a rendered 3D spin echo image of a cracked cement paste cube. There are three cracks present in the image; a large triangular shape, a slot along the top, a small crack on the bottom left side. The sample is 10x10x10 mm and the cracks range in size from 150 μm down to 60 μm in thickness. The main crack visible in this view is triangular and approximately 100 μm thick. The field of view set at 20x20x20 mm with a 128x128x64 matrix, resulting in a nominal resolution of 156x156x312 μm. Our estimate of the minimum detectable crack width is 15 μm.

Although developed for concrete materials research, we anticipate the ideas and methodologies are directly translatable to other porous media research.

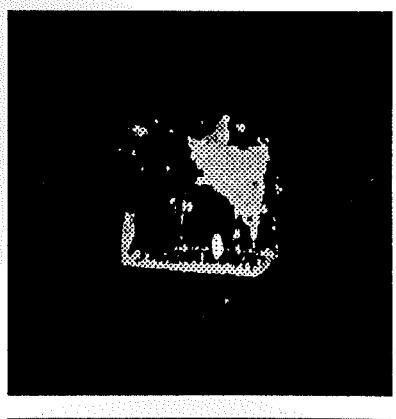

Figure 1: A rendered 3D MRI image of water filled cracks in a cement paste cube.

References

[1] J.J. Young, P. Szomolanyi, T.W. Bremner, B.J. Balcom, *Cement and Concrete Research*, submitted.

[2] D. Winslow, D. Liu, *Cement and Concrete Research* **20** (2), 227-235 (1990).

[3] W.P. Halperin, J.Y. Jehng, Y.Q. Song, *Magnetic Resonance Imaging* **12** (2), 169-173 (1994).

[4] S.D. Beyea, B.J. Balcom, T.W. Bremner, P.J. Prado, D.P. Green, R.L. Armstrong, P.E. Grattan-Bellow, *Cement and Concrete Research* **28** (3), (1998) 453-463.

Electron Paramagnetic Resonance Imaging using a pure phase encoding technique

Gregory Stoch[1,3], Fred Goora[1], Bruce C. Colpitts[2], Bruce J. Balcom[1]
[1]MRI Center, Department of Physics, University of New Brunswick,
[2]Department of Electrical and Computer Engineering, University of New Brunswick,
Fredericton, New Brunswick, E3B 5A3 Canada
[3]Institute of Nuclear Physics, Radzikowskiego 152, 31-342 Kraków, Poland

Electron Paramagnetic Resonance Imaging (EPRI) provides noninvasive method for detection, characterization, and spatial localization of free radicals in a range of systems. The link between free radicals and chronic and pathological disease states has caused an increased interest in the detection of free radicals. We anticipate there may be similar interest in EPRI of a wide range of materials systems. The main problems that must be overcome are connected to short signal lifetimes of electron paramagnetic resonance and to handling huge data streams during the measurement. In addition to short signal lifetimes, the difficulties associated with a high power excitation pulse, and a very weak experimental signal occurring in close proximity to one another in the same RF probe must be resolved. The latter problem is common to all magnetic resonance instruments yet the weak EPR signal magnifies the problem in EPRI. The purpose of this work is to design, build, and test an EPR imaging instrument. The instrument uses a spiral k space trajectory with the SPRITE technique [1], which is novel to EPRI, as well as the use of 180 degree ring hybrid [2] and two identical resonant probes, which allow for sample excitation and signal acquisition. The ring hybrid reduces the deadtime of the instrument (caused by excitation pulse) below 250 ns. The short signal lifetimes permit rapid data acquisition but induce the problem of a very large data stream that has to be handled with appropriate timing online. This task requires leading edge PC architecture and software coding [3]. To maximize throughput two concurrent threads were applied to handle acquisition control and data transfer in parallel. Our current imaging time for 3D EPRI images is approximately 30 minutes for a 64^3 pixel cube. The system is of modular form, allowing the instrument to change and adapt as required, and is controlled using the LabVIEW software package within its non time-critical part.

References
[1] Bruce J. Balcom, Rod P. MacGregor et al., *Journal of Magnetic Resonance* **123,** 131-134 (1996).
[2] D. Pozar, *Microwave Engineering,* Toronto: John Wiley & Sons, Inc., (1998).
[3] Roger W. Lockhart, *Measurement & Control Magazine,* April, (1999).

Imaging Gases in Ceramics: Application of Techniques for Microstructural Characterization

Andrew McDowell, S. Jill Glass,[§] and Steven D. Beyea
New Mexico Resonance, 2301 Yale Blvd. SE, Albuquerque, New Mexico, 87106, USA
[§] Sandia National Laboratories, Albuquerque, New Mexico, 87185, USA

Recent work at New Mexico Resonance has shown that studies of the microstructure of ceramics and other porous materials using thermally polarized fluorinated gases are feasible [1-4]. Difficulties associated with the inherently low signal to noise of gaseous samples, as well as those stemming from their very short relaxation times, can be overcome using reasonable experimental procedures. In this poster, we present the application of gas-phase imaging techniques to samples of technological interest.

Gas-phase spin-density imaging reveals inhomogeneities in ZnO-based varistor materials. These inhomogeneities are regions of enhanced magnetic susceptibility, indicating localized variations in chemical composition (or perhaps structure) in the interior of the material. Work continues to relate these image features to localized variations in other physical properties, and to performance failures in devices made from these materials.

Ceramic samples designed with spatially varying properties present a special challenge for characterization experiments, as any determination of properties must be made locally. One example is a "layered" ZnO ceramic, developed by the Materials & Process Sciences Center at Sandia National Laboratories, in which an inner core compacted to higher density is surrounded by an annular ring of lower initial density. These materials are then co-fired, and characterization of the pore structure near the interface is of interest. We present gas-phase imaging results allows the local characterization of physical properties (porosity, pore size, specific surface area, pore shape, and gas/substrate adsorption energy) through measurements of NMR relaxation rates, effective diffusion constants, and adsorbate surface coverage.

Sandia is a multiprogram laboratory operated by Sandia Corporation, a Lockheed Martin Company, for the United States Department of Energy under Contract DE-ACO4-94AL85000.

References:

[1] A. Caprihan *et al* "Characterization of Partially Sintered Ceramic Powder Compacts Using Fluorinated Gas NMR Imaging", *Mag. Res. Imaging* **19**, 311 (2001).
[2] S.D. Beyea *et al* "Spatially Resolved Adsorption Isotherms of Thermally Polarized Perfluorinated Gases in Y-TZP Ceramic Materials using NMR Imaging" *Appl. Magn. Res.* **22** (2), 175 (2002).
[3] S.D. Beyea *et al* "Studies of Porous Media by Thermally Polarized Gas NMR: Current Status" *Mag. Reson. Imaging* **21**, in press (2003).
[4] S.D. Beyea *et al* "Non-Destructive Characterization of Nanopore Microstructure: Space Resolved BET Isotherms using NMRI" *J. Appl. Phys.*, in press (2003).

Coal is Impermeable

Dean O. Kuethe[1], Robert E. Botto[2], Jeana Quintana[1], Natalie Adolphi[1], Steven Beyea[1]
[1]New Mexico Resonance, Albuquerque, NM, USA;
[2]Argonne National Laboratory, Argonne, IL, USA

Tsiao and Botto (1991) introduced Xe gas (Lennard-Jones diameter about 0.52 nm) into Illinois #6 coal. From solvent shift they concluded that the sorbed gas was divided into two populations, one associated with aromatic components of coal, one associated with the aliphatic components. From restricted diffusion measurements, they concluded that the Xe was in pores averaging 0.65 nm in diameter. We figured that Xe adsorbs on pore walls so readily that assuming the gaseous diffusion coefficient in a restricted diffusion calculation would probably not yield an accurate reflection of pore size. We figured the pores should be at least 0.65 nm, so we sought to introduce CF_4 gas (diameter 0.58 nm) into coal. It is the smallest ball of Teflon, has a very low (227.6 K) critical temperature, and could care less about adsorbing on pore walls. In addition, the T_1 from spin-rotation interaction should be much longer than the bulk gas because the pore size is on the order of, or smaller than, the bulk mean free path, and collisions with pore walls would exceed the normal molecular collision rate. The T_1 could provide a method, independent of diffusion measurements, for measuring pore size.

We introduced CF_4 into powered Argonne Premium Coal Samples (Vorres, 1990) of Pennsylvania Upper Freeport, Medium Volatile Bituminous, coal #101, sample 02677; Illinois #6, High Volatile Bituminous, coal #301, sample 04653; Wyodak Subbituminous coal #202, sample 04073. There was no drop in pressure, typical after introducing CF_4 into a closed container containing a nanoporous sample. The T1 of the gas was identical to bulk gas. Either the pores were much bigger than we thought or there were no pores that admitted CF_4.

We then made an image of CF_4 surrounding chunks of coal from the Pokohantas mine in Bluefield, West Virginia, from DOK's garage, and images of CF_4 surrounding glass marbles. The intensity of the image pixels representing the coal were the same intensity as the pixels representing marbles, *i.e.*, that of the image noise floor. We achieved the same result with an Argonne Premium chunk of Pokohantas coal. Letting the coal sit in a vacuum oven overnight at 140°C did not change the results. As far as CF_4 is concerned, coal is not porous. Not to have our desires for a porous material completely dashed, we made some coke by putting chunks of coal in a coffee can, blowing in a stream of N_2 , and heating with a torch. The coke is porous.

We figure that coal is not porous or that the throats connecting pores are below 0.58 nm diameter, but that Xe dissolves in coal, i.e., it deforms its electron cloud as Xe is wont to do in order to fit in some very wee spaces. Its relatively high mobility - leading to a pore size estimate of 0.65 nm may reflect a rapid movement from one preferred interstitial site to another.

To test if a smaller gas would enter some alleged pores in coal, we tried putting H_2 (diameter 0.296 nm) around coal chunks. There was no decrease in pressure after introducing the H_2, there was no change in NMR relaxation. Perhaps coal is impermeable.

References

C. Tsiao and R. E. Botto, 129Xe NMR investigation of coal micropores, Energy and Fuels 5 (1), 87-92 (1991).
K. S. Vorres, The Argonne premium coal sample program. Energy and Fuels 4(5), 420-426 (1990).

Detection of Fractures and Pores in Granite by Magnetic Resonance Microimaging and T_2 Measurement

Makoto Yamaguchi[1], Takahiro Ohkubo[2], Kazuo Kobori[1], Kazunori Suzuki[1], Yasuhisa Ikeda[2], Koji Saito[3] and Stephen Altobelli[4]

[1]Institute of Research and Innovation, Kashiwa, Chiba 277-0861, Japan
[2]Tokyo Institute of Technology, Meguro, Tokyo 152-8550, Japan
[3]Nippon Steel Corporation, Futtsu, Chiba 293-8511, Japan
[4]New Mexico Resonance, Albuquerque, NM 87106, U.S.A.

Fluid flow through rock fractures has been extensively studied in relation to migration of radioactive elements from geological disposal sites. However, nondestructive imaging methods can help the understanding of how fluid flows are governed by local and network structures of fractures. We performed magnetic resonance imaging of liquids in slits and surrounding spaces of cylindrical granite to clarify methods and conditions adequate for imaging of fractures in crystalline rock cores which may suffer from image distortion by para/ferromagnetic grains [1]. Granite was chosen as it occurs widely in Japan and is extensively studied. It contains relatively small amount of para/ferromagnetic minerals compared to other igneous rocks. While images by spin echo method were distorted along readout gradient direction, they were less distorted by SPI method. However, dark areas appeared around paramagnetic grains due to local field gradients and they obscured images of 1.5mm wide slits in granite when G_{max} was limited to <10G/cm, which is typical for borehole rock core imaging.

We used two procedures to suppress magnetic susceptibility effects. The first was to use the SPI method and shorten sampling times by using microimaging systems that can generate stronger magnetic field gradients with smaller samples. MRI systems with 7T and 9.4T magnets were employed with water-cooled gradient coils and Techron amplifiers that could generate G_{max}~150G/cm. Cylindrical samples (8~15mm o.d.) of Inada granite (Ibaraki, Japan) were cut vertically and glass capillaries (1~1.5mm o.d.) were sandwiched to form parallel or tapered slits. Samples were immersed in CH_3OD or aqueous copper sulfate and 3D SPRITE images were made. The size of dark areas decreased by shortening encoding times and 1.5mm wide slits were clearly visible, although dark areas were not completely suppressed in images with the shortest encoding time of 39μs (G_{max}=143G/cm). Pixel sizes were 0.2~0.3mm it was possible to detect images of ~0.1mm wide slits.

The second was to decrease the static field strength. We compared two MRI systems with 7T and 1.89T magnets whose bores can accept borehole rock core samples (~50mm o.d.). SPRITE images of the same granite sample (35mm o.d.) with a 1.5mm parallel slit were taken at both fields with the same imaging parameters. Dark areas decreased at 1.89T almost to the size of the grains themselves.

These results show that it is possible to image fractures in crystalline rock cores by properly selecting samples, MRI systems, and imaging parameters. However, most voids in granite are smaller than the detection limit of microimaging. We considered whether relaxation time analysis for pore size distribution could be applied to granite, because the method has already been conventional in the case of porous sedimentary rocks. Spin-spin relaxation times of granite were measured at 0.55 and 0.05T with CPMG sequence. Fast relaxation condition was assumed in the case of unweathered Inada granite since relaxation time is not affected by temperature and echo spacings. Lognormal T_2 distribution was correlated with pore size distribution by mercury porosimetry and surface relaxation time constant was estimated to be ~1μm/s, which is within the range of typical values of porous materials. Granite samples from different locations and degrees of weathering showed different T_2 distributions and samples with deposited clays gave the shortest relaxation times. These results imply the method is also effective for analysis of crystalline rocks like granite.

References

[1] Makoto Yamaguchi *et al.*, *MRPM6 Abstract* P38 (2002).

MRI investigation of porous media using thermally polarized fluorinated gases

Maxim Terekhov, Dieter Höpfel.
Institut for Innovation and Transfer, University of Applied Science, Moltkestrasse 30, D76133, Karlsruhe, Germany. e-mail: maxim.terekhov@fh-karlsruhe.de;

Abstract
The 3D images of various porous media samples were obtained using the **thermally polarized** (TP) sulphur hexafluoride (SF_6) and tetrafluoroethane (CH_2FCF_3) gases. The substances with different pore size and structure, surface-to-volume ratio were probed by several imaging techniques. The gas under the 5 to 8 bar pressure was used providing the higher spin density to increase the signal-to-noise ratio and hence the spatial resolution. The fast diffusion of gases makes one T_2-sensitive to the pore size, providing the increase of the pore structure visualization contrast using the «T_2 weighted imaging».

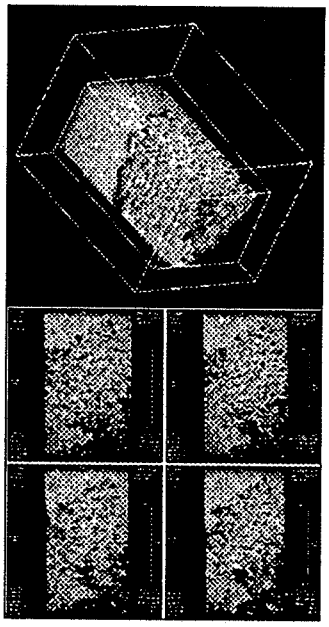

Fig. 1.
MRI of the polyurethane foam obtained using the SF_6 gas as an agent.
The 3D structure (top), and individual slices (bottom) are shown.
The light pixel corresponds to the SF_6 gas and the dark one to the foam material. The porous structure of the sample is well visualized.
The maximal spatial resolution is 75 μm/pixel (64x64x64 matrix acquired in 5 hours)

Magnetic resonance imaging (**MRI**) of porous media is usually associated with the liquid agents used for the visualization of the structure and investigation of the transport, diffusion and other phenomena. In the last years significant progress was achieved in using the hyperpolarized (**HP**) noble gases (^{129}Xe and ^{3}He) in MRI that opens a number of possibilities for the investigation of the porous media [1]. The penetration ability of the gases allows one imaging microstructures which are not accessible for the liquid agents. However, the devices for producing the HP gases are quit expensive (not telling about the cost of the ^{3}He). Therefore, using TP gases can be an inexpensive possibility to estimate the effectiveness (for example, the gas penetrability) of the gas-MRI for the specific material. Also, the HP state of ^{129}Xe quickly disappears, if any paramagnetic centers are present in the material. In such a case, using the TP gases can be a reasonable way for the structure visualization [2]. The main problem of using the gases in MRI is the lack of signal intensity caused by low spin density of the agent. The situation can be improved by using the gases with large number of observable spins per molecule and creating a high pressure. The hydrocarbon gases which could be used for the MRI are inconvenient in practice due to the danger of burning and bursting, poison effects, etc. In addition, the gas ^{1}H MRI may not provide the necessary contrast in the case of sample containing the protons itself. Therefore, the fluorinated gases (*fluorocarbons* or *sulphurhexafluoride*) which are (i) chemically inert, (ii) non-burnable, (iii) provide a high ^{19}F spin density, seems to be much better choice for MRI.

As an example, the MR image of polyurethane foam filled with SF_6 gas is shown on **Fig 1**. It was found, that the fast longitudinal relaxation allows making the repetition time T_R <100ms with minor signal losses. The resulting image quality is comparable with the one obtained by liquid MRI due to the larger number of signal averaging performed in equal experiment time. The SF_6 gas T_2 relaxation was found to be sensitive with the pore size, making it possible to increase the contrast by the T_2 weighting. Thus, the pore size distribution can be visualized by a T_2 contrast imaging. The useful property of the tetrafluoroethane is the coexistence at the room temperature of liquid and gas in equilibrium. This provides the interesting possibility for the comparison of liquid and gas imaging under the equivalent conditions. The obtained results and developed techniques are planned to be used also in combination with HP gases-MRI.

References

[1] R.W. Mair, R. Wang, M.S. Rosen, D. Candela, D.G. Cory, and R.L. Walsworth, accepted in: Magn. Res. Imaging (2002)
[2] E. Fukushima, Gordon Research Conference on Magnetic Resonance, Henniker, NH, June 27-July 2, 1999.

NMR flow measurements as an aid to the simulation of fluid dynamics in oil production technology

G. Maddinelli and N. Mancini
EniTecnologie S.p.A., via F. Maritano 26, 20097, S. Donato, Milan, Italy

NMR imaging technique can be applied in providing data useful in solving complex engineering problems. One the most promising applications are certainly velocity measurements methods based on the combination of pulsed field spin-echo (PGSE) and imaging experiments[1]. This type of technique is quite promising in applications to complex fluid dynamics studies[2], especially required in oil production and drilling technology. In fact, such engineering applications generally involve several simulations assessment to better investigate line assembly of industrial oil plants. MRI has great potential in discriminating oil/water mixtures even in optically opaque media (e.g. by chemical shift and relaxation differences) and also in measuring velocity profiles over a wide range of values avoiding interference with the flowing system[3]. This feature associated with high spatial resolution makes MRI more attractive than other conventional techniques (e.g. laser Doppler methods). In this application, aimed to simulate drilling and production operations, we have assembled a 9 mm (I.D.) flow loop line inside a 2 T, 31 cm horizontal-bore magnet. Flow was assured in a velocity range of 10-100 cm/sec. Preliminary studies were realized using a fluid constituted by a mixture of water/glycerin to ensure a laminar flow regime. Velocity profiles were measured in different points of the flow line and compared with data calculated from Computational Fluid Dynamics (CFD) methods[4], revealing a good agreement. Successive studies were dedicated to investigation of the fluid rheology on the flow properties. Viscous fluids with different concentration of added polymers, were adopted and consistent effects on flow regime were observed. In fact, restrictions or geometrical features introduced in the flow line to simulate drilling tools modified considerably the flow dynamics, giving rise to severe turbulence which could affect the process efficiency. FLASH imaging technique was also applied to evaluate transient phenomena induced in the flow line at high flow rates. This type of NMR simulator adopted was found very useful as an aid to evaluate conditions leading to the transition from laminar to turbulent regime. The results obtained from simulation experiments could be applied in determining the optimal conditions (i.e. fluid composition and flow rate) to minimize flow transition effects.

1. Callaghan P.T., Eccles C.D. and Xia Y. J. "NMR microscopy of dynamic displacements". Phys. Sci. Instrum. 21, 820-822, 1988;
2. Xia Y., Callaghan P.T., and Jeffrey K.R., "Imaging velocity profiles: flow through an abrupt contraction and expansion". AIChE Journal, 38, 9, 1408-1420, 1992;
3. Newling, B., Hall L.D. et al., "Chemical Resolved NMR velocimetry". Chemical Engineering Science, 52, 13, 2059-2072, 1997.
4. F. Donaggio, N. Mancini G. Maddinelli, S. Correra "Fluent CFD Code Performance Evaluation in Describing Oil in Water Dispersions Flow" Proceeding of 3rd International Conference on Multiphase Flow, Pisa, April 99.

Mapping a Flow Pattern Transition via Velocity Imaging

Marcos A. d'Avila[§], Nina C. Shapley[§], Jeffrey H. Walton[¶], Stephanie R. Dungan[§], Ronald J. Phillip[§], and Robert L. Powell[§]

[§]Department of Chemical Engineering and Materials Science

[¶]NMR Facility

University of California, Davis

Introduction

Two phase flow, emulsive and particulate, are found in many applications in the food, polymer and oil industries. The volume fractions encountered extend from quite dilute to very high concentrations. Because many of those systems are opaque, velocity measurements cannot be performed by conventional optical techniques such as laser Doppler velocimetry. Alternative techniques such as magnetic resonance imaging (MRI) are therefore required to study velocity fields in such systems. Here we use MRI to interrogate the velocity field via time-of-flight and velocity phase encoding methods.

Experimental

Both emulsions and particulate suspensions were placed in a horizontally oriented wide gap concentric cylinder geometry. The length to gap ratio was 40 and data taken in the center so end effects are negligible. The inner cylinder was stationary while the outer cylinder was driven to avoid Taylor instabilities. The emulsions were isooctane (□ = 0.69 g/cc) in water where the droplets (mean diameter = 3.2 □m) were stabilized with 0.5% Tween 20. The suspensions were PMMA (□ = 1.2 g/cc) beads (mean diameter 5.5 □m ± 2.2 □m) in water. Emulsion oil volume fractions ranging from 0.02 to 0.3 and bead suspension volume fractions ranging from 0.05 to 0.1 were studied. The apparatus was place in a Bruker 7T Biospec system with microgradients (G_{max} = 950 mT/m). Velocity imaging was performed via time-of-flight and velocity phase encoding[1] at several driving tangential velocities. The velocity phase encoding experiment was performed twice – once with velocity encoding gradients in X and once in Y. These were combined post process to reconstruct the 2D velocity field.

Results and Discussion

Previous results[2] demonstrated that well above a critical velocity, the emulsion co-rotated with the driving cylinder. As the driving velocity was lowered toward the critical velocity, asymmetry in the flow pattern developed. Below the critical velocity, a counter rotating flow pattern (a portion of the fluid moves in a direction opposite to the outer, rotating cylinder) was observed. Theoretical analysis suggests that the transitions are driven by buoyancy effects. The co-rotating and counter-rotating flow states at different rotation speeds can be characterized by a single dimensionless parameter, which relates buoyancy and viscous effects, i.e,

$$\tilde{V} \equiv \frac{V_b}{V} \sim \frac{|\rho_w - \rho_p| g a R_o}{\mu V} \sqrt{\frac{2}{9}\phi_0 (1-\phi_0)^5}$$

Because this expression depends on the density difference, the flow transition should also occur when the dispersed phase is denser than the continuous phase as well. This expression is experimentally verified for both emulsions and particulate suspensions. It is found that the transition between co-rotating and counter rotating regimes occurs when $\tilde{V} \approx 3$. This effectively maps out the phase diagram for this buoyancy driven transition between flow patterns.

References

[1] P. T. Callaghan, *Principles of Nuclear Magnetic Resonance Microscopy* (Oxford University Press, New York, 1991).

[2] N. C. Shapley, M. A. d'Avila, et al., *Physics of Fluids* **15**, 881-891 (2003).

GARField Magnetic Resonance Profiling of Skin Hydration

L. Backhouse[1], M. Dias[2], J.P. Gorce[1], J. Hadgraft[3], P.J. McDonald[1], J.W. Wiechers[4]
[1]School of Electronics and Physical Sciences, University of Surrey, UK; [2]Disperse Technologies, Surrey Research Park, GU2 7YF, UK; [3]Medway Sciences, University of Greenwich, UK; [4]Uniqema R&D, Gouda, The Netherlands

Introduction

There have been several previous magnetic resonance imaging (MRI) studies of human skin [1, 2, 3]. However for the most part these have been severely restricted by the resolution achievable on a clinical scanner as well as by the lower limit of accessible spin-spin relaxation times, T_2. Our approach to overcome these limitations is to use GARField [4]. GARField is a permanent MRI magnet specially designed to obtain depth profiles of thin planar samples (about 100 - 800 μm thick) with a pixel resolution of the order of 10 μm, and with access to T_2 times as short as a few 100 μs. Here, we use ^{1}H MR profiling to investigate changes in the MR response of the skin following application of light oils including mineral oil, glycerine and deuterated decanol. This extends our previous studies of skin hydration using GARField [5].

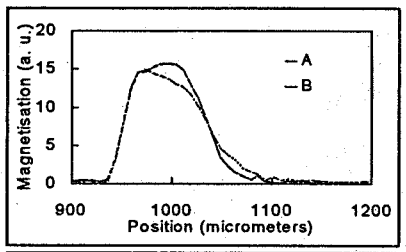

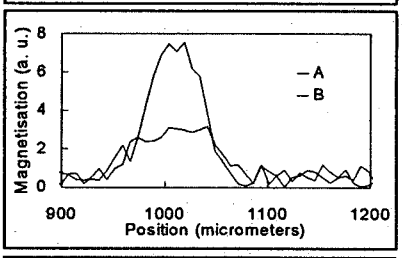

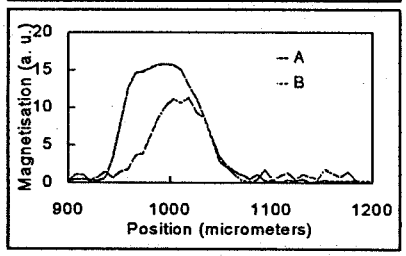

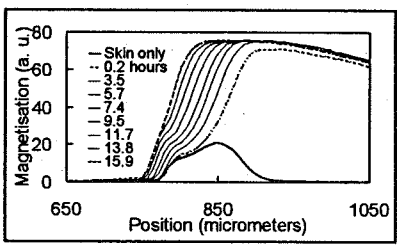

Experimental

Skin samples were obtained following abdominal surgery and were cleaned using standard methods. After partial hydration in water, the human epidermis was mounted on a glass cover slip with the *stratum corneum* uppermost at the air interface. The skin was spread evenly on the glass cover slip ensuring that the sample was flat. The samples were blotted dry with tissue paper and the fresh skin profile recorded. Oil was added, typically at 10μl/cm^2 and further profiles recorded over time. As an example, fully deuterated decanol was applied to a sample. Profiles of the skin were recorded before and after the application (top figure, upper and lower curves respectively, *stratum corneum* to the right). This figure clearly shows less ^{1}H signal in the *stratum corneum* region after decanol application and a slight increase in profile width. Profiles were also recorded with longer echo time, 500 μs compared to 150 μs, (second figure). The fractional change between the upper trace, before application, and the lower trace, after, is now much greater. Comparison of the first and second profile sets before application, (third figure), shows that the longer echo time preferentially visualises the *stratum corneum*. It is this layer which the decanol primarily invades and swells. The profile differences with different echo times arise from a complex inter-play of relaxation effects and self-diffusion attenuation of the signal in the strong constant gradient as explained in the presentation. As a second example, glycerine was applied to a partially hydrated skin sample (fourth figure). In the figure, the profile of lowest intensity and width shows the skin sample before the glycerine application. The skin sample is about 110 micrometers thick. The glycerine is applied and the MR profiles are acquired over a subsequent period of about 16 hours. The intensity of the region beyond 900 microns is due to the glycerine "reservoir". The glycerine invades the sample as shown. The position of the front varies with the square root of time from which a Fickian ingress mechanism is inferred. The effective diffusion coefficient is estimated to be ≈2 x10^{-10} cm^{2}s^{-1}.

References

[1] Ablett S., Burdett N. G., Carpenter T. A., Hall L. D. and Salter D. C. *Magn. Reson. Imaging* 1996 **14** 357.
[2] Stock W., Maurer J. and Felix R. *Hautarzt* 1997, **48**, 26.
[3] Querleux B., Richard S., Bittoun J., Jolivet O., Idy-Peretti I., Bazin R. and Leveque J. L., *Skin Pharmacology* 1994, **7**, 210.
[4] Glover P.M., Aptaker P.S., Bowler J.R., Ciampi E. and McDonald P.J. , *J. Magn. Res.* 1999, **90**,139.
[5] Dias M., Hadgraft J., Glover P. M., and McDonald P. J. *J.Phys. D: Appl. Phys.* 2003 **36** 364

Investigation of the State and Dynamics of Water in Hydrogels of Cellulose Ethers by MR Microscopy

Saša Baumgartner[1], Gojmir Lahajnar[2], Ana Sepe[2], Igor Serša[2], Julijana Kristl[1]
[1]University of Ljubljana, Faculty of Pharmacy, Aškerčeva 7, SI-1000 Ljubljana, Slovenia
[2]Jožef Stefan Institute, Jamova 39, SI-1000 Ljubljana, Slovenia

Cellulose ether polymer chains hydrate on contact with water, forming the hydrogel layer on the surface of the dry polymer matrix. This layer has been found to represent a diffusion barrier that retards processes of further water uptake and diffusion of other substances. Kinetics of drug release from hydrophilic matrix tablets is just one of the many cases where better understanding of a gel layer dynamics and its hydration structure is needed. Magnetic resonance imaging (MRI) is a very convenient method for this purpose as it is non-invasive and it can provide information on the gel layer thickness during the hydration process. A procedure for quantification of the MR images to determine the concentration of polymer in a gel was developed as well.

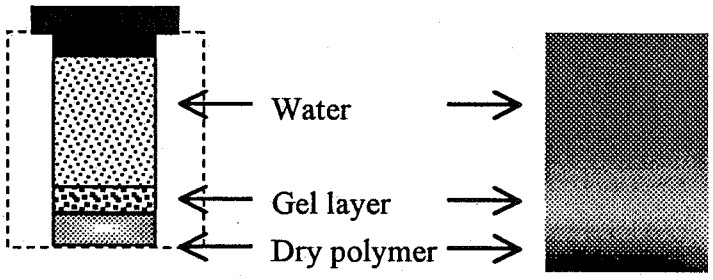

Figure 1: Scheme of the sample consisting dry polymer with the forming gel layer above the polymer tablet (left) and a corresponding MR micro-image of the sample (right).

To establish this purpose, a series of model samples - homogenous gels with known concentration - were prepared. First, relaxation times T_1 and T_2 for each of the samples were measured at identical conditions. The theoretical MRI signal for the actual imaging parameters was calculated for each sample, and a method to determine a water concentration from the MR image intensity was developed. In this way it was possible to follow dynamical processes of gel formation and changes in polymer concentration profile across the whole swelling tablet, and to learn more about the state and dynamics of water in the gel system.

References

[1] Melia C.D., *Crit. Rev. Ther.Drug Carrier Systems*; **8**, 395-421 (1991).
[2] Baumgartner S., Šmid-Korbar J., Vrečer F., Kristl J., *Pharma Science*, **3**, 182-187 (1998).
[3] Hyde T.M.,Gladden L.F., Payne R., *J. Controlled Release*; **36**, 261-275 (1995).
[4] Edzes H.T.,Samulski E.,*Journal of Magnetic Resonance* ,**31**, 207-229 (1978).

^{51}V Magic Angle Spinning Solid State NMR Spectroscopy of Vanadium Substituted Polyoxometalates: A Sensitive Probe for Geometric and Electronic Environment

Wenlin Huang, Lynn C. Francesconi, Tatyana Polenova
Department of Chemistry, Hunter College and The Graduate Center
of The City University of New York, 695 Park Avenue, New York, NY10021

Polyoxometalates (POMs) are attractive for the design of new materials, due to diverse chemistry and favorable structural and electronic properties. Vanadium-containing polyoxometalates have become the object of interest in optoelectronics due to their putative electro-, photo-, and thermochromism, and potential applications as solid nanocomposite molecular devices.

We addressed the local geometric and electronic environment of the vanadium site in vanadium-substituted POMs of Lindqvist, Keggin, and Wells-Dawson families, by ^{51}V solid-state magic angle spinning NMR spectroscopy. The anisotropic quadrupolar and chemical shielding interactions are extremely sensitive to the details of the geometric and electronic environment. Remarkably, the ^{51}V fine structure constants in the Lindqvist-type POMs are dictated by the nature and geometry of the counteractions, the organic $[(C_4H_9)_4N]^+$ ion vs. mixed alkali metals Na^+ /Cs^+ ions. Electrostatic calculations of the electric field gradients at the vanadium atoms have been performed. Experimental trends are well reproduced with the simple electrostatic model, and explain the sensitivity of the anisotropic NMR parameters to the changes in the cationic environment at the vanadium site.

References

[1]Pope, M. T.; Muller, A. *Angew. Chem., Int. Ed. Engl.* **1991**, *30*,34-48.
[2] Coronado, E.; Go´mez-Garcý´a,C.J.*Chem. ReV.* **1998**, *98*, 273-296.
[3] Katsoulis, D. E. *Chem. ReV.* **1998**, *98*, 359-387.
[4] Gomez-Romero, P. *AdV. Mater.* **2001**, *13*, 163-174.
[5] Yamase, T. *Chem. ReV.* **1998**, *98*, 307-325.
[6] Liu, S. Q.; Kurth, D. G.; Mohwald, H.; Volkmer, D. *AdV. Mater.* **2002**, *14*, 225-229.
[7] Mu¨ller, A.; Peters, F.; Pope, M. T.; Gatteschi, D. *Chem. ReV.* **1998**, *98*, 239-271.

^{51}V Solid-State Magic Angle Spinning Spectroscopy and DFT Studies of Oxovanadium (V) Complexes Mimicking the Active Site of Vanadium Haloperoxidases

Neela Pooransingh[‡], Ekaterina Pomerantseva[‡], Martin Ebel[†], Sven Jantzen[†], Dieter Rehder[†], Tatyana Polenova[‡]

[‡]Department of Chemistry, City University of New York- Hunter College, and the Graduate Center, 695 Park Avenue, New York, New York 10021, USA

[†]Institut für Anorganische und Angewandte Chemie, Universität Hamburg, D-20146 Hamburg, Germany.

Abstract

A series of eleven oxovanadium (V) complexes mimicking the active site of vanadium haloperoxidases have been investigated by ^{51}V Magic Angle Spinning NMR Spectroscopy and Density Functional Theory (DFT). The MAS spectra are dominated by the anisotropic quadrupolar and chemical shielding interactions; for these compounds C_Q ranges from 3 to 8 MHz, and $\square_\square$ is in the range of 340 to 730 ppm. The quadrupolar coupling and chemical shielding tensors as well as their relative orientations have been determined by numerical simulations of the spectra. The spectroscopic NMR observables appear to be very sensitive to the details of the electronic and geometric environment of the vanadium center in these complexes. Different fine structure constants were obtained for compounds with chemically and geometrically similar vanadium first coordination spheres. This indicates that the local environment at the vanadium site is affected by both the proximal and distal ligands and may thus explain why subtle variations in the active site structure of haloperoxidases lead to profound differences in their enzymatic activities. For the four crystallographically characterized compounds from the series, the quadrupolar and chemical shielding anisotropies were computed at the DFT level using two different basis sets, and the calculated tensors were in general agreement with the experimental solid-state NMR data. A combination of ^{51}V solid-state NMR and computational methods is thus beneficial for investigation of electrostatic and geometric environment in diamagnetic vanadium systems with moderate quadrupolar anisotropies.

References

Neela Pooransingh et al, *Inorganic Chemistry* **42**, 1256-1266 (2003).

Structural And Photostructural Properties Of Chalcogenide Glasses

C. B. Nelson[a], T. Su[a], W. A. Harrison[b], and P. C. Taylor[a]
[a]Department of Physics, University of Utah, Salt Lake City, UT 84112-0830, USA
[b]Department of Applied Physics, Stanford University, Stanford, CA 94305 USA

Abstract
The structures of the prototypical chalcogenide glasses, As_2Se_3 and As_2S_3, have been the subject of some debate for many years. Although the local, nearest-neighbor order is well established, the intermediate range order on a scale of several interatomic spacings is still controversial. For example, there is evidence in these glasses for the presence of twelve-membered ring structure, such as occurs in the layered crystalline compounds, but the ways in which these rings are cross-linked or terminated are not well understood. We report detailed structural information in these glasses as obtained from nuclear quadrupole resonance (NQR) and high-field nuclear magnetic resonance (NMR) experiments [1] and tight binding calculations [2].

The electric field gradients at arsenic nuclei in arsenic-chalcogenide crystals and glasses can be determined from ^{75}As NQR and NMR experiments. When combined with simple tight-binding calculations, these determinations provide very sensitive probes of the local structural order in these crystals and glasses. Using published x-ray diffraction data, the calculations in crystalline As_2S_3, As_2Se_3, As_2O_3, orthorhombic As, and rhombohedral As agree with the NMR and NQR measurements of the electric field gradients to within ±20%. Given this agreement, the local structural order in the corresponding amorphous solids can be inferred with confidence using the same tight-binding procedures.

The NQR and NMR results, which yield asymmetries in the electric field gradient at the arsenic sites, provide detailed information on the local structural order and the photo-induced structural changes in these glasses and crystals – order that cannot easily be obtained from other techniques such as x-ray or neutron scattering. In particular, the As pyramidal units in both crystalline and glassy As_2Se_3, As_2S_3, and As_2O_3 are nearly axially symmetric. Evidently, in the glasses the two-fold-coordinated chalcogen (Se, S or O) can provide the bond angle distortions necessary to build a three dimensional network. In amorphous As, on the other hand, the pyramidal units are highly distorted, and the vast majority of the As sites are far from axial symmetry. This is also understandable since the "weak" chalcogen link is missing.

The tight binding calculations employ pseudo-wavefunctions on the As and three nearest neighbor atoms [3]. Diagonalization of a seven by seven matrix yields orthogonalized valence hybrids on the As atom that depend on the local geometry. Orthoganalization of the P states on the As with respect to the core P states then yields an estimate of the charge asymmetry that is most important in determining the electric field gradients at the As nucleus. This charge distribution is then used to calculate the electric field gradients.

References

1. T. Su, P. Hari, P. C. Taylor, P.L. Kuhns, W. G. Moulton, and N. S. Sullivan, Phys Rev. **B67**, 085203-1-14 (2003).
2. C. B. Nelson, P. C. Taylor, and W. A. Harrison, J. Vac. Sci. Technol. (2003), submitted.
3. W. A. Harrison, *Electronic Structure and Properties of Solids*, (Freeman, Oxford, 1979).

Transient effects in nitrogen-14 quadrupolar spin-systems

T. N. Rudakov, V. T. Mikhaltsevitch
Research Group, QRSciences Limited., 8-10 Hamilton Street, Cannington, WA 6107, Australia

Investigation of dynamical properties of a nitrogen-14 qudrupolar spin-system is very important for the development of nuclear quadrupole resonance (NQR) spectroscopy and for its practical applications such as detection of specific substances. In the present work we studied the behavior of nuclear magnetization created by a preparatory pulse in "observation windows" between RF pulses of a multi-pulse sequences. The main purpose of our experiments was to investigate the transient effects in such spin systems in the effective field of a multi-pulse train. There exist two types of these transient signals: a time-dependent nutation signal and echo signals in the effective field of the multi-pulse train. In our experiments we used polycrystalline hexamethylenetetramine ($C_6H_{12}N_4$) as a sample with axially symmetric electric field gradient (EFG) tensor and polycrystalline sodium nitrate ($NaNO_2$) in which the EFG tensor is not symmetrical. Multiple echoes in the effective field were detected in both samples which supports the fact that this effect does not depend on the value of the asymmetry parameter η. However some differences in signal were observed. For example the strong dependence of nutation signals on the value of asymmetry parameter η was observed.

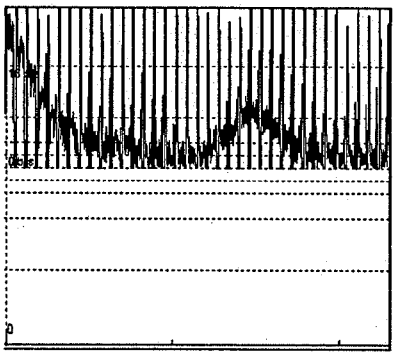

Figure 1: Spin-echo signal in effective field of multi-pulse sequence.

To study the transient signals in the effective field of a multi-pulse train we used different pulse sequences based on well known phase alternated pulse sequence (PAPS). These sequences consist of two or more blocks in which the phase of the RF pulses is reversed. As the sample of $C_6H_{12}N_4$ has very short relaxation times we used the small values of τ ($\tau \leq 0.3$ms). In this case the FID component of the NQR signal excited by RF pulses needed to be cancelled. In order to do it we used a phase cycling method described in our previous paper [1].

The experiments permitted to reveal some peculiarities in the behavior of the signals which are obviously characteristic of a quadrupolar spin-system.

References

[1] T. N. Rudakov, V. T. Mikhaltsevitch, *Chem. Phys. Lett.* **363,** 1-6 (2002).

Magnetic Resonance Imaging of Water-Sealing Clays Used for Waste Disposal Sites

Kaz Nagashima, Hironobu Saitoh,Takahiro Sugano
Port and Airport Research Institute, Yokosuka, Kanagawa 239-0826, Japan
J-Power Co. Ltd., Chigasaki, Kanagawa 253-0041, Japan

Sodium bentonite is a kind of smectite clay which is highly water-swellable. The sheet-like three-dimensional molecular structure can entrap water molecules of more than three times of its weight. Its most notable and attractive use is for seepage barrier (what civil engineers call "liner") in waste disposal sites because of the exceptional sealing capability with easy-to-shape plastic characteristics. For minimizing leakage of poisonous and radioactive contaminants, it is important to understand the leaching mechanism of water into the clay layers.

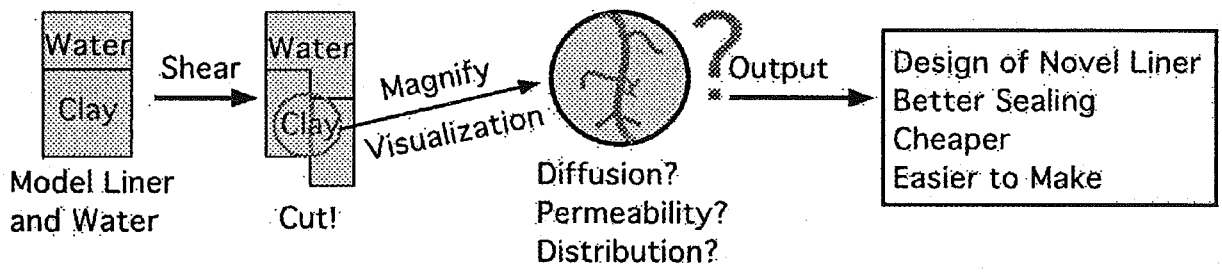

Figure 1: Scope of this study

Little is known about the microscopic behavior of water molecules when cracks are formed in a clay layer via shear forces due to earthquakes, ocean waves, and the weight of waste materials. In this line of research, magnetic resonance imaging can be a powerful tool, since it enables in situ and real-time observation of water progression and self-healing of clay matrix. Dynamics, diffusion, and dispersion of water in bentonite clay were investigated with ^{1}H magnetic resonance. A U-shaped low-field permanent magnet was used in this study in order to mitigate interferences from dipolar broadening and magnetic susceptibility mismatching. Shear forces were applied to clay at water/clay interfaces and the migration and magnetic parameters of water spins were studied as a function of applied force, times of weight loading, and water contents.

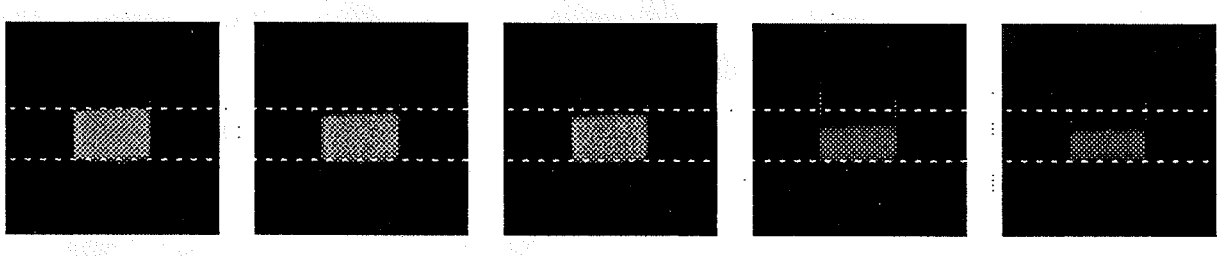

Figure 2: Preliminary results of this study. A series of spin-echo images of bentnite aqueous slurry under compression (8.51 MHz; 2D 128*128 projection). Image contrasts get less as the sample was compressed, possibly due to the migration of water molecules into pores of clay matrix. This change was observed immediately after the compression. Water drainage from the sample is the minor reason, since it takes a quite long time. Details of the mechanism are under investigation.

Local heat flux measurements using MRI : Non-uniformity of heat transfer in an ice thermal storage capsule pack

Kuniyasu OGAWA, Shinichiro NARUSE
Department of Mechanical Engineering, Faculty of Science and Technology, Keio University,
3-14-1 Hiyoshi, Kohoku-ku, Yokohama, 223-8522, JAPAN

Objective

The existence of spatial non-uniformity in the heat transfer coefficient induced by non-uniform coolant flow is a strong influence on the performance and the optimized design of an ice thermal storage vessel randomly packed with water capsules. Although the non-uniform distribution of heat transfer induced by fluid channels near the wall of a packed bed reactor in chemical engineering has almost been experimentally and numerically understood [1], the spatial non-uniformity in the heat transfer coefficient in the internal region of a thermal storage vessel has not been satisfactorily clarified to improve the performance and the optimized design of the vessel due to the absence of an appropriate measurement technique.

Method and experimental apparatus

A new method to measure the local heat flux distribution at capsule surfaces in an ice thermal storage capsule pack using magnetic resonance imaging (MRI) was developed to investigate the effect of non-uniform flow on the heat transfer in the storage vessel. With this method, the local heat flux distribution at a capsule surface was calculated from the time-evolution of the water-ice interface positions in the capsule.

A schematic of the cylindrical storage vessel used in this study is illustrated in Figure 1. Spherical polypropylene capsules of 10 mm diameter, which contain water, AgI and nitrogen gas, were randomly packed in the 110 mm ID cylindrical vessel as the test section. The time-evolution of the water images in the all capsules at the test section was obtained using the multi-slice spin-echo sequence with the 4.7 Tesla horizontal MR imaging system (UNITY INOVA-200 (330), Varian, USA).

Local heat flux maps in the ice thermal storage capsule pack

Based on the obtained time-evolution of the water volume image, the heat flow, Q, during the acquisition time, t_m, was calculated from the phase changing rate of water in each capsule using the image analysis technique[2]. The heat transfer coefficient, h_i, for each capsule was calculated from the equation of $Q/\{S\, t_m\, (T_{in,test} - T_{melt})\}$, where S is the surface area of one capsule and T_{melt} is melting point of ice.

The contour maps on the xz plane of the heat transfer coefficients obtained at the melting and freezing coolant conditions are shown in Figures 2 (a) and (b), respectively. The map at the freezing condition had a strong non-uniformity compared with the map at the melting conditions. The reason for this is that the solidification time of supercooled water in each capsule differs and that it is happen randomly.

Acknowledgements

We are grateful for the use of the MRI at the Department of Biomolecular Engineering, Graduate School of Bioscience and Biotechnology (Tokyo Institute of Technology). We are also grateful for our interaction with the Diagnostics Research Team, Drug Discovery Institute (Nihon Schering K.K.) during the MRI investigations.

References

[1] M. Kaviany, "Principles of Heat Transfer in Porous Media", Second edition, Springer, (1995).
[2] Kuniyasu Ogawa, et al, Proceedings of the Twelfth International Heat Transfer Conference, 333-338 (2002).

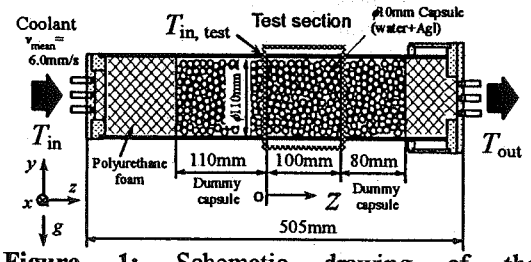

Figure 1: Schematic drawing of the experimental apparatus to measure the heat transfer coefficients from the capsule surfaces in the ice thermal storage vessel.

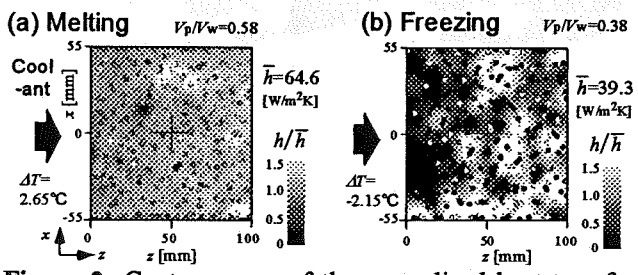

Figure 2: Contour maps of the normalized heat transfer coefficients, h_i/h, in the ice thermal storage vessel on the xz plane; (a) For melting case, (b) For freezing case.

High Pressure NMR Microimaging Studies of Gas Hydrate Formation.

Igor L. Moudrakovski, G.E. McLaurin and John A. Ripmeester
Steacie Institute for Molecular Sciences, National Research Council, Ottawa, Ontario, K1A 0R6, Canada

Gas hydrates, or clathrate hydrates, are guest-host compounds in which guest molecules reside in cages formed by hydrogen-bonded water molecules. Small molecules such as CH_4 and CO_2 form cubic structure I hydrate with the ideal unit cell $6M_L2M_S46H_2O$, where M_L and M_L are the guest sites associated with the large tetrakaidecahedral and small dodecahedral cages, respectively. Deposits of naturally occurring hydrates with methane as guest are considered to be a promising energy source of the future because of their vast extent. On the other hand, hydrates of CO_2 are considered to be a possible way of sequestering this green-house effect promoting gas. Understanding the details of the formation and decomposition of hydrates is therefore of considerable importance.

Using high pressure ^1H NMR microimaging we performed extensive *in -situ* studies of CH_4 and CO_2 hydrates formation. In our experiments we start by forming a thin layer of hydrate on the surface of ice by exposing it to a hydrate forming gas at a sufficiently high pressure and a temperature below 0 °C. In this setup when the temperature is increased above the ice melting point, the integrity of the particles is maintained and liquid water stays confined inside a thin hydrate shell [1]. Formation of hydrate phase inside these particles can be detected by observing a decreased ^1H density in the images, since the hydrate phase is essentially invisible because of the very short T_2s.

Our ^1H microimaging data show that the formation of hydrate is spatially a highly inhomogeneous process, and that only a minor part of the hydrate phase grows uniformly with time inside the liquid phase. Instead, the many droplets in the sample show sudden and spontaneous conversion. This suggests the presence of several mechanisms, where the hydrate skin acts as a semi-permeable membrane as well as a low thermal conductivity, insulating layer, making each drop a separate mini-reactor. Low gas permeability of the hydrate layer allows only for slow development of the hydrate inside the shell toward the center. A remarkable observation is that growth inside the hydrate shell is not gradual, but sudden after long periods of inactivity. This event initiates a phase of rapid growth inside the drop that is reminiscent of renewed nucleation-growth cycles. As well, the hydrate shell is seen to rupture, presumably the result of stress, giving way to yet more relatively rapid hydrate growth. This appears to be a common feature for structure I hydrates, as we observed this for both CH_4 and CO_2 hydrates. Overall, this newly found information will allow for the selection of experimental conditions that promote fast growth of hydrates.

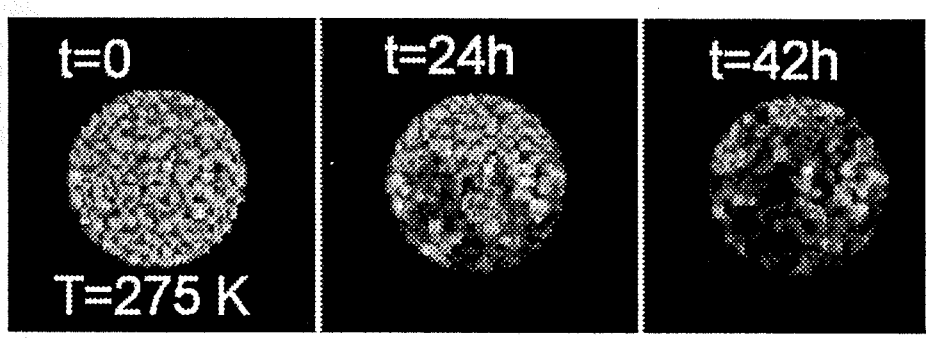

Figure 1: ^1H MRI of CO_2 hydrate formation at pressure of 840 psi and T=275K.

References

[1] I.L. Moudrakovski, C.I. Ratcliffe, G.E. McLaurin, B. Simard, J.A. Ripmeester, *J. Phys. Chem. A* **104**, 4969-4972 (1999).

Nuclear Magnetic Resonance of Hyperpolarized ^{129}Xe in aqueous Na-montmorillonite emulsions

Takahiro Ohkubo[1,3], Ryou Tanaka[2], Koji Saito[3], Yasuhisa Ikeda[1]

[1]Research Laboratory for Nuclear Reactors, Tokyo Institute of Technology, 2-12-1 O-okayama, Meguro-ku, Tokyo, 152-8550, Japan

[2]Toyoko Kagaku Corporation, Reseach & Development DEPT., 1280 Nakamaruko Nakahara-ku Kawasaki City, Kanagawa, 211-8502, Japan

[3]Nippon Steel Corporation, Advanced Technology Research Laboratory, 20-1 Shintomi Futtsu City, Chiba, 293-8511, Japan

Na-montmorillonites are used as engineered barriers to inhibit the migration of contaminants from the waste to surrounding environment. This ability is strongly related to the swelling behavior of Na-montmorillonite by water molecules. To understand the character of Na-montmorillonite in an aqueous emulsion of high water contents, hyperpolarized ^{129}Xe NMR as a probe of its surroundings is applied to aqueous Na-montmorillonite emulsions.

The sample used in this study was high purity Na-montmorillonite (Na-mont). A uniform mixture of the Na-mont and heavy water was made by mixing in a NMR sample tube (diameter = 10 mm). The heavy water contents of the emulsions, defined as the weight ratio of water to Na-mont, were determined by differential thermal analysis.

We produce hyperpolarized ^{129}Xe by alkali metal (Rb) spin exchange optical pumping. The condition of optical pumping cell is follows as; cell temperature: 393 K, magnetic field: 120 G, cell capacity: 300 ml. The hyperpolarized ^{129}Xe gas was removed from pumping cell and was bubbled through the emulsions in a NMR sample tube, and then the NMR signal was acquired instantly by only single radio frequency pulse. The values of the chemical shift are referenced to xenon gas (0 ppm).

Aqueous emulsions of Na-mont are semitransparent and faint brown color. The spectra of hyperpolarized ^{129}Xe dissolved in emulsions are shown in Figure 1. The ^{129}Xe spectrum with 99.9 wt.% water content exhibits two lines separated by approximately 190 ppm and considerably broadened from chemical exchange. The down field signal corresponds to ^{129}Xe in the heavy water. Compared with chemical shift of xenon dissolved in pure heavy water, it is slightly shifted to higher field. Because of very little dissolved Na-mont, it is considered that the ^{129}Xe in 99.9 wt.% water content forms clathrate hydrates with water, which consist of an ice-like network of host water molecules linked together by hydrogen bonds. The peaks of about 0.3 ppm with 95.1 wt.% aqueous emulsion perhaps correspond to the xenon surrounded to Na-mont layers.

A zig-zag column model of Na-mont layers in 95 wt.% aqueous emulsions is proposed from variation of interlayer spacing measured by X-ray diffraction study [1]. The broadening of peaks in 0.3 ppm accompanied by increment of water contents are supposed that a zig-zag column model of Na-mont layers are broken for dominant water amount.

The enhanced signal of hyperpolarized ^{129}Xe has shortened considerably the acquisition times for experiments, and makes it possible to study dynamics and formation of water in aqueous emulsions.

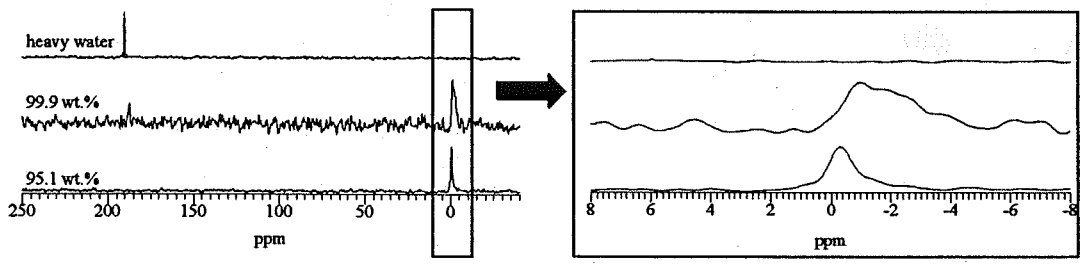

Figure 1: 110.6 MHz NMR spectra of hyperpolarized ^{129}Xe dissolved in aqueous emulsions with various heavy water contents, and pure heavy water. The spectra are scaled to the same maximum amplitude.

References

[1]Yoshiaki Fukushima, *Clays and Clay Minerals* **32**, 320-326 (1984).

Visualization of complex gas dynamics by laser-polarized Xe129 NMR

Kimberly Pierce, Song-I Han, Alex Pines
Materials Science Division, Lawrence Berkeley National laboratory and
Department of Chemistry, University of California, Berkeley, CA 94720, USA.

An understanding of gas flow dynamics is essential in applications such as aerodynamics, heterogeneous catalytic reactions, and chemical engineering problems, e.g. gas/liquid extraction phenomena [1]. Complex flow dynamics in general, but especially air/gas dynamics in real systems –why Beckham's soccer ball trajectory bends in air, how airplane wings function?- are difficult to simulate, not only due to the lack of computational power, but also appropriate models. Experimentation and observation is the best alternative approach, but little progress has been made with the few means of measuring and visualizing gas flow [2,3]. NMR flow imaging provides one of the few ways to directly visualize a flow process non-invasively, quantitatively, and in a three-dimensional fashion. Most efforts in the field have been limited to liquid state whereby the visualization of complex flow patterns [4,5] and turbulences [6,7] are still rather rare investigations. In the last years, the laser-polarization (LP) of noble gas atoms has become one tool to overcome the low sensitivity of NMR, and allows spectroscopy and imaging of the dilute gas phase (pure or within materials) within a reasonably short experimental time. Xe^{129} is especially attractive for this prospect because of a highly polarizable electron cloud which is extremely sensitive to the local environment.

We are particularly interested in using LP-Xe^{129} for the visualization of complex gas dynamics, whereby in the first approach, xenon is regarded as an ideal inert gas. Our investigation includes gas flow through capillaries, over airplane wings, and around constrictions, whereby often even simple flow patterns can only be approached experimentally, and there are few reports of gas visualization in the literature [2,3,8,9]. In the simplest model experiment, we have obtained high-resolution xenon gas phase flow images through millimeter and sub-millimeter scale channels manifesting the Newtonian character of gas (Fig. 1) [9]. First experiments of gas flow around constrictions give promising insight into the complex behavior. Further interests include the addition of spectroscopic information for the investigation of gas dynamics in surface active materials and even reactive systems [10]. Xenon's large chemical shift range can be exploited for the recognition of absorption onto surfaces as would occur in catalytic reactions [11].

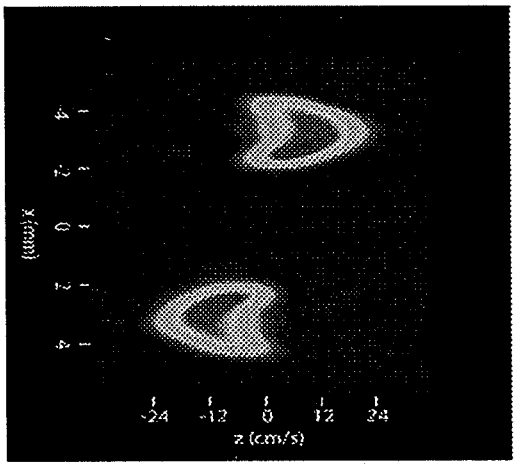

Figure 1: High resolution LP-Xe^{129} gas flow imaging through a U-shaped channel (2mm I.D.). The straight section of counter-flow reveals laminar flow pattern.

References

[1] Moustin, S., Hebrard, G., Thakre, S.S., Roustan, M., *Chem. Eng. Science* **56**, 1041-1047 (2001).
[2] Koptyug, I.V. et. al., *Journal Magn. Reson.* **147**, 36 (2000).
[3] Mizeraczyk, J. et.al., *Journal of Electrostatics* **51-52**, 272-277 (2001).
[4] Weber, M., Klemm, A., Kimmich, R., Phys. Rev. Lett. **86** (19), 4302-4305 (2001).
[5] Han, S., Stapf, S., Bluemich, B., Phys. Rev. Lett. **87** (14) 144501 (2001).
[6] Kose, K., *Journal of Magn. Reson.* **92**, 631-635 (1991).
[7] Kose, K., *Journal of Magn. Reson.* **96**, 596-603 (1992).
[8] Kaiser, L., Meersmann, T., Logan, J., Pines, A., *PNAS* **97**, 2414-2418 (2000).
[9] Kaiser, L., Logan, J., Meersmann, T., Pines, A., *Journal Magn. Reson.* **149**, 144-148 (2001).
[10] Moudrakovski, I.L. et. al., *Journal Magn. Reson.* **144**, 372-377 (2000).
[11] Koptyug, I.V., Ilyina, L.Y., Matveev, A.V., Sagdeev, R.Z., Parmon, V.N., Altobelli, S.A., *Catalysis Today* **69**, 385-392 (2001).

An Approach to MR Spectroscopy and Imaging in Permanently Inhomogeneous Magnetic Fields

Vasiliki Demas, Jeffrey Reimer Department of Chemical Engineering, **Carlos Meriles, Dimitris Sakellariou, Songi Han, Alex Pines** Department of Chemistry, University of California, Berkeley, CA 94720

Previous work [1-3] has established the efficacy of pulse sequences that allow "outside the magnet" or "ex-situ" MR. This is an attempt to couple ex-situ spectroscopy with imaging and allow for use of MR in applications where sample insertion in the magnet and rf coil is not feasible. We have developed a pulse sequence that allows for ex-situ spectroscopy and imaging and have performed a proof of principle experiment in an emulated "outside the magnet" environment. We have further designed and constructed a set of flat rf and gradient coils that could be used in a one-sided magnet as shown in Figure 1.

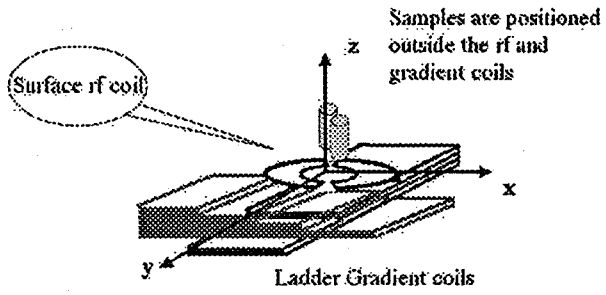

Figure 1: The new setup has ladder-coils for the static magnetic field gradients (for simplicity only half of the coil is shown) and a surface rf-coil for sample excitation and signal detection.

References

[1] Godward, J., E. Ciampi, M. Cifelli, and P.J. McDonald, "Multidimensional Imaging Using Combined Stray field and Pulsed Gradients," *Journal of Magnetic Resonance* **155**, 92-99 (2002).

[2] Meriles C.A., D. Sakellariou, H. Heise, A.J. Moule, and A. Pines "Approach to high-Resolution ex Situ NMR Spectroscopy," *Science* **293**, 82-85 (6 July 2001).

[3] Meriles, C.A., D. Sakellariou, and A. Pines, "Broadband Phase Modulation by Adiabatic Pulses," Manuscript Submitted for Publication (2003).

Xenon NMR at very high concentrations

K. Münnemann [a], S. Han [b], F.W. Häsing [c], B. Blümich [a], S. Appelt [c]
[a] Institute of Macromolecular Chemistry and Technical Chemistry, RWTH-Aachen, D-52056, Germany
[b] Max-Planck Institute for Polymer Research, Ackermannweg 10, D-55128, Mainz, Germany
[c] Zentrallabor für Elektronik, Forschungszentrum Jülich, D-52425, Germany

The noble gas Xenon provides two extraordinarily advantages to NMR: Firstly the chemical shift of Xe is extremely sensitive to its local environment due to its highly polarizable electron cloud and secondly the nuclear polarization of Xenon can be enhanced by several orders of magnitude compared to its equilibrium value by means of optical pumping. Therefore NMR with hyperpolarized xenon has found widespread applications in material science and medicine [1-5].

It is a challenge to find a storage and carrier system, which transports highly concentrated polarized Xe to the sample, which should be examined. The system in demand has not yet been reported for liquid-state applications, where two different requirements must be fulfilled: a high xenon concentration in the carrier-liquid and a long T_1 relaxation time for Xe dissolved in the liquid [6]. Therefore we examine the solubility and the T_1 relaxation times of xenon in several deuterated and non-deuterated solvents.

We study the melting and dissolvation process of hyperpolarized Xe ice into different solvents by means of Xe NMR imaging and spectroscopic imaging. Starting from the initial condition of a hyperpolarized Xe ice layer on top of an ethanol (ethanol/water) ice block we measured the Xe phase transitions as a function of time, space and temperature. Regarding the pure ethanol pieces of Xe ice fall through the supercooled viscous ethanol phase on to the bottom of the sample tube forming there a thin layer of highly concentrated Xe/ethanol mixture. The Xe polarization in this liquid layer is traped for quite a long time. It exists up to room temperature and is a promising candidate for a storage system. For the ethanol/water mixture (80 vol%) most of the polarized Xe liquid stays on top of the ethanol/water ice block and then evaporates almost completely into the gas phase.

We examined highly concentrated Xe/ethanol mixtures in more detail under thermal equilibrium conditions. The solubility of gases in liquids increases generally with decreasing temperature. We have visualized this correlation by taking spectra of ethanol at different Xe pressures and different temperatures (295 K – 135 K). Even under initially high pressure conditions we observed no liquid and solid Xe phase down to 145 K. This is due to supercooled ethanol which absorbed a huge amount of Xe. We obtained arbitrary concentration ratios of Xe to supercooled ethanol.

References

[1] M.S. Albert, G.D. Cates, B. Driehuys, W. Happer, B. Saam, C.S. Springer, A. Wishnia, *Nature* **370**, 188 (1994).
[2] C.H. Tseng, R.W. Mair, G.P. Wong, D. Williamson, D.G. Cory, R.L. Walsworth, *Physical Review E* **59**, 1785-1788 (1999).
[3] G. Navon, Y.-Q. Song, T. Rõõm, S. Appelt, R.E. Taylor, A. Pines, *Science* **271**, 1848 (1996).
[4] A. Bifone, Y.-Q. Song, R. Seydoux, R.E. Taylor, B.M. Goodson, T. Pietrass, T.F. Budinger, G. Navon, A. Pines, *Proc. Natl. Acad. Sci. USA* **93**, 12932-12936 (1996).
[5] E. Brunner, *Concepts in Magnetic Resonance* **11**, 313 (1998).
[6] P. Berthault, H. Desvaux, *Eur. Phys. J. D* **22**, 65-73 (2003).

Automated Hyperpolarized ^{129}Xe Gas Generator for Biomedical MRI/S Applications

Mineyuki Hattori[*1], Norio Ohtake[2], Ryo Tanaka[2], Morio Murayama[2], Kazuhiro Homma[1], Moyoko Saito[3], Toshiharu Nakai[3], and Takashi Hiraga[3]

[1]Photonics, AIST, Tsukuba, Ibaraki, 305-8568, JAPAN,
[2]Toyoko Kagaku Co. Ltd., Kawasaki, Kanagawa, 211-8502, JAPAN,
[3] Human Science and Biomedical Engineering, AIST, Tsukuba, Ibaraki, 305-8564, JAPAN,
[4]Life Electronics Laboratory, AIST, Ikeda, Osaka, 563-8577, JAPAN.

Purposes

The hyperpolarization technique can increase ten thousand times the signal sensitivity of NMR for ^{3}He and ^{129}Xe and make instantaneous imaging of the cavity gases. This technology is expected as practical uses of medical equipment that makes it possible to carry out instantaneous diagnostic of lung functions and of medical technologies for diagnosis and prevention of cerebral infarction based on high-accuracy and high speed imaging of the blood flow in the brain.

Experiments

An automated batch type apparatus for Xe hyperpolarization, including ultra pure gas application system and using high-power diode laser arrays was developed. The stray field of the horizontal superconducting magnet (2T) was used for the optical pumping processes. In this apparatus, small pieces of the alkaline metal Rb and Xe and N_2 gas with pressure of around 1.2 atm are sealed in a cylinder cell of 60mm diameter and 100mm length made of Pyrex glass with a flat window for irradiation. The cell is heated to 100°C in a magnetic field of around 100G and irradiated by 30W semiconductor laser light of 794.7±1nm in wavelength, circularly polarized through a quarter-wave plate. After 20 minutes, spin-polarized xenon gas is produced with a polarization rate of several %. We have prepared a birdcage coil and a surface coil for ^{129}Xe frequency at 2T (~23.56MHz) with the 50Ω matching circuits.

Results

We successfully developed a practical device that uses a batch method[1] to provide a continuous supply of hyperpolarized xenon gas with a high rate of polarization. We achieved 1~4% polarization of ^{129}Xe for Xe(98%) and N_2(2%) gas mixture and performed magnetic resonance imaging experiments. In our experiment, the quality of image obtained by using FLASH (TE=3.7ms, NEX=1, 64X64) is almost same as that by segmented EPI (Number of segments=4, TE=9.68ms, NEX=16, 64X64) for the Xe in a glass tube. Furthermore, MRI images of hyperpolarized Xe gas extracted in a syringe were acquired.

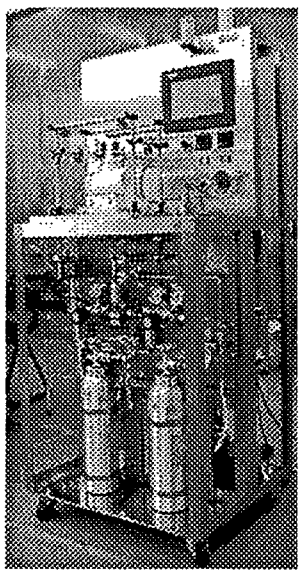

Conclusion

The time resolution of acquisition was enhanced from about 60s for the FLASH sequence to about 500ms for the 4-shots segmented EPI sequence. The faster acquisition sequences, for example EPI sequence, is essential technology for the high-accuracy and high speed imaging of the blood flow in the brain. The research should facilitate work on NMR/MRI to shorten measuring times, produce more diverse information, and increase accuracy. The research should also facilitate the development of technologies suitable for industrial applications, including measurement of pore size distribution, analysis of gas dynamics, and nondestructive testing.

References

[1]Hideaki Fujiwara, Atsuomi Kimura, YasuhiroYanagawa, Takashi Kamiya, Mineyuki Hattori, Takashi Hiraga, *Journal of Magnetic Resonance*, **150**, 156-160 (2001).

A Combined Confocal/^{1}H-NMR Microscopy Study of Water Dynamics and Compartmentalization in Apoptotic CHO Cells

Kevin R. Minard, Don S. Daly, Gary R. Holtom, Loel E. Kathmann, Paul D. Majors, Brian D. Thrall and Robert A. Wind

Pacific Northwest National Laboratory, P.O. Box 999, MS K8-98, Richland, WA 99352, USA

Abstract

During cancer therapy apoptosis is an important mode of cell death that is characterized by stereotypical morphological changes as cells shrink, deform, loose contact with neighbors, and finally fragment into compact, membrane-enclosed structures. In order to identify potential surrogate ^{1}H-NMR markers for this dynamic programmed death process this study has exploited a unique integrated magnetic resonance and laser-scanning confocal fluorescence microscope for following apoptosis in monolayer cultures of Chinese Hamster Ovary (CHO) cells [1]. In this way observed morphological changes can then be correlated with the dynamics and compartmentalization of water measured during *simultaneous* pulsed field gradient (PFG) ^{1}H-NMR experiments. In this presentation initial results from this investigation will be described. Figure 1 shows how typical optical images collected at different times can be employed for clearly visualizing changes in the morphology of individual cells. The accompanying PFG data shows how *simultaneous* changes in the dynamics of cell water, and possibly its compartmentalization, alter asymptotic PFG data collected at high b-values (> 3500 s/mm^2). In ongoing efforts aimed at understanding this result T_1 and T_2 measurements were performed with different b values during chemically induced apoptosis. Results support the idea of three distinct water compartments – one corresponding to bulk water in the surrounding culture media and two slower diffusing compartments (each with a different T_1, T_2, and apparent diffusion coefficients). Remarkably, the volume fraction and measured diffusion coefficient for the slowest compartment is identical to that obtained for hydration water in both quasi-elastic neutron scattering and PFG NMR experiments conducted with dehydrated cells and tissues [2]. Since the largest ^{1}H-NMR changes are routinely observed in the slowest compartment during apoptosis, data suggests that PFG data collected at large b-values might serve as a sensitive indicator for apoptotic cell death and that observed alterations reflect changes to tightly bound water that is typically left behind when cells and tissues are dehydrated.

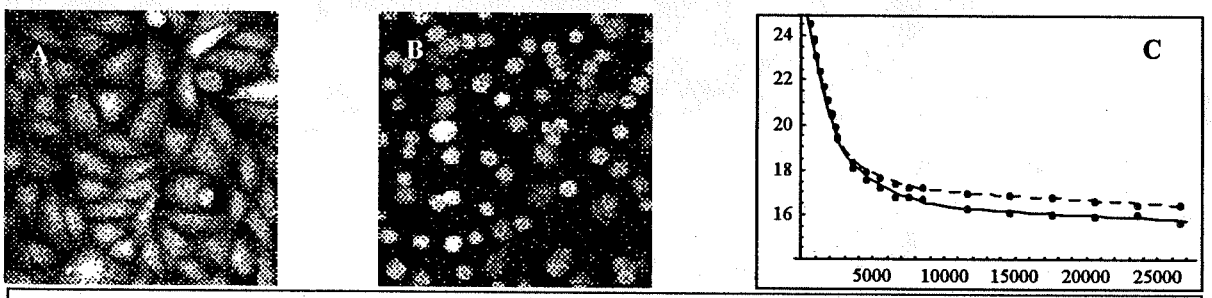

Figure 1: A) Green fluorescence optical image of healthy CHO cells in a 205x205 micron square field-of-view (FOV). B) Same FOV showing apoptotic cells after 16 Hrs of exposure to Okadaic Acid. C) Experimental PFG data (dots) showing the natural log of water's ^{1}H-NMR signal as a function of increasing sensitivity to molecular diffusion (b-values in s/mm^2). Raw PFG ^{1}H-NMR data was collected using a simple spin-echo characterized by isotropic diffusion weighting, a diffusion time of 4 msec, an echo-time of 12 msec, and a repetition time of 6 seconds. The solid line shows a three-compartment fit to data collected during A), and the dashed line shows the fit for data collected during B).

References

[1] R.A. Wind, P.D. Majors, K.R. Minard et al., *Applied Magnetic Resonance* **22,** 145-158 (2002).

[2] I.L Cameron et al, *Cell Biology International,* **21**(2), 99-113 (1997).

^{1}H-NMR Microscopy of Respiratory Airway Architecture in Laboratory Animals

Kevin R. Minard, Rick A. Corley, Chuck Timchalk, Harold E. Trease, *Charles G. Plopper, and ^Jack R. Harkema
Pacific Northwest National Laboratory, P.O. Box 999, MS K8-98, Richland, WA 99352
* University of California, One Shields Avenue, Davis, CA 95616
^ Michigan State University, East Lansing, MI 48824-1316

Abstract
Computational fluid dynamics (CFD) simulations of airflow in geometries representing the respiratory tract of laboratory animals is an important aspect of inhalation toxicology. Compiling detailed descriptions of airway architecture has, however, remained a difficult and time consuming process that has traditionally been based on either the painstaking analysis of serial tissue sections [1], or hand measurements derived from delicate airway casts [2]. To speed CFD model development, this study has examined how realistic descriptions of airway architecture can be rapidly compiled by exploiting three-dimensional (3D) ^{1}H-NMR microscopy in conjunction with advances in image segmentation and 3D mesh generation. Results presented in Figure 1 illustrate the remarkable level of detail that can be derived using 3D images of excised nasal-sinus tissue and pulmonary airway casts of the rat. For comparison, results are shown side-by-side with analogous data that required months to compile using traditional methods. Considering that MR image collection and data processing typically required only a day, results illustrate the dramatic reduction in processing time required for 3D CFD model development. Encouraged by these findings, efforts to extend the methodology for developing meshes of airways in the monkey have been initiated and progress towards this goal will also be presented.

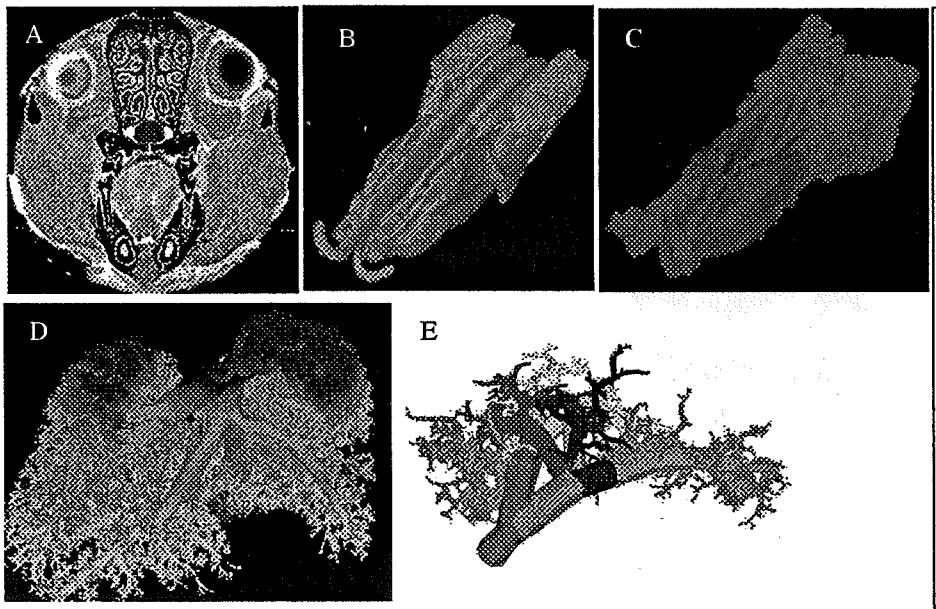

Figure 1: A) Single slice of raw 3D image data showing the segmented nasal-sinuses in red, B) 3D rendering of nasal-sinuses derived from processed image data collected with 117 micron resolution, C) comparable data from standard histology [1], D) 3D rendering derived from images of a silicone rubber cast collected with same resolution as in B, E) analogous cast data compiled using hand measurements of branching angles and airway diameters [2].

References
[1] J.S Kimbel et al, Toxicol Appl Pharmacol, 145, 253-263 (1997).
[2] O.G. Raabe et al, Report LF-53, Inhalation Toxicology Research Institute, Lovelace Foundation of Medical Education and Research, Albuquerque, NM (1976).

MR Microscopy and Spectroscopy of *in vitro* Alginate Constructs: The Engineering of a Bioartificial Pancreas

S.C. Grant[1], N.E. Simpson[2], S.J. Blackband[1] & Ioannis Constantinidis[2]
Dept. of Neuroscience[1] & Medicine[2], University of Florida, Gainesville, FL 32610, USA

Introduction

The bioartificial pancreas is a potential diabetes treatment that can regulate blood-glucose levels without the need for extensive immunosuppressive therapy. The preferred biocompatible matrix has been the alginate/poly-L-lysine/alginate (APA) bead, which has been used to encapsulate a variety of cells including mammalian islets and transformed beta-cell lines. MR microscopy and microspectroscopy provide robust, non-invasive methods for monitoring the viability and function of cells as well as the integrity of the encapsulating matrix under both *in vitro* and *in vivo* circumstances. This current presentation details recent *in vitro* work that has investigated the MR microscopy and localized spectroscopy of mouse insulinoma cells and human islets during the growth cycle. Additionally, high-resolution ^{1}H imaging has been applied to establish baseline data concerning the MR properties of various alginate substrates.

Methods

Using a solenoidal microcoil interfaced with a Bruker 17.6-T magnet and Micro2.5 microimaging system, unperfused transformed cells (□TC3) and harvested human islets were interrogated at different time points following their encapsulation in 800-□m alginate beads. High-resolution, T_2^* images were acquired at isotropic resolutions of between 25 and 6.25-□m resolutions using a three-dimensional gradient echo sequence. T_2- and diffusion-weighted images also were acquired, although at lower resolutions (~25x25x100 □m) and with a multi-slice 2D spin echo sequence. Using these images, water-suppressed ^{1}H spectra were acquired using PRESS localization from 215-nL voxels within single beads. In addition, blank alginate beads of different compositions (varying ratios of mannuronic/guluronic acid linked residues and molecular weight) and different concentrations of Ca^{+2} gellating agent were investigated via MR microscopy. For these substrate samples, T_1, T_2 and ADC values were calculated.

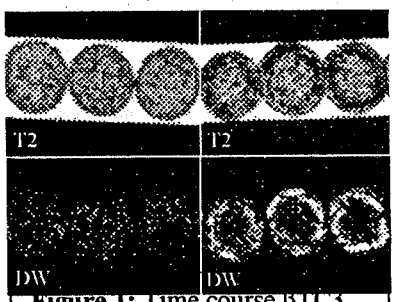

Figure 1: Time course βTC3 images acquired in 50 min.

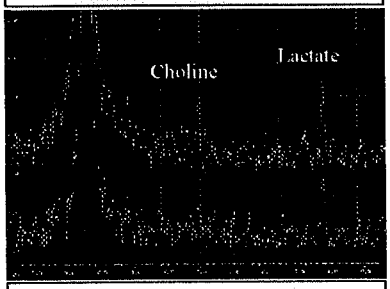

Figure 2: Top – sample loaded
Bottom – 2.5 hrs later

Results

MR microscopy (Fig. 1) shows definable clusters of □TC3 cells that become localized to the periphery of the bead during the growth cycle. Displaying decreased signal in T_2 images, islets (which do not experience cellular growth) and □-cell clusters also were defined easily by hyperintense signal regions in diffusion-weighted images. High-resolution T_2^* images display more detail, with the interior of cell clusters appearing as moderate signal regions encompassed by areas of signal void—possibly indicating the exaggerated presence of an extruded extracellular matrix. Localized spectra (Fig. 2) confirmed the presence of cell growth and viability. Because of the lack of perfusion, choline—an indicator of cellular membrane integrity and viability—decreases as the external oxygen reserve is expended, while lactate increases. Although T_1 and ADC values varied little from bulk water, the T_2 of water within blank beads displayed large differences as a function of Ca^{+2} concentration and mannuronic/guluronic ratios. Independent of molecular weight, low [Ca^{+2}] resulted in higher T_2s (related to decreased gel rigidity) while high mannuronic acid yielded reduced T_2s (related to increased gel disorder).

Conclusions

High-resolution T_2^* and diffusion imaging appear to be feasible methods of assessing cell cluster heterogeneity and proliferation in alginate bead constructs, while microspectroscopy is an strong indicator of cellular viability. Additionally, T_2 contrast appears to be a potential tool for interrogating alginate matrix stability and integrity, both *in vitro* and *vivo*.

Mapping the Mouse Brain: MR Microscopy, Structural Verifications & Volumetrics on Excised Normal & Mutant C57BL6/J Brains at 17.6 T

S.C. Grant[1], L. Zhang[3], A. Siram[3], P.R. Hof[4], P.K. Thanos[2], N.D. Volkow[2], D. Grandy[5], S.J. Blackband[1] and H. Benveniste[2,3]

[1]Deptartment of Neuroscience, University of Florida, Gainesville, FL 32610, USA
[2]Medical Department, Brookhaven National Laboratory, Upton, NY 11793, USA
[3]Department of Anesthesiology, SUNY-SB, Stony Brook, NY 11794, USA
[4]Kastor Neurobiology of Aging Laboratories & Fishberg Research Center for Neurobiology, Mount Sinai Medical School of Medicine, New York, NY 10029, USA
[5]Deptartment of Physiology, Oregon Health & Science University, Portland, OR 97239, USA

Introduction

In this presentation, recent advancements in the application of MR microscopy to intact, excised mouse brains are discussed. These datasets revolve around the creation of a true probabilistic C57BL6/J mouse brain atlas anatomical template to be used as a normalization template for a wide variety of data.

Methods

A homebuilt, inductively coupled split-ring resonator was interfaced with a Bruker 17.6-T magnet and Micro2.5 microimaging system for all imaging studies. Intact and perfusion-fixed C57BL6/J mouse brains were interrogated using three contrast mechanisms to generate ^{1}H images. T_2^*-weighted datasets were acquired with a three-dimensional gradient-echo pulse sequence (TE/TR=7.5/150 ms) at a 47-□m isotropic resolution in 5.5 hours. T_2- and diffusion-weighted (b=500 s/mm^2) MR datasets were acquired with a three-dimensional spin-echo pulse sequence (TE/TR=20/1000 ms) at a 53-□m isotropic resolution in 18.5 hours. Ten days prior to animal sacrifice, granule lesioning was instigated by direct colchicine injection (CI) of the left dentate gyrus of the dorsal hippocampus (the right dentate was used as a contralateral control). To investigate transgenic phenotyping, modified dopamine-receptor mouse brains were imaged after 10-months of ethanol intake.

Results

One of the key elements of any brain atlas is its ability to provide anatomical landmarks and structures that are both visualized and identified. As an initial foray into the validation process, we have focused on the granule cell layer (GC) of the dentate gyrus of the hippocampus. In addition to histological identification by a neuroanatomist and co-registration of MR micrographs that exploit different MR contrast mechanisms (Figure 1), we have utilized the toxic sensitivity of granule cells to colchicine to validate structure by site-specific anatomical lesioning (Figure 2). Although the generation of the MR-based C57BL6/J mouse brain atlas is an ongoing process, we have begun to compare the initial atlas results to the morphologically phenotyping of transgenic, targeted mutations. With a focus on neurodegenerative diseases and changes induced by drugs of abuse, we have compared preliminary MR microimages of D_2(-/-) & D_2(+/+) mutants under the prolonged influence of ethanol (ETOH), showing changes in brain volumes with treatment (Figures 3 and 4).

Figure 1: 3D GE surface renderings of co-registered brain datasets

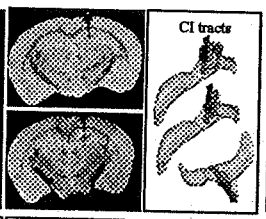

Figure 2: CI sites, GC lesions & tracts in 3D GE (top left), DW-SE (bottom left)

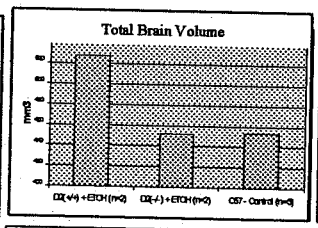

Figure 3: Comparison of total mouse brain volume between D_2 mutant and normal C57BL6/J mice

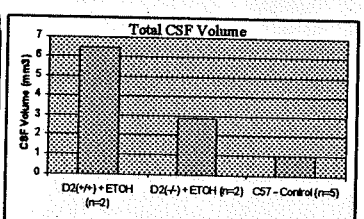

Figure 4: Comparison of total cerebrospinal fluid volume between D_2 mutant and normal C57BL6/J mice

Imaging of Spinal Cord Disease Models in the Rat Post Mortem at 17.6 T

T. Weber[1,2], T. Neuberger[1], N. Weidner[2], M. Vroemen[2], A. Müller[2], G. Giegerich[2], U. Bogdahn[2], A. Haase[1], A. Steinbrecher[2], and C. Faber[1]

[1] Experimentelle Physik 5, Institute of Physics, University of Würzburg

[2] Department of Neurology, University of Regensburg

Introduction

^{1}H MRI is a commonly used method to detect spinal cord pathology in humans. In vivo MRI of the spinal cord in experimental animals is hampered by limits in spatial resolutions and artefacts caused by respiration and blood flow. Therefore spinal cord MRI data in animal models are virtually non-existent so far. We present a method to gain high resolution morphological information to rapidly detect and quantify lesions in both spinal cord injury (SCI) models and Experimental Autoimmune Encephalomyelitis (EAE).

Objects and Methods

MR imaging

Imaging experiments were conducted on a Bruker Avance 750WB system at 17.6 T (750 MHz proton resonance frequency). The probe contained a linear 5 mm birdcage resonator. A 3D gradient echo sequence with an echo time of 13.5 ms and a repetition time of 50 ms was used. In a scan time of 5.5 hours a spatial resolution of 35x35x58 μm^3 was achieved.

Spinal cord injury

Adult female Fischer 344 rats received contusions of the midthoracic spinal cord using an IH Impactor (200kdyn applied force). One week after contusion animals were sacrificed by transcardial perfusion with 4% paraformaldehyde. Spinal cords were excised, postfixed with 30% sucrose and placed in a NMR tube.

EAE

Adult female DA-rats with EAE, immmunized 28 days previously with a peptide of myelin oligodendrocyte glycoprotein in complete Freund's adjuvant were sacrificed by transcardial perfusion with 4% paraformaldehyde. Spinal cords were excised, postfixed and placed in the NMR-tube.

Results

Spinal cord injury

MRI data of the thoracic part of the spinal cord around the injured tissue was acquired. In normal appearing tissue gray and white matter could be easily distinguished whereas in the contusion area the contrast between gray and white matter disappeared, i.e. injured tissue could be identified.

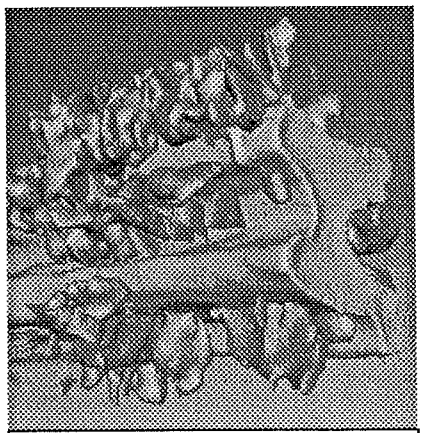

Figure: 3D rendering of MR EAE data set; gray matter regions are visualized in green and white matter lesions in light blue

EAE

Healthy gray and white matter were easily differentiated with high contrast. Lesions appear bright in the otherwise dark normal appearing white matter. Results from MR imaging correspond very well with results from histopathology as far as white matter lesions are concerned. Gray matter lesions seen in histopathology were not detectable in the MR images.

Discussion

Direct visualization of spinal cord lesions with high resolution MR imaging could be achieved in a total scan time 5.5 hours. This is much shorter than needed with the standard method of histopathological analysis and therefore enables a higher throughput of samples and still yields all important disease related information.

Imaging of Embryonic Development

Bianca Hogers, Madelon L. Fekkes, Cees Erkelens, Robert E Poelmann
Department of Anatomy, Leiden University Medical Center, Leiden, The Netherlands

The real time visualization of embryonic development was thought to be idealistic, and for that reason our challenge. In some pilot experiments we established that the resolution and contrast obtained by MRM was sufficient to study even the youngest stages of avian and murine development in a death and fixated condition. We also explored the benefits of higher magnetic field strengths for imaging and found that there was a three times SNR increase after increasing the field from 7.0 to 17.6 Tesla [1].

For imaging of living embryos the sequence had to be very fast to avoid moving artefacts. For simplicity we started with avian embryos (1 embryo in an egg). Experiments were performed on a Bruker 89 mm vertical bore magnets, working at 400 Mhz (9.4T), a gradient system of 20 G/cm with the Mini 0.5 probe with fixed 38 mm birdcage resonator. Multislice RARE gave the best anatomical detail (TR/TE=10000/6, MTX 256, RARE factor 32, NEX 4, slices of 0.5 mm without gap and a resolution of 58 micrometers (after zerofilling)). With this protocol we performed time course imaging of quail embryos at embryonic day 4, 5, 11 and 12. The older embryos were sedated by exposing them to room temperature for half an hour. To study any effect of the magnetic field or the hypothermia on the embryonic development we retrospectively compared the embryonic weight of the MRM group versus a group of control embryos. The results are presented.

For imaging of mouse embryos pregnant mice were anesthetized with isoflurane (O_2/air) and mounted in an Animal Handling System (ID of 25 mm). The mother mouse was connected to an ECG and a respiratory gating device with pneumatic sensor and signals were registrated with a Bruker Physiogard. Again, multislice RARE was the best method for anatomical details (30 slices of 0.5 mm, RARE factor 32, TR/TE=10000/6 ms, MTX 256, NEX 2, with a resolution of 68 micrometers (after zerofilling).

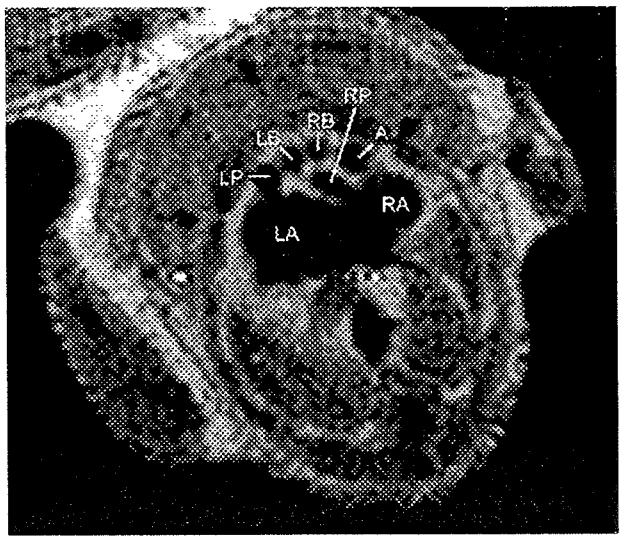

Figure 1: MRM-image through the heart of a living quail embryo. The resolution of 58 um is sufficient to see the individual great arteries and the heart chambers. A, aorta; LA/RA, right/left atrium; LB/RB, right/left brachiocephalic artery; LP/RP, right/left pulmonary artery

References
[1] Bianca Hogers, Dieter Gross et al, *Journal of Magnetic Resonance Microscopy* **14,** 83-86 (2001).

Evaluation of the Internal Structure Change of Articular Cartilage with Weight-bearing in terms of 1H-NMR Relaxation Behavior

Kazuya Ikoma*, Yoshiteru Seo, Yasuo Mikami*, Yoshiaki Kusaka*, Daisaku Tokunaga*, Yoshinori Marunaka**, Toshikazu Kubo***
Department of Orthopaedics * and Physiology**, Graduate School of Medical Science, Kyoto Prefectural University of Medicine, Kyoto, 602-8566, JAPAN

Introduction: Articular cartilage plays an extremely important role in absorption and dispersion of external force with load. In the present study, we analyzed a change of articular cartilage internal structure with load by the proton nuclear magnetic resonance method (^{1}H-NMR method).

Materials and Methods: Materials were obtained from 15 freshly prepared bovine femoral condyles. Two cylinder shaped articular cartilage specimens with underlying cancellous bone (7 mm in diameter) were obtained from weightbearing and non-weightbearing regions of a medial femoral condyle. These materials were subjected to NMR measurements with static load (0.15, 0.3, 0.5, and 1.0 MPa) by using the compression device. The ^{1}H longitudinal (T_1) and transverse (T_2) relaxation times were measured by fast-inversion-recovery method and multi-spin-echo method, respectively. The ^{1}H DQF MR images were measured by changing the creation time (□) from 0.3 to 10.0 ms. NMR measurements were recorded on an AMX-300wb Bruker NMR spectrometers. All the experiments went in room temperature (about 25°).

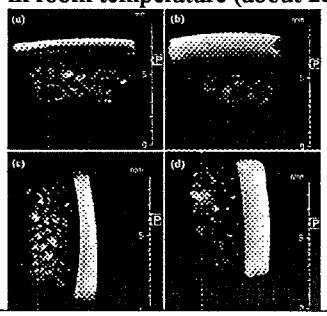

Fig. 1: GRE images of articular cartilages.
(a, c) weightbearing region
(b, d) non-weightbearing region

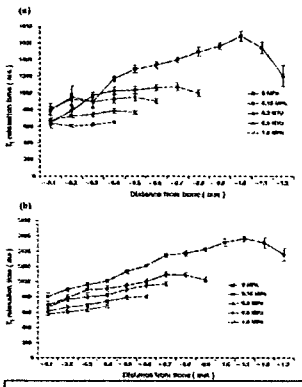

Fig. 2: Effects of external load on the T_1 profiles of the articular cartilage obtained from weight bearing (a) and non-weight bearing (b) regions.

Results: The stress - strain curve provided from thickness of the articular cartilage which I measured with a GRE image (Fig. 1) did not recognize the statistically significant difference between in cartilage of weightbearing and non-weightbearing regions. T_1 relaxation time at the layer directly below the cartilage surface was decreased remarkably with weight load on the articular cartilage in both loaded and unloaded regions. The reduction rate of T_1 at the layer directly below the cartilage surface was 59.7 % in loaded and 57.9 % in unloaded region under 1.0 MPa of weight load. On the other hand, the deep parts of the articular cartilage within 0.1 mm from the deepest layer showed relatively small changes of T_1 relaxation time. These tendencies were remarkable at the loaded regions of the cartilage samples. With 1.0 MPa of weight load, T_1 relaxation time was distributed nearly uniformly in the cartilage (Fig. 2). T_2 relaxation time at the layer directly below the surface was greatly shortened with weight load in the loaded region. T_2 relaxation time at the middle layers showed relatively short values before the weight was loaded, and was not greatly changed with weight load.

Discussions: Depending on weight load, the tension of articular cartilage was increased. This change presents that articular cartilage supports an external force in accordance with the Donnan's formula by an increased swelling pressure that is induced by an increased amount of water squeezed-out by the weight load. It was found that the distribution of water content in articular cartilage is drastically changed at this moment. As the T_1 relaxation time, water transfer by an external force is largest at transitional zone, so that the water is suggested to contribute to viscosity for absorbing external forces. Moreover, the water squeezed out from this zone can easily effuse to the sliding surface via the top layer of the articular cartilage, thereby playing an important role in lubricating the joint.

References

[1] Xia Y, Moody JB et al, *Osteoarthritis Cartilage* **10,** 370-380 (2002).
[2] Shinar H, Seo Y, *Magnetic Resonance in Medicine* **48**, 322-330 (2002)
[3] Ikoma K, Kusaka Y, *J Orthopaedic Surgery* **21**, 149-156 (2003)

Comparison of High-resolution MRI, Optical Microscopy and SEM in Quantitation of Trabecular Architecture in the Rat Femur

T.A.J. Hopper, R. Meder and J.M. Pope

School of Physical and Chemical Sciences, Queensland University of Technology, Brisbane, Australia.

Synopsis

Recently, magnetic resonance micro-imaging (μMRI) has been applied to the study of trabecular bone structure in the diagnosis of osteoporosis [1-5]. In vitro studies using clinical MR scanners have shown the potential of μMRI tc predict the biomechanical strength of bone [2], and in vivo studies have demonstrated the ability to discriminate between patients with and without osteoporotic fractures [3-5]. MRI also has the potential to quantify both trabecular bone density and architecture. The aim of this project was to compare quantitative measures of rat femur bone morphology obtained from MRI with those obtained by conventional optical microscopy and scanning electron microscopy (SEM).

Methods

Magnetic resonance imaging was used to analyse trabecular bone architecture in the femur heads from 14 adult Wistar rats. The MR images were obtained on a Bruker Avance 4.7 T micro-imaging system using a 3D spin echo sequence with spatial resolution of 23 μm in-plane and a slice thickness of 43 μm. The following parameters were used: TR of 500 ms, TE of 4.08 ms, bandwidth of 80 kHz, matrix size 256 × 256 × 128 and FOV of 6 mm × 6 mm ×5 mm. The optical images were obtained by decalcifying the bone in EDTA and then sectioning 5 μm thick slices. The SEM images was obtained by embedding the bone in epoxy resin and diamond grinding until the desired location was obtained and then imaged using a AE 400 SEM machine. Correlation coefficients between the MRI, SEM and optical measures of morphology, including ratio of bone to total volume (BV/TV), trabecular spacing (Tb.Sp), trabecular number density (Tb.N) and trabecular thickness (Tb.Th) were calculated.

Results

Correlation between the optical and data was lowest for parameters sensitive to trabecular architecture such as Tb.N (r^2 = 0.40) whilst being high for BV/TV (r^2 = 0.59) measurements. These relatively low correlations are thought to be caused primarily by distortion of the bone structure in the decalcification process used to section the bone and hence obtain the optical images. MRI of decalcified bone samples prior to sectioning confirmed this. The correlations increased (Tb.N had r^2 = 0.77) between the MRI and SEM. This is thought to be due to the reduction in the damage caused to the sample prior to obtaining the images.

Discussion

There is growing evidence to suggest that variations in trabecular structure are important in determining bone strength, independent of bone mineral density (BMD). This work demonstrates the potential of MRI in determining quantitative information on bone morphological parameters. The high resolution achieved in this study was essential to reducing the large partial volume effects normally associated with small animal bone studies. Due to the much larger trabecular architecture in humans a much lower resolution can be used. The ultimate aim of this work is to be able to assess the efficacy of various therapeutic regimes on patients with osteoporosis.

R^2 values		
Parameter	MRI vs Optical	MRI vs SEM
BV/TV	0.59	0.35
Tb.N	0.40	0.70
Tb.Sp	0.51	0.62
Tb.Th	0.51	0.77

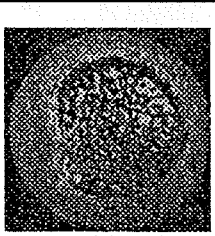

Fig 1a. Axial MR image of rat bone

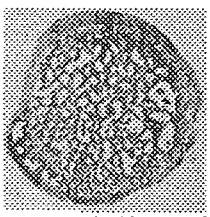

Fig 1b. Optical image of corresponding section of bone to Fig.1a

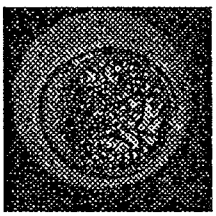

Fig 2a: Axial MR image of rat bone

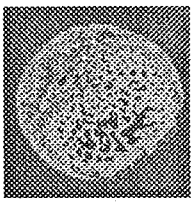

Fig 2b: SEM image of corresponding section of bone to Fig 2a

References

[1] Kleerekoper M et al, Calcif Tissue Int **37**, 594, 1985.
[2] Link T et al, J Bone Miner Res **13**, 122-132, 1998.
[3] Majumdar S et al, Osteoporosis Int **10**, 231-239, 1999.
[4] Link T et al, J Bone Miner Res, **13**, 1175-1182, 1998.
[5] Lin J.C et al, Osteoporosis International **8**, 16-24, 1998
[6] Vieth, V et al, Investigative Radiology **36**, p210-217, 2001
[7] Majumdar S et al, J Bone Min Res **12**, 111-118, 1997

Mapping the refractive index distribution through the crystalline lens using magnetic resonance micro-imaging (μMRI)

Catherine Jones and Jim Pope
School of Physical and Chemical Sciences, Queensland University of Technology, Australia

By exploiting the mutual dependence of refractive index and transverse relaxation rate (R2) on local protein concentration in the crystalline lens, a novel μMRI technique for mapping the refractive index distribution through the eye lens has been developed[1]. The method is both direct and non-invasive and has the potential for *in vivo* application.

Refractive index and bulk R2 measurements of porcine lens homogenates were obtained over a range of values corresponding to those present in the intact lenses. The empirical dependence of refractive index on R2 was determined by fitting the index versus R2 data using a non linear regression. The result is shown in Figure 1.

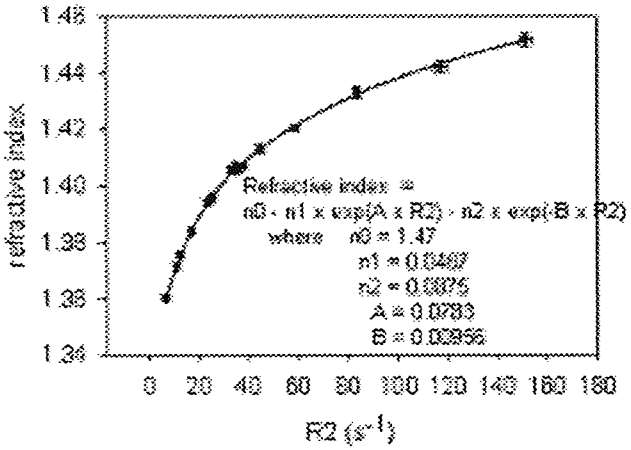

Figure 1: Refractive index versus R2 for porcine lens homogenates

A series of magnetic resonance micro-images with increasing echo times was obtained for intact lenses immersed in artificial aqueous humor, a synthetic medium similar to that surrounding the lens *in situ*. Image intensities, I, acquired at different echo times, TE, were fitted to a single exponential decay, $I = I_0\exp(-TE \times R2)$ on a pixel by pixel basis to obtain R2 maps through the lens. Using the empirically determined refractive index versus R2 dependence, the R2 maps were converted into refractive index maps. Using a ray tracing algorithm for non-homogenous media[2], the paths of rays incident parallel to the optical axis of the lenses were simulated, and the focal lengths estimated. The focal length was also determined directly by digitally capturing the paths of laser beams through the lens. A comparison between the simulated ray trace through an index map and the corresponding optical measurement for one of the porcine lenses is shown in Figure 2.

Figure 2: Typical fitted beams and lens surface from optical method (left). Typical ray trace through MRI derived refractive index map (right).

References

[1] B.A. Moffat, D.A. Atchison and J.M. Pope, *Vision Research* **42**, 1683-1693 (2002).
[2] A. Sharma, D. Kumar and A. Ghatak, *Applied Optics* **21(6)**, 984-987 (1982).

Measuring the optical properties of the eye lens using magnetic resonance micro-imaging (μMRI)

Catherine Jones and Jim Pope
School of Physical and Chemical Sciences, Queensland University of Technology, Australia

Image formation in human eye

As illustrated in Figure 1, image formation in the human emmetropic (good) eye results from refraction of incident light by the cornea and the lens to be focused on the retina. The refracting power of the cornea is constant (for an individual at a particular age), while the power of the young lens can change so that an individual is able to focus on near or far objects as required. Figure 1 shows light being focused from a far object, while Figure 2 shows focusing of light from a near object. The process of the lens increasing its refracting power to focus on a near object is called accommodation.

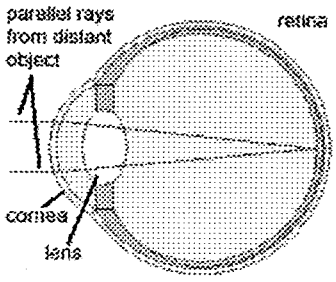

Figure 1: Image formation from distant object in human eye.

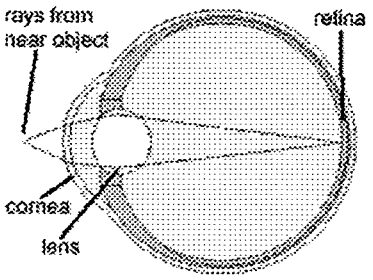

Figure 2: Image formation from near object in human eye. The lens is in an accommodated state.

Reduction in visual performance with age

The human lens gradually loses its ability to accommodate with age so that a significant proportion of the population above the mid forties cannot focus clearly on near objects. Other trends in the optics of the human eye include the loss with age of a "correlating mechanism" between the corneal power, lens power and axial length that maintains emmetropia in younger lenses[1] and a similar loss of compensation of the aberrations between cornea and lens[2]. While the shape and hence optical properties of the cornea can be measured using corrected Scheimpflug photography[3], corresponding measurements of the lens are complicated by the fact that its optical properties depend on both its geometry and refractive index distribution. Although attempts to measure refractive index of the eye lens go back to the 19th century, the actual distribution of the refractive index and how age-related changes affect the optical properties of the lens is still unclear.

Measurement of index distribution through an eye lens using μMRI

Eye lenses have a distribution of protein concentration (it is highest at the center of the lens and decreases towards its periphery). Refractive index maps of an eye lens can be determined using μMRI by exploiting the mutual dependence of the transverse relaxation rate and refractive index on local protein concentration[4]. The validity of the maps can be verified by comparing the focal power determined from a simulated ray trace through the index map with the power measured by digitally capturing the propagation of laser beams through the lens. Experiments have been performed on both porcine and human lenses with good agreement between the focal power determined optically and using the μMRI technique.

<u>References</u>

[1] A Sorsby, B Benjamin et al, *Emmetropia and its aberrations. A study in the correlation of the optical components of the eye* (1957).
[2] P Artal, E Berrio et al, *Journal of Optical Society of America A* (2002).
[3] M Dubbelman, H Weeber et al, *Changes in the anterior eye segment with age and accommodation: in vivo measurements of the human cornea and lens using Scheimpflug imaging and ultrasonography* (2002).
[4] B.A. Moffat, D.A. Atchison and J.M. Pope, *Vision Research* **42**, 1683-1693 (2002).

Evidence of shear banding and velocity fluctuations in wormlike micelles using NMR

M. Rosario López-González, William M. Holmes and Paul T. Callaghan
MacDiarmid Institute for Advance Materials and Nanotechnology, School of Chemical and Physical Sciences, Victoria University of Wellington, New Zealand.

Surfactants can form molecular aggregates known as micelles, which can take different shapes such as spherical, cylindrical, long flexible micelles (wormlike micelles), lamellar, hexagonal, and others. The way they associate depends on their concentration and ionic strength. Wormlike micelle systems have an unusual behaviour when subjected to flow, this behaviour has been associated to shear induced structures (SIS), shear banding and phase transitions [1,2]. In this work Nuclear Magnetic Resonance (NMR) and rheological measurements were used to study wormlike micelles in solution of cetylpyridinium chloride and sodium salicylate (CPyCl/NaSal) diluted in NaCl in water. The experiments were carried out on an NMR spectrometer of 7 T, using proton NMR in a couette cell. Shear is applied by rotating the inner cylinder of the couette cell, which is connected to a drive shaft and a stepper-motor gearbox in the bore of the magnet. All the experiments were performed at 25 °C. Using pulse gradient spin echo NMR (PGSE) and fast imaging sequences; evidence of velocity fluctuations was obtained at different velocities.

The NMR techniques of imaging and pulse gradient spin echo (PGSE) are combined to determine the displacement probabilities as a function of the position across the gap. The response of this sequence is given by:

$$E_{\Delta}(q) = \int \overline{P}_s(R,\Delta)\exp(i2\pi q \cdot R)dR \qquad (1)$$

where $q = (2\pi)^{-1}\gamma\delta g$ with γ the gyro-magnetic ratio, δ the gradient pulse duration, g the maximum amplitude of the pulse gradient and $\overline{P}_s(R,\Delta)$ the average probability of a molecule having a displacement R, along the gradient axis, in an observation time Δ. The velocity distribution can be obtained by Fourier transformation of $E_{\Delta}(q)$ with respect to q.

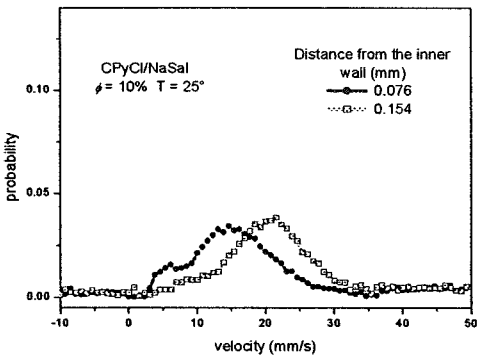

Figure 1: Velocity distributions at shear rate of $35s^{-1}$ for two different positions across the gap.

Velocity profiles were obtained at different shear rates from 5 to 50 s^{-1}. At small shear rates the sample behaves as a Newtonian fluid while at high shear rates a shear band appears.

Figure 1 shows the velocity distribution at two different positions through the gap at a shear rate of $35s^{-1}$. This shear rate corresponds to the plateau in the flow curve. At the outer wall the velocity distribution is peaked at zero velocity as expected from the boundary conditions. Close to the inner wall the velocity distribution shows a wide distribution of velocities, an evidence of fluctuations in the flow field. Moreover, the velocity distribution shows that the most probable value is at 21mm/s, which supports the idea of the formation of a thin band of very low viscosity near the rotating cylinder [3].

In conclusion the application of NMR velocity imaging to the study of cetylpyridinium chloride and sodium salicylate (CPyCl/NaSal) shows the presence of velocity fluctuations within the gap of the Couette cell. These velocity fluctuations just appear at shear rates above of the shear stress critic.

References

[1] P. Boltenhagen, Y. Hu, E. F. Matthys and D. J. Pine, Phys. Review Letters 79, 12 2359-2362 (1997).
[2] E. Cappelaere, J. F. Berret, J.P. Decruppe, R. Cressely and P. Lindner, Physical Review E 56, 2 1869-1879 (1997).
[3] William M. Holmes, M. del Rosario López-González and Paul T. Callaghan, to be published.

Quantification of the attenuation in the polarisation transfer efficiency induced by diffusion through magnetic field gradients: Simulations and experiments

Davide Santoro, Walter Köckenberger
Magnetic Resonance Centre, School of Physics and Astronomy, University of Nottingham, Nottingham, NG7 2RD, UK

Abstract
The use of the stable isotope ^{13}C in *in vivo* NMR experiments has great potential for studies of metabolic conversion rates in biological systems. The use of indirect detection schemes, such as cyclic cross polarisation (CYCLCROP [1]), allows the detection of ^{13}C nuclei with a sensitivity comparable to that of conventional ^{1}H NMR experiments and therefore combines the high sensitivity of ^{1}H NMR with a high chemical selectivity due to the high chemical shift dispersion of ^{13}C nuclei.
Here we present a detailed analysis of the detection efficiency for three possible polarisation transfer modules under *in vivo* conditions: a) INEPT (Insensitive Nuclei Enhanced by Polarisation Transfer [2]) b) CP (Hartmann-Hahn Cross Polarisation experiment [3]) c) PRAWN (Pulse Rotating frame trAnsfer sequence with WiNdows [4]) .

We performed computer simulations based on the Spin-Operator formalism, for the case of an AX system.
In our simulations we solved numerically the Liouville -von Neumann equation

$$\frac{\partial \rho}{\partial t} = -\frac{i}{\hbar}[H, \rho]$$

for the density operator □ in the rotating frame,
where the Hamiltonian includes an offset term dependent on the position in the 3D random walk around the perturber (sphere with a magnetic susceptibility different from the external medium).

The simulations can be used to analyse the trajectories in the zero and double quantum Liouville subspaces and therefore make it possible to determine the efficiency of the polarisation transfer experiments for varying conditions (Fig.1).

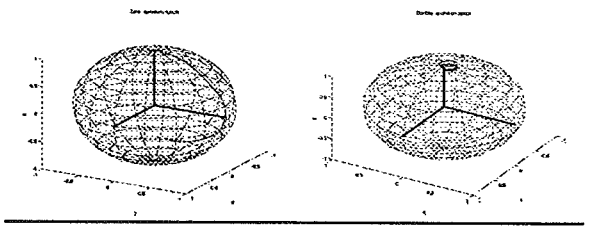

Fig.1 Trajectories in the zero and double quantum spaces for a CP experiment in the presence of diffusion in a constant gradient of 1 T/m. The non - complete inversion of the ZQ_z term is responsible for an attenuation of the final S - magnetisation.

In plant tissue such magnetic field gradients are generated by susceptibility differences between the intercellular spaces filled with air and the water within the cells. Our simulations also estimate the attenuation induced by a mismatch of the H-H condition for the sequences based on polarisation transfer in the rotating frame. The predictions of the simulations are compared with experiments on phantom samples with polystyrene micro-spheres.
On the basis of the simulation results and of the *in vitro* experiments we have chosen the CP sequence, optimising its parameters for the best transfer efficiency, for the editing part of our imaging experiments on castor bean seedlings [5].

References
[1] C. Kunze and R. Kimmich, *JMR* B **105,** 38 (1998). [2] G. A. Morris and R. Freeman, *J. Am Chem. Soc.* **101,** 760 (1979).
[3] S. R. Hartmann and E. L. Hanh, *Phys. Rev.* **128,** 2042 (1962). [4] N. Chandrakumar and R. Kimmich, *JMR* **137,** 100 (1999).
[5] M. Heidenreich et al., *JMR* **132,** 109 (1998).

Single-Point MRI of Fast, Turbulent Gas Flow

Ben Newling, Bruce J. Balcom, Christopher Poirier, Dale Roach, Yang Zhi
Department of Physics, University of New Brunswick,
PO Box 4400, Fredericton, NB E3B 5A3, Canada.

Single-point imaging techniques have found considerable application in materials imaging [1], because the interval between RF excitation and signal detection (t_p) can be kept short, even in comparison to very short sample T_2^* (< 100 □s). This is a result of phase encoding every **k**-space point individually, but careful choice of **k**-space sampling schemes can still make these measurements exceedingly time efficient Thermally polarized gases typically have short T_2 and are readily imaged by single point methods [2].

Short t_p confers a related advantage in the measurement of rapidly moving samples. Frequency-encoded pulsed field gradient imaging cannot be used to map flow fields in which the displacement of a fluid element during the frequency-encoding interval is significant on the scale of the desired spatial resolution. In practice, flows of greater than 1 m/s are often difficult to measure. During the short t_p interval of a single-point imaging method (~100 □s), however, displacement of a fast moving fluid can still be small or comparable to the desired spatial resolution [3]. We present single-point measurements of turbulent gas pipe flow in the presence of an obstruction. The measurements are made using an adaptation of the SPRITE technique (Fig. 1).

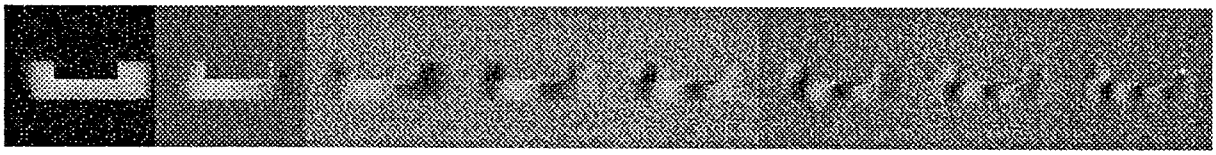

Figure 1: Change i n phase with increasing motion sensitization (L to R). One quadrature channel of image data is shown. Gas flow is from R to L in each image around the dark obstruction. The pipe extends beyond the field of view. In the unobstructed pipe, mean fluid speed is *c.* 5 m/s and Reynolds number is 350 000.

References

[1] B. J. Balcom, R. P. MacGregor, S. D. Beyea, D. P. Green, R. L. Armstrong, T. W. Bremner and A. Logan *J. Magn. Reson. A*, **123**, 131-134 (1996).
[2] P. J. Prado, B. J. Balcom, I. V. Mastikhin, A. R. Cross, R. L. Armstrong and A. Logan, *J. Magn. Reson.* **137**, 324-332 (1999).
[3] B. Newling, A. J. Coristine, B. J. Balcom, *Canadian Association of Physicists Congress*, Quebec, June 2002.

Direct Detection of Hydrocarbon Displacement in a Model Porous Soil with Magnetic Resonance Imaging

Yuesheng Cheng[1,2], Bryce MacMillan[2], Rod P. MacGregor[2], Bruce J. Balcom[1,2]
Department of Chemistry[1], MRI Center, Department of Physics[2],
University of New Brunswick, Fredericton, NB E3B 5A3, Canada

The direct detection of hydrocarbon fluids, and thereby discrimination of water, through direct carbon-13 magnetic resonance imaging (MRI) would be a significant advance in many scientific fields including food, petrol-geological and environmental sciences. In this work [1] we have explored a general method, multiple echo single point imaging, to quantitatively measure the hydrocarbon concentration as a function of time and space during a viscous hydrocarbon flow through a model realistic soil (Fig. 1).

Numerous authors have reported [for example, 2] MRI investigations of hydrocarbon distribution in porous media. The inherent disadvantage of these studies, employing ^{1}H MRI, is their inability to readily distinguish water and oil phases. One solution is to employ ^{19}F and fluorinated oils as a model oil phase [3]. This, however, is a significant departure from natural conditions.

In these experiments we employed a General Electric (GE NMR Instruments, Fremont, CA) CSI II imaging system with a home built 21.3 MHz ^{13}C probe, based on a 4 cm diameter solenoid in a horizontal wide-bore (31 cm) 2.0 Tesla Oxford (Oxford Instruments, Oxford, England) magnet. A 5 cm column of packed sand had 2.8 cm of oil added to the top. The column was placed at the center of the solenoid and held fixed for the length of the experiment. A constant fluid head over the sand was maintained by periodic addition of oil. 32 echoes were typically acquired. The nominal pixel resolution was 0.16 cm.

The relative concentration distribution of oil in sand has been observed. A one dimensional T_2 map of the oil distribution in sand was obtained by fitting a set of profiles, each derived from a separate T_2 weighted echo. The moving oil front position revealed a very good linear relationship to the square root of time, proving a capillary suction mechanism of imbibition. The detection limit, spatially resolved, was determined to be 26 mg however it should be recognized this is measurement dependent. Compared to traditional spin echo methods, the SNR can be improved by multiple spin echo single point imaging and susceptibility artifacts which plague traditional frequency encoding spin echo measurements are avoided.

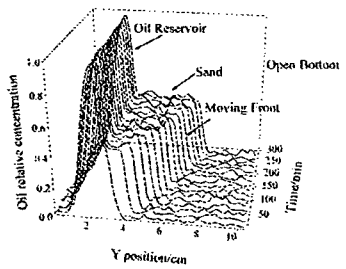

Figure 1: 1D images of relative oil concentration, spatially resolved, in the sand bed during an oil imbibition experiment.

References

[1] Yuesheng Cheng, Bryce MacMillan et al, *Analytical Chemistry* (submitted)

[2] M. Pervizpour, S. Pamukcu et al, *J. Comput. Civ. Eng.* 13, 96-102,1999

[3] D. A. Doughty, L. Tomutsa, *Magn. Reson. Imaging* 14, 869-873 (1996)

Thin Film MRI – High Resolution Depth Imaging with a Local Surface Coil and Spin Echo SPI

Alexei V. Ouriadov, Rodney P. MacGregor, Bruce J. Balcom
MRI Centre, Department of Physics, University of New Brunswick,
P.O. Box 4400, Fredericton, E3B 5A3, NB, Canada

The processes of polymerization, wetting, and drying in thin films are of constant scientific interest. However, the investigation of dynamic phenomena in thin films is quite difficult because depth analysis of physical and chemical processes requires very high spatial resolution. Spatially resolved NMR is a promising and powerful method of investigating planar samples through high resolution depth images. The most currently successful thin film MRI technique is Stray Field magnetic resonance imaging (STRAFI) [1]. This frequency-encoding method is based on using the strong static gradient generated by a fringe B_0 field.

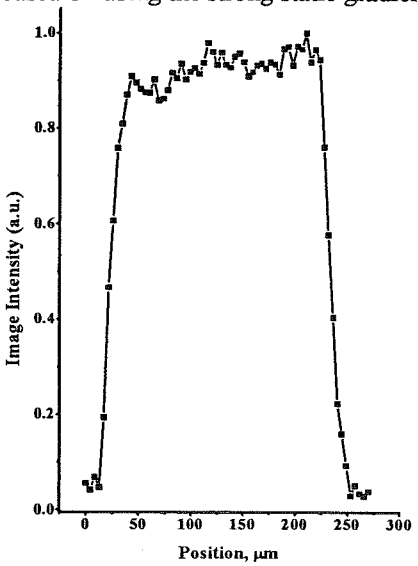

Figure 1: 1 D depth image of water saturated nafion. 64 points, TE=13.6 ms, t_p=6 ms, FOV=270 μm, nominal pixel resolution is 4.2 μm, 16 averages and acquisition time - 8 minutes. Thickness of sample was 200 μm. Image was derived from the first echo.

We present a multiple echo, single point imaging technique, which is a pure phase-encoding SPI based sequence [2]. It does not have a line width restriction on resolution and permits pure T_2 image contrast. The method designed for examination of thin film samples, employs a local surface coil probe for RF excitation/detection. The absence of pulsed magnetic field gradients during acquisition permits a very narrow filter [3], and due to this significantly improved signal-to-noise ratio. Depth images with nominal resolution of 5 μm are acquired with acquisition times on the order of ten minutes.

The 1D depth image of Figure 1 illustrates the capability of the method. The alignment problem, or non-orthogonality between planar sample and primary phase encoding gradient was overcame by applying a small secondary phase encoding gradient which corrected the orientation of the effective phase encoding gradient.

Pure phase encoded echoes, acquired in the absence of the magnetic field gradient, lack the diffusion attenuation inherent to frequency encoded echo based imaging methods. The technique is readily adapted to spatially resolved diffusion and T_2 relaxation time mapping. We have observed dynamic phenomena such as polymerization, wetting, and drying in polymer latex emulsion and other systems.

References

[1] P.M. Glover, P.J. McDonald and B. Newling, J. Mag. Res. **126**, 207-212 (1997)
[2] B.J. Balcom Spatially SPRITE imaging of short relaxation time nuclei, 75-86, Wiley-VCH, Weinham (1998)
[3] P.T. Callaghan L.C. Forde and C. J. Rofe, J. Mag. Res., **104**, 34-52 (1994)

Density Profiling, ^{1}H and Heteronuclei, with a Half-K-Space SPRITE Technique

Kumud Deka, Bruce J. Balcom, Igor V. Mastikhin, Rod P.MacGregor,
Department of Physics, MRI Center, University of New Brunswick, Fredericton, NB E3B5A3, Canada.

MRI methods for true density imaging, even if only 1D, would be highly advantageous for the study of a large number of molecular transport problems. To this end we have continued our earlier work on a 1-dimensional half k-space SPRITE technique [1]. One major advance of the current work is the design and construction of a dedicated, high strength, Z magnetic field gradient specifically for 1D profiling.

Centric SPRITE sampling techniques have been a research interest of this laboratory for some time [2]. The centric sampling SPRITE technique is free from artifacts due to magnetic field in-homogeneities, and is naturally immune to T_1 saturation effects. The technique is therefore also largely immune to changes in sample T_1 in terms of image contrast. The removal of T_1 as a contrast parameter is part of our drive to create simple profiling methodologies. The current goal is to control or remove T_2* as a contrast parameter. We have twp logical limits: (1) The local image contrast is directly proportional to the concentration of the species of interest. (2) The local image intensity depends also on T_2* but this term may be readily mapped through variation of the experimental encoding time tp in sequential images. Both goals require that the method be executable with the minimum possible tp.

The equation below relates the imaging field of view to the gradient increment in a pure phase encode SPRITE image. Clearly a reduction in tp and/or the examination of species with reduced □, requires that the gradient increment must increase, as must G_{max}.

$$FOV = \frac{1}{\Delta k} = \frac{2\pi}{\gamma \Delta G t_p}$$

We have constructed a dedicated 1D Z gradient set, very efficiently cooled, of a conventional Maxwell pair design, but with four layers of windings. This gradient (G_{max}>300 Gauss/cm, $G_{continuous}$>100 Gauss/cm, 7.6 cm id) has an increased inductance, and thereby a slower switching time compared to a more conventional coil, but this is not important for our technique.

We have also implemented a very simple zero filling scheme to effectively reduce the minimum tp by a factor of 2. Rather than G_{max} determining the last k space point, if it determines the $k_{max}/2$ point, then we may set the remaining k space points to zero (zero filling). This effectively doubles the apparent magnetic field gradient strength, or more importantly permits a tp reduction by a factor of 2 for constant field of view. The consequence of zero filling in the image profile is an interpolation between data points which is effectively a smoothing. This is actually a desired feature of a measurement where one anticipates a smoothly varying species concentration.
This presentation will highlight the gradient coil design and illustrate the application of these ideas to mass transport studies with ^{1}H, ^{35}Cl. ^{7}Li and ^{23}Na.

References
[1] I. V. Mastikhin, H. Mullally, B.MacMillan, and B.J.Balcom [1].J.Mag. Res. 156,122-130(2002).
[2] Igor V. Mastikhin, Bruce J. Balcom[1], Pablo J. Prado, and Christopher B. Kennedy. J. Mag. Res. 136,159-168(1999).

Spiral SPRITE MRI of Compact Bone

Igor Mastikhin, B.J. Balcom, D. Goodyear, P. Szomolanyi, N.J. Shah
Department of Physics, University of New Brunswick, Fredericton, NB, E3B 5A3 Canada

Traditionally, Magnetic Resonance Imaging is considered a soft tissues imaging modality. Rigid tissue, such as the solid bone mineral phase of compact or cortical bone, has a very short T_2^* (< 1 ms) and therefore appears as a signal void in traditional MRI images. Visualization of compact bone is usually considered within a field of application of X-ray, a hard tissue imaging modality.

Measurements of bone mineral density (BMD) and bone structure are of great importance in studies of osteoporosis, bone remodeling after a fracture and bone adaptation to implants. One may anticipate that, in principle, MRI could provide information on the chemical structure of the bone organic matrix, and bone mineral non-invasively and with no radiation load.

In this work, we demonstrate the application of a spiral variant of the SPRITE (Single Point Ramped Imaging with T_1-Enhancement) pulse sequence to compact bone as a method of direct detection of MR signal from rigid tissues. As a pure phase-encode method, the technique is immune to any time-evolution artifacts such as magnetic field inhomogeneity, chemical shift from the bone marrow, and susceptibility effects. The short encoding time (from tens of microseconds to milliseconds) allows for imaging objects with very short relaxation times. Both water of hydration in the bone mineral phase and bone mineral phosphorus are visualized with a reasonable Signal-to-Noise, and with no resolution loss. Spiral scanning of k-space greatly improves the experimental acquisition time in comparison to other phase-encode methods, decreases the gradient slew rate and decreases the gradient duty cycle, making clinical applications potentially feasible.

The flexibility of MRI depends on its ability to introduce various relaxation weightings into the image intensity. However, it is not always easy to unravel the impact of different relaxation parameters into the image for spin-warp techniques. In the proposed technique, the impact of different relaxation parameters may be readily analyzed. The centric spiral sampling increases the Signal-to-Noise and a combination of the imaging sequence with various magnetization preparation schemes is easily achievable.

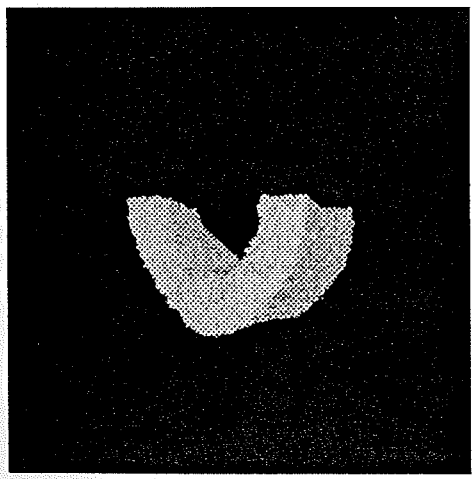

3D 1H MRI of 2-year dry bone, FOV 6cm, T2* 80 us, imaging time 6 min

2D slice of 3D 31P MRI of the same bone, imaging time 59 min

Rapid Measurement of RF Flip Angles and T_1 for samples with long T_1 and short T_2*

Igor Mastikhin
Department of Physics, University of New Brunswick, Fredericton, NB, E3B 5A3 Canada

Before performing MR imaging, one has to calibrate the RF probe to know what B_1 strength and duration of RF pulses are necessary. It is also desirable to have preliminary information on a sample's T_1. This information becomes essential in case of SPI/SPRITE methods where the flip angle value and longitudinal relaxation might define the image intensity due to T_1 saturation (sequential sampling) or the image resolution due to transient magnetization effects (centric sampling) [1].

In NMR, there are various methods of measurement of flip angles and T_1. However, when the sample's T_1 becomes longer than 10 s and T_2* becomes shorter than 200 μs, the most common methods become very time-consuming (inversion recovery) or inapplicable (flip-flop or single scan methods) [2]. To use the progressive saturation [3], one has to define the flip angle α of the RF pulse that can also be time-consuming for long T_1s and in case of imaging where samples of various size and shape might change the Q of the probe.

In this situation, a simple and rapid measurement of flip angles and T1 can be performed with a train of N pulses separated by a delay TR, TR << T2*, T2. If only a single point is acquired after each pulse, the observed signal will decay exponentially with longitudinal magnetization following

$M_{zn} = M_0(1-w)e^{-\frac{TR}{Tapp}n} + M_0 w$ where N is the number of pulses, $\frac{1}{T_{app}} = \frac{1}{T_1} - \frac{\ln(\cos\alpha)}{TR}$, and the steady state $w = \frac{1-E}{1-CE}$. If TR is much shorter than estimated T_1, that is easy to fulfill, the signal decay will be driven by the flip angle only, and monoexponential fitting of the signal will extract the flip angle value. This allows us to get the flip angle data in a single scan. In case of multiple scans, there is no need to wait for the complete magnetization recovery, as the information we are interested in is contained in the curve of the decay, not in the absolute intensity.

The T1 values can be extracted from the decay curve when $ln(cos\alpha)/TR$ is made comparable to T_1. In this case, a knowledge of α is not necessary to extract T_1: one has to acquire one more curve with doubled TR, normalize both and subtract one from the other.

This method was very easy to implement on our NMR spectrometer. Measurements of T_1s of 30 s - 2 min for solid ^{31}P and Li samples were performed within a few minutes and the total acquisition time was defined by the need for several accumulations to increase SNR. The method can be used for defining an exact flip angle value of the RF pulse of interest and acquiring information about the sample's T_1 for the imaging goals.

References

[1] I.V. Mastikhin, B.J. Balcom et al, *Journal of Magnetic Resonance* **136,** 159-168 (1999).
[2] D.E. Demco, V. Simplaceanu, I.Ursu, *Journal of Magnetic Resonance* 15, 166-169 (1974).
[3] R.Freeman, H.D.W. Hill, *The Journal of Chemical Physics* 14, 3367-3377 (1971).

Relative signal-to-noise efficiencies of phase- and frequency-encoding methods in NMR microimaging.

A.G.Webb[1,3], L.Ciobanu[1], A.Purea[3], T.Neuberger[3], and C.Pennington[2]
[1]University of Illinois at Urbana-Champaign, [2]Ohio State University, [3]Universität Würzburg.

In both frequency and phase encoding imaging methods, the spatial point spread function (PSF) is given by the convolution of a sinc function, related to the digital resolution, and a Lorenzian function from diffusional broadening (the additional term from the natural linewidth in frequency encoding can normally be ignored). Requiring the full-width-at-half-maximum of this spatial PSF to be of the order of 2-10 □m for NMR microscopy means that large gradients must be used. For a given field-of-view and number of acquired data points, the requirement that the diffusional broadening be less than or equal to the digital resolution constrains $G_{phase,\,max}$ and G_{freq} to values given by:

$$G_{phase,max} \geq 1.8\frac{2\pi D}{\gamma(\Delta x_{DR})^3}, \quad G_{freq} \geq 2.8\frac{2\pi D}{\gamma(\Delta x_{DR})^3}$$

In standard MRI one spatial dimension is typically frequency encoded since N points in k-space can be acquired in a single scan, as opposed to phase encoding where only a single k-space point is acquired, resulting in much more rapid scanning. However, in NMR microscopy data acquisition times are necessarily significantly longer, and so the optimum method becomes the one which maximizes the signal-to-noise (SNR) efficiency. NMR microscopy is an area in which phase encoding can have significant SNR advantages over frequency encoding. The figures below shows simulations performed to estimate the SNR efficiency and also necessary gradient strengths for phase and frequency encoding in NMR microscopy. As can be seen, at very high spatial resolutions, phase-encoding gives up to an order of magnitude increase in SNR efficiency, while also requiring smaller gradients. It is also clear that the required bandwidths for frequency encoding, > 2 MHz for ca. 2 □m resolution, may be prohibitive for commercial systems.

In addition to increased SNR efficiency, there are additional advantages of using phase encoding in terms of preserving chemical shift information, and the acquisition of images with different T_2^* weighting. The major problem is the large required data acquisition time. We are investigating various methods which can potentially be used to reduce the total imaging time, including partial Fourier, multiple-echo, and variable tip angle/TR methods (3).

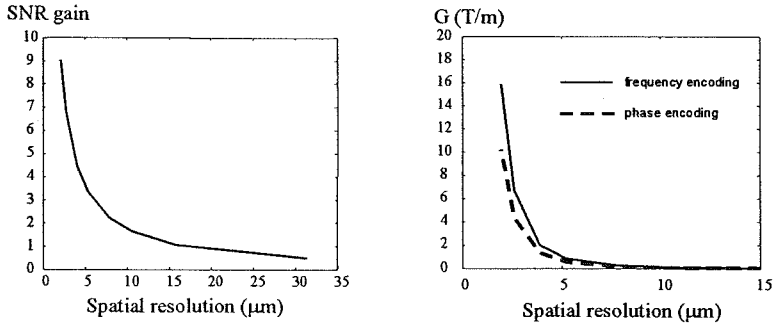

(left) SNR gain (phase/frequency encoding) as a function of the spatial resolution for a microimaging experiment. Simulation parameters: 500 □m FOV, data acquisition bandwidth of 100 Hz for phase encoding, diffusion coefficient of water (tissue) $1.8x10^{-9}$ m^2s^{-1}. (right) Required gradient strengths.

References.

[1] S.Gravina and D.G.Cory, *J.Magn.Reson.B*, **104**, 53 (1994).
[2] L.Ciobanu, D.A.Seeber and C.Pennington, *J.Magn.Reson*, **158**, 178 (2002).
[3] A.G.Webb, R.W.Briggs, and T.H.Mareci, *J.Magn.Reson.*, **94**, 174 (1991).

Spectral Resolution Enhancement by Spectroscopic MR Microscopy

Igor Serša[1], Slobodan Macura[2]
[1]Jožef Stefan Institute, Ljubljna, 1000, Slovenia, [2]Mayo Clinic, Rochester, MN 55905, USA

Introduction
Contrary to high resolution NMR spectroscopy in liquids, where samples could be are homogenous even on microscopic scale, samples of interest to imaging are naturally inhomogeneous. Then, different parts of the sample may have different magnetic susceptibilities, which induces local field gradients. Because of irregular geometry, such susceptibility magnetic field gradients are often very difficult to compensate by magnet shimming, which ultimately leads to line broadening in high-resolution spectra. Here we present a new method of enhancing spectral resolution by spectroscopic imaging at MR microscopy conditions. Spectroscopic imaging (SI) [1] is a MRI modality that combines MR imaging with NMR spectroscopy providing a high-resolution spectrum from each sample voxel separately.

Theory
The method relies on the fact that line broadening is proportional to the sample size; smaller the sample, narrower the lines. Similarly, in spectroscopic imaging, smaller the voxel, narrower the lines. However, by decreasing the voxel size the signal to noise ratio of the spectra deteriorates and the experiment time increases. For example, in the uniform sample, all voxels have the same SI spectra but with small shifts relative to one another, due to different magnetic fields. Direct summation of all the voxels yields the spectrum identical to one obtained from the whole sample. However, alignment of individual spectra before their co-addition, results in a spectrum with narrower lines and improved sensitivity. From known magnitudes and directions of the shifts applied to align individual voxel spectra it is possible to calculate the field map across the sample.

Results
To demonstrate the method experimentally, we used ethanol placed into cylinder with diameter 18 mm and length 12 mm. Spectral line in the standard spectrum was 75 Hz (Fig. a). Co-addition of aligned SI spectra (16 × 16 × 16 voxels with a 20 mm field of view) reduces the line with to 30 Hz (Fig. b). The image in Fig. c corresponds to the magnetic field map in the coronal cross-section through the sample. The highest difference between precession frequencies is equal to 75 Hz, which well agrees with the line width of the standard spectrum. The presented method for spectral resolution enhancement may be considered as a supplement to magnet shimming particularly effective when the sample has residual gradients that cannot be compensated by shims.

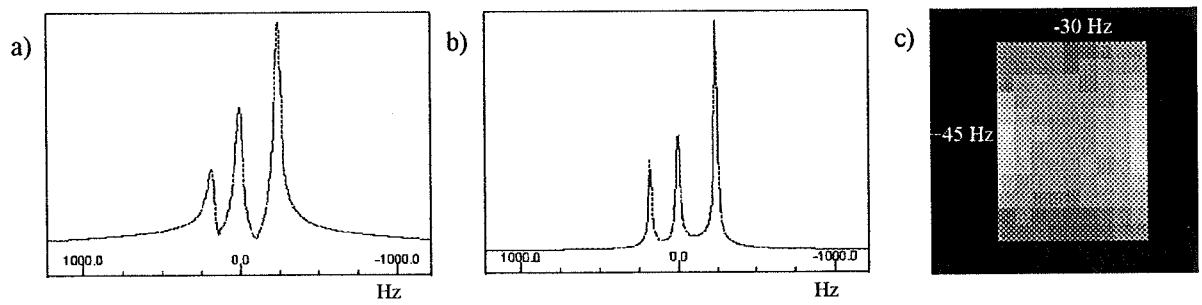

References
[1] A.A. Maudsley, S.K. Hlial, W.H. Perman, H.E. Simon, *J. Magn. Reson.*, **51** 147-152 (1983).

NMR Imaging of pico-Tesla fields?

I. Martin-Vicente, M. J. D. Mallett, P. Blümler*
University of Kent at Canterbury, School of Physical Sciences, Canterbury CT2 7NR, UK
* Max-Planck Institute for Polymer Research, Ackermannweg 10, 55128 Mainz, Germany

Imaging of small magnetic fields caused by local currents is of great interest for research in biomedicine and materials science. NMR offers some advantages over other detection schemes (Hall-sensors, flux-gates or SQUIDs) but is generally limited by relatively low sensitivity.
A new idea in NMR-detection methods is presented from the viewpoint of improvements in pulse-sequence design and data processing. Optimisation of phase-encoding of magnetic flux is discussed based on theory, simulation and experiments. Therefore, a simple setup was used for a feasibility study. Based on the results a sensitivity limit in the pico-Tesla regime was estimated. Further possible improvements in data processing and the limits, especially in spatial resolution, are discussed.
Comparison with the typical magnetic fields produced by the human body (e.g. strength and dynamics of the magnetic fields produced by a single nerve) shows that excitation in larger peripheral nerves should be detectable.

Characterization of Mechanical Induced Changes in Polyoxymethylene by NMR/MRI

H.-B. Ko, P. Blümler, H. W. Spiess
Max Planck Institute for Polymer Research, 55128 Mainz, Germany

The aim of this project is the detection and characterization of strain and fracture induced structures in polyoxymethylene (POM) using NMR spectroscopy and imaging. Thereby local changes in chemical composition, chain orientation and dynamics are of special interest.
Besides the expected semi-crystalline and amorphous structural elements a very mobile component was revealed by static and MAS ^{1}H spectroscopy. This component was identified as a water (moisture) induced decay product (half-acetale) and is located to a much greater extend in sample regions which were deformed most. Although relatively low in concentration this component allows the use of standard MRI sequences due to its high molecular mobility. Various experimental and spectroscopic methods were used to further characterize the decomposition process.
The highly mobile component can be used as a local probe to investigate the strained parts of the samples. Morphological features in the micrometer range were investigated by Diffusion Tensor Imaging revealing extremely anisotropic and restricted selfdiffusion which aligns with the mechanical force lines. These experiments also display local distortions which may be due to imperfections in production and ultimately causing mechanical failure.
Similar results were also obtained by goniometric NMR-spectroscopy and MRI showing strong orientational dependence of the spectra relative to the main field. First results with magic-sandwich echo sequences are presented to support the observations obtained on the mobile components in the sample by investigations on the amorphous parts.

Finally the different observations are summarized in a preliminary model of strain induced structures and reinforced decay in the presence of moisture. Present work on validation of these interpretations via alternative methods (e.g. light microscopy) will be included.

Tri-Axial Testing combined with MRI

Stephen Altobelli[1], Tang-Tat Ng[2]
[1]New Mexico Resonance, Albuquerque, NM, USA
[2]Civil Engineering Dept., University of New Mexico, Albuquerque, NM USA

Introduction

The mechanics of saturated soil is often crucial in civil engineering practice. For instance, saturated sandy soils may liquefy during an earthquake with catastrophic impact on both buried and surface structures. Continuum models of the stress-strain characteristics of soils rarely incorporate microscopic information, and are very difficult to verify non-invasively.

We seek to develop an experimental system that will allow us to perform standard soil testing[1] inside a magnetic resonance imager so that we may evaluate methods of sample preparation[2], test continuum mechanical models and eventually correlate the grain-scale soil fabric to macroscopic stress-strain relations.

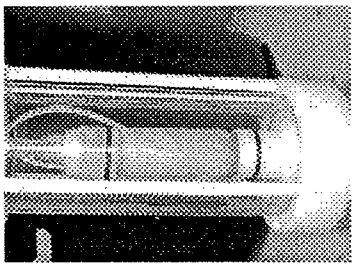

Figure 1(above): Sand sample ready for insertion into imager.
Figure 2(below): T_2 weighted images, unstrained, 11% and 15% strain.

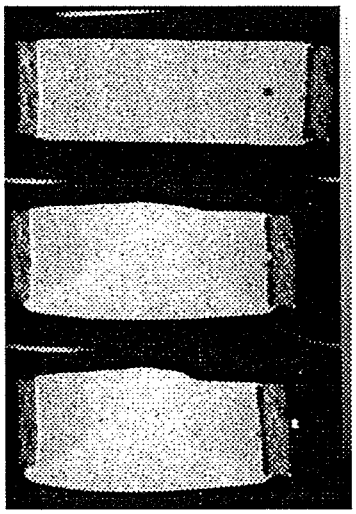

Methods

We have fabricated a non-conductive tri-axial test chamber and developed procedures to produce drained or un-drained saturated samples as shown in Figure 1. The samples are cylindrical, OD 3.6 cm by 8 cm long. They are prepared in layers inside a tubular flexible membrane using a wet tamping (under-compaction) method. They are saturated with de-gassed, Gd-doped ($T_1 \sim 200$ ms) water, and maintained by a confining pressure of 3-4 atm for 12 hours. Then the samples are loaded into the 30 cm horizontal bore superconducting magnet. This is possible because all the connections for maintaining confining pressure and for saturating the sample are at one end of the test chamber, the right side in Figure 1. Two- and three-dimensional spin-warp images are taken as the samples are strained by a Plexiglas piston, visible on the left of the figure. Spatially resolved measurements of T_2^* have also been made.

Results

Typical images are shown in Figure 2. Slices containing the long axis of a sample are shown. The top image shows clearly the five layers used to prepare the sample. Most of the contrast is due to T_2^* variation and slight variation in spin density due to reduced porosity at the layer boundaries. The signal intensity is encoded according to the grey scale shown on the right side of the image. The darker rectangles at the sample end are porous stone frits (disks passing through the imaged slice) which are also visible in Figure 1. The bright streaks above the images are water-filled tubing which is used to flush the sample during preparation and to drain the sample during strain if desired.

The middle image was taken after the length of the sample was shortened 11%. Note the appearance of a "shear band" – a near planar dislocation typical of drained saturated sand samples. The bottom image shows the result of increasing the strain to 15%

References

[1] R. D. Holtz and W. D. Kovacs, "An introduction to geotechnical engineering" Prentice-Hall (1981)
[2] R. S. Ladd, "Preparing Test Specimens using under-compaction", *Geotechnical Testing Journal* **1**(1) 16-23, (1978)

The study of solid – liquid interactions using T1rho spectroscopy

Sue C Stark*[♣] and John H Strange[♣]
*Sun Chemical, Cray Avenue, St Mary Cray, Kent, England. BR5 3PP
[♣]University of Kent, Canterbury, Kent, England. CT2 7NR

Interactions between solid- liquid interfaces are of interest to many industries including printing ink manufacturers. In this application the solid phase is pigment particles, which are crystalline particulates that impart their colour to printing inks. The liquid phase is usually a polymer solution that is used as a dispersing medium for the pigment. Using impact and / or shearing devices, the pigments are dispersed in the polymer solution to decrease particle size and increase colour strength. The interaction between the polymer solution and the pigment particles will depend upon the conformation of the polymer, the position and the chemistry of the active functional groups. It is believed that the interaction between the polymer solution and the pigment particle influences the rate of dispersion and the rheological properties of the product.

This study uses high resolution NMR to probe the degree of interaction between different functional groups and pigment surfaces. NMR was chosen as it is one of the only techniques that give an insider view to molecular motion. Spin lattice relaxation times were initially analysed in an attempt to detect any adsorbing groups without success. T1□, which probes slower molecular motions, has been used extensively as a method for measuring the Tg (glass transition) of polymers. This method proved to be more valuable, and combining this with NMR spectroscopy, the mobility of different regions of the liquid phase molecules was investigated. By comparing the mobility of the pure liquid to mobility in an ink dispersion, the regions of restricted mobility can be detected and hence the adsorbing groups can be identified.

As an initial systematic study, the T1□ of pure alkanes and various end-capped alkanes were measured. These were compared to a 1:1 dispersion of these solvents with one of two pigments. The pigments chosen for this study were red 57:1, which has a polar surface, and yellow 188 with a less polar surface. These pigments were chosen for their contrasting surface chemistry.

The T1□ relaxation rate for each peak in the spectrum was measured for the pure solvent and pigment dispersions. The ratio of relaxation rates for dispersed systems to pure solvent was taken as the Enhancement factor. The enhancement factors show that the alkanes have a greater affinity for the yellow pigment surface than for the red. As the chain length of the alkanes increases the relaxation rate of the yellow dispersions decreases. The largest interaction with the yellow pigment is seen for the branched alkane trimethyl-pentane. There is little interaction observed between the alkanes and the red pigment. This was to be expected due to the polar nature of the pigment surface.

The greatest interaction detected for the red was with the amine group. This was about eight times stronger than any other interaction observed during the study. As expected, the more polar solvents have a greater affinity for the red surface than the yellow. The non-polar solvents interact to a greater degree with the yellow.

These experiments have indicated the relative interaction strengths between pigments and solvents. We have yet to be able to define the changeover from a surface adsorption interaction to non-specific surface wetting in terms of the measured enhancement factor parameter.

Advanced MRI microscopy at low magnetic field strength

Frank J. Vergeldt, Carel W. Windt, P. Adrie de Jager, Henk Van As
Laboratory for Biophysics, Wageningen University, Wageningen, the Netherlands

Introduction
One of the advantages of NMR measurements at low magnetic field strength (0.7 T) is the fact that biological tissues show relatively long spin-spin or transverse relaxation times (T_2 > 100 ms). Compared to high magnetic fields, the decrease of T_2 due to diffusion in internal gradients caused by magnetic susceptibility differences in tissues is smaller. This is the basis for various types of advanced multi-spin echo (MSE) imaging sequences. These result in quantitative 2D- and 3D-maps of T_2 and proton density, and images hardly affected by susceptibility artifacts. To further increase the information content per pixel, T_2 mapping is combined with sequences for T_1 or displacement mapping. Alternatively the multi-spin echo train can be used to speed up k-space sampling by RARE schemes (also known as turbo or fast spin echo). This greatly enhances time resolution in time series to monitor T_1 or displacement maps. Here we report on the application of this versatile toolbox to study plants and models of biological systems.

Methods
All experiments were performed on a Bruker Avance system equipped with a 0.7 T electromagnet and a plan parallel 1 T/m gradient set (Resonance Instruments) for easy access. The open architecture of this system makes it possible to study living plants under well-defined environmental conditions. All imaging schemes are based on a multi-echo spin warp method [1]. The multi-spin echo part consists of a train of hard 180° pulses with a XY-8 phase modulation scheme to preserve phase information throughout the train.

Results
3D-MSE measurements of seeds, anthers and petiole explants resulted in proton density and T_2 maps with a spatial resolution of $(100\ \mu m)^3$. 3D-RARE enabled us to trace the process of cooking of rice with a time resolution of 1 minute and a spatial resolution of $(200\ \mu m)^3$. SE-PFG-RARE and STE-PFG-RARE yielded calculated displacement maps of xylem and phloem flow in plants with an in plane resolution of $(70\ \mu m)^2$ in time series with a resolution of 20 minutes [2-4]. Using STE-PFG-RARE linear flow speeds as low as 50 µm/s could be measured [3]. With SE-PFG-MSE and STE-PFG-MSE we were able to monitor complete displacement spectrum of flowing water in up to 128 echoes of an echo train. This enabled detailed studies of the water status in plant vessels and their surrounding tissue [4].

References
[1] Hommo Edzes, Dagmar van Dusschoten et al, *Magnetic Resonance Imaging* **16,** 185-196 (1998).
[2] Tom Scheenen, Dagmar van Dusschoten et al, *Journal of Magnetic Resonance* **142,** 207-215 (2000).
[3] Tom Scheenen, Frank Vergeldt et al, *Journal of Magnetic Resonance* **151,** 94–100 (2001).
[4] Carel Windt, Frank Vergeldt et al, *book of abstracts 7th ICMRM,* Utah (2003).

Playing with propagators: investigating water transport and tissue properties in plants using flow imaging and combined flow-T_2 imaging

Carel Windt, Frank Vergeldt, Adrie de Jager, Henk Van As
Laboratory of Biophysics, Wageningen University, Wageningen, the Netherlands

Introduction

In plant research, the physiology and regulation of transport processes in plants are attracting an increasing amount of attention. New techniques, such as the pressure probe and genetic engineering, have made it possible to study the driving forces of water transport in plants as well as identify some of the proteins involved in the loading, unloading and regulation of the xylem and phloem transport streams. However, additional noninvasive methods like MRI microscopy are needed in order to study parameters like phloem flow, xylem flow, membrane permeability and exchange between flow containing vessels and surrounding tissue. It has already been shown that it is possible to measure and quantify water flow in the relatively fast moving xylem transport pathway [1]. Here we demonstrate approaches to study the other parameters.

Methods

All MRI microscopy was performed in an open 0.7 T Bruker MRI system, with a plan parallel gradient set for easy access. This setup allows plants up to a size of 2 meters to be placed, upright, inside the electromagnet. Small poplar trees and full grown castor bean plants were used as model systems.

Linear displacement of water was measured using a full q-space approach, using either spin echo or stimulated spin echo where long observation times Δ were needed [1]. Measurement time was reduced using fast k-space sampling by RARE / turbo spin echo. An experiment like this yields a propagator for every pixel of an image, allowing the amount of stationary and flowing water per pixel to be calculated, as well as the average linear flow velocity (in both positive and negative direction) and the average volume flow.

In order to measure flow and T_2 relaxation simultaneously, we combined PFG with CPMG to yield SE-PFG-MSE [3]. In a typical flow-T_2 experiment 64 echoes were acquired and q-space was sampled completely using 32 equidistant steps, with an image matrix of 64 x 64. After Fourier transformation a multidimensional dataset results, in which for every voxel and for every echo a complete propagator is available for analysis.

Results and discussion

Flow measurements using SE-PFG-RARE and STE-PFG-RARE have yielded calculated flow maps of excellent quality (fig. 1). In addition to xylem flow, we have now also been able to measure the small amount of slowly downward flowing (up to 0.5 mm/s) phloem sap, sometimes even simultaneously with faster and upward flowing xylem sap. Using STE it even proved to be possible to demonstrate exchange processes between vessels and surrounding tissue, following the approach presented by Tallarek et al [3].

Flow-T_2 measurements conducted on a phantom showed that it is possible to accurately and simultaneously measure displacement and T_2 decay. Application of flow-T_2 measurements in plants showed that it is possible to distinguish the T_2's of stationary water, which is associated with cells surrounding flow conducting vessels, from the T_2's of flowing water within the vessels. Changes in plant tissue T_2 have been shown to reflect changes in membrane permeability, and T_2 is influenced by cell size [4]. Because T_2 is sensitive to both vessel size and membrane permeability, flow-T_2 imaging provides a method to correlate flow velocities with vessel diameters, and to study permeability changes of vessels and associated cells.

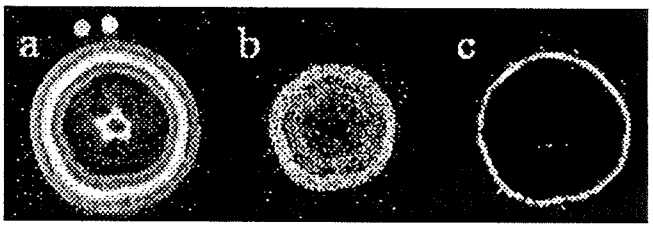

Figure 1: calculated flow maps of the stem of a small poplar tree. a) amount of stationary water, b) volume flow xylem, c) volume flow phloem

References

[1] T.W.J. Scheenen, F.J. Vergeldt et al, *Journal of Magnetic Resonance* **151,** 94-100 (2001).
[2] F.J. Vergeldt, C.W. Windt et al, *Book of Abstracts*, 7th ICMRM, Utah (2003).
[3] U. Tallarek, F.J. Vergeldt et al, *Journal of Physical Chemistry B* **103,** 7654-7664 (1999).
[4] L. van der Weerd, M. Claessens et al, *Journal of Experimental Botany* **52,** 2333-2343 (2001).

Contour averaging

Ilja Kaufmann, Axel Haase
Physikalisches Institut Universitaet Wuerzburg, Germany

Introduction
In processing and evaluation of NMR parameter maps of biological samples, segmentation of distinctive tissues is a common means to determine their averaged parameter value. In NMR microscopy this method is often limited due to low resolution, low SNR or partial volume effects.

Method
A polar coordiante system is used to define contours of imaged objects that, are roughly rotationally symmetric, as in tissues composed of concentric layers or that has radial value gradients. From an arbitrary number of customerily placed discret contour points, we have calculated via fourier transformation the coefficients s_i and c_i of a sin-cos series expansion that describes the countour as radius depending on angle a

$$R(a) = \mathrm{Sum}_i \left(s_i * \sin(a*i) + c_i * \cos(a*i) \right)$$

With these contours and the center point, contour lines for the whole area are extrapolated. Each map pixel can be assigned to one specific line which may be seen as iso value line. All pixel values belonging to one line are averaged and assigned to the first coefficient of the cos series expansion c_0 as mean radius of this contour line.

Results
Figure a) shows two user defined contour lines laid over the cutting of a spin densitiy map of a root of Zea mays (1mm in diameter, Xylem excluded, original image: 8 echo train TSE, saturation recovery T_1 map. 128*128 points, FOV=5mm*5mm, TE=9ms). In b) the calculated contour map is shown. Plot c) displays the averaged iso contour values, which reflects the radial spin density variation. The same method was succesfully applied to other samples (not shown) like flow maps of non-ideal circular blood vessles to determine an averaged flow profile.

Discussion
This averaging method allows one to determine mean values for tissue or material regions that are difficult to distinguish in parameter maps, particularily in consecutive thin layers or over value gradients, like the gradual spin density variation over the root cortex (fig. c). This method can also be applied to non concentric structures, while treating them as sectors of concentric structures. Problems like intense thickness variations of one layer could be addressed by more user defined contour lines, resulting in a more complex contour map.

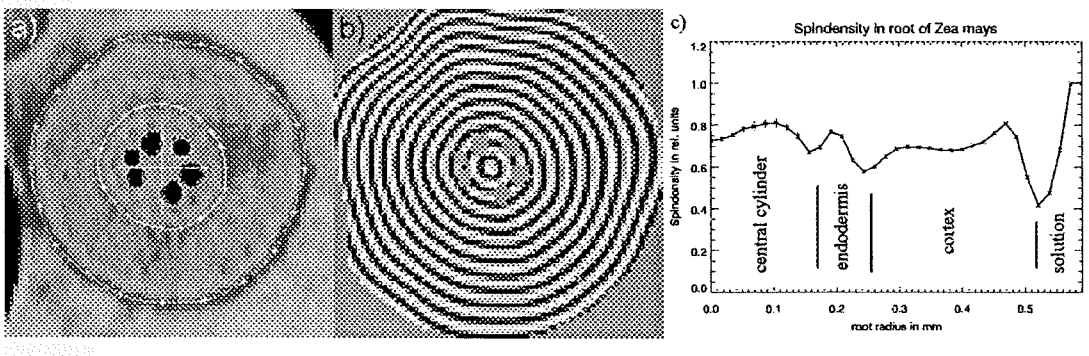

Diffusion barriers for macromolecules in intact plant roots

Ilja Kaufmann*, Lars Wegner[1], Ulrich Zimmermann[1], Axel Haase*
* Physikalisches Institut Universitaet Wuerzburg, Germany
[1] Institut fuer Biotechnologie, Universitaet Wuerzburg, Germany

Introduction
NMR microscopy is an ideal method for studying plant roots in nutrient medium, that often prevents direct experimental observation. Additionally inert NMR contrast agents can facilitate studies of internal structure and functionality in plant roots [1].

Subjects and Methods
The hardware used was a vertical Bruker 11.75T AMX500 spectrometer, a home-built probehead and a Helmholtz coil (R=5mm) fitted around a dedicated NMR-glass-tube for plant roots.The root of a Zea mays plant was allowed to grow into the glas tube, containing 4.0mmol NO_3 nutrient solution, for 5 days after germination. After the initial T_1 map, GaDTPA ("Magnevist") was added to the solution to achieve a final concentration of 10mmol. The uptake was observed with 40 consecutive T_1 maps. To minimize T2* effects (due to root aeration) and to achieve a high time resolution for functional studies, we used a Turbo Spinecho Method (TSE) [2] combined with saturation recovery (SR) [3] for T_1 maps (TE=9ms, 128*128 points, FOV=5mm*5mm, TSE with 8 echo train, duration=15min).

Results
The top figure shows T_1 maps, before, 0h, 1h and 10h after changing the solution. A reference capillary containing plain nutriant solution can be seen together with the root. The middle plot shows the T_1 development for different root components, and the lower plot the calculated Magnevist concentration variation from $1/T_1(c)=1/T_1+c*R$ [4].

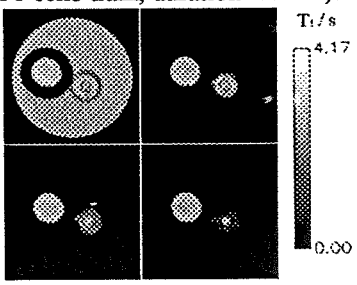

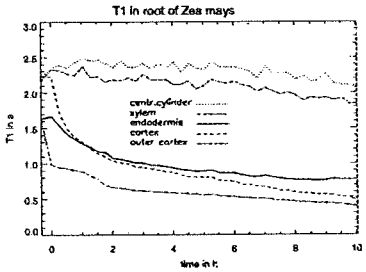

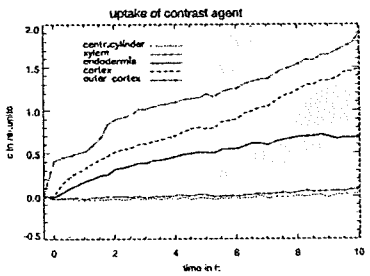

Discussion
As can be seen in the plots there is inflow of GdDTPA into the outer part of the root (cortex), which has large intracellular space. This is only limited by the diffusion velocity. Over the first 10h, the central cylinder and the xylem vessles show no significant increase in GdDTPA concentration, which implies the impermeability of the casparian band for the inert, neutral, lipophobic GdDTPA. For the endodermis, we observe an exponential inflow, to which a time constant of 5h could be fitted.

References

[1] Kai Zhong et al, *NMR in Biomedicine* 13, 392-397 (2000)
[2] J. Hennig, A. Nauerth, H. Friedburg, *Magnetic Resonance in Medicine* 3, 823-833 (1986).
[3] J. Evelhoch, J. Ackerman, *Journal of Magnetic Resonance* 53 (1), 52-64 (1983).
[4] M. R. Prince, *Radiology* 191(1), 155-164 (1994)

An improved Probebase and Resonator Setup for in-vivo body MR Imaging of small mammals at 17.6 T

Volker C. Behr, I. Wieland, M. Oechsner, D. Gareis, T. Weber, T. Neuberger, A. Haase, C. Faber

Department of Physics, EP5 (Biophysics), University of Würzburg, Würzburg, Germany

Synopsis

While recent spectrometers offer very high field strengths to achieve better signal to noise ratio for microscopic studies this advance goes along with smaller bores and therefore less space for the experimental setup. Especially in-vivo imaging of inner organs of rat-sized mammals requires elaborate hardware to provide as well room for the animal handling system and the animal as for the RF resonator and its feeds and connectors. An improved setup for that purpose will be introduced in this abstract and the performance will be evaluated in preliminary studies on the spinal cord and heart of rats.

Setup

For the experiments a Bruker Avance 17.6 T wide bore vertical magnet is used with a 200 mT/m gradient unit for in-vivo studies with a 56.5 mm inner diameter. The rats are studied in-vivo under iso-fluorane anesthetic. Breath and heart beat are monitored with a custom-built monitoring unit that is also employed to trigger experiments in order to avoid motion artifacts.

Hardware

For the study of inner organs of rats, especially of the spinal cord and the heart, an optimized probebase and coil was designed and built. As already pointed out in [1] at frequencies up to 750 MHz (larmor frequency of ^{1}H at 17.6 T) the electrical setup is very sensitive even to minor imbalances. Therefore balancing units (baluns) in the feeds are a pre-requisite especially for advanced designs like quadrature resonators. The probebase shown in figure 1 combines two feeds including baluns with an increased sample volume. To maintain the larger available volume within the resonator a transmit-receive surface coil mounted on a half-cylinder (fig. 2, right) replaces the volume resonators usually used in this setup. A shield made of copper foil with a thickness of only 7 µm to avoid eddy currents on a polyimide substrate covers the other side of the half-cylinder (fig. 2, left). The animal resting on a slide can be positioned from outside the magnet. This animal handling system is designed to be compatible to already existing commercial systems. While offering increased access to the animal it can also be employed in other probebases and/or with volume resonators. The probebase itself consists of a GFP outer cylinder, POM lead-throughs for 2 feeds with baluns at their ends and 4 PVC rods for tuning and matching. A PVC/aluminum basis offers two BNC connectors and a fixable adjustment screw for slide-positioning.

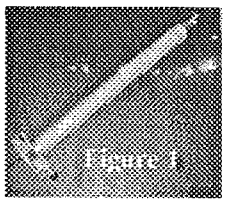

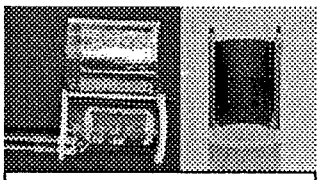

Figure 2: *left*: surface coil with open shield *right*: backside of coil mounted on probebase

Experiments and Conclusions

In preliminary studies several images on healthy rats were acquired. Figure 3 shows an axial slice with the spinal cord clearly visible and figure 4 is a short-axis view of a rat's heart. In both cases the new setup offers a sufficiently homogeneous and strong B_1 field and yields highest quality results. It provides a successful combination of animal handling capabilities, large sample volume and electrical demands for advanced resonator design for MR microscopy.

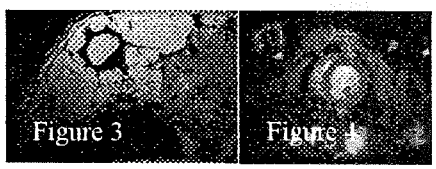

References

[1] V.C.Behr, D.Gareis, M.Oechsner, T.Neuberger, D.Haddad, C.Faber, A.Haase, "Resonator Designs for Very High Field ^{1}H and X-Nuclei in-vivo and ex-vivo Microscopic MRI Experiments", ISMRM Proc., Toronto, 2002

Resonator Designs and Results for Microscopic in-vivo and ex-vivo MRI at Highest Field Strengths up to 17.6 T

Volker C. Behr, I. Wieland, M. Oechsner, D. Gareis, T. Neuberger, D. Haddad, A. Haase, C. Faber

Department of Physics, EP5 (Biophysics), University of Würzburg, Würzburg, Germany

Synopsis

Ever increasing field strengths and faster and stronger gradient systems offer new and exciting possibilities in MR microscopy and MR spectroscopy. Along with these advantages, new challenges for hardware design arise. In this abstract, resonators designed to operate at frequencies up to 750 MHz, the larmor frequency of ^{1}H at 17.6 T, are presented. Their performance is demonstrated in in-vivo and ex-vivo imaging experiments and results of preliminary studies on phantoms as well as preserved dolphin fetuses and living mice are shown.

Setup

The Bruker Avance 750 MHz system employed in this research is a 17.6 T wide bore vertical magnet for which two gradient units are available: a 1 T/m system with an inner diameter of 40 mm and a 200 mT/m system for in-vivo studies with a 56.5 mm inner diameter. In this abstract resonator designs optimized for ^{1}H (750 MHz), ^{19}F (705.6 MHz) and ^{23}Na (198.4 MHz) imaging of different samples are presented.

Hardware

For the 200 mT/m gradient system several resonators were built for use in in-vivo studies. Figure 1a) is a quadrature birdcage on a 40 mm cylinder into which the Bruker animal handling system can be inserted. While linear operation was readily achieved at a length of 40 mm, the system was very sensitive to even small differences in the values of the capacitors employed when operated in quadrature. 1c) is a resonator with 38 mm inner diameter which was optimized for ^{23}Na imaging of mice and small rats with a proton channel available for positioning and shimming. It is a combination of two perpendicular saddle coils with the larger saddles being tuned to 198.4 MHz and the smaller ones to 750 MHz. The surface coil shown in figure 2 allows larger samples than the volume resonators described above. Designed for the 40 mm gradient system 1d) is a 20 mm inner diameter linear birdcage which is 42 mm long while b) offers 27 mm inner diameter in order to hold small animals like mice thus leaving only 7.5 mm on either side for socket, circuits and shielding.

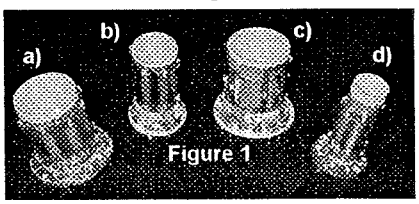

Figure 1

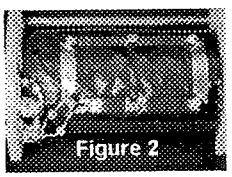
Figure 2

Experiments

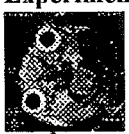

To verify the function of the resonators, imaging experiments were performed on phantoms, preserved dolphin fetuses and mice. As examples on the left an axial slice from a living mouse acquired with the quadrature birdcage resonator (Fig.1a)) and on the right a sagittal image of a dolphin fetus acquired with resonator 1d) where resolutions of below (100 $\mu m)^3$ were achieved [1] are shown. Homogeneity and B_1 field strength of all resonators proved sufficient to record images of highest quality.

Conclusions

Frequencies of up to 750 MHz combined with very limited available space aggravate all issues of resonator design. We were able to show that with careful selection of electrical elements and an optimized resonator design, birdcage or saddle coil setups can perform well under these conditions thereby granting access to the benefits of high field systems larger chemical shifts in spectroscopy or improved SNR in microscopic MRI.

References

[1] D.Haddad, V.C.Behr, H.H.A.Oelschläger, A.Haase, "High Field 3D-NMR Imaging of Dolphin Embryos and Fetuses", ISMRM Proc., Honolulu, 2002

High Field Magnetic Resonance Microscopy of Pig Cartilage

J.C. Tsai, T. Weber, T. Neuburger, A. Purea, V. Behr, A. Hasse, A. Webb
Experimentelle Physik 5, Institute of Physics, University of Würzburg

Introduction
^{1}H MRI is a promising method in detecting early degenerative changes in cartilage before volume loss and clinical symptoms develop in osteoarthritis. This would be particular valuable in early diagnosis and therapy evaluation for osteoarthritic patients. Prior works have pointed to several directions for possible early MR indicators of degenerative changes, e.g., the detection of striations in the radial zone, Na^+ concentration measurements, T_1 maping with $Gd(DTPA)^{2-}$, T_2 mapping, and diffusivity imaging. Nevertheless, progress for validation has been hampered by a shortage of high resolution MR microscopy images to correlate with histologic findings (1). We present our first attempt with MR microscopy at 17.6 T with rapid high resolution imaging of healthy pig femoral condylar cartilage.

Objects and Methods
MR imaging
Imaging experiments were performed on a Bruker Avance 750 WB system at a 750 MHz proton resonance frequency. The probe contained a 38 mm linear birdcage resonator. Optimal contrast was achieved using a 2D multi slice turbo spin echo sequence with 16 echoes and an effective echo time (TE) of 19.4 ms and a repetition time of 3s. In a total scan time of less than 7 minutes a spatial resolution of 117x117 μm^2 in-plane and a slice thickness of 350 μm was achieved.

Pig cartilage
A knee specimen from a healthy pig was obtained. The knee specimen was dissected and medial femoral condylar cartilage was excised and sectioned to fit into an NMR tube. It was fixed with 4% paraformaldehyde and placed into an NMR tube.

Results
The four cartilage layers, the low intensity superficial layer, intermediate signal intensity transitional layer, low intensity, heterogeneous radial layer, and intermediate intensity deep layer could be clearly distinguished with high contrast on the T_2 weighted MR images. These layers correspond to the four histologic cartilage zones, the surface zone, transitional zone, radial zone, and calcified zone. Some vertically oriented striation pattern is visible in the radial zone (see arrow).

Discussion

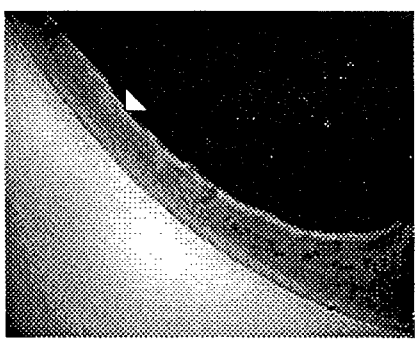

Vertical striation pattern in the radial zone occurs due to T_2 variations in the cartilage. We were able to demonstrate MR microscopy can be achieved with good resolution at 17.6 T with a scan time of just 7 minutes compared to hours in earlier works. Next steps in our study include optimized T_2 weighted imaging to accentuate striation pattern in the radial zone, Na^+ imaging, and DTI for histologic correlation.

References
(1) DW Goodwin, JF Dunn, Topics in Magnetic Resonance Imaging, 9(6):337-347. 1998.

NMR-microscopy with TrueFISP at 11.75 T

Sascha Köhler, Jens Maier, Karl-Heinz Hiller, Axel Haase, Peter M. Jakob
Physikalisches Institut, Universität Würzburg, Am Hubland, 97074 Würzburg, Germany

Introduction

The purpose of the present study was to demonstrate that a fully balanced gradient echo technique (TrueFISP) [1,2] can be used for microscopic experiments at high static magnetic field strengths. TrueFISP experiments were successfully performed on homogeneous and inhomogeneous objects at 11.75T with an in-plane resolution of 78 μm and a slice thickness of 500 μm. In addition, the sensitivity of TrueFISP to mesoscopic field inhomogeneities and the effect of intravoxel dephasing was investigated. The signal-to-noise ratio (SNR) gain of TrueFISP compared to conventional gradient echo or spin echo sequences will allow faster acquisition times or an improvement in spatial resolution for microscopic experiments.

Methods

The TrueFISP sequence was implemented on a Bruker AMX-500 microscopy system at 11.75T with a maximum gradient strength of 660 mT/m. A TR/TE = 4.0/2.0 ms was achieved with a matrix of 256x256. Experiments were performed on phantoms, plants, formalin-fixed samples and on isolated beating rat hearts (resolution: 78x78x500μm). For investigation of the sensitivity of TrueFISP to mesoscopic field inhomogeneities, numerical simulations of TrueFISP and RF-spoiled FLASH signal amplitudes were performed for different off-resonance distributions using the Bloch equations. The theoretical results were compared to MR experiments.

Results

Figure 1 shows a magnification of a region of a TrueFISP image and a FLASH image of an isolating beating rat heart. The SNR in myocardium is nearly the same in both images, whereas the TrueFISP image shows a 20% higher SNR in the balloon. The total acquisition time was 51s for the TrueFISP image and 14min for the FLASH image. The simulated signal behavior for TrueFISP and RF-spoiled FLASH for different off-resonance distributions showed similar characteristics. In Figure 2a the theoretical signal behavior of TrueFISP for a field inhomogeneity created by a cylinder placed perpendicular to the direction of the B_0 field is shown. Figure 2b shows the experimental signal behavior. Our results indicate that the sensitivity of TrueFISP to mesoscopic field inhomogeneities can be divided into 3 regimes which correspond to different widths of the off-resonance distribution: *Plateau*, *Amplitude* and *Phase regime.*

Discussion & Conclusion

The present study demonstrates that TrueFISP sequences can provide good contrast, spatial and temporal resolution for microscopic experiments. The high SNR efficiency of TrueFISP compared to conventional gradient and spin echo techniques allows faster acquisition times and/or an improvement in spatial resolution for microscopic experiments. Since the resolution in NMR microscopy is ultimately limited by the SNR available per unit time, refocused steady-state sequences such as TrueFISP could become a powerful tool for microscopic experiments at high fields. In case of mesoscopic field inhomogeneities, TrueFISP shows a similar sensitivity to off-resonance frequencies than conventional gradient echo techniques. In certain circumstances, TrueFISP has even a higher sensitivity to intravoxel dephasing than RF-spoiled FLASH. Generally, the signal behavior of TrueFISP in the presence of mesosocopic field inhomogeneities can be described with 3 regimes: *Plateau*, *Amplitude* and *Phase regime.*

Acknowledgements

This work was funded by the SFB 355/A7.

References:

[1] A Oppelt et al, Electromedica **54**:15-18 (1986)
[2] K Scheffler et al, Concepts Magn Reson **11**:291-304 (1999)

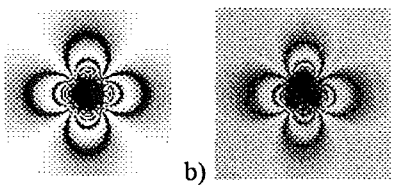

a) b)

Figure 2:
a) Simulation
b) TrueFISP image

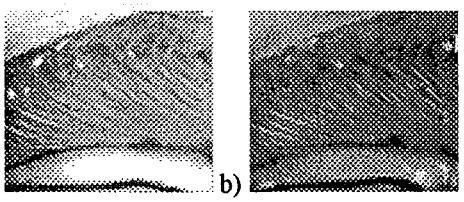

a) b)

Figure 1: a) TrueFISP image (T_{ACQ}=51s)
b) FLASH image (T_{ACQ}=14min)
of an isolated rat heart in the long axis view.

Development of Low Field NMR Microcoils

Artem Goloshevsky[1], Jeffrey H. Walton[2], Mikhail V. Shutov[3], Scott D. Collins[3], Jeffrey S. de Ropp[2], Michael J. McCarthy[1]

[1] Department of Food Science, UC Davis, Davis, CA, USA

[2] NMR Facility, UC Davis, Davis, CA, USA

[3] MicroInstruments and Systems Laboratory (MISL), University of Maine, Orono, ME, USA

We report the design and construction of an NMR probe with a Helmholtz micro RF coil where the microcoils are constructed using high precision micromachining and microfabrication techniques. Dimensions of the Helmholtz RF microcoil are as follows: 5 turns, the average diameter is 3.5mm, the substrate thickness (or separation between the halves of the coil) is 3.5mm, the trace width is 120 □m, the pitch is 160 □m, and the trace thickness is 15 □m. The probe was designed for flow experiments; therefore the sample delivery system was built around Teflon tubing with an outer diameter of 1/16" (1.59mm) and inner diameter of 0.04" (1.02mm). The useful sample volume is 1.62 μl.

The microprobe was tested using a low magnetic field 0.6T (26 MHz) connected to a GE NMR spectrometer with a Tecmag Libra pulse programmer. We obtained ^{1}H NMR spectra and images. A spectrum of propanol is shown in Fig. 1. The proton spectra demonstrates a reasonable ability to perform useful chemical identification at low fields on small samples. A linewidth of 0.6 Hz was achieved on a water sample. A 2-D velocity profile of water in laminar flow is shown in Fig. 2.

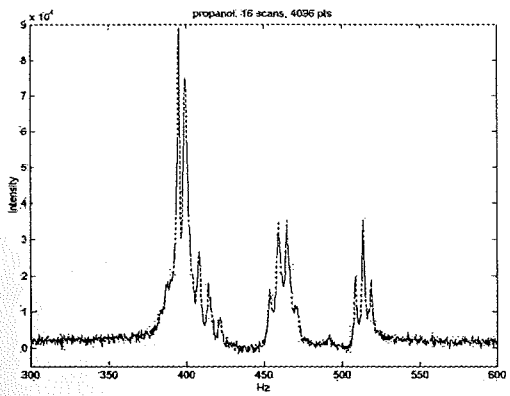

Figure 1: A spectrum of propanol.

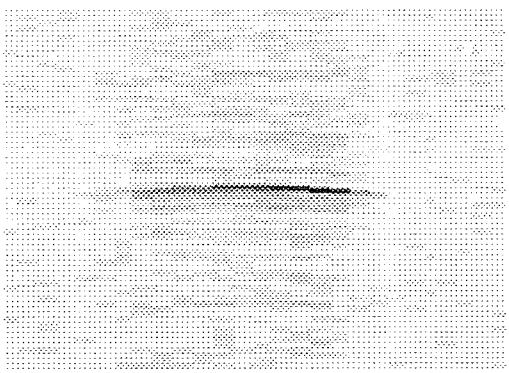

Figure 2: A 2-D velocity profile of the laminar flow of water.

A Mouse MRI using a Yokeless Permanent Magnet

T. Shirai, Y. Matsuda, T. Haishi, S. Utsuzawa, K. Kose
Institute of Applied Physics, University of Tsukuba, Ibaraki 305-8573, Japan
MR Technology Inc, Tsukuba, Ibaraki 305-8573, Japan

Introduction

Many biologists want to use MRI for mice in their own laboratories, which can be used as a complementary imaging tool against the other measurement modalities; an optical microscope, micro-PET, or micro-CT. However, existing MRI systems developed for mice or small animals are very large (installation space: ~ 20 m^2) and expensive. In the present study, we have developed a compact mouse MRI using a yokeless permanent magnet and acquired images of a chemically fixed adult mouse.

Mouse MRI System

A mouse MRI which we have developed consists of a yokeless permanent magnet [1] and compact MRI console [2] (Fig.1). The specification of the permanent magnet is as follows; magnetic field: 1.04 T, gap: 90 mm, homogeneous region: 35 mm dsv, size: 50 cm (W) x 53 cm (H) x 50 cm (D), weight: 980 kg. The installation space is less than 2 m^2. Several solenoid-coil RF probes were developed for this system.

Experiments

A chemically fixed adult mouse (age: 8 weeks) was imaged with 3D spin-echo sequences using an internal NMR lock technique to compensate the Larmor frequency drift caused by temperature change of the magnet during a long data-acquisition time [2].

Results and Discussion

Figure 2 shows 2D cross-sectional images of the mouse selected from a 3D image data set (128 x 128 x 128, 200 micron cube voxel) acquired a 3D SE sequence (TR/TE=100/10, 20NEX). As shown in the figure, detailed anatomical structures are clearly observed. We think the SNR is sufficient for a conventional mouse MRI.

Conclusion

A compact mouse MRI was developed using a 1.0 T yokeless permanent magnet. The SNR is sufficient for routine use in biological laboratories. We are now preparing for *in vivo* mouse imaging.

References

[1] Akio Nakanishi, *The Transactions of the Institute of Electrical Engineers of Japan*, **D121**, 715 (2001).
[2] Tomoyuki Haishi, Takaaki Uematsu, Yoshimasa Matsuda, Katsumi Kose, *Magnetic Resonance Imaging* **19**, 875-880 (2001).

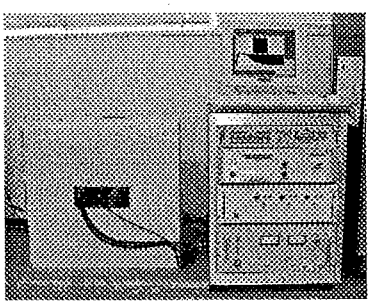

Fig.1 Overview of the mouse MRI.

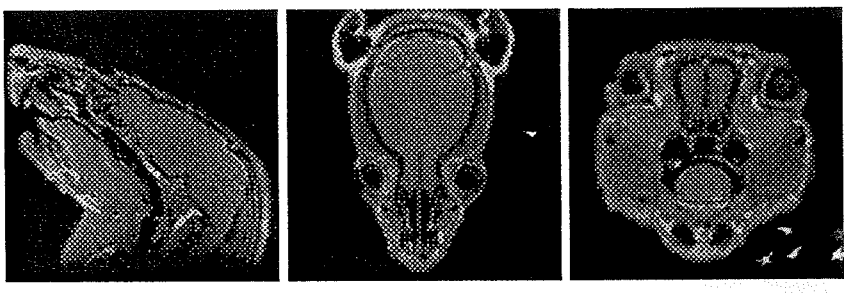

Fig.2 2D cross-sectional images of a chemically fixed adult mouse selected from a 3D isotropic image data set (128 x 128 x 128). 200 micron cube voxel resolution. TR/TE=100/10, 20 NEX, Data acquisition time; 10 hours.

Numerical simulations of NMR responses on micro-tomographic images

Christoph H. Arns, Arthur Sakellariou, Tim Senden, Adrian P. Sheppard, Rob M. Sok, Mark A. Knackstedt

Department of Applied Mathematics, Research School of Physical Sciences and Engineering, Australian National University, Canberra 0200 ACT, Australia

One of the most important parameters describing reservoir quality in the petroleum industry is permeability. Unfortunately, permeability cannot be directly observed in a subsurface environment and correlations with other petrophysical properties are required. A most promising correlation has been with NMR relaxation times [1-2]. A critical assumption in NMR/permeability correlations is that the dominant relaxation time within each pore is related to the surface-to-volume ratio of the pore (fast-diffusion limit). The decay rate is primarily determined by larger pore bodies with minimal contribution from narrow constrictions or pore throats. Pore constrictions however dominate the permeability. This suggests that NMR/permeability correlations are valid if constriction size is correlated to pore size; this is believed to be true for siliclastic reservoirs.

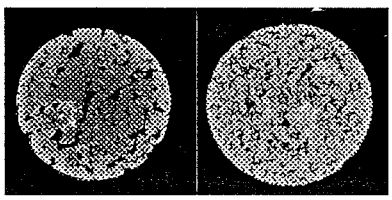

Fig. 1: Slices through 1000^3 tomograms of two reservoir sandstones (6μm resolution).

Although NMR measurements are used extensively to predict permeability in siliclastic reservoirs, numerical/theoretical studies testing the correlations have been limited to simplified geometries (e.g. periodic arrays of spheres [2]). We use X-ray micro-Computed Tomography (□XCT) to image the pore structure of a homogeneous sandstone, as well as a reservoir sandstone (Fig. 1), at pore-scale resolutions (~6□m). The permeability, formation factor, and NMR relaxation response of the sands are numerically derived. We use a grid-based method to simulate the NMR T_1- and T_2-relaxation response [3-4]. Comparisons with available experimental measurements show good agreement. Popular empirical NMR/permeability correlations are compared with computed permeabilities.

There is concern that conventional NMR correlations do not work well in carbonate reservoirs, due to the presence of both micro- and macro-pore systems in close proximity. Recently a new NMR technique, "decay due to diffusion in the internal field" or DDIF [5], was introduced to characterize the complex pore geometry in carbonate rocks. We use □XCT to image carbonate cores (Fig. 2) at resolutions down to 2□m. From the images one can directly measure the characteristic intergranular and vug pore sizes. This allows us to test the predictions of the DDIF technique. The DDIF ratio [5] is simulated directly on the □XCT-images and a comparison between the pore size distribution (PSD) derived from analysis of the □XCT-images and the PSD derived from an analysis of the DDIF ratio decay is made.

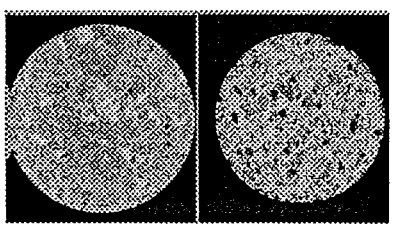

Fig. 2: Slices of carbonate tomograms at different resolutions (left 42μm, right 5μm).

References

[1] P. N. Sen, C. Straley, et al., *Geophysics* **55**, 61-69 (1990).
[2] K.-J. Dunn, et al., *Geophysics* **64**, 470-478 (1999).
[3] D. J. Bergman, et al., *Phys. Rev. E* **51**, 3393-3400 (1995).
[4] R. M. E. Valckenborg, et al., *Physical Review E* **65**, 021306.
[5] Y.-Q. Song, S. Ryu, P. N. Sen, *Nature* **406**, 178-181 (2000).

NMR Microscopy for Measurement of Water Distribution in a Polymer Electrolyte Membrane under Fuel Cell Operation

Shohji Tsushima, Kazuhiro Teranishi, Shuichiro Hirai
Research Center for Carbon Recycling and Energy, Tokyo Institute of Technology, Tokyo, 152-8552, JAPAN

Introduction

Polymer electrolyte fuel cell(PEFC) is a promising candidate for future vehicle application and on-site power generation. In PEFCs, water distribution and its transport is of great interest because electric conductivity in a polymer electrolyte membrane(PEM) in cells is high in case of membrane hydrated(wet) [1]. Hence, appropriate humidification to membrane by supplying vapor into a fuel and/or oxidizer should be carried out not only to keep membrane hydrated but also to avoid condensation of water that plugs gas supply channels [2]. To establish a method to control membrane hydration under fuel cell operating condition, it is important to develop visualization technique to measure water distribution in a PEM under an operating fuel cell although conventional optical method can not be applied. In this study, we thus applied NMR microscopy on fuel cell research especially for visualization of water in thin membrane under cell operation.

Methods

We constructed a polymer electrolyte fuel cell free from magnetic materials for NMR microscopy measurement. The configuration of constructed PEFC and spatial arrangement to place the cell in the test section of NMR microscopy equipment (Bore diameter 150 mm, 300 MHz, ^{1}H observed) was carefully chosen to acquire magnetic resonance image of water in a PEM under fuel cell operation in the NMR system. Polymer electrolyte membrane used in this study was a perfluorinated sulfonic acid polymer (Aciplex®-S1112, Asahi Kasei corp, Thickness 340 □m), sandwiched between two platinum impregnated porous electrodes. The fuel cell settled in the NMR system was operated with supply of pure hydrogen and oxygen with regulation of electric load connecting to the cell.

Results and Discussion

Figure 1 shows measured MR images of a PEM in three different operating conditions of fuel cell. The spatial resolution along anode to cathode was 25 □m using a spin-echo sequence. The 16 images was averaged with acquisition time of 16 min. From the left to the right (see Figure 1), output current density of cell was increased. The right side in each image is cathode in which water is generated by electrochemical reaction ($2H^+ + 1/2O_2\ 2e^- \rightarrow H_2O$). Water distribution in a PEM is clearly visualized by NMR microscopy showing less water content in a PEM with increase of output current density of the cell (compare Fig.1 A with D). This observation implies that generation of water at cathode is not back into the membrane. Furthermore, with increase of output current density, anode side of membrane is dehydrated, resulting in water concentration gradient in the membrane. This suggests that humidification of anode side in the PEM should be more effective in higher output current density in PEFCs.

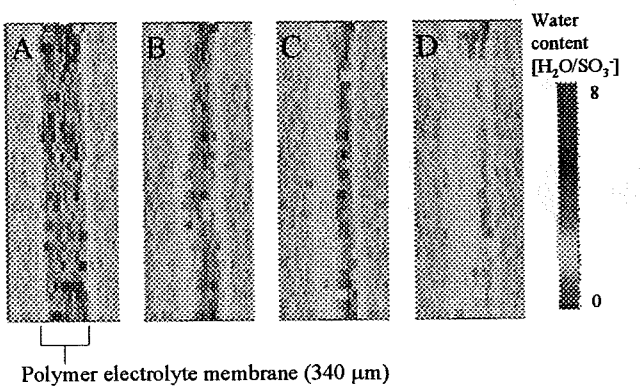

Figure 1: Water distribution in a PEM under fuel cell operation. Output current increases from left to right.

References

[1] Zawodzinski, T. A., et al., *J. Electrochem. Soc.*, **140**-4, 1041 (1993).

[2] Okada, T., et al., *J. Electroanalytical Chem.*, **413**, 49, (1996).

Time-series NMR Microscopy to Measure Dehydration Process of a Polymer Electrolyte Membrane in Fuel Cell Startup

Shuichiro Hirai, Shohji Tsushima, Kazuhiro Teranishi
Research Center for Carbon Recycling and Energy, Tokyo Institute of Technology, Tokyo, 152-8552, JAPAN

Introduction

Polymer electrolyte fuel cell(PEFC) is being developed for vehicular power application due to its high power density and low temperature operation [1]. The PEFC system, that allows for faster startups and immediate response, shows its high energy efficiency in case of a polymer electrolyte membrane(PEM) hydrated [2]. Therefore, control of membrane hydration is of great importance in operating condition. In vehicle application, immediate response to changes in the demand for power is also needed. To satisfy these demands, basic understanding about transient response of water behavior in a PEM is vital while visualization of water in a PEM assembled in the cell is never in ease. In this study, we demonstrated that NMR microscopy shows its great potential to visualize time-transient response of water distribution of a PEM under the fuel cell startup condition.

Methods

A home-made polymer electrolyte fuel cell consisting of non-magnetic materials was constructed for visualization study by NMR microscopy system. The structure of cell and configuration between the cell and NMR system was carefully investigated for NMR signal acquisition. The polymer electrolyte membrane (Aciplex®-S1112, Asahi Kasei corp, Thickness 340 □m) was sandwiched between two platinum dispersed porous electrodes in the cell. The operating condition of cell placed in the NMR system was manipulated by electric load. Spin-echo sequence was used to acquire time-series MR images of water distribution in the PEM in every 50 seconds after the cell starts to be operated.

Results and Discussion

After the fuel cell startup, the membrane inside the cell was seen to dehydrated (see Figure 1). In the images, left side is anode ($H_2 \rightarrow 2H^+ + 2e^-$) and the right is cathode ($2H^+ + 1/2O_2 + 2e^- \rightarrow H_2O$). Time-series NMR microscopy images also show that anode side in the membrane tends to be more dehydrated in initial stage of startup up to about 270 seconds compared to the cathode. Dehydration of anode side in fuel cell startup was firstly revealed by time-series NMR microscopy. This observation can be explained by both electro-osomotic effect from anode to cathode and water production resulted from electrochemical reaction at cathode. Thus, we concludes that hydration at anode side of the membrane is important under fuel cell startup.

References

[1] Hirschenhofer, J. H., Stauffer, D. B., Engleman, R. R. & Klett, M. G., Fuel Cell Handbook 4th Edition. 6-1, Parsons Corporation, Reading, (1998).

[2] Zawodzinski, T. A., et al., *J. Electrochem. Soc.*, **140**-4, 1041 (1993).

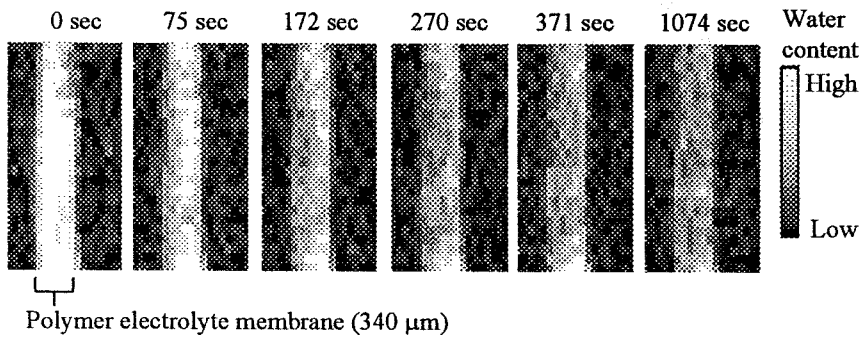

Figure 1: Time-series MR images of water distribution in a PEM after fuel cell startup.

NMR Imaging of Drainage Channels in Sea Spray Icing

Toshihiro Ozeki[1], Katsumi Kose[2], Tomoyuki Haishi[3], Shunichi Nakatsubo[4], Yoshimasa Matsuda[2]

[1]Hokkaido University of Education, Iwamizawa, 068-8642, Japan
[2]Institute of Applied Physics, University of Tsukuba, Tsukuba, 305-8573, Japan
[3]MR Technology, Inc., 169-1 Kouya, Tsukuba, 300-2642, Japan
[4]Institute of Low Temperature Science, Hokkaido University, Sapporo, 060-0819

Reduced visibility due to sea-spray ice accretion is a big problem for the operation of lighthouses in northern harbors. Spray icing also causes marine disasters for trawlers and vessels in cold sea areas. Brine pockets, which are trapped in a spray ice matrix during ice growth from sea spray, are structural feature of the sea-spray icing. The salt entrapment and drainage of the brine controls the growth rate and physical properties of spray ice. To address this problem we designed an MR microscopy system to visualize the drainage channels in sea spray icing.

Figure 1: Sea spray icing on a small lighthouse.

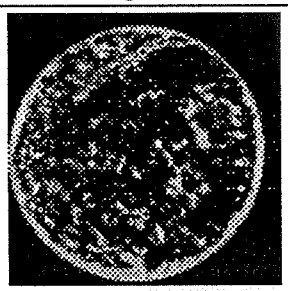

Figure 2: Horizontal 2D cross section of spray ice. FOV = $(25.6\ \text{mm})^2$, Voxel size = $(200\ \mu\text{m})^3$.

The sea spray icing samples came from ice accretion on a lighthouse on the west coast of Hokkaido, Japan (Figure 1). Because the brine in the spray ice had already drained out, we used a suction pump to fill the air gaps in the drainage channels with dodecane ($C_{12}H_{26}$). The signal from dodecane doped with iron acetylacetonate $C_{15}H_{21}O_6Fe$ was sufficient to detect the location of the drainage channels.

3-D microscopic images were obtained with an NMR imaging system composed of a 4.74-tesla, 89-mm, vertical-bore superconducting magnet and an actively-shielded gradient coil. The imaging sequence used 3-D gradient echoes, the image matrix was 128^3 voxels, and the voxel size was 200-μm on a side. To obtain one 3-D image, 0.5 - 1 h was needed; thus, we used a specimen-cooling system to maintain the sample at a constant temperature. The chamber had a double-pipe cylinder through which flowed cold air, and the temperature of the sample holder was controlled by adjusting the volume of cold airflow.

Figure 2 shows a horizontal cross-sectional image cut from a 3-D MR image. Because the NMR signal from the ice was negligible compared to that from dodecane, drainage channels appear as bright regions. We also used MIP and 3-D rendering to visualize the network structure of the drainage channels. For quantitative analyses, we need to directly compare the ratio of open channels with dodecane and closed channels with brine; nevertheless, this experiment shows that MR microscopy can be used to image the structure of drainage channels in sea spray ice.

Development of Compact MRI Systems for Sports Injuries

T. Kurimoto, T. Shirai, Y. Matsunaga, Y. Matsuda, T. Haishi*, S. Utsuzawa*,K. Kose, H. Yoshioka**
Institute of Applied Physics, University of Tsukuba, *MR Technology Inc.,
**Institute of Clinical Medicine, University of Tsukuba

Introduction

MRI is very useful for diagnosis of sports injuries because it can visualize anatomical structure and, often, physiological status of bones, joints, and tendons. For sports injuries, compact MRI systems can play an important role because about 80% of them take place at limbs. In the present study, we have developed two compact MRI systems for limbs and obtained MR images of several sports injuries such as baseball elbow and knee injuries of soccer players.

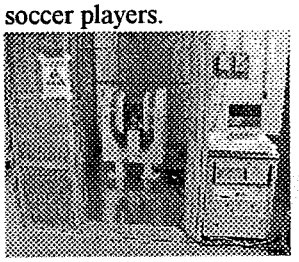

Fig.1 System overview

Compact MRI systems

Two compact MRI systems were developed using a compact MRI console [1] and two permanent magnets. The specifications of the magnets are as follows; magnetic field: 0.2 T, gap: 16 and 25 cm, homogeneous region: 12 and 15 cm dsv, weight: 500 and 1,400 kg. Two solenoid-coil RF probes were developed for the two magnets; inner diameter: 10.8 and 19 cm, number of turns: 10 and 4. The magnets were installed in home-built electromagnetic shield rooms (1.0 m (W) x 1.7 m (H) x 1.5 m (D), 1.6 m (W) x 2.1 m (H) x 2.4 (D), respectively) to reduce external electromagnetic noise as shown in Fig.1.

Experiments

MR images of elbows of eleven baseball players (age: 19-23), knees of four soccer players (age: 19-23) and several normal volunteers were obtained using the MRI systems described above. For two normal volunteers, MR images of knees were obtained for lying and standing pose.

Results and discussion

Figure 2 shows a 2D gradient echo (TR/TE=100/10) image of baseball elbow. This image clearly shows an injury at an elbow joint and was diagnosed as (lateral-type) baseball elbow. Figure 3 shows a 2D gradient echo (TR/TE=80/16) image of a knee injury. This image shows an injury at a knee joint and was diagnosed meniscus injury. Figure 4 shows 2D knee images at nearly the same slices selected from 3D images acquired for lying and standing pose. The size of the dark region in the femur seems slightly different but more study is required for the cause of the signal loss. These images will be useful for diagnosis of knee injuries, because the standing pose is natural for knees. In conclusion, the compact MRI systems developed in this study is useful for routine diagnosis of sports injuries at limbs.

References

[1] Tomoyuki Haishi, Takaaki Uematsu, Yoshimasa Matsuda, Katsumi Kose, *Magnetic Resonance Imaging* **19**, 875-880 (2001).

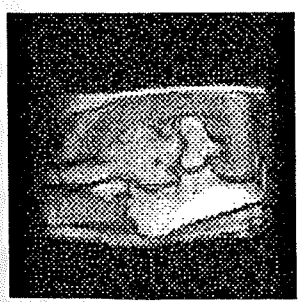

Fig.2 Image of a baseball elbow

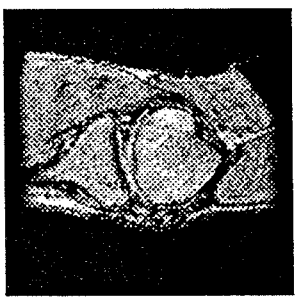

Fig.3 Image of a meniscus injury

Fig.4 (a) lying pose

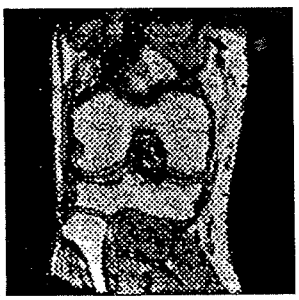

(b) standing pose

Efficient and Linear RF Power Amplifier for Unilateral NMR Apparatus

Jörg Felder
Institute of High Frequency Technology, Aachen University, 52056 Aachen, Germany

Introduction

Efficient amplification has rarely been considered in NMR tomography because of the high amount of energy required for cooling the magnet to superconducting temperatures. Low field NMR employs resistive or permanent magnets so that amplifier power consumption becomes predominant. This is of interest especially when mobility and miniaturization of the apparatus are considered. While efficient implementations have been investigated for gradient amplifiers recently [1] the RF amplifier has received little attention. This paper derives specifications and demonstrates a possible realization for a high bandwidth, highly efficient linear RF power amplifier required in an unilateral NMR tomography system.

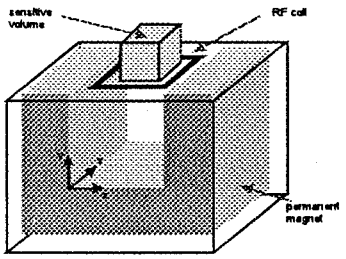

Figure 1

System setup

Fig. 1 shows the experimental setup and principle of operation. A specially shaped permanent magnet excites $\mathbf{B}_0$ which decreases linearly in direction of penetration with 12.5 mT/cm. A RF coil placed in the gap between the two pole shoes is used for excitation and reception of the NMR signal while planar gradient coils (not shown) allow frequency and phase encoding.

Efficient amplification

Conventional RF amplifiers operate in class-A for its inherent linearity. Since, except for hard pulsing applications, the amplifier is not driven at peak envelope power (PEP) during most of the transmit time, average power conversion efficiency is poor. The wasted energy has to be dissipated as heat requiring large heat sinks and sufficient power supply. On the other hand switched mode amplifiers achieve high efficiencies but are inherently nonlinear. Remedy is found employing signal processing and combining multiple nonlinear amplifiers to an efficient and linear amplification system. One possible realization, called "envelope elimination and restoration" (EER) [2], is shown in fig. 2. It splits the amplitude and phase modulated input signal into its polar components and amplifies both separately. The signal components are recombined by means of drain source modulating the final amplifier. Power added efficiency of over 70% can be sustained with this kind of amplifier even for high power back off levels. An EER Transmitter has been constructed and adopted for NMR applications showing low harmonic distortion and high modulation bandwidth.

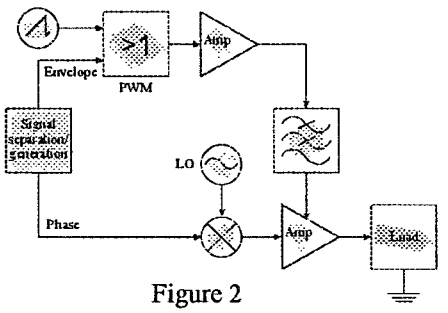

Figure 2

Linearity requirements

Limited information is available on the linearity required in NMR transmitters and articles focus on modulator design assuming the power amplifier to be sufficiently linear [3]. For the proposed design two major differences are encountered. First, the amplifier cannot be assumed à priori to be sufficiently linear but has to be built according to certain specifications and, second, the impact of amplifier nonlinearity in both inhomogeneous $\mathbf{B}_0$ and $\mathbf{B}_1$ has to be investigated. Calculations based on the Bloch equations reveal that amplifier distortion causes a spatial shift in the selected slice. The spatial shift becomes negligible for distortion levels below approximately -35 dBc.

References

[1] S. Watenabe, H. Takano, E. Hiraki, Trans. IEE Japan **121**, 756-763 (2001)
[2] L. R. Kahn, Proc. IRE **40**, 803-806 (1952)
[3] P. Devoulon et al., Meas. Sci. Technol. **4**, 1029-1032 (1993)

Acknowledgement : DFG-Grant "Surface NMR on elastomeres and biological tissue"

A Human Scale, Open-Access Low Field MRI System

F. W. Hersman[1], M. I. Hrovat[2], R. W. Mair[3], I. Muradyan[1], J. Ng[3], S. Patz[4], M. S. Rosen[3], I. C. Ruset[1], L. L.Tsai[3] and R. L. Walsworth[3]

[1] Dept. of Physics, University of New Hampshire, Durham, NH, USA

[2] Mirtech Inc., Brockton, MA, USA

[3] Harvard-Smithsonian Center for Astrophysics, Cambridge, MA, USA

[4] Brigham and Women's Hospital and Harvard Medical School, Boston, MA, USA

A current subject of much debate in the lung physiology community concerns the role of gravitational effects on lung inhalation and function, including the role of gravity in fundamental cardiopulmonary physiology [1]. The recent advances in spin-exchange optical pumping [2] have made laser-polarized ^{3}He MRI a powerful method for studying lung structure and function. Nevertheless, in conventional MRI systems, patients are restricted to lying in a horizontal position. However, as the laser-polarization is produced without the aid of a large applied magnetic field, we can benefit from novel magnet design that does not restrict the patient, while still permitting high-quality laser-polarized gas MRI. We have previously demonstrated very low field (~ 20 gauss) imaging of small samples of laser-polarized ^{3}He gas [3] and have now developed an open-access human-scale imager to operate at similarly low magnetic fields in which we can vary the orientation of the subject in a 2D plane.

The basic components of the open-access human scale MRI system include a B_0 field of 20 - 70 Gauss, created by two pairs of Helmholtz coils. Custom-designed planar gradients allow complete orientation of subjects in a plane ~ 75cm wide. Large B_1 coils for human imaging have been built, and are shown in Fig. 1 in place in the imager. Fig. 2 shows a 2-D ^{1}H image of a large tub of water with dimensions similar to human lungs, and resolution comparable to human scanners. Fig. 3 shows a 2-D image of a Tedlar bag that has been filled with laser polarized ^{3}He, transferred from a large-volume ^{3}He polarizer outside the magnet room.

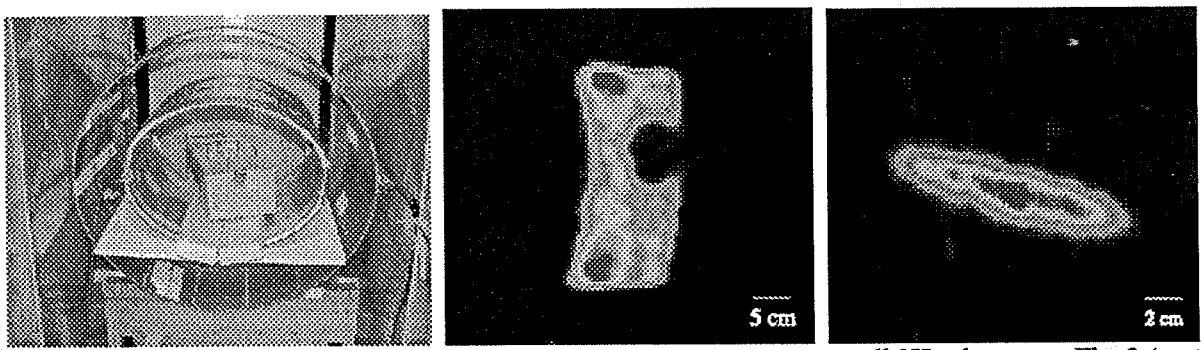

***Fig. 1** (left) Large RF coils for human imaging at kHz frequencies, containing small 3He phantoms.* ***Fig. 2** (center) ^{1}H image of a large tub of water containing a structural object acquired at 30 G (127 kHz) using a spin echo sequence in ~ 4 hours. Fig. 3 (right) Image of a plastic gas transfer bag containing laser-polarized ^{3}He, acquired at 39 G (127 kHz) using a gradient echo sequence with ~ 5□ flip-angles, acquired in ~ 20 seconds..*

The results with phantoms indicate the potential for MRI experiments at low field strengths in a large, open-access system, despite low-field limitations of narrow-bandwidth RF coils, and gradient pulses not necessarily small compared to the applied field. Human inhalation studies have begun, and initial results will be reported

References

1. J. West, H. Guy and D. Michels, *Physiologist.* **25**, S21 (1982).
2. T. G. Walker and W. Happer, *Rev. Mod. Phys.*, **69**, 629 (1997).
3. C.-H. Tseng, G. P. Wong, V. R. Pomeroy, R. W. Mair, D. Hinton, et. al., *Phys. Rev. Lett.* **81**, 3785 (1998).

T_2 relaxometry in the mouse brain

Stephen J. Dodd, Trevor J. Andrews, Jack L. Lancaster, Peter T. Fox
Research Imaging Center, U. Texas Health Science Center, San Antonio, TX, 78229, USA

Introduction

The multi-component relaxation properties of T2 has been proposed as a method of monitoring myelin content in white matter, wherein a short T2 component (~10-50 ms) is believed to be related to myelin water content (e.g. [1]). Despite a number of genetic models involving various levels of myelination, we are unaware of the existence of any short T2 data using imaging in the mouse brain. Here we use a 3D multiple spin-echo sequence to obtain T2 relaxation curves in the mouse brain, in an attempt to observe myelin water.

Methods

The method of Poon and Henkelman [2] involving an adiabatic 180^0 pulse for refocusing and alternating and decreasing crusher gradients is used as the basis for the imaging. This has been adapted to a 3D slab select sequence. To reduce partial volume effects, a ROI may be drawn on one of the central slices and the slices either side of this can determine if the region is completely within the desired tissue volume. To improve sampling of the decay curve, we interleave two imaging sequences, the first starting with a TE of 8 ms and proceeding in steps of 8 ms. The second part uses an initial TE of 12 ms, proceeding in steps of 8 ms. Each has 16 echoes. Initial simulations using a non-negative least squares algorithm (NNLS) suggested using more points would provide more stable results, as opposed to performing more signal averages over the same time.

The procedure has been implemented and tested on a dead mouse, allowing the luxury of signal averaging. The scan was performed on a 89-mm 7T vertical bore magnet equipped with home built 45-mm shielded gradients and a 25-mm quadrature birdcage for the transceiver. Imaging parameters were as follows: TR = 2.2s, slab thickness = 2.4 mm, Matrix size = 256 x 112 x 7 (zero-filled to 256 x 128 x 8), resolution = 0.085 x 0.125 x 0.5 mm, acquisition bandwidth = +/- 40 kHz, number of averages = 10, total scan time = 10 hours. A phantom of 10 mM NiCl (T2 = 60 ms from spectroscopy experiments) was placed next to the mouse.

Results

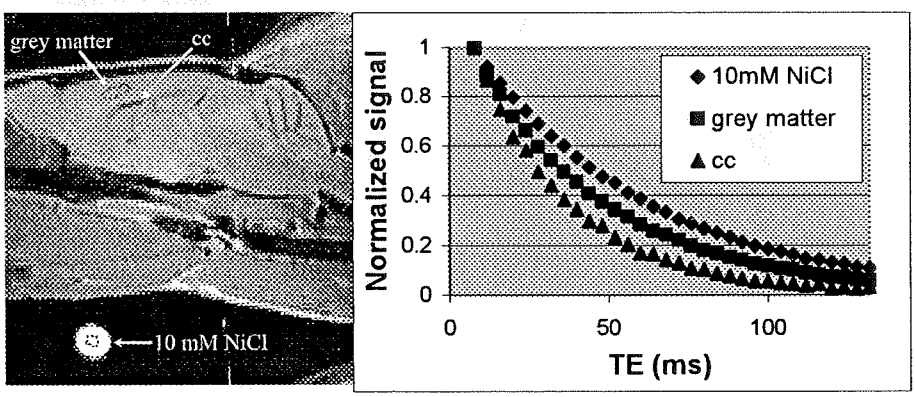

Figure 1 shows an example of the image quality at a TE of 32 ms, along with decay curves for the ROIs. The SNR of the first image in the series for grey matter was 85 and for the corpus callosum (cc) was 67. NNLS analysis found mono-exponential decay for the phantom with a T2 of 56 ms and for grey matter – 42 ms. For the cc two components were found, one at 7.6 ms accounting for 15% of the curve and one at 31 ms. Several ROIs drawn on the cc yielded T2 values of the short component varying from 5-15 ms indicating the sensitivity of the method to noise. However, two components were always found.

Discussion

Encouraged by the initial results, we are attempting to adapt this to *in vivo* studies, where we are limited to a few hours of acquisition time. The effects of diffusion, primarily from the readout gradient are significant (signal drop of ~10% by 16^{th} echo) and this will be addressed by decreasing the number of points in the acquisition window, sacrificing resolution in this direction (although increasing overall SNR). This will also allow for the echo spacing to be shortened.

References

[1] Mackay AL, Whittall KP, et al. *Magn Reson Med* 31(6):34-43 (1997)
[2] Poon CS, Henkelman RM. *J Magn Reson Imaging* 2(5):541-553 (1992)

A simple cooled copper radio frequency coil

Stephen J. Dodd, John Roby, Peter T. Fox
Research Imaging Center, U. Texas Health Science Center, San Antonio, TX, 78229, USA

Introduction

Thermal noise reduction from radio frequency receivers has been a subject of recent study, in particular with high temperature superconductors in conjunction with cryogen cooling (e.g. [1]). Much of the advantage of cooling for cases where the sample noise is significant may be obtained using copper cooled to liquid nitrogen temperatures [2]. We report an initial experiment using the method of Hall et al [3] adapted to a setting more suitable for microscopy, using a simple coil (in terms of construction) built from refrigeration tubing and cooled by pumping through liquid nitrogen.

Methods

The coil is a single loop design, 45 mm in diameter, made from 6.4 mm (0.25 inch) copper tubing. Liquid nitrogen is pumped continuously from a dewar through the piping. The coil and nitrogen line are insulated with foam. Coil tuning is adjusted during the experiment using a trimmer capacitor attached to the copper tubing. Dry air is blown across this capacitor to prevent freezing. Initial tuning is achieved using a fixed ceramic capacitor connected between the two ends of the copper tubing. The capacitor is connected through small pieces of copper tape, allowing flexibility. The coil is matched inductively using a loop of copper tape, 4-cm in diameter, placed 2 cm above the coil and which may be repositioned during the experiment. The matching coil is not cooled in nitrogen. The coil was operated in transmit/receive mode.

Results

The unloaded Q was measured at 190 +/- 5 at 290K and the unloaded Q with liquid nitrogen was 258 +/- 6. When loaded with a 10-mm diameter tube of water, placed through the coil, the Q increased from 184 +/- 5 to 250 +/- 8. Using equations from Wright et al. [2] the sample Q was calculated to be ~6000 and the expected increase in SNR to be a factor of 2.15 if the coil is assumed to be operating completely at liquid nitrogen temperature. The coil tuning appeared to be quite stable when liquid nitrogen was running through the tubing, and images were taken at this stage (the coil has been operated for up to 30 minutes at a time). For our images, acquired at a field of 2T, we measured an SNR for the room temperature coil of 45 +/-2, and for the cooled coil of 69 +/-2, an increase of 53%, somewhat less than predicted if liquid nitrogen temperature was assumed. (Images were gradient-echo, TR/TE = 100/8 ms, resolution of 0.15 mm, slice thickness = 2 mm, FA = Ernst angle, cooled coil required less power). Temperature of the sample was not directly measured. It was cool though not cold after 30 minutes of operation.

Discussion

Measured temperatures on the copper tubing reached down to 113 K (-160^{0}C), however as the end of the probe cannot be completely immersed in the copper, this measurement is inevitably higher than the actual temperature of the copper. Most of the difference in expected gain is due to the higher temperatures of the tuning and matching circuitry. These sections of the coil will be improved in later versions. The mechanical stability of the coil needs to be improved. It was noted that pressure was occasionally uneven for nitrogen exiting the pipe, leading to some minor vibration. Some artifacts were noted on the images for this reason. This is expected to be remedied shortly, through better insulation and greater stability in the coil structure.

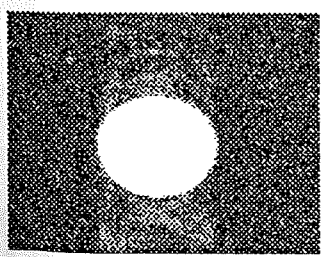

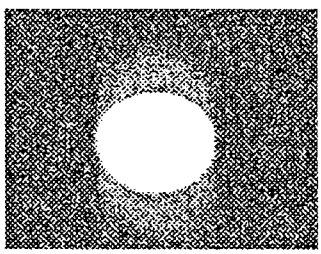

Figure 1A Cooled coil image **B** Room temperature image scaled to show noise and vibration artifact

References

[1] Miller JR, Hurlston SE et al. Magn Reson Med 41: 72-79 (1999)

[2] Wright AC, Song HK, Wehrli FW. Magn Reson Med 43:163-169 (2000)

[3] Hall AS, Barnard B et al Magn Reson Med 7:230-235 (1988).

Low SNR Performance of a 3-Pool Model for Myelinated Tissue

Trevor J. Andrews, Jack L. Lancaster, Carmen Contreres-Sesvold, Stephen J. Dodd
Research Imaging Center, U. Texas Health Science Center, San Antonio, TX, 78229, USA

Introduction

This work examines the performance of a method for extracting multiple components from T_2 relaxation data for myelinated tissue at SNR values possible for imaging studies. In recent years, white matter has been seen to exhibit multi-exponential T_2 relaxation. This is often seen as evidence of physically separate water pools. Previous methods used to extract the T_2 values however, require very high SNR (>500) to obtain accurate pool fractions [1][2]. Such SNR values are typically not possible for imaging. *In vitro* T_2 studies of myelinated nerve tissue have found three major T_2 values [3], and human studies of children have shown that this may be true in the brain[4]. In this study we attempted to use these findings to improve accuracy at lower SNR by further constraining the fit.

Methods

We chose to use the slow exchange model to describe T2 relaxation in myelinated tissue. We assumed,

$$S(t) = \sum_{i=1}^{n} S_i(0) e^{-t/T_2} + B$$

where S(t) is the magnitude of the net relaxation signal as a function of time, $S_i(0)$ is the magnitude of the signal for pool "i" at time = 0, T_i is the relaxation time for pool "i", B is the baseline, and n=3. To test its effectiveness, pool fractions obtained using the model were compared to actual values of Monte Carlo simulated data. The same was done with another method that has been shown to fit 2-pool data well at relatively low SNR [1]. For each of six SNR values (500. 250, 200, 150, 100, 50), 10 sets of simulated WM signal magnitude data were generated (128 echoes, TE=2ms) with signal S(t) in one channel and equal Gaussian noise in both channels (weighting and T_2 values obtained from *in vitro* relaxometry of bovine FWM). The squared magnitudes were corrected for the effect of Rician noise [5]. The method of Graham, et al [1] was used to analyze the data, and produce a discrete spectrum of T_2 values using 300 points and a resolution of 1ms. The last spectral point was set to 3000ms to reduce the influence of residual baseline in the data. (χ^2_{opt} was chosen to be 0.1% greater than χ^2_{min}.) Results from the 3-pool model were also calculated using an iterative Levenberg-Marquardt algorithm in Mathcad (Mathsoft, Cambridge, Massachusetts). During fitting both the T_2 values and the pool fractions were allowed to vary for each of the three pools, and both mean and standard error of the mean (SEM) were calculated for each pool fraction at each SNR.

Results and Conclusions

The pool fractions obtained from the 3-pool model compared well with the simulated values (Fig. 1). The 3-pool model was highly accurate above SNR=100. Thus, correction for the effects of Rician noise did not produce the T_2 and pool fraction biasing that has been previously reported [5]. The Graham method, however, often failed the even more basic task of finding three distinct T_2 values. Even at SNR=500, the Graham method found three distinct values only 80% of the time and thus mean and SEM could not be unambiguously calculated.

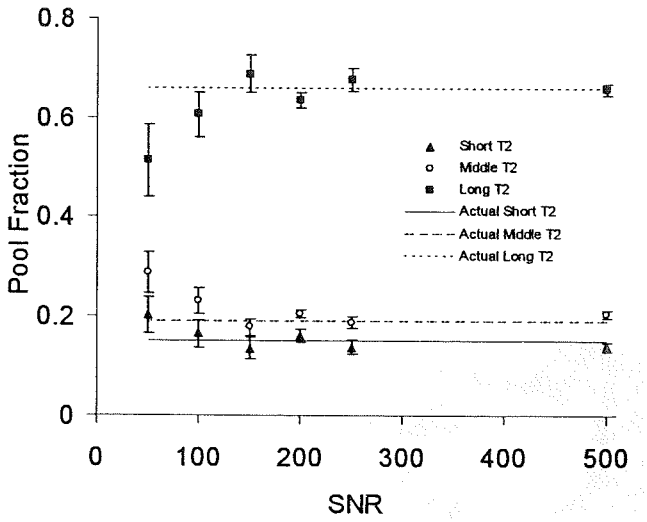

Figure 1: Pool fractions calculated by the 3-pool model

References

[1] Graham, et al, MRM **35**, 370-378 (1996).
[2] Gareau, et al, MRI **17**, 1319-1325 (1999).
[3] Does, et al, MRM **47**, 274-83 (2002).
[4] Lancaster, et al, JMRI **17**, 1-10 (2003).
[5] van der Weerd, et al, MRI **18**, 1151-1157 (2000).

High Sensitivity, High Resolution ^{1}H NMR Spectroscopy of Excised Muscle Tissues Using Slow MAS

Jian Zhi Hu[1], Hanne C. Bertram[2], Donald N. Rommereim[1], and Robert A. Wind[1]
[1])Pacific Northwest National Laboratory, P. O. Box 999, MS K8-98, Richland, WA 99352, USA,
[2])Danish Institute of Agricultural Sciences, Department of Food Science, Research Centre Foulum, PO Box 50, DK-8830 Tjele, Denmark

^{1}H NMR spectroscopy is one of the premier methods for obtaining biochemical information *in vitro* and *in vivo* in biological objects. However, due to the intrinsic magnetic susceptibility variations between intra- and inter-cellular structures, the observed ^{1}H resonance lines are usually relatively broad. Traditionally, magic angle spinning (MAS) at sample spinning rates of several kHz is used to eliminate this line broadening. However, the large centrifugal force from fast MAS destroys the integrity of the sample, even part of the cells. Two complementary 2D methods have been developed recently in our laboratory that provide high-resolution ^{1}H NMR spectra of biological objects at a substantially lower spinning rate, thus preventing structural damage in the object [1, 2]. One is based on the phase-corrected magic angle turning (PHORMAT) [3] and the other is based on the phase-altered spinning sidebands (PASS) [4]. It was found that for small (a few mm or less) samples, where spinning rates of 40 Hz or larger are allowed, PASS is the method of choice because it produces isotropic spectra with the highest resolution, the highest sensitivity, and in the shortest measuring time [2].

In this presentation a PASS study of the degradation of muscle tissue excised from mice and rabbits will be reported. For this study several extensions of the PASS method have been developed, including lactate-editing PASS to separate the lactate methyl line from the lipid methylene line, and PASS combined with RF sequences to determine the ^{1}H T_1, T_2 and $T_{1\rho}$, values of individual metabolite protons. Figure 1 shows standard and lactate-edited (water-suppressed) PASS spectra acquired on muscle tissue excised from a female BALBc mouse, before and after adding additional lactate into the tissue. The editing is based on the J-coupling patterns, where doublets such as the lactate methyl line at 1.3 ppm and quartets such as the lactate methane line at 4.1 ppm are inverted while, e.g., the multiplet lipid methylene peak at 1.28ppm remains positive.

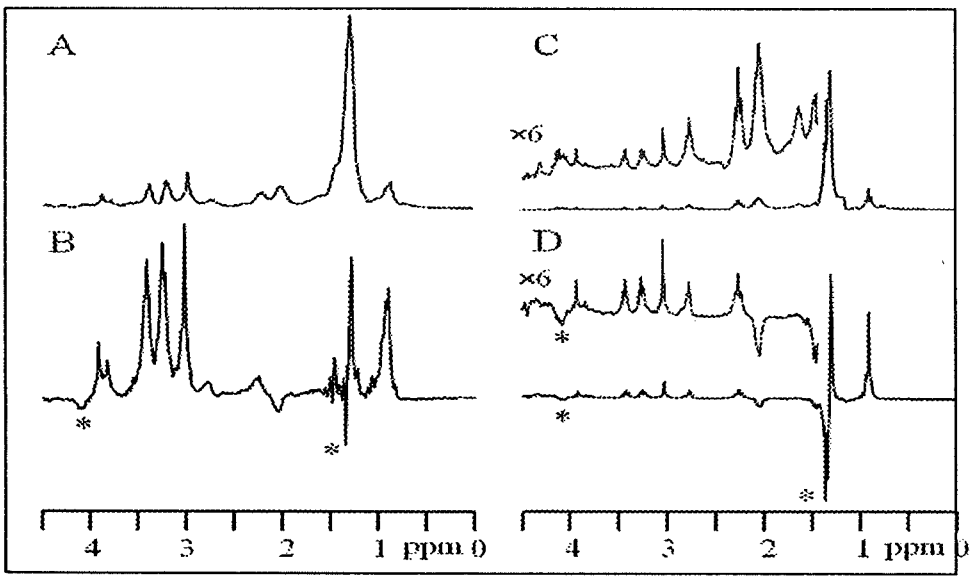

Figure 1. The center band PASS spectra of excised mouse muscle before (A, B) and after adding several drops of 200mM lactate solution (C, D). A,C: Regular PASS. B,D: Lactate-edited PASS. The experiments were carried out using a 7T Chemagnetics CMX300 spectrometer, a 5 mm I.D. rotor, and a sample spinning rate of 44Hz. The lactate doublet and the quartet are labeled by "*".

References

[1] J.Z. Hu, D.N. Rommereim, and R.A. Wind, Magn. Reson. Med. **47,** 829-836 (2002).
[2] R. A. Wind, J. Z. Hu, and D. N. Rommereim, Magn. Reson. Med. **46,** 213-218 (2001).
[3] J. Z. Hu, W. Wang, F. Liu, M. S. Solum et al, J. Magn. Reson A **113,** 210-222 (1995).
[4] O. N. Antzutkin, S. C. Shekar, and M. H. Levitt, J. Magn. Reson, A**115**, 7-19 (1995).

High Resolution ^{1}H NMR Spectroscopy in Intact Biological Objects Using Slow Magic Angle Spinning

Jian Zhi Hu, and Robert A. Wind
Pacific Northwest National Laboratory, P. O. Box 999, MS K8-98, Richland, WA 99352

The lines of the ^{1}H NMR metabolite spectra in intact biological objects are significantly broader than those obtained by dissolving the metabolites in water. This broadening is mainly caused by the local magnetic field gradients arising from variations in the isotropic (usually diamagnetic) magnetic susceptibility near boundaries of inter- and intra-cellular structures that are present in intact cells and tissues. It is well known that magic angle spinning (MAS) at sample spinning rates of several kHz can be used to eliminate this broadening. However, the associated large centrifugal forces destroy the integrity of the sample and even part of the cells. In order to overcome this problem two complementary 2D methods, originally developed for solid-state NMR and both employing lower MAS frequencies, have been modified in our laboratory for studies on biological samples. One is based on the phase-altered spinning sidebands (PASS) [1, 2] and the other is based on the phase-corrected magic angle turning (PHORMAT) [3, 4]. Figure 1 shows ^{1}H isotropic spectra of excised rat liver, obtained with different techniques. It follows that with both PASS and PHORMAT a spectral resolution is obtained comparable to that observed with standard fast (4 kHz) MAS. It is found that PASS is the most sensitive technique and requires the shortest measuring time, but that the spinning frequencies are restricted to values of 30 Hz or larger. With PHORMAT spinning speeds as low as 1 Hz can be employed, but at a cost of a reduced sensitivity and a long measuring time. Hence it appears that PASS is the method of choice to study small biological objects, and that PHORMAT can be used to study larger intact biological objects, including live animals [5].

In the presentation the following issues will be considered:

(I) Experimental details of PASS and PHORMAT will be given and the limitations of the techniques will be discussed.
(II) The impact of the diffusion of the metabolites in the susceptibility gradients on the isotropic line widths and its dependence upon the spinning speed will be outlined.
(III) Methods to increase the sensitivity and decrease the measuring time of a PHORMAT experiment will be discussed.
(IV) The prospects of combining PASS and PHORMAT with volume-selective spectroscopy will be discussed and, if available at the time of the conference, first results will be shown.

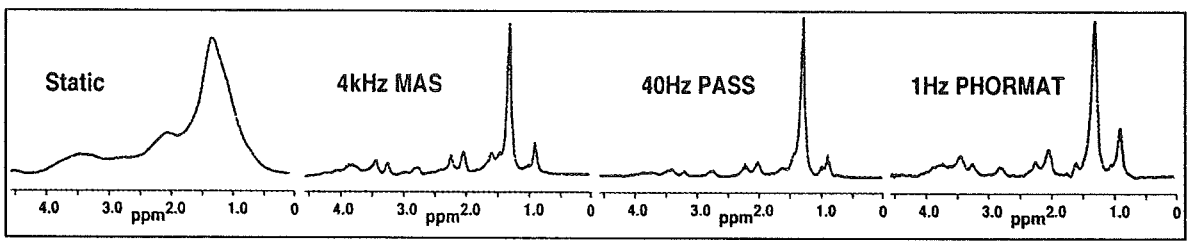

Figure 1. ^{1}H NMR spectra of excised rat liver, obtained with different methods. The experiments were carried out using a 7T Chemagnetics CMX300 spectrometer and a 5 mm I.D. rotor.

References

1. O. N. Antzutkin, S. C. Shekar, and M. H. Levitt, J. Magn. Reson, A**115**, 7-19 (1995).
2. R. A. Wind, J. Z. Hu, and D. N. Rommereim, Magn. Reson. Med. **46,** 213-218 (2001).
3. J. Z. Hu, W. Wang, F. Liu, M. S. Solum et al, J. Magn. Reson A **113,** 210-222 (1995).
4. J.Z. Hu, D.N. Rommereim, and R.A. Wind, Magn. Reson. Med. **47,** 829-836 (2002).
5. R. A. Wind et al, Invited Presentation, ICMRM (2003).

In-situ MR microscopy and spectroscopy of microbial communities

Paul D Majors, Jian Z Hu, Fred J Brockman, James K Fredrickson, Yuri A Gorby, Eric A Hill, William P Kovacik, Jeffrey S McLean, and Robert A Wind
Pacific Northwest National Laboratory, MSIN: K8-98, Richland, WA 99352, USA

Abstract
The engineering of microbes to enhance and exploit their useful metabolic properties requires the detailed knowledge of microbial gene expression in relation to microbial metabolic function under known environmental conditions. In this presentation, first results are shown for the application of advanced magnetic resonance microscopy (MRM) and spectroscopy (MRS) methods developed at PNNL to study metabolism and transport processes in *in-situ* bacterial systems. These methods include integrated confocal optical and MR microscopy [1] to simultaneously study microbial growth, metabolic function, and materials transport, and a modified version [2] of two-dimensional ^{1}H phase-altered spinning sideband (PASS) MRS [3] employing slow (40 Hz) magic angle spinning to enhance spectral resolution. Microbial systems being investigated are *Shewanella oneidensis* (strain MR-1) monoculture bacterial films and *methanogenic* anaerobic biogranules (The Retec Group Inc., Lansing MI; a coculture of bacteria and archaea employed in wastewater treatment).
Work has included methods and hardware development for establishing and measuring *in-situ* biofilms, the initial assignment of PASS metabolite spectra, and the mapping of water MR properties [*spin-lattice* (T_1) and *spin-spin* (T_2) relaxation times and apparent diffusion rates (D_{app})]. Figure 1 shows a MRM constant-time image acquired for a few, millimeter-sized methanogenic biogranules, showing significant internal structural detail. (The live samples were maintained under anaerobic conditions in a 3 mm O.D. NMR tube and maintained their biological activity during the experiment as evidenced by significant gas formation; TR/TE= 500/3.2 msec; b = 9 sec/mm^2; 30 μm in-plane resolution; 200 μm plane thickness; 2 repetitions; 9.1 hour acquisition time.) Figure 2 shows the isotropic spectrum from ^{1}H PASS data collected for free *Shewanella oneidensis* cells that were carefully removed from a culture plate and densely packed into a sample rotor immediately before measurement, demonstrating the significant spectral enhancement obtained via PASS MRS with a sample spinning rate of only 40Hz.

References

[1] R.A. Wind, P.D. Majors, K.R. Minard et al., *Applied Magnetic Resonance* **22,** 145-158 (2002).
[2] R.A. Wind, J.Z. Hu, and D.N. Rommereim, *Magnetic Resonance in Medicine* **46,** 213-218 (2001).
[3] O.N. Antzutkin, S.C. Shekar, and M.H. Levitt, *Journal of Magnetic Resonance Series A* **115**, 7-19 (1995).

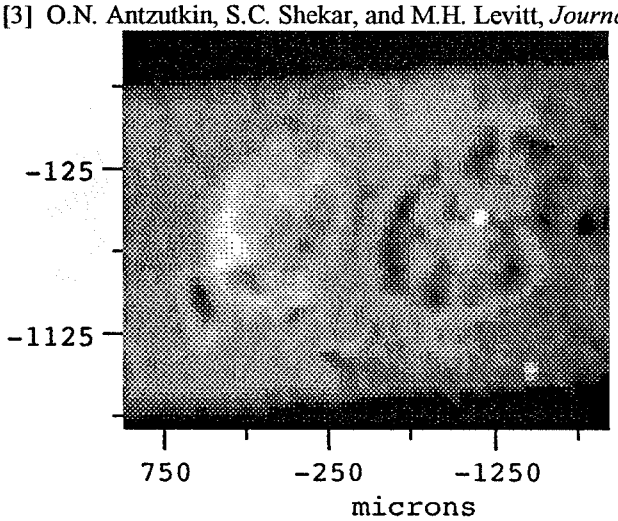

Figure 1. ^{1}H MRM constant-time image for methanogenic biogranules maintained under anaerobic conditions

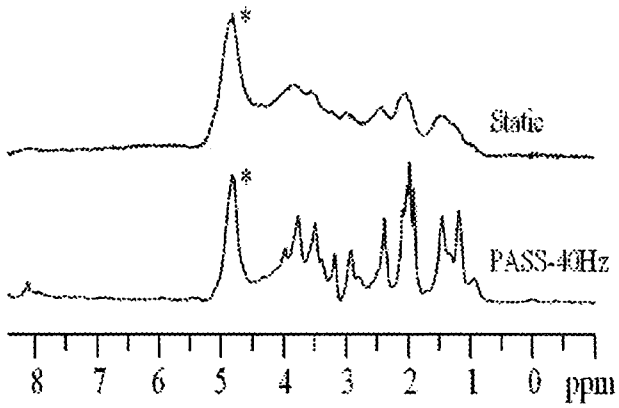

Figure 2. Water-suppressed 300 MHz ^{1}H MRS of *Shewanella oneidensis* (strain MR-1) cells obtained for a static sample (top) and with PASS (bottom, 40 Hz rotation rate).

Non-invasive investigation of insect morphology with NMR microscopy

Cornelius Faber[1], Thomas Hörnschemeyer[2], Axel Haase[1]
[1]Physikalisches Institut, Universität of Würzburg, D-97974 Würzburg, Germany
[2]Institut für Zoologie und Anthropologie, Universität Göttingen, D-37037 Göttingen, Germany

Introduction:
Insect morphology is commonly investigated by light or electron microscopy which inevitably leads to the destruction of the specimen. For rare insects non-invasive methods are highly desireable. Recently, micro X-ray tomography has been described as a useful tool for such investigations [1]. Here we report on a morphological study of two rare beetle species with NMR microscopy.

Materials and Methods:
With a 17.6 Tesla widebore NMR spectrometer (Bruker) we have studied one intact, fixed specimen of *Ascioplaga mimeta* in a 5 mm birdcage resonator and one fixed specimen of *Tenomerga cinerea*, comprising the head and prothorax, in a 2.5 mm solenoid coil. A 3D spin echo experiment (TE/TR = 18/500 ms) yielded a dataset of *A. mimeta* with 25 µm isotropic resolution in 18 hours scan time. A 3D dataset of *T. cinerea* was recorded with a spin echo sequence (TE/TR = 15/500 ms) with an isotropic resolution of 18 µm in 64 hours. To further improve resolution we have doped the sample with Gadovist™ (1:100). With a spin echo experiment (TE/TR = 12/50 ms) an isotropic resolution of 18 µm was obtained in 55 minutes and an isotropic resolution of 12 µm in 18 hours. A gradient echo experiment (TE/TR =3.5/20 ms) with an isotropic resolution of 12 µm was recorded in 16 hours.

Results and Conclusion:

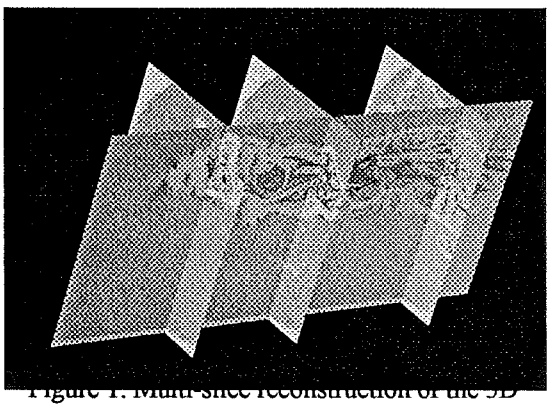

Figure 1: Multi-slice reconstruction of the 3D dataset of *A. mimeta* with 25 µm isotropic resolution.

The images of *A. mimeta* allowed identification of the thoracic muscles (Figure 1). In particular, muscles responsible for the movement of the head and the flight muscles could be characterized. Together with X-ray images that allowed identification of muscles of the mouthparts and internal muscles of the appendages, a detailed morphological description and a phylogenetic classification of the yet uncharacterized beetle was possible.

The data from *Tenomerga* showed that the use of contrast agent allowed, in spin echo experiments, a reduction in scan time by a factor of 70 while reducing SNR only by a factor of two. A gradient echo sequence enabled similar contrast to be obtained with far shorter echo times. Thus, in the gradient echo images SNR (~79 for muscle tissue, Figure 2) was higher by a factor of seven compared to the spin echo images (~ 12 for muscle tissue) obtained in a similar scan time.

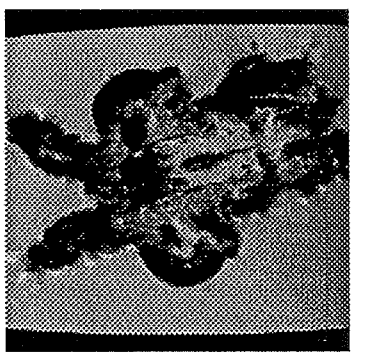

Figure 2: Slice from the 3D gradient echo dataset of *T. cinerea* with 12 µm resolution.

Our data show that NMR microscopy is a valuable tool for the investigation of insect morphology. With gradient echo methods in doped samples resolutions on the order of X-ray methods (5 µm) [1] may be approached in the future.

References:
[1] T. Hörnschemeyer, R. G. Beutel, F. Pasop, *J. Morphol.* **252**, 298-314 (2002).

NMR microscopy of the lipid distribution in air-dry branches of the resurrection plant *Myrothamnus flabellifolia*

Thomas Neuberger[1], H. Schneider[2], D. Haddad[1], A. Purea[1], M. Westhoff[2], A. Haase[1], U. Zimmermann[2],C. Faber[1], A. Webb[1]

[1]Department of Physics, EP5 (Biophysics), University of Würzburg, Würzburg, Germany
[2]Department of Biotechnology, Biocenter, University of Würzburg, Würzburg, Germany

Introduction

The productivity of agricultural crops in arid and semi-arid areas is severely limited by their inability to allocate water efficiently, but irrigation leads to soil salinization on the long run. The most promising way out of this impasse seems to be the genetic engineering of drought-tolerant cultivars on the basis of a fundamental understanding of the general strategies of drought survival. Among the naturally drought-tolerant plants, the poikilohydric resurrection plant *Myrothamnus flabellifolia* is one of the most interesting species because of its ability to transform from a desiccated state of suspended animation into a fully hydrated green shrub within only one day upon watering. The distribution of lipids within the plant body plays a crucial role in drought survival and in the mechanism of re-hydration [1,2]. In this work the proton distribution of air-dry branch material of *M. flabellifolia*, corresponding to its lipid distribution [2], is investigated by using NMR microscopy.

Objects and methods

High-resolution proton imaging was conducted on c. 2-cm-long pieces cut from air-dry branches and trimmed to a diameter of c. 2 mm and 450 µm, respectively. The larger piece was placed into a solenoid coil with an inner diameter of 2.5 mm (Bruker, Rheinstetten, Germany), and the smaller one into a homebuilt solenoid microcoil with an inner diameter of 700 µm. In both cases high-resolution proton distribution images were obtained by using a standard 3-D spin echo pulse sequence. With a field of view (FOV) of 6.0 x 2.2 x 2.2 mm^3 and a matrix size of 60 x 154 x 154 the resolution of the larger sample was 100 x 14 x 14 μm^3. The echo time (TE) was 3.5 ms, the repetition time (TR) was 1 s and the number of averages (NA) was 10, leading to a total scan time of 66 hours. In the case of the 700-µm coil, a voxel resolution of 100 x 6 x 6 μm^3 (FOV = 2.0 x 0.7 x 0.7 mm^3, matrix: 20 x 110 x 110) was achieved in 24 hours (TE = 5.4 ms, TR = 900 ms, NA = 8).

Figure 1. Cross-sectional images of the nodal region of the branch after removal of the bark and of the outermost part of the conducting xylem area (acquired with the 2.5-mm solenoid coil).

Results

In Figure 1, two representative slices from a 3-D data set, acquired with the 2.5-mm coil, close to and within the node are shown. High concentrations of lipids (signal-to-noise ratio = 12) can be clearly distinguished at the pith periphery, in fragments of a cylindrical structure (left) and in the leaf traces (right). The spatial resolution was sufficiently high to visualize the lipid-containing uniseriate rays. Figure 2 shows an image acquired by using the 700-µm coil. The image resolution was high enough to distinguish single (or at least two), lipid-rich parenchyma cells forming the rays. These non-invasively acquired results corroborate the data obtained by means of light and transmission electron microscopy [1].

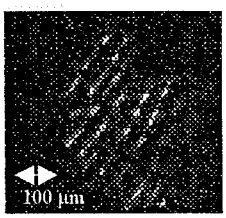

Figure 2. Part of the conducting xylem area, imaged by using the 700-µm microcoil).

Discussion

With the spatial resolution achieved here the lipid distribution in air-dry branches of the resurrection plant *M. flabellifolia* could be investigated at the level of single cells within the intact xylem tissue. NMR results and further studies described in [1] provide supplementary details about the mechanisms leading to organized de- and re-hydration of the branches. The understanding of these mechanisms is a small, but important step on the way towards genetically engineered, drought-tolerant crop plants.

References

[1] Schneider H et al., *New Phytologist* **159** (in press)
[2] Zimmermann U et al., *New Phytologist* **151**:314-317 (2001).

The effects of chemical fixation on intracellular NMR relaxation times

Armin Purea, Daniel Haddad, Thomas Neuberger, Axel Haase, Andrew G. Webb
Experimentelle Physik V (Biophysik), Universität Würzburg, 97074 Würzburg, Germany

Introduction

Nuclear magnetic resonance (NMR) imaging experiments are often performed on tissues which have been chemically fixed, typically with formalin, during preparation. Since the T_2 of fixed tissue is shortened significantly in formalin [1], the tissue is reperfused in buffered saline before imaging. Bossart et al. have suggested that the T_2 shortening is primarily due to free fixative effects in the interstitial spaces of the tissue. To investigate further the effects of fixation on a cellular level, we have measured relaxation times on fixed, fixed/ reperfused, and perfused-only Xenopus laevis oocytes.

Experiments

We performed our experiments on a Bruker Avance750 spectrometer at 17.6T, with imaging gradients of 1T/m, using a Bruker solenoid coil with an inner diameter of 2.5mm. T_1 maps were acquired using saturation recovery magnetization preparation prior to a 2D spin echo imaging sequence, T_2 maps using a CPMG preparation prior to imaging. The spatial resolution was $(20\mu m)^2$ in-plane with a slice thickness of 200μm. Total acquisition time was 3h. The relaxation time maps were obtained using monoexponential fit functions. One group of Xenopus laevis oocytes was fixed using formalin solution several weeks before the experiments Some of these oocytes were transferred to Barth's medium several hours before the experiments, while others were imaged in the formalin solution. A second group of oocytes was isolated and placed immediately into Barth's medium.

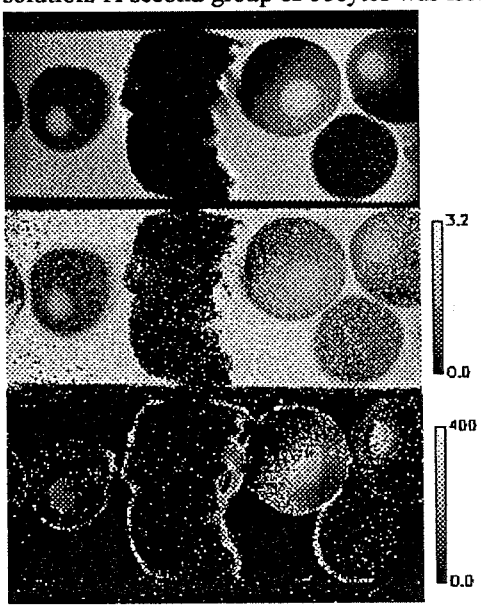

(top) 2D Spin echo image of the cell sample (left:fixed/perfused oocyte, right: perfused oocytes), FOV 5.0x2.5x2.5 mm³, (center) T_1-map (T_1 in s), (bottom) T_2-map (T_2 in ms).

Results

The calculated relaxation times in the nucleus are presented below.

	T_1 (s)	T_2 (ms)
perfused only	2.0 ± 0.1	222 ± 28
fixed/reperfused	1.37 ± 0.1	77 ± 13
fixed	1.23 ± 0.07	-

Discussion

The formalin fixation process shortens both the T_1 and T_2 of the nucleus, with T_2 affected to a greater degree. These intracellular measurements agree with extracellular measurements of Bossart et al. [1]. However, even after perfusion in Barth's solution, the results show that the nuclear T_1 and T_2 values are reduced substantially with respect to unfixed cells. One possibility is a limited penetration of Barth's solution into the cell post-fixation. Another possible cause is the formation of double adducts between formalin and proteins in the nucleus: these produce methylene bridges that are not easily broken, unlike the single adducts which can be reversibly broken by perfusion with buffered saline. We are currently performing experiments to clarify the explanation for the relaxation time measurements. We also note that the visible subdivision of the cytoplasm into animal and vegetal hemisphere in perfused cells (see figure) is no longer observable in the fixed cells. We are, therefore, also investigating the effects of fixation on lipid composition and relaxation times using the methodology of Sehy et al. [2].

References

[1]. E.L.Bossart, B.A.Inglis, X.S.Silver and T.H.Mareci, *7th ISMRM*, Philadelphia 1999, p1928.
[2] J.V. Sehy, J.J.H. Ackerman, J.J. Neil, *Magn Reson Med* **46**, 900-906 (2001)

MR-Histology: Embryonal and Fetal Brain Development in Bovines

D. Haddad, A. Purea, M. Schmidt*, M. Haas-Rioth*, H.H.A. Oelschläger*, A. Haase
Experimentelle Physik V (Biophysik), Universität Würzburg, 97074 Würzburg, Germany
*Dr. Senckenbergische Anatomie (III), Johann Wolfgang Goethe-Universität, Frankfurt a.M., Germany

Introduction: MR-Histology is a fast and efficient alternative to conventional histological sections when then contrast and resolution obtained in the MR images are sufficient to answer the biological or medical questions of a specific study. This is often the case in 'soft-tissue studies', since in this type of tissue MR methods are able to provide a distinct and adjustable contrast. In these cases, MR-Histology leads to the desired information without the tedious preparation process which is necessary for conventional histological sections.

Here we present first results of an ongoing study on the development of the brain in prenatal bovines. The study is performed, because neither zoological nor veterinary anatomical textbooks provide detailed information about bovine brain development and therefore comparative studies with other mammals are still impossible. Especially allometric growth and differences in the development of the brain are key issues in this context.

Seven formalin fixed specimens at different stages in the prenatal bovine development were chosen. Their crown-rump-lengths (CRL) range from 1.8 to 8.0 cm, thus covering a large period in the prenatal bovine development. The smaller embryos still show the common mammalian organization, whereas the larger fetuses already exhibit typical bovine features like rudiments of the hooves. On account of the high water content, preparation of embryonic brain tissue in toto without severe damage is almost unfeasible. MR-Histology leaves the embryos uninjured, and provides life-like renderings of the natural structures.

Materials and Methods: All MR experiments were performed on a Bruker Avance 750 spectrometer with 17.6 T and imaging gradients of 1.0T/m. So far, the smaller specimens with CRLs up to 2.9 cm were scanned in a 20 mm Bruker birdcage coil. Different spin- and gradient-echo MR imaging sequences were used, depending on the desired contrast and spatial resolution of the images. Isotropic spatial resolutions of $(58.6\ \mu m)^3$ were easily reached. During data processing a zero-filling by a factor of 2 was applied in each direction.

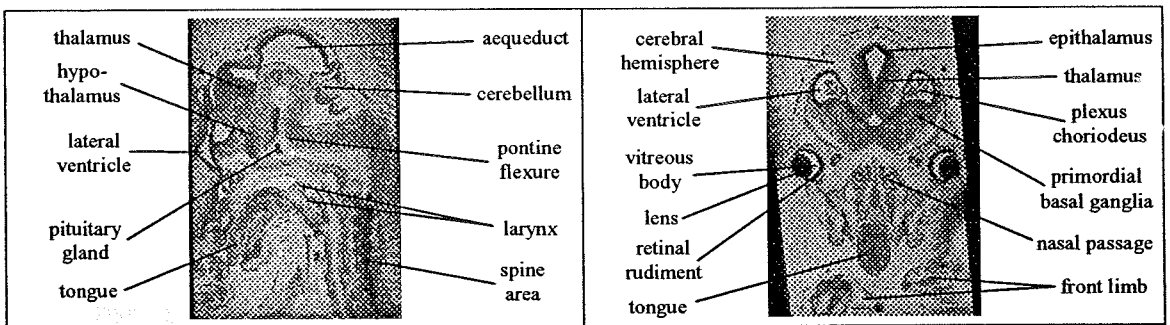

Fig. 1: Sagittal (left) and coronal (right) slices of a fetus with a CRL of 2.9 cm. Different substructures of the brain as well as other morphological details like tongue, larynx and spine are cleary visible. 3D spin-echo sequence, TR:1.9 s, TE:29 ms, isotropic voxel resolution in the images: $(29.3\ \mu m)^3$

Results and discussion: The MR images of the already scanned specimens exhibit various details of the prenatal bovine anatomy. In the brain, different substructures are distinguishable (cf. Fig.1). The eyes, the tongue and the nose with the air passage as well as the larynx are also clearly visible. Furthermore, the upper and lower jaws and the spine are to be seen.

In conclusion, for this study MR-Histology was able to provide the desired anatomical details to visualize the prenatal brain development in bovines. After the acquisition of 3D datasets of the remaining specimens, the MR images will be segmented manually in order to perform surface reconstructions of the different parts of the brain. With these reconstructions, the development of the bovine brain can be displayed three-dimensionally and the volumes and surface areas of the brain's subcompartments can be calculated. This allows a quantitative comparison with the brain development in other mammals.

Magnetic Resonance Microscopy of Tissue Engineered Phalanges

Kimberlee Potter[1], Paul Anderson[2], Noritaka Isogai[3], William Landis[4]
[1]Armed Forces Institute of Pathology Annex, Rockville, MD, USA, [2]Queen Mary College, University of London, London, UK, [3]Kinki University School of Medicine, Osaka, Japan, [4]Northeastern Ohio Universities College of Medicine, Rootstown, OH, USA

Introduction: Tissue engineering intends to fabricate biological materials for the augmentation or replacement of impaired, damaged or diseased human tissue (1). In this context, novel models of human phalanges have been developed recently through suturing of polymer scaffolds supporting osteoblasts, chondrocytes, and tenocytes to mimic bone, cartilage, and tendon, respectively. Characterization of the model constructs has been accomplished previously through histological and biochemical means, both of which are necessarily destructive to the constructs. This report describes the first application of MRM to evaluate non-invasively the spatial arrangement and developmental status of tissues within an engineered phalanx.

Experimental: Tissue-engineered phalanges were prepared by suturing two polyglycolic acid scaffolds seeded with bovine chondrocytes to the ends of a polyglycolic acid/poly-L-lactic acid copolymer wrapped with a sheet of bovine periosteum as described previously (1). Constructs were maintained in athymic mice for up to 38 weeks. At the end of the implantation period, constructs were removed from the host animals, dissected free of connective tissue, and subjected to further analysis by MRM, XMT, and routine histology. MRM images were acquired on a Bruker DMX spectrometer coupled to a wide-bore magnet operating at 9.4T. Quantitative T2, PD, and MT maps had a nominal in-plane resolution of 70 μm and a 1-mm slice thickness. MT maps were calculated using the following equation: [1 – Mso/Mo], where Mso/Mo gives the ratio of image intensities acquired with and without the application of a 5-s, 12- μT saturation pulse, 6000 Hz off-resonance. Mineral density maps were calculated from XMT images, with 15 μm isotropic resolution, acquired with an X-TEK HMX system as published (2). Model phalanges were embedded in paraffin and consecutive sections were stained with H&E and Alcian blue to reveal morphologic and compositional information, respectively.

Results and Discussion: A histologic section through a model human phalanx, dissected 38 weeks after implantation, is shown in **Fig. 1A**. A significant feature was the appearance of a rudimentary growth plate at the cartilage-bone junctions at each end of the construct. The subjacent bone with intervening matrix was similar in appearance to trabecular bone and much of the white space observed in the whole-mount section was attributed to clusters of adipocytes. Finally, interpenetrating blood vessels were located in the cartilage-filled central cavity. T2 and PD maps of the construct confirmed that the tissues at the ends of the construct and within the central cavity were hydrated. The high MT values for these tissue elements indicated that the matrix was cartilaginous (3,4). In contrast, the matrix found in the construct mid-shaft had low T2 and PD values which suggested a considerably less hydrated tissue. This result was consistent with a heavily mineralized tissue (5). Notably, there was a higher density of mineral on one side of the construct (left of Fig. 1B) compared to the other (right of Fig. 1B). This mineral distribution was consistent with that observed in the mineral density map (**Fig. 1C**) extracted from a 3D XMT data set for the same phalanx model. XMT axial images also confirmed that the mineral density at the ends of the construct was lower than that for the middle of the construct. The spatial distribution of lipid in the construct, determined from fat-suppressed MRM images, was consistent with that observed in the histologic section and was suggestive of possible early marrow elements. By comparing XMT data with MRM images, it was found that the mineral density measured by XMT correlated directly with the T2 relaxation times of water from the same regions of interest. Thus, MRM images can provide a surrogate measure of mineral density.

Conclusions: MRM can be used to monitor changes in both hard and soft tissue elements of a calcifying structure. It can also provide an approximate measure of mineral density based on an assumed uniformity of intervening matrix. This work establishes the value of MRM correlated with XMT in providing unique information on implanted models of human phalanges and suggests application for examining biological responses to such constructs *in vivo*.

Acknowledgements: The authors thank Drs. Asamura and Kusuhara and Ms. Jacquet and Ms. Hillyer for their assistance in the preparation of tissue-engineered constructs. The authors are grateful to Drs. Becker and Sweet for the histology shown.

References: 1. Isogai N et al., 1999 J Bone Joint Surg Am 81:306-316. 2. Wong FS et al., 2000 J Anat 196:405-413. 3. Potter K et al., 1998 Matrix Biol 17:513-523. 4. Potter K et al., 2000 Arthritis Rheum 43:1580-1590. 5. Potter K et al., 2002 J Bone Miner Res 17:652-660.

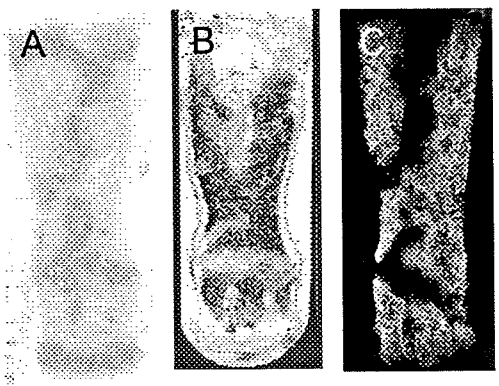

Figure 1. (A) Alcian blue stained section of tissue-engineered phalanx together with corresponding (B) proton density and (C) XMT images.

NMR Relaxation Time of Navel Oranges – A Screening Parameter for Identifying Freeze-Damage

Prem N. Gambhir, Young J. Choi, Michael J. McCarthy
Department of Food Science and Technology, University of California, Davis, CA 95616

The development of a rapid and non-invasive method to detect and separate freeze-damaged oranges is very important for fresh fruit marketing. Proton spin-spin relaxation time (T_2) of peel and juice sac (flesh) parts of varieties of navel oranges have been measured at 10 MHz using Bruker Minispec NMR spectrometer. The oranges were subjected to chilling (~ 5°C) and freezing (~ -5°C) temperatures overnight and thawed to room temperature before peeling for T_2 measurements. The exposure to chilling or freezing temperature did not affect T_2 values of peel, but freezing caused appreciable decrease (~ 15%) in T_2 values of juice sac of the varieties of navel oranges studied.

The T_2 values of whole oranges were also measured at 4.25 MHz using SMIS NMR instrument before and after exposing the oranges to chilling and freezing temperatures. The chilling did not affect T_2 values, whereas freezing reduced the T_2 values by ~ 10%. The bio-exponential fit showed that both long and short components of T_2 decreased due to freeze injury, however, decrease in the short component was relative higher.

The possible cause of reduction in T_2 values when exposed to freezing temperature may be due to break down of membrane of juice sac and leakage of juice to peel parts. The difference in T_2 values between freeze-affected and normal oranges (10-15%) can be potentially used for separation and grading of damaged fruits. The differential values of T_2 of normal and freeze-damaged oranges can be utilized to develop a portable NMR system useable in orchard, post-harvest storage and in-line sorting.

Detection of freeze injury in oranges by Magnetic Resonance Imaging

Natalia Hernández-Sánchez, Pilar Barreiro, Margarita Ruiz-Altisent, Jesús Ruiz-Cabello[(1)], Xavier Gimeno[(2)], Sebastián Idelsohn[(2)], Sandra Aguilar[(2)]
Physical Properties Laboratory, E.T.S.I.A., Polytechnic University of Madrid,
Avda. Complutense s/n, 28040 Madrid, Spain
(1) Instituto de Estudios Biofuncionales, Complutense University of Madrid,
P° Juan XXIII n° 1, 28040 Madrid, Spain
(2) DAUMAR S.A., C/ Guifré 794-796, 08918 Badalona, Spain

Introduction
Fruit and vegetables quality is becoming a mandatory condition in a worldwide market. Nuclear Magnetic Resonance technique allows a non-destructive study of internal properties and may be used on-line for inspection [1][2]. The aim of this work is to study the applicability of dynamic MRI in order to detect freeze injury in oranges, which produces dried flesh and hollows.

Materials and Methods
A set of 6 oranges affected by freeze conditions and a set of 6 unaffected oranges were studied. A Bruker BIOSPEC 47/40 (4.7 T) with a birdcage coil was used. Oranges were conveyed through the spectrometer by a specially designed conveyor. The conveyor controller is connected to the trigger of the BIOSPEC console allowing the synchronization of the motion with the acquisition. Oranges were placed with their central axis along the z direction. Pulse gains, attenuator and shimming settings were adjusted with the first sample and remained unchanged. A fast low angle shot sequence (FLASH), was used to reduce motion effect. The phase encoding direction was selected along the y-axis obtaining axial images at the equatorial fruit zone. The Field-of-view (FOV) was 12×12 cm and the slice thickness was 5.0 mm. Images were collected at 50 mm/s and 100 mm/s as 128×64 points and as 128×32 points (zero-filled to 128×128) with a total acquisition time of 780 and 390 ms respectively; three repetitions were carried out. Images were acquired and reconstructed using the same parameters. The analysis was developed using Matlab. Images were segmented obtaining 2 regions. Region 1 corresponded to the whole orange. The area of an averaged circle was calculated from this region. Region 2 corresponded to the undamaged tissue. Two ratios were calculated:
OUR = (whole orange area / undamaged area); and CUR = (circle area / undamaged area).

Results and discussion
Segmentation was performed with reliable results. Figure 1 shows that any of the calculated ratios allows differentiation of damaged from undamaged oranges by establishing a detection threshold of 1,5. Some difficulties appear when the damage is slight. Repeatability error was 0.13 for CUR and 0.11 for OUR. Images collected at different speed belt and acquisition dimensions showed similar results.

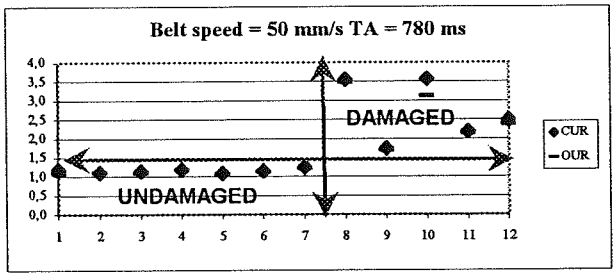

Figure 1: Identification of damaged fruit through the Magnetic Resonance Imaging technique.

Conclusions
Dynamic Magnetic Resonance Imaging gives encouraging results for freeze injury detection. These results are under validation. Optimisation of this application involves optimisation of the segmentation in order to achieve a lower detection threshold.

References
[1] P. Chen, M.J. McCarthy, S.M. Kim, B. Zion, Transactions of the ASAE **39**(6), 2205-2209 (1996).
[2] P. Barreiro, A. Moya, E. Correa, M. Ruiz-Altisent, M.E. Fernández-Valle, A. Peirs, K.M. Wright, B.P. Hills, Appl. Magn. Reson. **22**, 387-400 (2002).

Examples for clinical application of NMR Microscopy

J. Constantin Széles, Jana Kainerstorfer, Bence Csapo, Csilla Balássy, Raschid Hoda, Markus Klarhöfer, Peter Polterauer
Department of Vascular Surgery, University of Vienna Medical School, Vienna, Austria

Introduction
The fast progress in magnetic resonance and computer technology, as well as the growing interest in better spatial resolution give promising prospects for clinical applications. Until now experiments in vivo focused on the human extremities. The best results until now were seen at the human finger.[1] On the other hand in vitro examination, for example of cervical tissue samples, show as a useable method that high resolution magnetic resonance imaging of cervical tissue samples can assist in the identification of both normal and pathologic changes of the tissue. Our in vivo experiments focused on designing a method to investigate the structure and fine morphology of the distal parts of human extremities. The feasibility of in vivo high-resolution magnetic resonance micro-imaging of fine anatomic structures of human toes was tested [2]. In particular, attempts were made to detect Vater-Pacini sensory nerve endings in healthy subjects to define normal MR based anatomy as a basis for future in vivo exploration of pathology in this confined region by MR micro-imaging. In another study, blood flow velocities in the index finger were measured. Further more, we investigated the MR presentation of normal and pathologic anatomic structures in cervical tissue samples[3]. In vitro HR-MR imaging of cervical tissues correlates well with low magnification histology assisting in the identification of both normal structures and pathologic changes. HR-MR imaging allows identification of most elements of the cervical tissue, such as the epithelium and its mucus layer, the connective tissue of the stroma, glands of various sizes, and blood vessels, and adds information about tumor content and margins.

Materials and Methods
For the measurement of the toe, big toes of five healthy individuals were imaged at 3T. Measurements were performed on a Bruker Medspec 30/80, equipped with an asymmetric head gradient system B-Ga33 and a small radio-frequency surface coil. A custom built positioning device was constructed, enabling exact positioning and fixation of feet and surface coil, markedly reducing motion artefacts and also compensating for different foot shapes and sizes. A standard 3D gradient echo sequence was used for imaging. Total acquisition time was 30.7 min. For the blood flow measurement, MR experiments were performed on a 3Tesla whole body scanner. Cervical tissue samples were obtained from five LLETZ cone biopsies and in one case from a surgical specimen of a radical hysterectomy. MR imaging was also performed on a 3T whole body scanner with a strong gradient system.

Results
Measurement of the toe: The feasibility of MR micro-imaging for small structures of the toe was demonstrated in this study. The MR presentation of these structures corresponds well to that observed by high resolution studies of the upper extremity. The important result of this study was that we were able to localize and visualize Vater-Pacini corpuscles. Vater-Pacini sensory bodies in the subcutis of distal human extremities are known to be terminal nerve endings responsible for sensation of vibration. Because of this visualization, MR micro-imaging may become a helpful tool for strengthening the diagnosis of some diseases including diabetic angio- and neuropathy, Raynaud`s phenomenon, alcoholic neuropathy as well as spondyloarthropathy and tophaceous gout, or other systemic diseases presenting in the lower extremities. Blood flow velocity measurement of the finger: Commonly, blood flow velocities in the human distal extremities are obtained by ultrasound investigations. The disadvantage is that they do not provide detailed anatomic information. MR flow measurements provide excellent anatomical information. With MR flow measurement we are able to identify the two bigger vessels in the lower part of the image as arteries and the small one in the lower and the two vessels in the upper part as veins. Cervical Tissue Samples: High resolution MR imaging of cervical tissue samples assists in the identification of both normal structures and pathologic changes. The MR imaging could be used to define the exact tumor staging of the uterine cervix, what is important for clinical examination, for example to avoid a hysterectomy.

References
[1] M. Klarhöfer, B. Csapo, Cs. Ballasy, J.C. Szeles, E. Moser, Magnetic *Resonance in Medicine* **45**, 716-719 (2001)
[2] Széles, Csapo, Klarhöfer et al, *Magnetic Resonance Imaging* **19**, 1235-1238 (2001)
[3] Csapo, Széles, et al, *Investigative Radiology* **37/7**, 381-385 (2002)

Early Detection of Osteoarthritis in Cartilage by μMRI and PLM

Yang Xia, Hisham Alhadlaq
Department of Physics, Oakland University, Rochester, MI 48309, USA

Introduction

Osteoarthritis (OA) is a slowly progressive disease of articular cartilage and is considered one of most common types of arthritis. Via the study of the mobility of water molecules interacting with collagen fibrils and proteoglycans, we recently showed that T2 anisotropy could be used as a sensitive and specific tool to study ultrastructural changes in articular cartilage. The current work aims to detect physical and morphological changes in articular cartilage during the early stages of a canine OA model [1,2], using nuclear magnetic resonance microscopy (μMRI) and polarized light microscopy (PLM) [3].

Material and Methods

Eighteen cartilage specimens from three matched pairs of the medial tibia of a canine OA model were used. For each specimen, eight 2D proton images of 1mm slice were acquired and two T2 maps were calculated at two specimen orientations (0° and 55°) in a 7T magnet, with the pixel resolutions between 13.6 and 23.1μm. Subsequently, mechanical properties of each specimen were tested at the same MRI slice location and the tangent Young's modulus from the stress-strain relationship was calculated. Finally, ten to twenty frozen sections were prepared histologically at the same MRI slice location from each specimen; and 2D retardance and angle images were constructed in PLM. From these μMRI and PLM images, disease-induced changes in tissue were examined across the depth of the cartilage.

Results

Fig 1 shows two proton images from a matched pair of tibia jo from the same animal. The OA and normal specimens displa the same laminar appearance [4], which shows that at the e: stages of OA, the collagen fibril network has not yet suffered se disruption to its structure of three-histological zones. Upon cl examination, several distinct changes related to the disruptior collagen network in early OA tibia can be found. The μM changes include a significant shift in the depth of the maximum T2 peak (Fig 2), a significant decrease in the superficial zor thickness, and a significant increase in cartilage total thicknes These μMRI findings also have a topographical dependency on tl tibia surface since they were not significant in the central locatio of the tibias where there was no meniscus. The μMRI results we confirmed by PLM measurements, and correlated well with tl mechanical properties of the specimens (Fig 3).

Figure 1

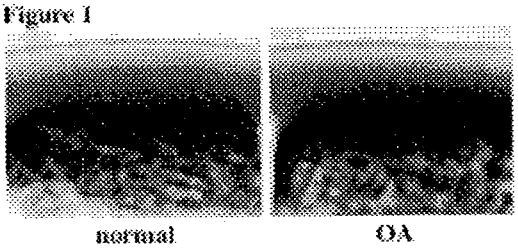

Figure 2

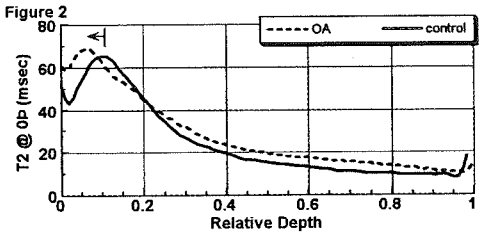

Figure 3

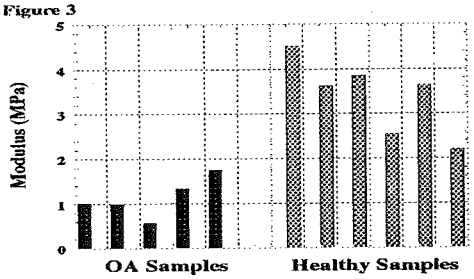

Conclusions

Experimental OA at the early stages is marked with focal lesio of cartilage. We show in this study of animal OA model that μMI is a sensitive imaging technique that has the ability to detect son early signs of the diseases.

References

[1] Alhadlaq H, Xia Y, et al, *The 49th Meeting of Orthopaed Research Society*, New Orleans (Feb 2-5, 2003). [2] McDevitt (Gilbertson E, Muir H., *J Bone Joint Surg Br* **59**(1), 24-35 (1977). [3] Xia Y, Moody JB, et al, *Osteoarthritis Cartilage* **9**(5), 393-406 (2001). [4] Xia Y, *Investigative Radiology* **35**(10), 602-621 (2000).

Acknowledgement: OU (REF Biotech, Bennett NMR Facility), NIH (AR 45172).

Evaluation of Brain Atrophy in PPT Gene-Targeted Mice by MRI

Jeeva Munasinghe [1], Garry Zhang [2], Sandra L. Hofmann[3], Alan Koretsky [1] and, Anil B. Mukherjee [2].

[1] NINDS, [2] NICHD, National Institute of Health. Bethesda. MD. 20892 [3]University of Texas Southwestern Medical Center, Dallas, TX 75390-8593, USA

Inactivating mutations in the palmitoyl-protein thioesterase (PPT) gene causes infantile Neuronal Ceroid Lipofuscinosis (INCL), a heritable lysosomal storage disease. PPT facilitates the degradation of posttranslationally acylated polypeptides by cleaving thioester linkages that connect the lipids with the polypeptides that are acylated. A deficiency of this enzyme leads to abnormal deposition of acylated proteins or peptides (ceroids) causing INCL pathogenesis. Since PPT gene is expressed at high levels in the retina and in the brain, the children afflicted with INCL become blind by 2 years and brain dead by age 4. Recently, a mouse model of INCL has been developed by gene targeting allowing detailed pathophysiologic analyses and the development of novel therapeutic approaches for this disease. Evaluation of potential therapeutic approaches would require techniques to assess the outcome of new treatment modalities. Here we report the preliminary results of evaluation of brain atrophy in PPT-deficient mice by MR imaging.

Age and sex matched PPT knockout (KO) mice (n=5) and wild type (WT) littermates (n=5), were investigated by MRI at 7 Tesla horizontal scanner operating on a Bruker avance platform. Mice were anesthetized with 1.5% isofluorane and the brain was centered in a 32 mm transmit-receive RF coil. Image acquisition was synchronized with the respiration rate. The body core temperature was monitored and maintained at 37^0C using a circulating water pad. Contrast agent, Gd DTPA (0.2 cm^3 /kg), was given via the tail vein. Fast spin echo, multi slice images in the transverse and sagittal planes were acquired to encompass the whole brain; parameters: FOV/slice = 32/1 mm, Resolution = 250 □m, echos = 4, TR/TE = 2500/10 ms. In addition, T_1 and T_2 weighted images were acquired in five selected slices (1 mm apart) using, respectively, spin echo (echo time = 10 ms x 16 echos) and saturation recovery experiments (No. of TR = 5, from 60 ms to 5000 ms). T_1 and T_2 maps were generated using an analysis algorithm.

The gross appearances of the brains from PPT-KO mice are smaller than those of their WT littermates. In addition, in the PPT-KO mice there were clear changes in the space (gap) between the brain surface and the interior surface of the skull but these atrophic variations at different locations were irregular (16-50%). The PPT-KO model showed reduction in brain (Table-1) and increase in ventricular CSF volumes compared with their WT littermates (Fig-1). These results suggest that like the INCL patients PPT-KO mice manifest cortical atrophy and enlargement of the ventricles that are measurable by MRI. Interestingly, in the PPT-KO mice intravenous administration of Gd DTPA readily infiltrated the cortical surface when the WT mouse brain showed virtually no infiltration. This may implicate that the blood-brain barrier is more permeable in the PPT-KO mice. Our results indicate that MR imaging of the brain may be a useful method in evaluating cortical degeneration, ventricular volume and permeability of the blood-brain barrier in PPT-KO mice and therefore, may be useful in evaluating novel therapeutic measures in this animal model.

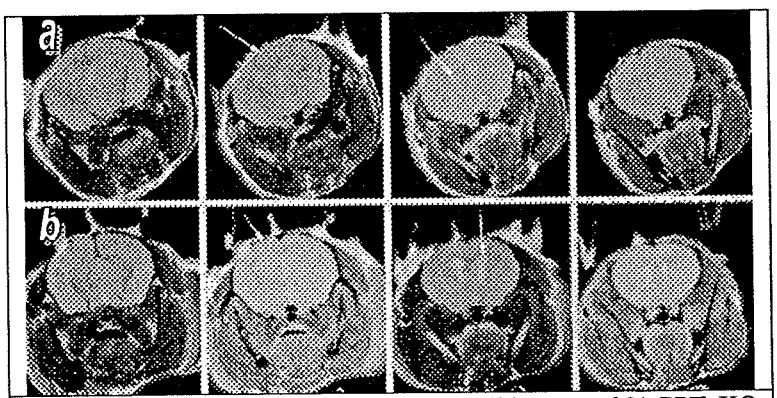

Fig-1: A series of axial 2-D through **a)** Wild type and **b)** PPT_KO mouse brains.

Mouse	WT (cm^3)	PPT_KO (cm^3)
1	0.630	0.508
2	0.629	0.435
3	0.582	0.484
4	0.576	0.489

Table-1: Volume of the brain calculated from 2- D MR images.

High Resolution MRI of Limbs using a Low Cost/ Low Field Resistive Magnetic System.

Dieter Höpfel, Maxim Terekhov
Institut for Innovation and Transfer/Sensorsystemtechnik, University of Applied Science, Moltkestrasse 30, D76133, Karlsruhe, Germany. e-mail: hoepfel@fh-karlsruhe.de;

MR- images of fingers have been acquired with a spatial resolution up to 80 µm/pixel. The magnetic field strength has been only 0.35 T, provided by a pair of Helmholtz- coils combined by an iron yoke. The advantage of this resistive magnet system is that (home built) solenoid rf-coils with a high sensitivity could be used, especially adapted to the fingers. Besides healthy persons also a people suffering on arthritis have been investigated. We are currently installing a new magnet system with a homogenous volume of ca. 13 cm dsv compared to 5 cm dsv, to which we have been limited so far. Bigger limbs (hand, elbow and knee) can then be investigated.

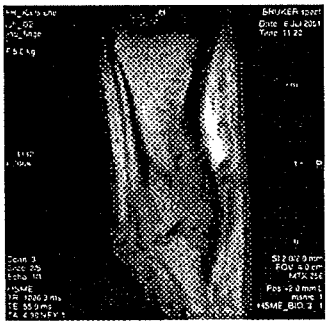

Fig. 1: Finger of a patient suffering on arthritis. Clearly the building of solid bone matter around the joints is visible.

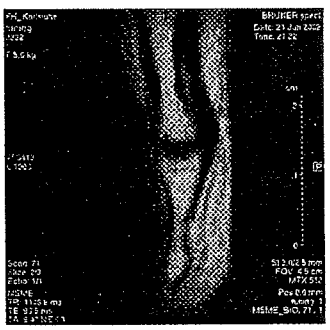

Fig. 2: MR- Image of a (healthy) finger using a 512x512 image matrix resulting at a FOV of 4 cm to a spatial resolution of 78 µm/pixel.

The magnetic field strengths B_0 in clinical MRI-systems has raised in the time during last 20 years from standard value of ca. 0.3 T to 1.5 T, providing high quality MRI images in a normal clinical environment. However, for limbs, especially for fingers, a standard clinical system is usually too expensive and technically not prepared for MRI with a high spatial resolution and the necessary optimized rf-equipment. In our laboratory we used until recently the resistive Helmholtz-coil magnet system with B_0=0.35T (^{1}H resonance frequency of 14.5 MHz) and a homogenous volume of 5 cm dsv (diameter spherical volume). The home-built actively shielded gradient system provides a maximum gradient strength of 200 mT/m at the current of 100 A. The main advantages of this equipment are: the relatively low cost, the easy access for the patients and the possibility of using solenoid probe coils. The disadvantages however are: the low signal sensitivity due to the low field and the limited homogenous volume.

The achievable spatial resolution of MR-image finally is restricted by the ratio of the acquired signal to noise (S/N). To improve the sensitivity we used a Multi-Slice-Multi-Echo pulse sequence (MSME), adding 6 echo signals per image. The echo time T_E varied between 10 and 20 ms, resulting in acquisition times in the range of 60 to 120 ms for each image voxel. The T_E depends on the desired resolution and gradient strength. Typically the images of 5 slices with a thickness between 1 and 2 mm were acquired in each experiment.

To optimize the rf-probe regarding signal/noise (S/N) ratio, the solenoid coils with a standard length-to-diameter ratio (≈1) have been used which provide a factor of 3 higher S/N ratio compared to a "birdcage" rf-coil with the same volume [1]. The acquisition time being proportional to $(S/N)^{-2}$ thus can be reduced by using the solenoid coil by a factor of 9 for the same resolution.
Spatial resolutions of 160 µm/pixel (256x256 pixel matrix) in measuring times between 4 and 5 minutes were achieved. As an example in **Fig 1** the MR-image of a patient suffering on arthritis is shown. The image in **Fig 2** represents the finger of a healthy person with a 512x512 pixel matrix resulting in a spatial resolution of 78 µm/pixel, acquired in only 9 min and providing a good quality for medical application.

We are currently exchanging the magnet system to another one which provides the field strength of B_0=0.5 T and a homogenous volume of 13 cm dsv. This will give us the possibility to measure also limbs like a hand, elbow, foot or knee. The main advantage of our system will be the easy access and the low cost. With optimized rf-probes we should be able to measure also these limbs with a high spatial resolution in a reasonable time and quality.

References

[1] Callaghan P. T., *Principles of Nuclear Magnetic Resonance Microscopy, Oxford Press, New York,* (1995).

Applications of surfactant micelles as a sensitive NMR probe in physics of biopolymer systems

Anatoly A. Khripov, V. I. Chizhik, K. Nishinari
Department of Physics, St. Petersburg State University, 198504, Petrodvoretz, St. Petersburg

This article presents recent results obtained in our laboratories on studying a microstructure of polyelectrolyte-surfactant aqueous systems using NMR, DSC, CD and rheology methods. It could be summarized as follows[1-8]:
1. The same charged surfactant micelle with sizes comparable to a network pore raduis in a polyelectrolyte solution is a a sensitive NMR probe that provides a quantitative information on the network geometry (fiber and pore sizes, microinhomogeneity scale) in a very wide range $0.1\text{-}10^6$ nm. The important feature of the method is an opportunity to monitor geometrical changes of the network during sol-gel transitions caused by temperature variations in a range 15-90 ^{0}C.
2. New diffusional cell was developed to trace the spacial NMR parameters during forming of crystal nanostructures of gel-surfactant systems without the removal of buffer surfactant solution. It is quite actual as such processes greatly depend on the preparation conditions.
3. New strategy is proposed to capsulate the low soluble and protein drugs in a hydrogel-surfactant micelle systems. PGSE NMR studies suggest the appications of such systems in control drug release technology. The work is initiated on a capsulation of human interleikin in gellan gum-surfactant-water system.
4. It was experimentally found that a molecular transport in biopolyelectrolyte-the same charged surfactant-water systems is similar to a one of hydrocarbons in zeolites. On that basis we are developing design variants of molecular sieves for water cleaning applications.
5. A method was proposed to monitor a drug transport solubilized in surfactant micelles inside a human body using MRI relaxation maps. A new express method of reconstruction of spin-relaxation maps was developed. The study is going on an earlier MRI diagnosis of osteoarthritis.
6. Several results are obtained on a theoretical description of the molecule diffusion in inhomogeneous polymer networks. Analytical formulas for diffusion tensor components are calculated using an apparatus of mesomorphic complex functions.

The work was supported by Russian Ministry of Education (Grant RF TO2-10.1-3375), St. Petersburg Mayor Office (M96-2.2D-869), Russian-Japan Exchange Program of the Universities of St. Petersburg and Osaka and Deutche Forschungsgemeinschaft (collaboration with Prof. R. Kimmich's group).

References

[1.] Physical Chemistry and Industrial Applications of Gellan Gum (ed. K. Nishinari), Progr. Colloid. Polym. Sci., 114 (1999)
[2.] V. I. Chizhik, A. A. Khripov, K. Nishinari, Abstracts of the 6th Intern. Conference on "NMR in Porous Media", Ulm, Germany, P99 (2002)
[3.] A. Khripov, V. Chizhik, Yu. Tschernichev and K. Nishinari, Abstracts of the 5th Liquid Matter Conference, Konstanz, Germany, pp. 120 (2002)
[4.] A. A. Khripov, V. I. Chizhik, Yu. S. Tshernishev, St.Petersburg State U. Letters Ser. 4, No. 1, pp. 122-123 (2002)
[5.] A. A. Khripov, PhD Thesis, St. Petersburg State University (2002)
[6.] A. A. Khripov, N. A. Mitrofanov, N. A. Karlova, V. I. Chizhik, Proceedings of the Interm. Conference on Molecular dynamics, Yalchik, Bashkortostan, pp. 41-45 (2003)
[7.] V. I. Chizhik, A. A. Khripov, K. Nishinari, Phase States of Gellan Gum – SDS –water system, Mol. Liquids, in press (2003)
[8.] A. A. Khripov, V. I. Chizhik, B. A. Scherbakov, Biopolymer Gels, Chemical Reviews (Russia), in press (2003)

INDEX

INDEX

INDEX

INDEX

INDEX

INDEX

INDEX

INDEX

INDEX

INDEX